UNIVERSITÉ PARIS-NORD
INSTITUT GALILÉE

LABORATOIRE DE PHYSIQUE DES LASERS

THESE DE DOCTORAT DE L'UNIVERSITÉ PARIS XIII
Spécialité : Physique

présentée par
Bruno Naylor

pour obtenir le titre de
Docteur en Physique

Sujet de la thèse : Quantum gases of Chromium: thermodynamics and magnetic properties of a Bose-Einstein condensate and production of a Fermi sea

Soutenue le 6 Décembre 2016, devant le jury composé de:

M.	**Antoine BROWAEYS**	**Rapporteur**
M.	**Fabrice GERBIER**	**Rapporteur**
M.	**Vincent LORENT**	**Président du Jury**
M.	**Matteo ZACCANTI**	**Examinateur**
M.	**Laurent VERNAC**	**Co-directeur de thèse**
M.	**Bruno LABURTHE-TOLRA**	**Directeur de thèse**

Remerciements

Dans cette thèse, je vais présenter les résultats scientifiques de l'équipe Gaz Quantiques Dipolaire du Laboratoire Physique des Lasers des trois dernières années. Il est évident que les résultats présentés dans ce manuscrit ne sont pas le travail d'une seule personne. Ces résultats sont le fruit du travail de toute l'équipe GQD et de tout le laboratoire. Je voudrais toutefois rendre compte du travail et de l'aide de chaque personne.

Je voudrais commencer par remercier mes directeurs de thèse: Bruno et Laurent. Il m'est difficile de concevoir de meilleurs directeurs que vous. J'ai vraiment le sentiment que vous m'avez fait grandir, tant d'un point de vue scientifiques qu'humain. J'espère que je pourrais un jour vous apporter quelque chose aussi. Bruno, en plus de tes capacités scientifiques, tu as un don avec les gens. Tu sais les comprendre, te faire comprendre, donner confiance, et à partir de là tout échange est plus facile. Quand tu es là, j'ai l'impression que tout est facile et faisable. Par ailleurs, je voudrais te remercier de m'avoir redonné le goût de la lecture. Je n'avais pas lu de livres non scientifiques depuis le lycée, et tu m'as fait découvrir des textes/livres incroyables. Laurent, la clareté de ton raisonnement et ta pédagogie sont très enviables. Ton soutient inconditionnel pendant ma thèse a été très essentiel: dès que j'avais besoin de toi tu étais là. Que ce soit pour des prises de données, comprendre la physique, les dernières repet' (si precieuses!), mais aussi pour le canon de la victoire bien mérité après de nombreuses semaines/mois de dur labeurs! Par ailleurs, il nous a fallu trois ans pour nous trouver à "la fête" (un accomplissement en soi), j'espère qu'à présent nous nous retrouverons sans encombres!

Le laboratoire a été un endroit d'épanouissement scientifiques formidables pendant ma thèse. Cela n'est possible que parce que chaque membre participe à son bon fonctionnement et je vous en remercie. Je voudrais remercier ici en particulier Solen, Maryse, et Carole de l'administration; Fabrice, Haniffe et Germaine, de l'atelier électronique; Albert et Samir de l'atelier mécanique; Marc et Stéphane de l'atelier informatique; et Thierry de l'atelier d'optique. Chacun d'entre vous m'a été d'une grande aide pendant mon temps au LPL.

L'équipe GQD a quatres autres membres permanents qui assure le bon fonctionnement de l'équipe: Olivier, Etienne, Paolo, et Martin. Même si nous ne travaillons pas forcément toujours sur le même projet cela ne les a jamais empêché de m'aider, me débloquer, ou juste prendre un café et discuter. J'ai aussi eu la chance de travailler avec Johnny qui venait régulièrement des Etats-Unis, son entousiasme débordant pour la physique a toujours été un grand bol d'air frais pour l'équipe.

Je voudrais remercier toutes les personnes qui ont, à un moment, travaillé en salle Chrome et en particulier Aurélie qui m'a appris tous les rouages de la manip'. A vous tous, vous m'avez confié une manip' en très bon état. J'espère que je l'ai laissé en tout aussi bon état à mes successeurs. Steven, Lucas, Kaci, je n'ai pas l'ombre d'un doute quand aux succès futurs de l'équipe Chrome et je vous souhaite beaucoup de plaisir. Je voudrais particulièrement remercié Steven: nous Nous sommes Cotoyés seulement quelques Mois sur la Manip' mais, du moins de mon point de Vue, cela a été Suffisant pour créer un Lien fort (bon j'arrête de te taquiner avec mon habitude de mettre des majuscules partout...). Les interactions avec toi m'ont beaucoup appris. Je regrette que nous n'ayons pas pu travailler ensemble plus longtemps!

Le soir nous avions pour habitude de partir en équipe, mais le matin être dans le même train que l'un de vous était le fruit du hasard. Malgré le fait que vous soyez les gens avec qui je passais toute ma journée, tous les matins je me réjouissais de vous croiser et de pouvoir discuter avec vous sur le chemin du labo. Merci à vous tous mais aussi aux nombreu-se-s autres collègues du laboratoire pour ces moments.

Je tiens également à remercier l'ensemble du Jury d'avoir accepté un tel rôle, surtout quand cela impliquait un long déplacement. En lisant les remerciements de thèse de collègues, je ne comprenais pas bien pourquoi on remerciait le jury. Je comprends maintenant que chacun de vous a donné énormement de son temps (j'ai encore un peu honte de la longueur de mon manuscrit...) afin de comprendre ce que j'ai voulu dire, m'apporter des commentaires, me poser des questions, bref me faire progresser. Je vous en suis très reconnaissant.

Au moment d'écrire ces remerciements, je repense aux moments partargés (la plupart du temps autour d'un café) avec les thésard-e-s de Paris 13. Les "plus vieux": Camilla avec ton énergie et ta bonne humeure débordante, Dany qui est en quelque sorte mon grand frère thésard, Daniel avec qui on a partagé de longues conversations sur l'avenir; mais aussi les plus jeunes: Franck, Mathieu, Joao, Amine et Thomas. Vous êtes la jeunesse du labo et je vous souhaite du courage pour ceux qui n'ont pas fini, et du courage pour ceux qui ont fini (car oui n'oublions pas quand même la réalite de la vie de la recherche...).

Je ne pense pas qu'une thèse puisse être accompli sans le soutien d'amis et de proches. J'ai eu la chance d'avoir le soutient de nombreuses personnes pendant mes études. A commencer par mes parents, qui se sont toujours assurés que je puisse étudier dans les meilleurs conditions possibles et qui m'ont soutenu dans les moments difficiles. Merci à ma mère d'avoir pu etre présent pour la soutenance, et à mon père pour la relecture du manuscrit. Merci à Martin d'avoir été à la soutenance, de m'avoir suivi et soutenu tout au long de mes études. Mes fréres et soeur, quelle chance j'ai d'avoir partagé tant de bons moments avec vous. Adam, malgré toutes les bêtises que je te dit, ta vie est une inspiration pour moi. Alice, ton entousiasme pour toutes les choses que tu fais est incroyable et je compte sur toi pour réussir à avoir des matchs de water polo à chaque endroit où je serais! Carl, toujours là pour moi et avec qui les études à Grenoble ont été marqué par les Simpsons... Et Peter, mon partenaire

de crime. Je voudrais particulièrement te remercier Pet', tu as été à Paris avec moi pendant les études, tu as toujours été partant pour m'aider pour tous mes problèmes informatiques, de codage (je suis désolé que la soutenance s'est fait sous windows...), mais aussi pour tous les moments de détente. Quelle chance j'ai eu que tu sois à Paris aussi. Ta présence auprès de moi, pour ce qui est pour le moment la totalité de ma vie, est nécessaire je pense à mon bien être. Merci à Julien et Laure, maintenant que vous êtes professeur des écoles, je comprends comment cela a été possible que vous ayez eu la force de nous supporter tout ce temps...

J'ai eu, tout au long de ma vie, de nombreux amis qui m'ont guidé et soutenu. Je voudrais les remercier ici. Tout d'abord le commencement: le lycée. Merci à vous de ne pas m'avoir abandonner même si je donnais trop peu de nouvelles. Aude, Jean, Louis, Louis, Marion, Marion, Pauline et Simon pour avoir continuer à garder notre groupe vivant. Antoine, Felix, Quentin, pour continuer de me faire sortir dans Paris. Merci à Julien K. (un autre partenaire des Simpsons!), Mathieu G., Etienne B., Quentin et Robin pour mes années à Grenoble, nos discussions ont eveillé ma curiosité scientifique. Merci à tous les copains et copines que j'ai rencontré à Paris, que ce soit en classe ou en dehors: Alexandra, Alexis, Arnaud, Charlie, Cyril, Enzo, Erwan, Félix, Frankek, François, Fyf', Martin, Michou, PVG, Thibault. Vous m'avez fait passer de superbes années. Enfin un grand merci à Valentine, qui est probablement la personne qui m'a suivi tout au long de mon "parcours", pour toute ton amitié et aussi (et surtout!) de me permettre de jouer encore aux tarots. Merci aux copains de rando: Camille, Florian, Lucas, Maité, Mathilde et Romain, pour les belles aventures, le tarot, et tous les bons moments passés ensemble (et encore beaucoup à venir!).

Pendant ces années de thèse, j'ai aussi eu le soutien de la coloc'. Antoine, Camille, Léo, Marie, Marion, Martin, Nelly, Pet', Thibaud, Tommy, il y a eu tellement de moments inoubliables, que ce soit les cours du soir de "Darts", les "séances cinémas", les belotes, le ping-pong, la pétanque, le traditionnel sushi, les chutes en velo (je ne donnerais pas de noms...) et j'en passe. J'espère n'oublier aucun de ces souvenirs...(mais bon vous connaissez ma mémoire...). Je tiens néanmoins à preciser que je compte revivre de tels moments avec vous quelque part au long de la route. Vous êtes ma deuxième famille et vous quitter a été "la dure... réalité"... Je voudrais prendre quelques lignes pour remercier en particulier Antoine, qui est venu lancer le projet de refroidissement du fermion. On m'avait mis en garde de la difficulté que c'est de travailler avec un ami. Je pense qu'en effet ce n'est pas toujours évident, mais avec toi ça l'a été. Quel plaisir ça a été. Toi aussi tu as un don avec les gens (décidemment tous les gens que je connais ont des dons...). Sans vraiment croire à l'eventualité que nous soyons tous les deux dans la recherche plus tard, j'espère revivre de tels moments encore. Enfin et surtout, je voudrais remercier Camille. Qui a du le plus me supporter pendant cette thèse et avec qui j'ai partagé tellement de bons moments. J'espère que tu t'es autant marrer que moi pendant ces années et je te garantis qu'on va s'eclater comme des patates encore et encore!

Contents

Introduction

Degenerate gases

Following Bose's seminal work on the statistics of photons [1], Einstein predicted that below a certain temperature a system of bosons cross a phase transition [2]. Below this critical temperature, bosons behave as non-interacting particles which may accumulate in the ground state of the system. In honour of their work, this is called a Bose-Einstein Condensate (BEC). The size of this quantum object can be arbitrarily large without adding to the complexity of the problem because the BEC behaves as one quantum object. This is particularly appealing since it enables the exploration of the quantum world with a macroscopic object. Despite how appealing a BEC is, its production remained elusive for 70 years. Intensive laser developments and cooling techniques [3, 4, 5] paved the way for the first production of a BEC in 1995 with Rubidium atoms, closely followed by the condensation of Sodium atoms and Lithium atoms [6, 7, 8].

This opened up the very active field of quantum gases. Since, many other atomic species have been Bose condensed with each atomic species having its own specificity. Potassium and Cesium were cooled to degeneracy [9, 10]. These species have broad and easily accessible Feshbach resonances, enabling tunable control of contact interactions [11, 12, 13]. Soliton behaviour as well as exotic three particle states called Effimov states were observed with such atoms [14, 15]. Atoms with non-negligible dipole-dipole interactions have been condensed. First Chromium [16], then Lanthanides of Dysprosium [17] and Erbium [18]. Two valence electron atoms (alkaline-earth atoms), such as Calcium or Strontium have also been cooled to degeneracy [19, 20]. Ytterbium has been cooled [21] and with Strontium it is particularly interesting since these elements have very narrow optical transitions ("clock" transitions) which enable precise measurements and also they display an appealing universal $SU(N)$ behaviour.

Physicists were also preoccupied in studying fermionic degenerate gases. The degeneracy of a Fermi gas is not characterized by a macroscopic occupation of the ground state. Pauli principle forbids two fermions to be in the same quantum state. Despite its interest, a degenerate Fermi gas was produced only some time after the first degenerate Bose gas [22]. This is associated with the difficulty in thermalizing polarized fermions, owing to Pauli principle. Since then, many fermionic degenerate gases have been produced, and the study of the Fermi gas became a very intense field of research at the beginning of the year 2000's.

Contact Interactions

Interactions are not necessary in order to explain Bose-Einstein Condensation (which is intrinsically due to Bose statistics). Nevertheless they are of fundamental importance in the physics of Bose Einstein condensates. The main interaction in most BEC experiments is the Van der Waals interaction. The Van der Waals potential is short-ranged and isotropic ($V_{VdW} \propto 1/r^6$). At very short distance, the interaction potential is complex and an exact description of the interaction often makes calculations challenging if not unfeasible. In cold atoms, the real potential is accounted for by a pseudo potential, which takes the form:

$$V(r) = \frac{4\pi\hbar^2}{m} a_S \delta(r) \tag{1}$$

for a pair of atoms in molecular spin state S, where $\delta(r)$ is the Dirac's delta-function (thus branding these interactions as contact interactions), $\hbar = h/2\pi$ with h Planck's constant, m the atom mass, and a_S the scattering length associated with the molecular potential of spin S. Interactions are so basically important that they fix the size of the BEC and give it a parabolic shape (in a trap and in the Thomas-Fermi regime [23]). The molecular potential through which atoms interact thus depends on the spin state of each colliding atom. This is because contact interactions depend on the spin state of the pair of colliding atoms through the molecular potential specific to the spin of the pair, S (i.e. a_S depends on S).

Chromium

The first experiment on BECs only dealt with one spin state. Despite how interesting that is, physicists also turned their attention to producing BEC in several internal spin states [24, 25]. This is often referred to as spinor BECs. Despite the large number of atoms and molecules produced in the cold regime, not all are well suited for the study of spinor physics. In this thesis, we will be particularly interested in spinor physics.

Chromium, with its large spin s=3, is particularly well suited for this. It has 7 spin states which can all be trapped equally in optical dipole traps. In the optical dipole trap atoms of different spin states may interact through contact interactions. Due to the large number of spin states, there are several possible molecular channels a_S for atoms to interact through. This leads already to very rich physics. For example, the ground state of the system, which is the state of lowest energy, results from a competition of the different interaction energies associated to different molecular potentials.

Besides contact interactions, other interactions may take place. In the case of Chromium, its six valence electrons yield a relatively strong magnetic dipole moment $\mu = 6\ \mu_B$ with μ_B Bohr's magneton. The dipole-dipole interaction potential between

two atoms of magnetic moment $\vec{\mu}_i = g_s \mu_B \vec{s}_i$ separated by $\vec{r}$ is:

$$V_{DDI}(\vec{r}) = \frac{\mu_0 (g_s \mu_B)^2}{4\pi r^5} \left(r^2 \vec{s}_1 . \vec{s}_2 - 3(\vec{s}_1 . \vec{r})(\vec{s}_2 . \vec{r}) \right) \tag{2}$$

with g_s the Landé factor, and μ_0 the vacuum permeability. This interaction differs substantially from contact interactions since it is long range and anisotropic. This allows for atoms to collide even though they are not close together. Dipole-dipole collisions, as contact collisions do, have spin exchange collision channels (where the total spin is conserved) but also dipolar relaxation channels. In a dipolar relaxation process, the spin projection is not conserved, it is the total angular momenta of the pair of atoms which is conserved. Spin (meant here as longitudinal magnetization) is not a good quantum number.

There are only a few quantum gas experiments with non-negligible dipole-dipole interactions, and they have recently attracted a lot of interest, with many experiments around the world being built. Our focus is two-fold: (i) the impact of dipole interactions on the magnetic properties of a BEC of atoms with large spin and (ii) observe spin dynamics due to dipolar interactions. A Chromium gas is particularly well suited. It has a long lifetime in a conservative trap which allows for study of its thermodynamic quantities. Chromium can also successfully be loaded in a lattice. There, atoms in different sites can be coupled and lead to spin dynamics.

The recent production of Dy and Er ultracold gases [17, 18], with larger dipolar interactions and tunable interactions [26, 27], may hamper the edge Chromium once had. The Dysprosium and Erbium experiments have produced quantum droplets [28, 29]. Contact interactions are tuned to small negative values, then dipolar interactions and quantum flucutations stabilize the gas [30]. The hydrodynamic properties of this system promise to be fascinating.

Other systems than a Chromium BEC, such as Rydberg atoms or polar molecules have been produced and display large dipole-dipole interactions [31]. Polar molecules display a large electric dipole interaction and lead to strong dipolar effects. However, polar molecules are yet to be put in the degenerate regime due to bad collisions during the cooling process (even though there are experiments close to degeneracy [32, 33]). It is the same collisions which prevent polar molecules from being stable in the bulk long enough for any thermodynamic purpose. However, polar molecules have been successfully loaded in an optical lattices [34]. The low filling factor achieved is compensated by the large interactions they display. Rydberg atoms consist of atoms with one of their electrons in a highly excited state. The higher the excited state, the stronger the interaction but the shorter the lifetime of the Rydberg state. The recently demonstrated control in preparing experiments with larger and larger Rydberg atoms provides exciting venues for the field of quantum mechanics [35, 36].

This thesis

I started my PhD in October 2013 in the Dipolar Quantum Gas group at the University Paris XIII under the supervision of B. Laburthe-Tolra and L. Vernac. Most of the work and results performed by the group during my three years at the Laboratoire Physique des Lasers are summed up in the following. I decided to present our work in three parts.

Part One

Part I describes the experimental setup I used throughout my PhD.

In chapter 1 I present the experimental setup which produces a Chromium BEC. Due to the fact that Chromium does not have a closed cooling transition and owing to large light assisted inelastic collisions, it was particularly challenging to produce a Chromium BEC. Here I will describe the apparatus and tools developed by my predecessors to produce a BEC, but also the modifications which took place during my PhD.

In chapter 2, I present the experimental work performed at the start of my PhD where we set up a new laser system specifically dedicated to the fermionic isotope of Chromium: ^{53}Cr. I present the different spectral lines used for cooling and trapping atoms in a Magneto-Optical-Trap. Finally I present our strategy to load a maximum fermionic Chromium atom number in a conservative trap where evaporative cooling may take place.

Part Two

Part II is dedicated to thermodynamic properties of a Chromium gas and we will be particularly interested in collisions, thermalization processes, and in the role of spin degrees of freedom.

The chapter 3 will act as an introduction to materials used in this part. We will discuss the study of interactions and of thermalization of the internal and external degrees of freedom due to contact and dipole-dipole collisions. We will distinguish two types of collisions: coherent and incoherent collisions. Both processes involve the internal and external degrees of freedom and may lead to spin dynamics. It is therefore crucial to be able to pinpoint to the origin of spin dynamics. We will illustrate coherent and incoherent spin dynamics with two experimental results. The experiment of coherent spin dynamics was not performed during my PhD, this result was observed during Aurelie de Paz's thesis [37]. However, I studied the agreement of the observed spin oscillation with our understanding of coherent spin collisions. We then discuss an experiment performed during my PhD. Here we prepare approximatively half of the atoms in $m_s = -3$ and half in $m_s = +3$. We observe spin dynamics due to contact interaction. We established a theoretical model based on incoherent collisions

to account for our data with one free parameter: a_0 the scattering length associated with the molecular potential S=0. The model which best fits the data yields a_0. This value was unknown at the time. We find $a_0 = 13.5^{+15}_{-10} a_B$. This measurement has deep consequences for the ground state properties of a Chromium gas: the ground state is then predicted to be cyclic.

In chapter 4, we present results of the co-evaporation of a Bose-Fermi gas to degeneracy which led to the production of a Chromium Fermi sea of approximatively 1000 atoms at $T/T_F \sim 0.66$. Evaporation relies on efficient thermalization of the mechanical degree of freedom. We analyze the thermalization process during evaporation and are able to estimate the favourable value of the scattering length associated to collisions between bosons and fermions. We measure $a_{BF} = 80 \pm 10 a_B$ with a_B the Bohr radius.

In chapter 5, I discuss the main part of my thesis where we focus on the thermodynamics of a Bose gas with a spin degree of freedom. We start by introducing the basic thermodynamic properties of an ideal Bose gas with a spin degree of freedom which displays 3 phases. Phase A corresponds to a thermal gas in each Zeeman component; Phase B to a BEC only in $m_s = -3$; Phase C to a BEC in all spin states. This will help us understand the motivation of the two experiments I present next. In the first experiment, we start with a Chromium gas in phase A. We rapidly cool the gas in order to enter Phase C. We observe that it is difficult to produce a BEC in spin excited states. We find that the dynamics of Bose-Einstein condensation is affected by spin-changing collisions arising from relatively strong spin-dependent interactions. Thermalization of the spin degrees of freedom is influenced by the occurrence of BEC, and in turn influences which multi-component BECs can be produced. In the second experiment, we take advantage of our understanding of the phase diagram of large spin atoms to implement a new cooling mechanism. The cooling mechanism takes place in phase B. There, a Chromium BEC can only be in $m_s = -3$ (it forms in only one spin state). Atoms in other spin states are necessarily thermal atoms. Then the magnetic field is lowered and we let the mechanical degree of freedom reach equilibrium with the spin degree of freedom (through dipolar collisions) by populating thermal spin excited states, and subsequently removing them. We end up with a polarized BEC, with increased BEC fraction provided the initial BEC fraction is large enough. We also propose how this cooling mechanism may be achieved with non-dipolar atoms, such as Rubidium or Sodium, and discuss the limits and efficiency of the process.

Part Three

In Part III, we will be interested in understanding the conditions of appearance of quantum magnetism.

The chapter 6 will serve as an introduction to this part. We first explain what we mean by classical and quantum magnetism. Classical magnetism dynamics will be characterized by the absence of correlations between particles, and dynamics will be governed by mean field equations. Deviation from these mean field predictions will be

a signature of the breakdown of the "no correlations" hypothesis, crucial for any mean field approximation. We will specifically be interested in how quantum magnetism mediated by dipolar interactions (our main originality) may arise in a Chromium gas.

In chapter 7, we present an experiment where a chromium BEC is loaded in a double-well trap. Atoms of each well are prepared in opposite spin states. No spin dynamics is observed. The atoms' spin states of each well remain in their initial states. This is in agreement with the classical result of two magnets in opposite directions in a large external magnetic field. Absence of dynamics is due to a competition between Ising and exchange terms in the Hamiltonian, which helps in understanding the quantum to classical crossover observed as the number of atoms in each well is large.

In chapter 8, we present two spin dynamics experiments driven by contact and dipolar interactions which differ by the spin excitation preparation. Both experiments are performed in the bulk and at large lattice depth in a 3D Mott regime. In the first experiment, a majority of atoms are prepared in $m_s = -2$. We observe that for a shallow lattice depth, dynamics is well accounted for by a mean field equation. In the large lattice depth regime, dynamics scales with a beyond mean field theory. In the second experiment, the spin excitation is prepared via a radio-frequency pulse. We present preliminary results and try to assess how the presence of a lattice (or not) or the spin preparation may affect the appearance of quantum magnetism due to dipole-dipole interactions.

Part I

Experimental setup

CHAPTER 1

The Boson machine

In this chapter, I will introduce the experimental system I was handed at the start of my thesis. I will briefly describe the methods that my predecessors developed to routinely produce Chromium Bose Einstein Condensates and describe the new tools implemented throughout my thesis. A reader who desires to deepen his understanding of the different experimental techniques should refer to [38].

1.1 Specificity of Cr

Chromium is not an alkali unlike most atoms in Bose Einstein Condensation (BEC) experiments. It is situated on the 6^{th} column of the periodic table and therefore has more than one valence electron. Actually, the electronic structure of Chromium in state $|^7S_3>$ is an exception to the standard filling rules: the 3d subshell is half filled and there is only one electron in the 4s subshell (its electronic structure can be written as $[Ar]3d^5 4s^1$). Chromium therefore has 6 aligned valence electrons in its ground state, its total electronic spin is $s = 3$, and its permanent magnetic moment in $|^7S_3>$ is $|\vec{\mu}| = g_s \mu_B s = 6\mu_B$ (with μ_B Bohr's magneton and $g_s \approx 2$ the Lande factor of $|^7S_3>$).

Naturally occurring Chromium is composed of four stable isotopes with relatively high natural abundance (Table 1.1): three bosons (^{50}Cr, ^{52}Cr, ^{54}Cr) and one fermion (^{53}Cr). This property gives us the flexibility to study the physics associated to bosonic statistics with ^{52}Cr, fermionic statistics with ^{53}Cr, or even both together.

Isotope	^{50}Cr	^{52}Cr	^{53}Cr	^{54}Cr
Abundance	4.35%	83.79%	9.50%	2.36%
Nuclear Spin	$I = 0$	$I = 0$	$I = 3/2$	$I = 0$
Statistics	Boson	Boson	Fermion	Boson

Table 1.1: The naturally abundant Chromium isotopes.

The bosonic isotopes have no nuclear spin and therefore do not have a hyperfine structure. The fermionic isotope, on the other hand, has a hyperfine structure. At the early stages of the experiment, the team produced a simultaneous ^{52}Cr-^{53}Cr Magneto-Optical-Trap [39]. They then focused their attention on the bosonic isotope, where they optimized the accumulation of atoms in a magnetic trap and then in an Optical

Dipole Trap [40, 41, 42], and achieved BEC in 2007 [43]. In the following, I will explain the different processes involved in the production of ^{52}Cr BEC.

The relevant electronic levels involved in cooling and trapping ^{52}Cr are shown Fig.1.1. The $|^7S_3> \rightarrow |^7P_4>$ transition is used to cool and trap the atoms in a Magneto Optical Trap. The properties of this transition are given in Table 1.2. The cooling transition is not a closed transition: atoms in $|^7P_4>$ can naturally leak towards metastable $|^5D>$ states. These transition should be forbidden since they do not conserve spin (see Table 1.3 for the relative transition rates from $|^7P_4>$). However, they are not completely forbidden due to spin-orbit coupling [44].

We refer to $|^5D>$ or $|^5S_2>$ states as metastable because their energy level is higher than the energy of the ground state, but they are not coupled to any lower energy level. They therefore have a long lifetime, greater than the optical trap lifetime [45]. Accumulating atoms in metastable states in the Optical Dipole Trap actually turns out to be favourable because atoms in state $|^7S_3>$ can suffer from light assisted inelastic collisions at a high rate which leads to large losses [46, 47]. In metastable states, atoms are protected from these collisions.

Vacuum wavelength	$\lambda=\frac{2\pi}{k}=$ 425.553nm
$^7P_4$ linewidth	$\Gamma=2\pi\times$ 5 MHz
Saturation Intensity	$I_{sat}=\frac{\pi hc\Gamma}{3\lambda^3}=8.52$ mW.cm^{-2}
Doppler Temperature	$T_D=\frac{\hbar\Gamma}{2k_B}=124\mu$K
Recoil Temperature	$T_{rec}=\frac{\hbar^2k^2}{mk_B}=1.02\mu$K
Recoil Velocity	$v_{rec}=\frac{\hbar k}{m}=1.8$ cm.s^{-1}

Table 1.2: Relevant properties of Chromium for laser cooling.

To perform an efficient loading of atoms in metastable states, it is more advantageous to excite atoms towards the electronic state $|^7P_3>$. The $|^7S_3> \rightarrow |^7P_3>$ transition, which we call the depumping transition, allows accumulation of atoms in $|^5D>$ states at a much better rate than through $|^7P_4>$ (Table 1.3), and, also, has the advantage of allowing fast accumulation in $|^5S_2>$. This state is more favourable for accumulation since it has better collisional properties and a bigger light shift compared to the $|^5D>$ states [43]. This J $\rightarrow$ J transition will be used as well to polarize atoms in the Zeeman ground state $m_s=-3$ before evaporation (s=3 for Cr).

	$\|^7S_3>$	$\|^5S_2>$	$\|^5D_4>$	$\|^5D_3>$
$\|^7P_4>$	3.15×10^7	Forbidden	127	42
$\|^7P_3>$	3.07×10^7	2.9×10^4	6×10^3	Unknown

Table 1.3: Transition probabilities (in s^{-1}) between metastable or ground state and excited states $|^7P_3>$ or $|^7P_4>$ [48].

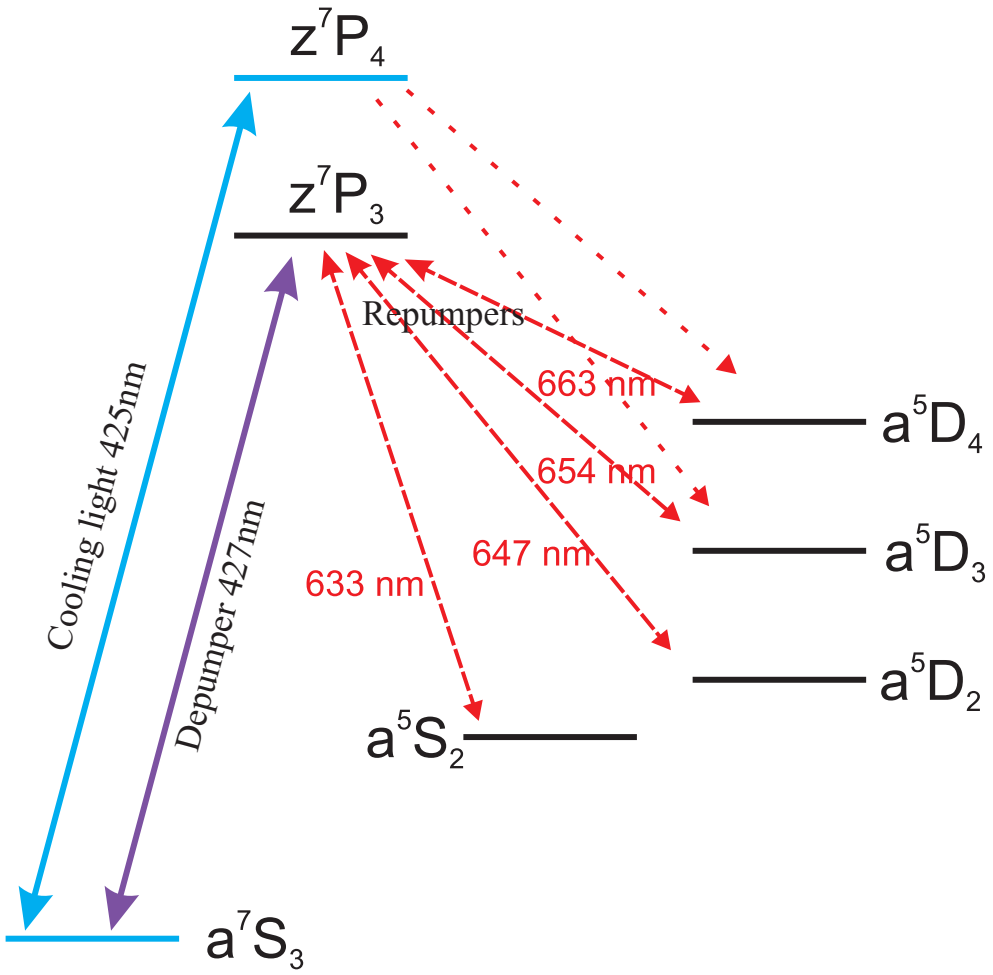

Figure 1.1: ^{52}Cr Electronic Structure. The $|^7S_3> \rightarrow |^7P_4>$ transition is used to cool and trap atoms in a MOT. From $|^7P_4>$ there is a leak towards $|^5D>$ states. We use light resonant on $|^7S_3> \rightarrow |^7P_3>$ to force a leak towards state $|^5S_2>$. Atoms can accumulate in metastable states $|^5D>$ and $|^5S_2>$ where they are protected from light assisted collisions (see text).

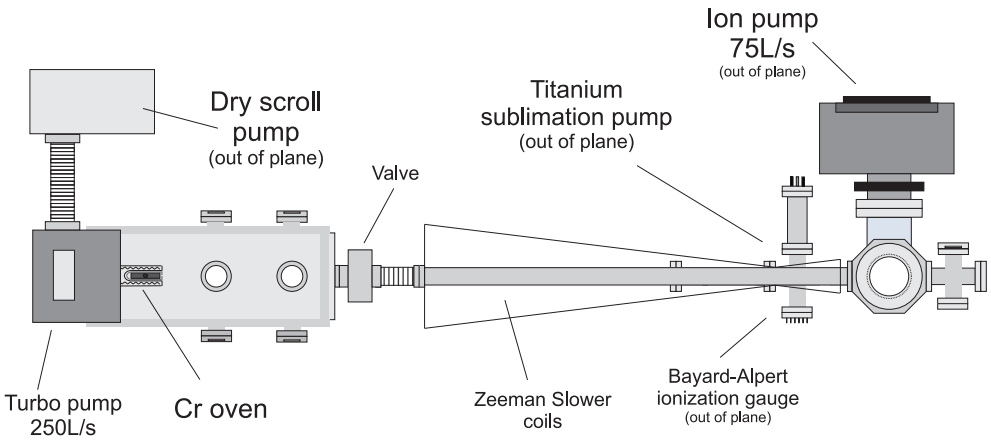

Figure 1.2: Vaccum system. View from above.

1.2 Vacuum system

The experimental system, shown in Fig.1.2, has two vacuum chambers. One chamber contains the atomic source and is called the oven chamber. The other one is where the Bose Einstein Condensate is produced and all the experiments take place, it is referred to as the science chamber. Because the vacuum quality at the oven chamber is insufficient compared to what is needed for the science chamber, a 25 cm long, 9 mm diameter tube between the two chambers ensures vacuum isolation in the ultralow pressure regime.

The oven chamber is pumped by a turbo pump of pumping speed 250 L/s, and prepumped by a dry scroll pump of 110L/min. We measure the pressure in the oven chamber by a Bayard-Alpert ionization gauge. Typical pressure in the oven chamber is 1.10^{-9} mbar at 1500 °C and 5.10^{-10} mbar at 1000 °C.

The pressure in the science chamber is also measured by a Bayard-Alpert ionization gauge and maintained at 5.10^{-11} mbar due to a 150L/s ion pump. If ever the ion pump is not sufficient in maintaining such a low pressure, there is a Titanium sublimation pump (which we used typically once every 6 months) which lowers the pressure inside the science chamber from 8.10^{-11} mbar to 4.10^{-11} mbar.

A security system is set up in order to protect the vacuum in the science chamber and the turbo pump. A gate is installed between the two chambers and is set to close if the pressure in either the science chamber or the oven chamber becomes too high. A gate was also set up between the turbo pump and the oven and is set to close if ever the pressure inside the oven chamber increases over a set value.

1.3 Oven

Chromium possesses a very low saturated vapor pressure at room temperature. Therefore temperatures in the 1400 °C range are needed in order to create a sufficient atomic flux for a cold atom experiment. The oven consists of tungsten W filaments which heat a crucible made of W[1] , in which there is an inset in Zircon[2] containing a 20 g Chromium bar. The inset is an empty cylinder of external diameter Φ_{ext}= 12.5 mm and internal diameter Φ_{int} = 8 mm, 6.4 cm long, and is open on one side in order to be able to place the Chromium bar within. The Chromium bar is 6 cm long, and has a 7.5 mm diameter. The opening of the inset is partly covered by a Zircone lid with a hole of Φ = 4 mm diameter. The lid is glued[3] to the inset. The temperature of the oven is measured by a thermocouple. The DC current which feeds the W filaments and heats the oven is governed by a controller through a PID loop and has an impedance of $Z = 0.5\ \Omega$ at 1500 °C.

We measure the pressure in the oven chamber correctly with the Bayard-Alpert ionization gauge. However, there is a relatively large inaccuracy in the temperature measurement of the chromium bar ($\approx$ 100 °C). For our experiment, the critical parameter is the flux of Chromium atoms at the exit of the oven. Since the atomic flux is a function of the temperature at the exit of the Chromium bar, we adapt the temperature in order to have an appropriate Cr flux. Therefore we measure the flux of Cr atoms at the exit of the oven nozzle. To do so we measure the absorption signal of the atoms by sending polarized σ^+ light while scanning the frequencies around the $|^7S_3> \rightarrow |^7P_4>$ transition. We know that we need a typical absorption of at least 1% in order to produce a BEC in optimal fashion. Therefore we adjust the temperature read by the programmable controller in order to obtain a sufficient atomic flux. Fig.1.3 illustrates this experiment performed on the 31/07/2014. Typically we work at 1450 °C in order to have at least 1% absorption, which was no longer the case on that date. In the latter stage of my thesis, the oven was first raised to 1490 °C to reach 1.5% absorption (result of the 31/07/2014 absorption measurement), and then gradually to 1600 °C where no absorption could be seen and very small BECs were produced. The oven was changed at the end of my experimental work in the laboratory. This Chromium bar had a lifetime of 6 years. There was less than 1g of Chromium left in the oven out of the initial 20 g and it took 3 weeks before the experiment was up and running again.

[1] Made in China, distributed by Neyco.
[2] Zirconium Dioxyde. Made by Keratec.
[3] 904 Zirconia, Cotronics. T_{Max}=2200 °C

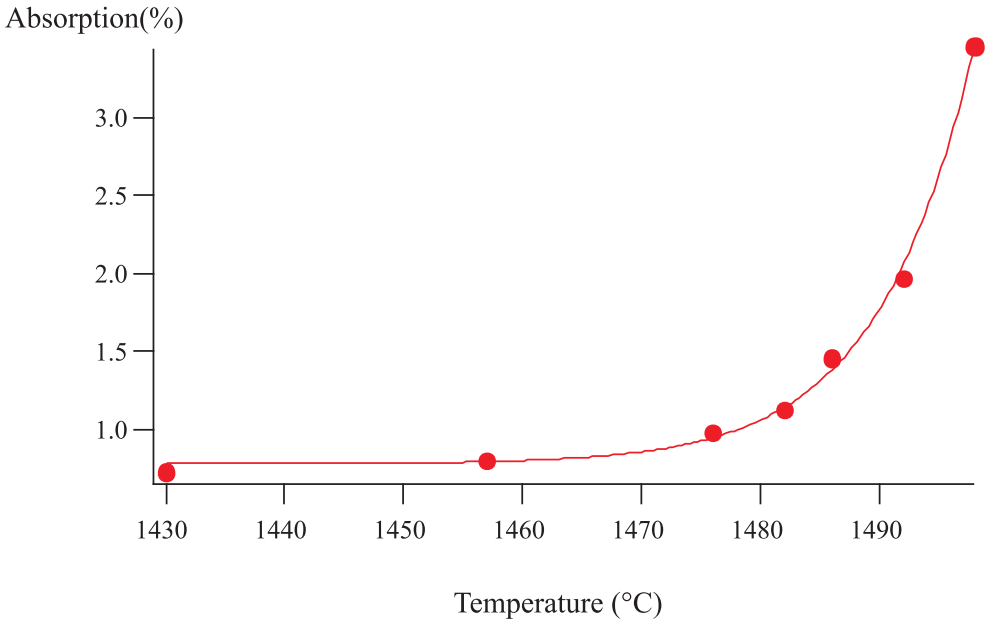

Figure 1.3: Absorption measurement of the atomic flux at the exit of the oven in function of the temperature performed on the 31/07/2014. Here we can see that we need a temperature read by the controller of at least 1490 °C in order to have an atomic flux of at least 1%.

1.4 From the oven to a BEC

Cooling beams

To produce a sufficient amount of cooling light at 425.553 nm, the team decided on frequency doubling a Titanium Sapphire laser Ti:Sa1[4]. We pump the Ti:Sa1 with 15 Watts of a Verdi laser V18 and are able to produce 1.5 Watts of laser light at 851.105 nm. We then frequency double the light at 851.105 nm with a doubling cavity[5] and produce 300 mW of 425.553 nm light. We pre-stabilize the frequency of Ti:Sa1 by locking it to a Fabry Pérot (FP) reference cavity. The doubling cavity is then locked using a Hänsch-Couillaud locking scheme [38, 49] in order to always be resonant with the Ti:Sa1 laser. We finally lock the FP cavity via saturation absorption using a chromium hollow cathode[6]. The laser beam is then separated into four beams which all go through different beam shaping and/or frequency shifts depending on the different task needed: Zeeman Slower (ZS), the Magneto Optical Trap (MOT), Transverse Cooling (TC), imaging.

[4] In order to avoid confusion with another Ti:sapph laser that I will describe later, we will refer to this Ti:sapph (which is entirely dedicated to producing a BEC) as Ti:Sa1

[5] Cavity brand TechnoScan

[6] Cathode brand: Cathodeon. Model: 3QQKY/Cr

Zeeman Slower

At the exit of the oven, atoms have a mean velocity of about 1000 m·s^{-1}. We slow atoms with a speed $v < v_c = 600$ m·s^{-1} with a Zeeman Slower. We use for the ZS 100 mW of σ^+ light at 425.553 nm detuned from the $|^7S_3> \rightarrow |^7P_4>$ by 450 MHz in the red of the transition. Light is coupled to the atoms using an in-vacuum mirror (see Fig.1.4). The magnetic field used in order to compensate for the Doppler shift along the ZS is provided by three sets of coils with independent DC current sources.

The third set of coils is at a distance of approximatively 10 cm from the atoms and produces a field of typically 1 G. This produces a magnetic gradient on the atoms (estimated in the order of 0.3 G·cm^{-1} along the ZS axis).

During my thesis, we installed an electronic switch in the DC current source of this coil. During the MOT stage of the experiment, the ZS is needed and the switch is on. As soon as the loading of the 1D Far Off Resonance Trap is completed, we turn off the switch so that evaporation can proceed with no magnetic gradient.

Transverse Cooling

In order to increase the flux of atoms that will be slowed down by the ZS and then captured by the MOT, a horizontal and vertical transverse cooling scheme is implemented at the exit of the oven nozzle. These beams collimate the atomic flux in order to increase the number of atoms which exit the oven aperture and enter the MOT capture zone.

We use for transverse cooling 20 mW of light at 425.553 nm, at the same frequency as the MOT beams. In order to optimize the detuning between the electronic transition and the light frequency, two pairs of compensation coils were added and the magnetic field applied is approximatively 5 G.

MOT

At the exit of the ZS, atoms are captured in a MOT. The magnetic field is produced by two coils set in a anti-Helmholtz configuration placed on each side of the experimental chamber (Fig. 1.4). These coils are capable of delivering magnetic field gradients at the MOT position of ≈ 18 G·cm^{-1} in the vertical direction (and therefore ≈ 9 G·cm^{-1} in the horizontal plane). The optical trap is formed by two retro-reflected beams detuned by 12 MHz ($\approx 2.5\ \Gamma$) in the red from the $|^7S_3> \rightarrow |^7P_4>$ transition. One beam is a retro-reflected vertical beam, it ensures vertical trapping. The other beam follows a retro-reflected butterfly configuration and ensures trapping in the horizontal plane (see Fig. 1.4).

A Cr MOT is a lot smaller than alkali MOTs due to its large light assisted inelastic collisions rate. An atom in $|^7S_3>$ can collide with an atom which has been promoted to $|^7P_4>$ by light, the atom pair is then lost. For Chromium, the associated rate parameter is measured to be $(6.25 \pm 0.9 \pm 1.9) \times 10^{-10}$cm^3·s^{-1} at a detuning of -10 MHz and

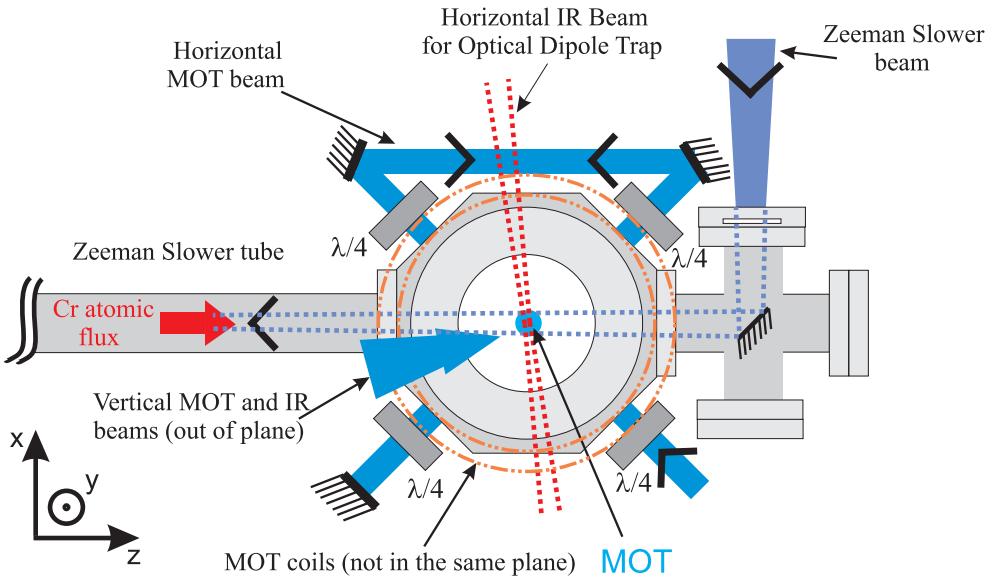

Figure 1.4: Sketch of the experimental chamber (Top view). The MOT, Zeeman Slower, and IR beams are explicitly shown.

a total laser intensity of 116 mW·cm^{-2} [50]. This is typically two orders of magnitude worse than for alkalis. As a result, a typical Cr MOT contains approximatively 1.10^6 atoms and has a radius of $\approx$ 100 μm. The temperature of the MOT is given by the Doppler Temperature (and was confirmed by a cloud expansion measurement) which for the case of Chromium is $T_{Doppler} = \frac{\hbar\Gamma}{2k_B}$ =120μK [50].

Accumulation in a 1D Far Off Resonance Trap

Chromium was successfully condensed by the Stuttgart group after accumulating atoms in a magnetic trap and transferring them in an Optical Dipole Trap [16]. Our team chose to try and accumulate directly in a 1D Far Off Resonance Trap (FORT) made of one IR beam. For typical MOT systems, loading a 1D FORT from a MOT leads to inefficient loading. For Chromium, however, this statement is not true. A chromium MOT is smaller than typical MOTs due to (i) large light assisted collisions and (ii) less efficient multiple photon scattering due to blue cooling light (which typically reduces the MOT density and is $\propto \sigma^2 \propto \lambda^4$ [51]). It has a size of typically 100 μm, which is similar to the dimensions of realistic 1D FORTs. In order to perform evaporation in the best possible conditions, we need as many atoms in the conservative trap as possible. In the following I will describe the beam which produces the 1D FORT and the different steps we use in order to accumulate as many atoms as possible in the 1D FORT.

IR beam

At the very beginning of my thesis, we changed the IR laser system producing the 1D FORT in which atoms are accumulated. Before, a Ytterbium doped fibre laser at 1075 nm of 50 W laser power[7] was used. The beam goes through an Acousto Optic Modulator (AOM). We send to the AOM a Radio Frequency (RF) signal at 80 MHz of controllable power which enables us to control the IR power seen by the atoms. The beam was then retro-reflected onto the atoms so that the laser power seen by the atoms was doubled. We were unsatisfied with the stability of this trap, the biggest instability coming from the retro-reflected beam. A new laser was bought: a 100 W, 1075 nm Ytterbium fibre laser from IPG[8]. It has sufficient power so that we could stop retro-reflecting the beam. We also removed the optical isolator at the exit of the laser since we were worried by thermal effects induced by the optical isolator and we are now less concerned by retro-reflected light coming back into the fibre (which would damage the laser). These changes resulted in a considerably different laser beam mode. To optimize the mode volume of the trap we first changed the focusing lens. We then modulated the RF frequency of the AOM in order to fine tune the volume capture. The modulation is fast enough ($\omega_{mod} >> \omega_{Trap}$) that the atoms see a time averaged potential where we are able to tune the anisotropy of the trap by changing the amplitude of the frequency modulation: the horizontal waist is effectively enlarged while the vertical waist is unchanged.

After loading the dipole trap, we found that evaporative cooling was very inefficient. This was attributed to amplitude noise in the analog control of the Voltage Control Oscillator, presumably introducing heating due to parametric excitation [52]. In Fig.1.5a we show the spectrum when the driver of the AOM is fed by its internal current source. A very clean spectrum is observed. Fig.1.5b shows the spectrum obtained with our cleanest external current source: the Delta Elektronica source. With such a source, evaporation gave better results but it was still not as good as with the internal source. If we look closely at Fig.1.5a and Fig.1.5b, we see that the spectrum of the Delta has a background noise of -28 dBm. We therefore installed a low pass filter with cut frequency $f_c = 70$ Hz. This attenuated the background noise by 20 dBm as shown Fig.1.5c and we were able to condense our chromium gas with an internal or external current source in the same manner. We then added a modulation to the DC signal provided by the Delta source with a Mini-Circuits summator[9]. We found that a frequency modulation at 100 kHz and amplitude 90 mV_{p-p} optimized the production of our BEC. Later during my PhD, we realized that the time average potential was such that we had two parallel traps (see Fig.1.6) during the loading: the modulation is such that the beam actually spends more time on the edges than in the center. This results in a deeper trap on the edges than in the center. We have not studied this

[7] model YLR-50-LP by IPG
[8] model YLR-100-LP-AC by IPG
[9] reference ZFBT-4RG2W+

in detail. We find that thermal atoms can go from "one" tube to the other, they are connected. At lower temperatures, only one trap populates and efficiently loads the dimple in which evaporation takes place. To optimize our modulation process in the future, we could modulate the power of RF signal sent to the AOM in such a way to increase the potential depth between the two tubes. This would result in a trap with just one tube which would be a more preferable situation.

We then measured the trapping frequencies of this new time averaged IR trap at the end of the evaporation ramp. To do so, we modulated the trapping light amplitude at a frequency ω by modulating at a frequency ω the intensity of the RF signal sent to the AOM controlling the IR beam. When this frequency matches twice the trapping frequency of the trap the modulation heats the atoms in the trap [53]. We measured trapping frequencies of $\omega_{x,y,z} = 2\pi(520 \pm 12, 615 \pm 15, 395 \pm 12)$ Hz (Fig.1.7) which is similar to before the IR laser was changed.

Accumulating metastable atoms

One severe limitation to accumulating atoms in the electronic ground state is that these atoms suffer from a large light assisted inelastic collision rate due to the presence of the MOT beams during the loading process. To circumvent this limitation, the group decided to accumulate atoms in the 1D FORT in other states, which would be dark states (for $|^7S_3> \rightarrow |^7P_4>$ light) and wouldn't suffer from light assisted collisions.

Chromium has no closed cooling transition (Fig.1.1). Atoms can leak out of the $|^7S_3> \rightarrow |^7P_4>$ transition towards metastable $|^5D>$ states where they are no longer sensitive to the $|^7S_3> \rightarrow |^7P_4>$ light. We can therefore accumulate atoms in the 1D FORT in $|^5D>$ states. Although this enhanced the number of atoms [41] it is not sufficient to reach BEC.

By shining light on the $|^7S_3> \rightarrow |^7P_3>$ during the MOT, we create an extra leak in the cooling transition towards the metastable $|^5S_2>$ state. Accumulating atoms in this state is more favorable than in $|^5D>$ states because it has better collisional properties (a $|^5D>$ state is less stable than a $|^5S>$ state) and the light shift on $|^5S_2>$ is estimated to be twice the one of the $|^5D>$ states [43]. Therefore through $|^5S_2>$ we can accumulate more atoms and for longer. The optimisation of the accumulation of metastable atoms is studied in detail in [54].

Dark Spot

To help the accumulation process we use a dark spot technique [55]. On the light path of the repumping transition we place a wire. We then image the wire on the atoms. This results in a dark spot at the position of the MOT. We then overlap the dark spot with the 1D FORT. Only metastable atoms that are in the MOT region but not in the 1D FORT will be sensitive to this light. Thus metastable atoms which are not in the 1D FORT (because they had too much energy for example) will re-enter the cooling

a)

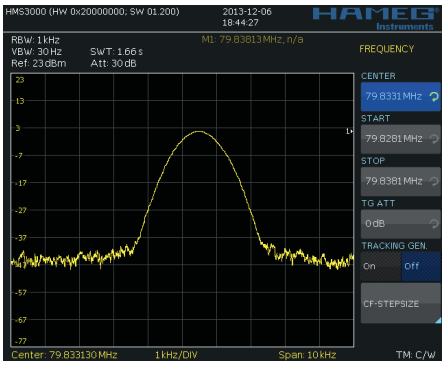

b)

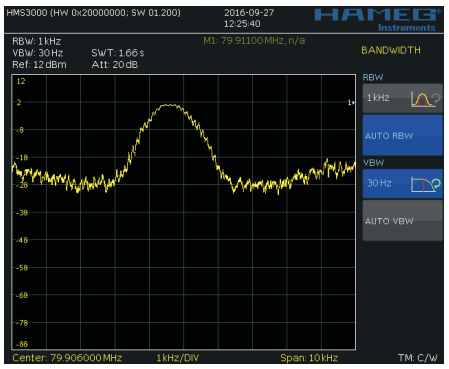

c)

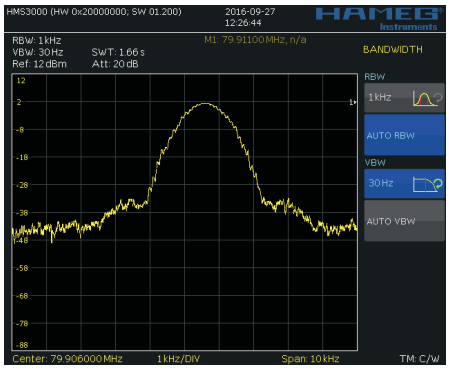

Figure 1.5: Spectrum analysis of the RF produced by the VCO driving the IR AOM for different controlling voltage sources. a) The spectrum using the internal source. b) Spectrum using our cleanest external source: a Delta Elektronica generator. c) Spectrum using the Delta Elektronica generator filtered with a low pass filter, attenuating the background noise.

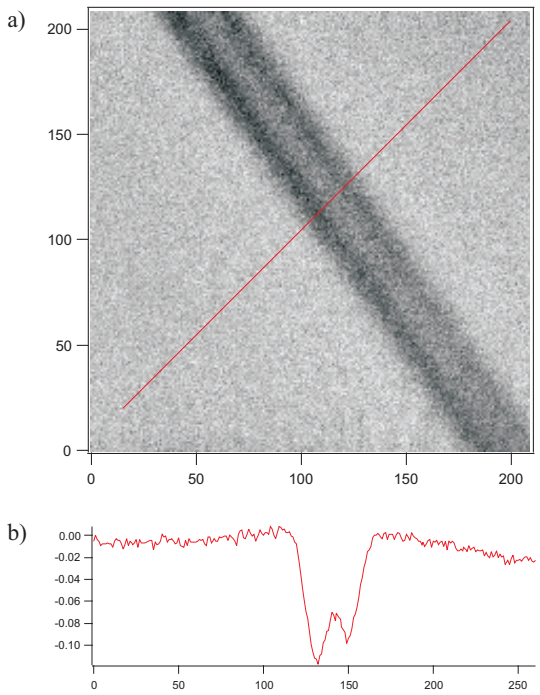

Figure 1.6: a) In Situ absorption image of the 1D FORT. b) Integrated line profile. Both a) and b) illustrate the "two parallel" traps mentioned in the text.

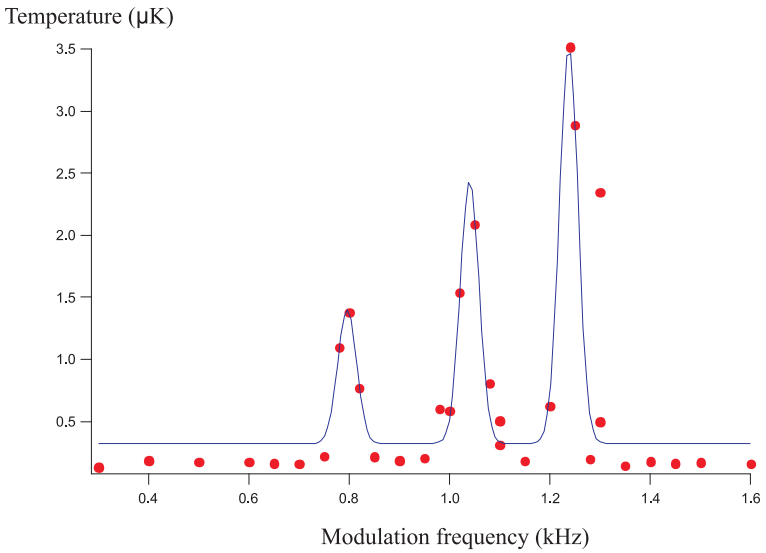

Figure 1.7: Trapping frequency measurement. We modulate the trapping light power for 200 ms at a frequency ω. This modulation induces heating when ω matches twice the trapping frequencies [52].

cycle and have a greater chance of being accumulated in the 1D FORT. For an optimal Dark Spot alignment, this technique enhances the 1D FORT loading by 20%.

Radio Frequency sweeps to cancel out the m_s dependence of our loading scheme

Accumulation is performed in a 1D Far Off Resonance Trap. Unfortunately, only metastable atoms with $m_s > 0$ will be trapped in this configuration because of the magnetic field applied during the MOT: metastable atoms with $m_s < 0$, which are high field seekers, are expelled by the magnetic force along the propagation axis of the 1D FORT. We use fast linear radio-frequency sweeps to flip the spins of atoms at a fast rate. This averages out the magnetic forces and optimizes the accumulation in an 1D FORT from a MOT. The potential experienced by a metastable atom in any Zeeman sub-level is solely the 1D FORT, thus this procedure allows for trapping all magnetic sublevels [42]. This technique does not affect the properties of the MOT since the optical pumping rate is much greater than the sweeping rate. Cancelling the magnetic forces increases the number of atoms loaded in the 1D FORT by a factor of up to two.

Repumping dark states

Once the 1D FORT is loaded with metastable atoms, we turn off all light relevant for the MOT (ZS, MOT, and TC beams). Atoms can now safely be transferred to $|^7S_3>$. We apply repumper beams for 200 ms between each metastable state and state $|^7P_3>$ (see Table 1.3 for typical transition probabilities). We typically load 1-2 $\times$ 10^6 atoms in the 1D FORT at 120 μK.

Polarization

After the repumping process, atoms are in the electronic ground state $|^7S_3>$ and are distributed over all the Zeeman states. We then optically pump atoms in the Zeeman ground state. We apply with the 427.6 nm laser a retro-reflected σ^- pulse on the J-J $|^7S_3> \rightarrow |^7P_3>$ transition for 5 μs in the presence of a 2.3 G magnetic field. Atoms are pumped in the lowest energy state $|^7S_3, m_s = -3>$ and can no longer suffer from losses associated to dipolar relaxation collisions. These collisions transfer internal magnetic energy into kinetic energy and would heat up a system which we intend to cool [56]. We are now ready to proceed to cooling atoms to degeneracy through the efficient forced evaporation process.

"Making and Probing a BEC" [57]

Evaporation ramp

Once the atoms have been pumped to the Zeeman ground state, we rotate a wave plate in front of a Polarizing Beam Splitter (PBS) which is on the optical path of the IR

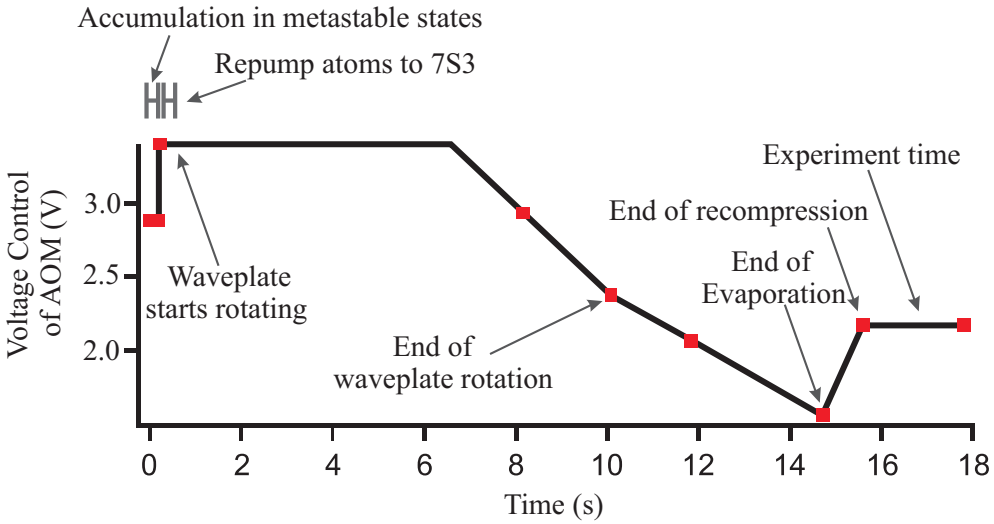

Figure 1.8: Sketch of the voltage ramp sent to the AOM of the IR beam in order to efficiently load Cr atoms in the ODT, load the dimple, evaporate, and reach BEC.

trapping beam. This results in a transfer of the IR light from the horizontal beam to the vertical beam and creates a dimple. As the dimple is loaded, we reduce the IR power in order to produce forced evaporation of the atoms. The most energetic atoms escape the trap as the trap depth is lowered, and the atomic sample can rethermalize at a lower temperature [58, 59]. We show the experimental ramp Fig.1.8.

Control system

All the operations performed during an experimental run are controlled by a Labview program. This program has been optimised over the years. The program defines the output of two analog cards and one digital card. The different cards are kept in synchronisation by the internal clock of the digital card of frequency 20 MHz. This allows a good synchronisation for over a minute (an experimental sequence is typically 30 s) and can program times as short as 1 μs. The digital card also defines temporal steps of variable length. At each temporal step, TTL signals are adapted to the desired output and command different instruments (AOM, shutters,power supplies,...). The analog cards are able to generate signals between -10 and 10 V which can be modified discontinuously, or continuously by programming a linear ramp. We show in Fig.1.9 some of the experimental ramps that the control system executes in order to produce a BEC.

The image taken at the end of the experimental ramp is sent, via another Labview program, to a commercial analysis program IgorPro. It is from such images that we are able to extract most of the different physical properties we are interested in.

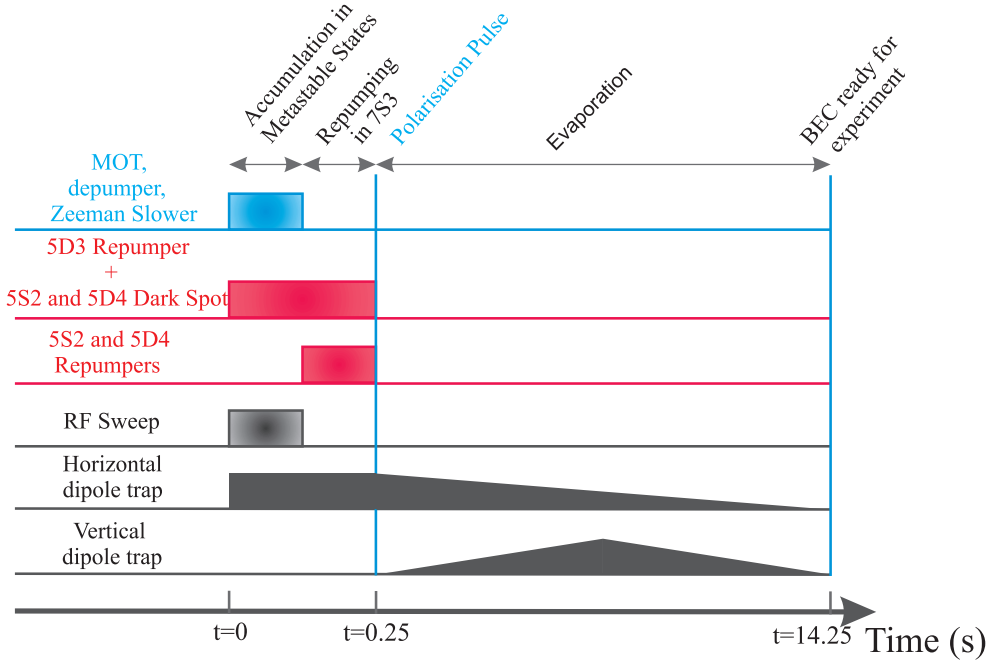

Figure 1.9: Cartoon depicting the experimental sequence.

Imaging system

We have at our disposal an absorption imaging system which is shown Fig.1.10 and is described in detail in [60]. It images the gas along the vertical y axis onto a pixelFly camera. This camera is a 12 bit 1392×1024 pixels with a quantum efficiency of 50% at 425 nm. The actual size of a pixel is 6.5 μm. Our imaging system comprises a × 3 telescope meaning that the size of a pixel on our image is 2.2 μm. The resolution Δx of our system is fixed by the aperture D and the distance f of the atoms from the first lens (L1):

$$\Delta x = \frac{1.22\lambda f}{D}. \tag{1.1}$$

An upper limit to the experimental resolution of this imaging system was set by performing a Point Spread Function like measurement. We fit the intensity distribution of two BECs in situ, separated by a distance a, by the sum of the two gaussian functions. We may extract from this procedure an effective aperture for our imaging system, from which we extract the estimate of our experimental resolution. We obtained an experimental resolution in the order of the diffraction limit: $\Delta x \approx 2\mu$m.

Atom calibration

In our experiment we estimate the number of atoms of an experimental sequence from an image formed by two pulses of resonant light at weak light intensity ($I << I_{sat}$). In

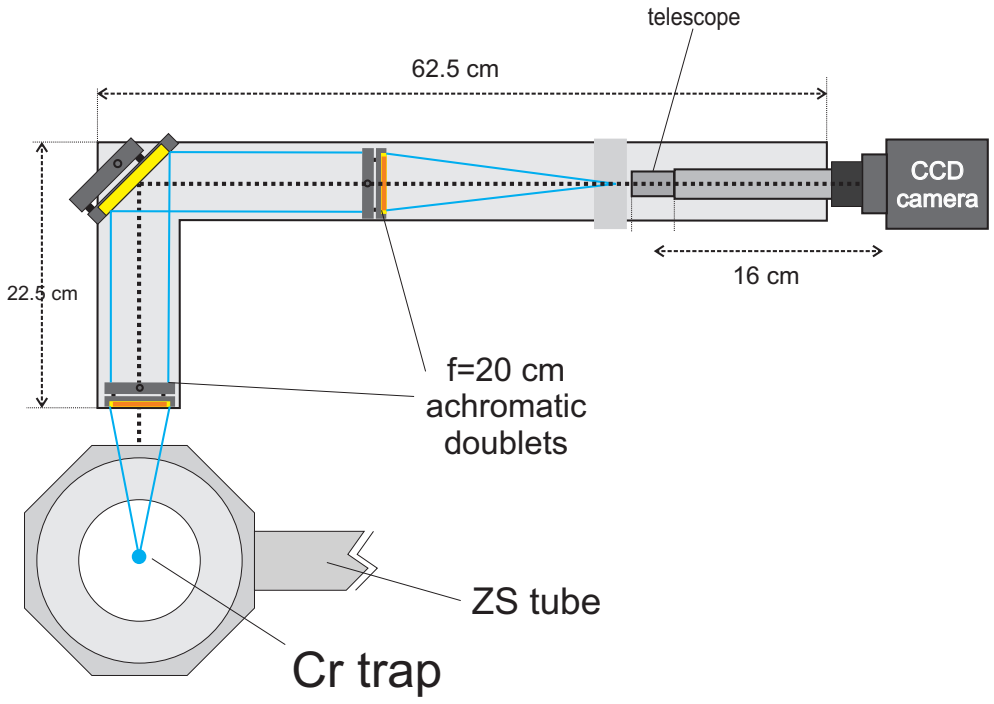

Figure 1.10: Scheme of the imaging system (Top view).

this regime, we can evaluate the number of atoms through Beer-Lamberts law:

$$dI = n\sigma I dz \tag{1.2}$$

where dI is the absolute variation of the light intensity I while crossing an atomic sample of thickness dz, density n, and cross section σ. The atom number can be assessed through the normalisation condition $\int_{-\infty}^{\infty} n(x,y,z)dxdydz = N$.

For a thermal gas, the density distribution follows a Boltzmann distribution. Therefore we fit the integrated atomic distribution by

$$n_c(x,y) = n_{c_0} e^{-(\frac{x^2}{w_x^2}+\frac{y^2}{w_y^2})} \tag{1.3}$$

with n_{c_0} the integrated peak density, and w_i the 1/e size of the gas in direction i. In a 3D harmonic trap the size, the size of the thermal cloud along direction i is

$$w_{i,0} = \sqrt{\frac{2k_B T}{m\omega_i^2}} \tag{1.4}$$

with m the atomic mass, T the temperature, and ω_i the trapping frequency along direction i. When all trapping potentials are removed, the thermal gas will expand following

$$w_i(t) = \sqrt{w_{i,0}^2 + \frac{2k_B T}{m} t^2} \tag{1.5}$$

where t corresponds to the time of free expansion of the gas between the moment trapping potentials were turned off and the imaging pulse (commonly referred to as Time Of Flight TOF). The size of the thermal gas thus gives access to the temperature T.

A Bose Einstein Condensate on the other hand follows a bi-modal distribution at T $\neq$ 0. In a 3D harmonic trap, when the interaction energy is greater than the kinetic energy, the distribution of condensed atoms follows the Thomas Fermi distribution and at T=0 we have:

$$n(x,y,z) = n_0\big(1 - \frac{x^2}{R_x^2} - \frac{y^2}{R_y^2} - \frac{z^2}{R_z^2}\big) \tag{1.6}$$

with $n_0 = \frac{\mu}{g}$ the peak atomic density, μ the chemical potential of the gas, g the interaction strength, and $R_i = \sqrt{\frac{2\mu}{m\omega_i^2}}$ is the Thomas Fermi radius of the condensate in direction i [61]. Once the trapping potentials have been switched off, the expansion of condensed atoms follow the scaling laws established in [62]. Non-condensed atoms approximately follow the Boltzmann distribution as described above. The temperature of the gas can be extracted through the width of the distribution of non-condensed atoms or by the condensate fraction as will be discussed in chapter 5.

1.5 A new imaging system

We have implemented two different Stern-Gerlach procedures which enable us to separate the different spin states before imaging them.

One Stern-Gerlach method consists in turning off the vertical trapping light beam, and letting the gas expand in an optical horizontal trap with a small magnetic gradient of approximatively 0.25 G·cm^{-1} along the tube, which spatially separates the different Zeeman states. We apply a small gradient such that the magnetic field experienced by all the atoms is small enough, so that all are almost equally resonant with the absorption imaging process. This results in an accurate measurement of the atomic distribution in different spin states. Our imaging axis and the horizontal trap in which the atoms propagate have a slight angle between them (of $\approx 7\,^\circ$). Combined with the fact we apply a small magnetic gradient, a 50 μm separation between two adjacent spin states (which is sufficiently large so that we can differentiate the different clouds) takes typically 40 ms. This long expansion time renders impossible a time of flight measurement at the end of spin separation since the atomic density becomes too weak. This imaging technique was used for the experiments presented in chapter 3 and chapter 7.

A new imaging system along the vertical y axis was conceived during my thesis. It was installed vertically so that we have a new imaging axis. It is also orthogonal to the direction of the 1D FORT, and combined with a high resolution imaging and a low noise camera it could allow for measurements of spin textures (in the spirit of [63] for example). Also the spin separation axis and the new imaging axis are orthogonal. This

means the spatial separation of the different spin states can be achieved quickly (access to momentum distribution) and we developed tools in order to accurately measure spin population of each state. This imaging technique was used for the experiments presented in chapter 5 and chapter 8.

1.5.1 New imaging set up

Fig.1.11, shows the experimental setup of the new imaging system. The absorption light beam impinges the bottom and top glass cell with a slight angle of 7°. The optical system that follows is a one to one telescope followed by a 7.5 magnification telescope. The first telescope is a "relay system" and translates the image by $4f$. The resolution of the optical imaging system is defined by the diffraction limit of the first lens L1[10]. The diffraction limit of an aperture of diameter D at a distance l of a point object is

$$\Delta x = 1.22 \times \frac{\lambda l}{D}. \tag{1.7}$$

In our optical system the mirror M1, which collects the coherent forward field of the atomic sample and sends it to the optical system, is smaller in one spatial direction. The diameter of the first lens is D=50.8 mm and it is at the focal distance f=200 mm of the atoms. The collecting mirror is at approximatively 100 mm from the atoms and has a diameter of d=25.4 mm. The effective size of the mirror in the z direction is $d \times \cos(45°)$. The resolution of our optical system is necessarily different along these two orthogonal directions. The diffraction limit is 2 μm along the x direction and is 3 μm along the z direction (eq.(1.7)).

The mirror cannot be placed any closer to the atomic gas (because of the presence of the MOT coils) and cannot be any larger. Along the vertical axis there are many trapping beams: the vertical MOT beam (λ =425 nm), optical lattice beams (λ =532 nm), and the vertical optical dipole trap (λ =1075 nm). A bigger mirror would block one of these beams.

The second telescope is composed of a divergent lens L3 of focal length -20 mm and a convergent lens L4 of focal length 150 mm. The magnification of this telescope is 7.5 and was chosen so that the smallest resolved object would match the pixel size of the camera.

The camera used for the imaging system is an Andor camera[11]. It has high sensitivity for light at 425 nm, with a quantum efficiency of approximatively 0.9 due to back illumination [64]. It can be cooled down to −100 °C, which is critical for reducing the dark current detection limit. It has 512×512 pixels of 16 by 16 μm size. It is a single photon sensitive camera which has an electron multiplier feature with very little electronic noise. The electron multiplier feature is particularly relevant in the case of

[10] when no aberrations are considered
[11] Andor Ixon ultra 3

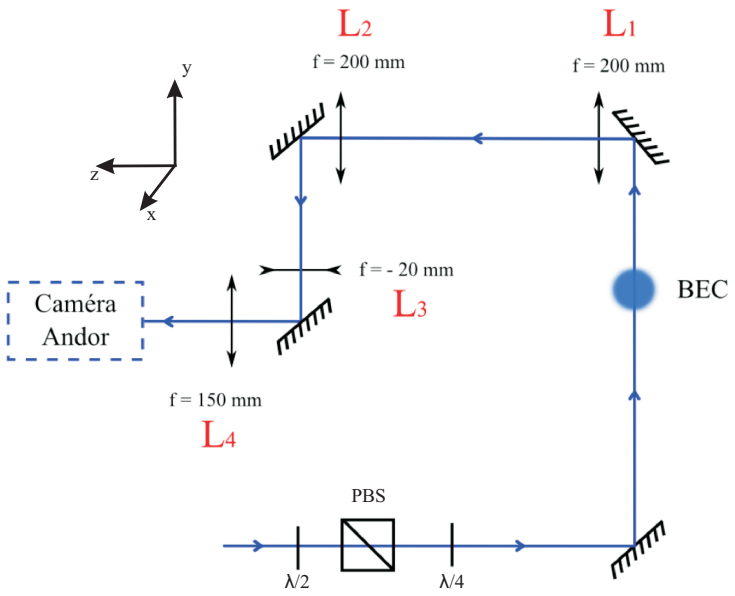

Figure 1.11: Setup of the new optical imaging system (adapted from [37]).

fluorescence imaging. The photon signal and dark current can be multiplied, but the electronic noise is not. Therefore this process may lead to a substantial gain in signal to noise ratio. This is not the case for absorption imaging: the electron multiplier stage increases in the same manner the atomic signal and the noise of the image. Therefore the signal to noise ratio is not modified.

The Fast kinetics mode enables fast temporal resolution and relies on fast frame transfer of the image. The sensor of the camera can be divided in N parts. One of the parts is exposed to the light pulse for the image while the other $N-1$ are protected from any photons (so that stored parts are not perturbed by any background photons). The imaged part is then transferred to be stored while another part is exposed for the image and so on until all the N parts have been imaged. Each image is therefore decomposed in N images of $\frac{512}{N}$ $\times 512$ pixels. We found that dividing the camera in 2 parts is optimal for our 2 pulse absorption imaging protocol: one part is dedicated to the light pulse when atoms are present and the second part for the background light pulse. In our absorption imaging process, the information contained in the image part of the sensor is transferred to the storage part at a speed of 1.7 μs per line. The time between two light pulses can therefore be as short as $1.7 \times 256 = 435.2$ μs and in practice is 600 μs. This short time reduces the delay between the absorption image and the reference image, which lowers the amount of fringes (see below).

1.5.2 Stern-Gerlach analysis

To image both momentum and spin distribution simultaneously we developed a Stern-Gerlach analysis like imaging protocol. We turn off all trapping lights and let the gas expand for a 6 ms Time Of Flight (TOF). During this TOF, we pulse a magnetic field gradient along the Zeeman direction. In order to apply this gradient as fast as possible, 15 ms before turning off all trapping lights we send the maximum voltage command to the MOT coils while their switch is off. The integrated error associated to the current control of the power supply is saturated at the moment when we turn the switch on. This results in obtaining a large current pulse in a faster manner than without this "trick". The value of this gradient evolves during the TOF due to induction in the coils and eddy currents. From the separation of the spin states we can estimate an average value of the magnetic gradient of approximatively 3.5 G·cm^{-1} present during the TOF.

In an absorption imaging process, two light pulses are needed. The first light pulse is produced with atoms present and is called the absorption image. The second light pulse is produced with no atoms present, it serves as a reference image for the intensity and we shall refer to this image as the reference image. The image from which we analyze our data results from the division of these images. It is crucial that no atoms are present in the reference image since it would underestimate the number of atoms. At first, we noticed that atoms appeared in the reference image. This is because when the Andor camera is in "Fast Kinetics mode" the time between the two light pulse ($\approx$ 0.7 ms) is so short that atoms are still present during the second light pulse. In order to remove all atoms after the absorption light pulse, we shine the 427 nm beam along the x axis while blocking the retro-reflection to efficiently push the atoms away.

We show in Fig.1.12 an example of an image obtained with this procedure. The color code is such that in red we have the signal corresponding to the highest absorption and in green the lowest one. On the integrated signal, we may distinguish 7 atomic clouds along the left to right diagonal. The leftmost atomic cloud corresponds to the $m_s = -3$ cloud and the one on the far right the $m_s = +3$ cloud.

Imaging calibration

Atoms in different spin states are not imaged with the same efficiency. At non zero magnetic field, even though spin states of the same electronic state are equally separated in energy (^{52}Cr has no magnetic quadratic Zeeman shift), the transitions between the electronic ground state and the excited states are m_s dependent. This is due to the difference in Landé factor in different electronic states ($g_{^7S_3} = 2$ and $g_{^7P_4} = 7/4$). The imaging pulse can only be resonant for a given m_s, the other spin states are therefore imaged with off resonant light. Moreover, a different Clebsch-Gordan coefficient is associated to each transition. Even though the absorption pulse is designed to optically pump atoms towards $m_s = -3$ during the imaging pulse, we find that in practice we do not measure as well atoms in $m_s \neq -3$: the imaging pulse is not long enough

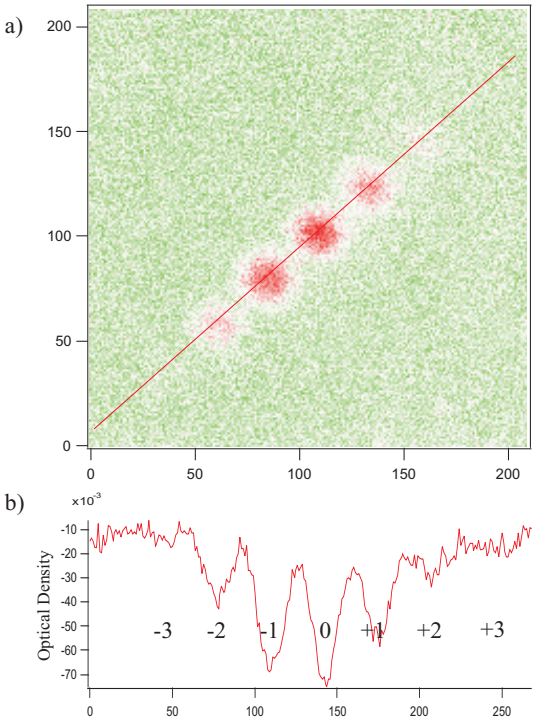

Figure 1.12: a) Absorption image of the atomic sample after the new Stern-Gerlach separation method after having applied a $\pi/2$ RF pulse to a BEC in m_s=-3. The color code is such that in red we have the signal corresponding to the most absorption and in green the least. Our image clearly shows 5 distinct atomic clouds along the left to right diagonal. b) Doubly integrated optical density along the red line of a). The position of the different m_s states are indicated. The integrated lineprofile enables us to distinguish another two (small) atomic clouds. The leftmost atomic cloud corresponds to the $m_s = -3$ cloud and the one on the far right the $m_s = +3$ cloud.

($\tau_{pulse} < \tau_{opt.pump.}$), because in practice longer imaging pulses results in heating and less signal to noise.

When the absolute population of each spin state is crucial (e.g. in the experiments of the second part of chapter 8), we attribute correcting coefficients to each spin states in order to determine correctly the atom number of each spin states. The procedure used to determine these coefficients is presented in section 8.4.

1.5.3 Image analysis: fringe removal

In addition to photon shot noise, dark current noise and electronic readout noise, absorption images suffer from fringes. These fringes arise from the fact that small vibrations of optical elements give rise to fluctuating fringe patterns between the absorption and reference images, resulting in imperfect cancellation between the intensity pattern of the first light pulse with the second light pulse. These fringes can be greatly reduced thanks to a fringe removal analysis developed in [65].

In a typical set of measurements, one has many absorption images and many reference images. The basic idea of the fringe removal analysis is that the intensity profile of the reference image is not necessarily the intensity profile which matches best the one of its corresponding absorption image. For each absorption image, the algorithm finds the associated optimal reference image, which is a linear combination of all reference images of the given set. To find the weight c_k of each reference image k in the optimal reference image, the algorithm finds the set of c_k that minimizes the least square difference between the absorption image and the optimal reference image.

This technique reduces the noise in fringes dramatically for a set of a few reference images. In principle, the more reference images N, the better the optimal image one achieves but the longer calculation time is needed. In practice, a set of data with 50 images gets rid of the fringes and is not too time consuming. This technique also has the benefit of reducing dark current, electronic, and photon noise by a factor $\sqrt{2}$ at best (for $N \to \infty$ and if all images are weighted the same). For example, let us consider photon noise. To each image i there is an associated shot noise σ_i:

$$\sigma_i \propto \sqrt{n} \tag{1.8}$$

with n the number of photons on an image. The shot noise associated to the optimal reference image σ_{opt} is the average of the shot noise of all reference images:

$$\sigma_{opt} = \sum_{k=1}^{N} \frac{\sigma_k}{N} \propto \frac{1}{\sqrt{N}}. \tag{1.9}$$

For large N, $\sigma_{opt} \to 0$. However, the shot noise associated to the absorption image remains.

We show in Fig.1.13 an example of absorption image obtained via this procedure employing 100 images. Underneath each image, is the same integrated line profile of

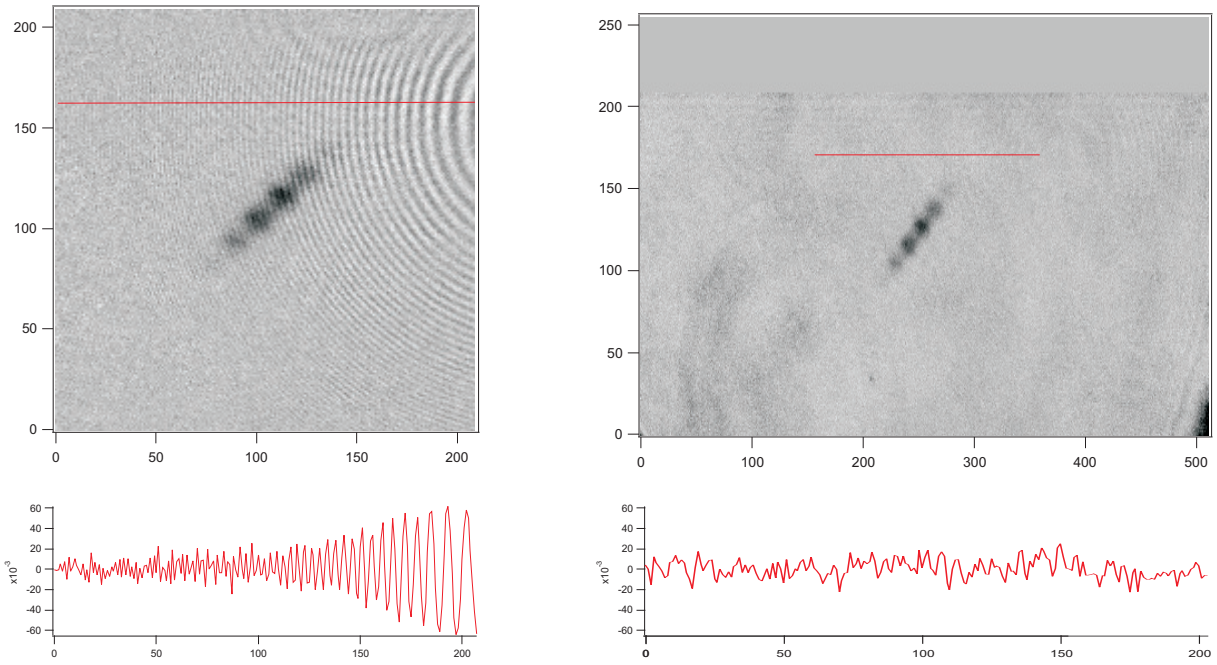

Figure 1.13: Top: Images of the atomic sample with and without the fringe removal algorithm. Bottom: Integrated signal along the red line (same position for both images) where no atoms are present. The image without this algorithm has up to a factor of 6 more noise.

the image. As one can see, the algorithm is efficient in removing the fringes. Moreover, the average mean standard deviation for the "optimal" images is typically 20% smaller than without the algorithm.

CHAPTER 2

Loading an Optical Dipole Trap with ^{53}Cr atoms: a first step towards producing a Chromium Fermi sea

In this chapter, I will describe the experimental setup we implemented in order to load as many ^{53}Cr atoms in a 1D FORT as possible. We followed the same strategy as for the boson: we load atoms directly in a 1D FORT from a ^{53}Cr MOT implemented by a new laser scheme, used metastable states in order to protect the atoms from light assisted inelastic collisions, repumped them in their electronic ground state and optically pumped atoms in the lowest Zeeman state so that the sample is ready for evaporation.

2.1 Introduction

Ultracold fermionic gases with long range interactions are an appealing system since for cold polarized Fermi gases the long range interaction is the leading interaction term. In 2006, the team produced a simultaneous MOT of bosonic and fermionic chromium atoms [39]. The fermionic setup has since then been put aside in order to progress on the bosonic sample. The main reason is that it is a real technical challenge to produce large samples of ultracold chromium atoms and a new laser system was needed.

In 2012, the first degenerate atomic dipolar Fermi gas was produced with Dy atoms [66], followed by a degenerate dipolar gas of Er [67] and the production of cold molecules with strong electric dipole moment [32]. In the following, we shall describe the new laser system dedicated to producing a ^{53}Cr MOT and the route we used to perform an efficient loading of ^{53}Cr atoms in an 1D FORT.

To produce a ^{53}Cr Fermi sea, we need to accumulate the largest amount of ^{53}Cr in the 1D FORT. To achieve that, we followed the route used in a previous work where the loading of a ^{52}Cr gas in an 1D FORT was optimized [54]. The optimization process relies on direct loading of the 1D FORT with atoms in metastable states. These atoms are produced by optical leaks from a MOT. The corresponding fermionic setup is implemented in order to be independent of the bosonic setup.

In the following, we will describe in detail the optimization of the fermion MOT. Then we analyze the loading of metastable fermionic atoms in the 1D FORT, presenting in particular our measurement of new spectral lines of ^{53}Cr. Finally we describe the

optimal experimental sequence for producing a chromium Fermi sea.

2.2 Producing a ^{53}Cr MOT

2.2.1 Laser system

In 2006, the team produced a simultaneous MOT of bosonic and fermionic chromium atoms [39]. In the setup, they used the same laser to produce cooling light for the boson and for the fermion. From there on, the team cooled to degeneracy the boson [43] and to do so, all laser power was devoted to cool the boson. We therefore set up a whole new laser system specifically dedicated to the cooling of the fermion (Fig.2.1) so that the setup of the boson could remain unchanged.

Fig.2.2 shows the energy level diagram for ^{53}Cr. We use the $|^7S_3> \rightarrow |^7P_4>$ (λ =425.553 nm) transition to decelerate ^{53}Cr atoms in a Zeeman Slower (ZS) and to cool and trap them in a MOT.

The Ti:Sapphire laser

At the time when the laser system was purchased, there were no commercial diode systems available at the correct wavelength and with sufficient laser power in order to perform cold atom experiments. To meet our needs, the team followed the same path as for the boson, that is frequency doubling a Titanium Sapphire laser. We pump a Ti:Sa[1] with 15 W of a Verdi laser V18 and are able to produce 3.5 W of laser light at 851 nm (this yields a 22% conversion efficiency). We stabilize the frequency of Ti:Sa2 by locking it to an ultrastable Fabry Pérot reference cavity which is described in detail in [68, 54]. The stability of this cavity allows frequency locking with an accuracy and stability better than 1 MHz. We use a Pound Drever Hall [69] technique to lock Ti:Sa2. The laser beam goes through an Electro Optic Modulator (see Fig. 2.1) which implements two sidebands to the carrier frequency which are reflected from the ultrastable cavity into a photodiode. The absolute frequency of the laser Ti:Sa2 is measured by beating Ti:Sa2 with Ti:Sa1 on a fast photodiode. We lock the Ti:Sa2 laser 112 MHz to the red of the Ti:Sa1 laser.

The doubling cavity

The Ti:Sa2 laser frequency is then doubled with an efficiency of 20% in a doubling cavity MBD produced by Coherent. We then have at our disposal 800 mW of 425.5 nm light which we separate in four beams. The beams are then shaped and shifted in frequency (with lenses and AOMs) depending on the needs and then coupled to the

[1] called Ti:Sa2 from now on to avoid any confusion with Ti:Sa1 which is dedicated to the Boson

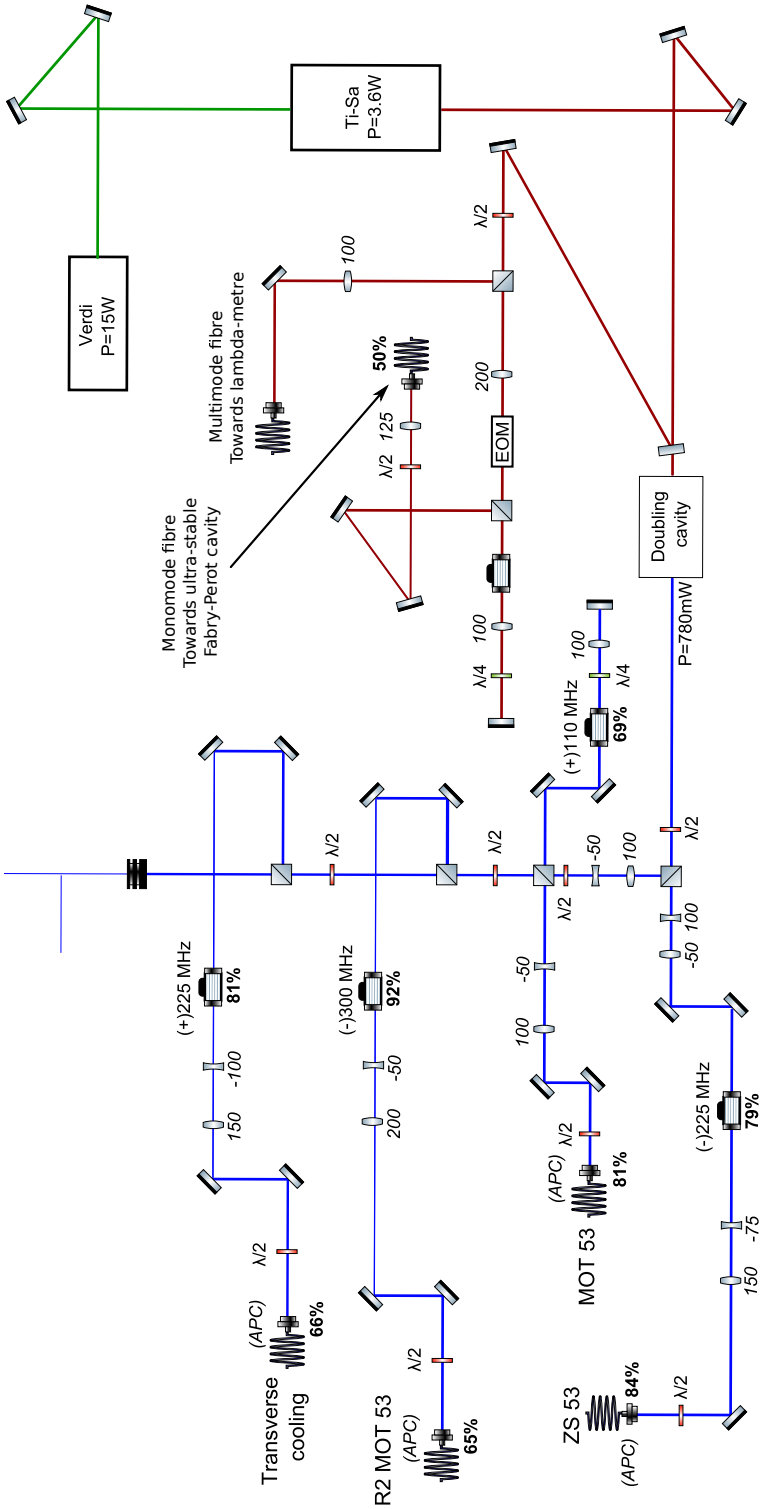

Figure 2.1: Scheme of the fermionic table.

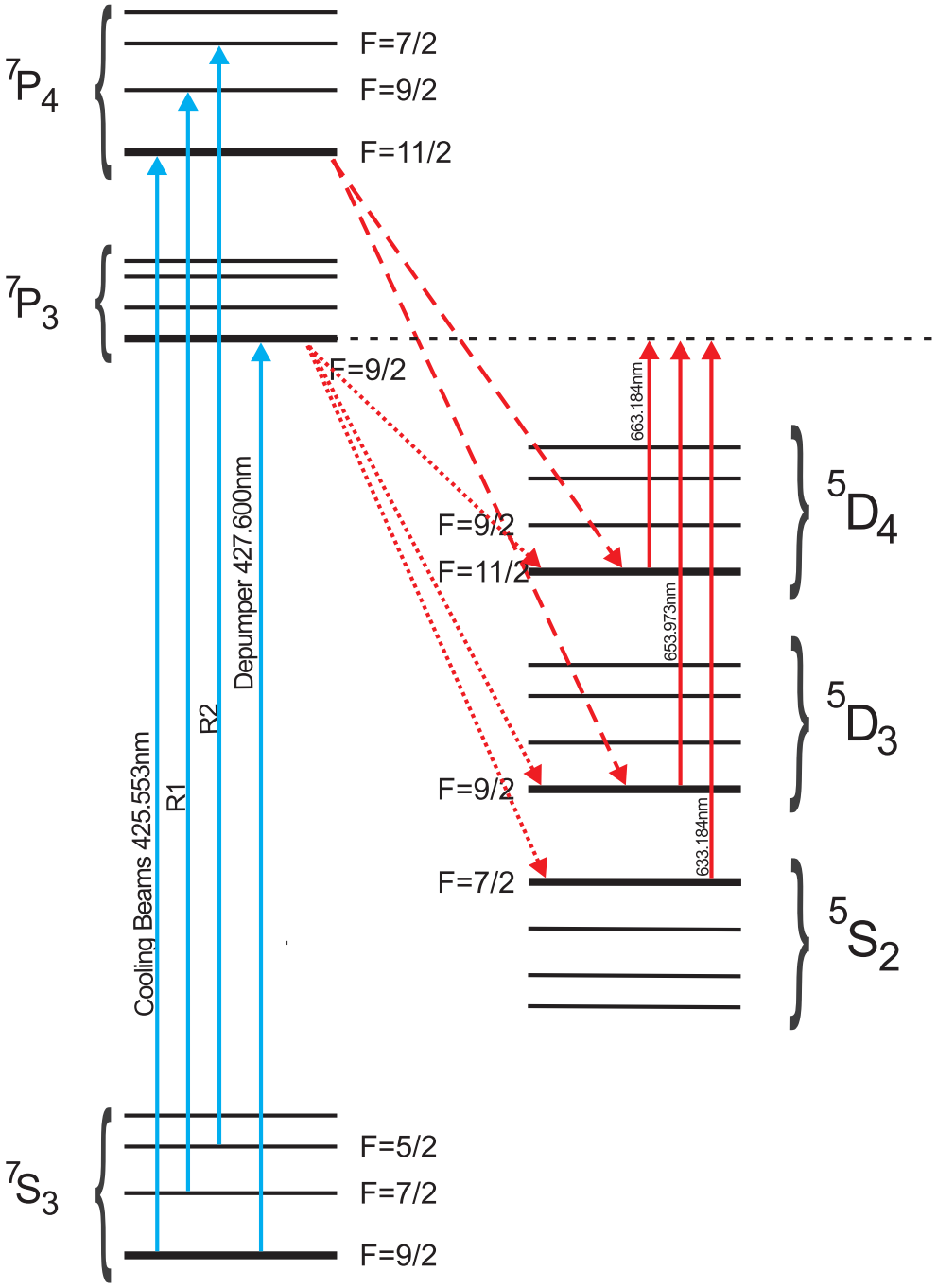

Figure 2.2: Atomic Structure of ^{53}Cr. In blue we show the transitions necessary to produce a fermionic MOT (cooling and trapping beam, R1 and R2) and the Depumper beam. In dashed red lines we illustrate the main decay lines from the excited states to metastable dark states. In red the transitions to repump atoms back in $|^7S_3>$.

main optical table through monomode polarizing maintaining fibers[2](see Fig. 2.1).

2.2.2 Zeeman Slower

As discussed earlier for the boson, the fermionic atoms emitted by the oven are decelerated by a ZS. At the exit of the oven, the populations of the fermionic isotope are equally distributed into the 28 Zeeman sublevels of the four hyperfine ground states. Only atoms in the $|F = 9/2, m_F = 9/2>$ Zeeman sublevel will be slowed down in the ZS.

The ZS is optimised for the bosonic $|^7S_3, J = 3, m_J = 3 > \rightarrow |^7P_4, J = 4, m_J = 4 >$ transition, and therefore the magnetic field profile should also be optimal for the fermion transition $|^7S_3, F = 9/2, m_F = 9/2 > \rightarrow |^7P_4, F = 11/2, m_F = 11/2 >$. Indeed, the energy difference between $|^7P_4, F = 11/2, m_F = 11/2 >$ and $|^7S_3, F = 9/2, m_F = 9/2 >$ is exactly the same than for $|^7P_4, J = 4, m_J = 4 >$ and $|^7S_3, J = 3, m_J = 3 >$. The reason for that is that these are Zeeman states that are pure eigenstates of the system (these stretched states are eigenstates to the hyperfine Hamiltonian and to the Zeeman Hamiltonian).

Therefore we just need to add to our setup a σ^+ beam[3] on the $|^7S_3, F = 9/2, m_F = 9/2 > \rightarrow |^7P_4, F = 11/2, m_F = 11/2 >$ transition in order to slow fermionic atoms which were in $|^7S_3, F = 9/2, m_F = 9/2 >$. We find that 200 mW of light red-detuned by 453 MHz from resonance optimizes the fermionic ZS (as for the bosonic transition, see Table 2.2).

Along the Zeeman slower, there is a value of the magnetic field (B=25G) which makes the two atomic transitions $|^7S_3, F = 9/2, m_F = 9/2 > \rightarrow |^7P_4, F = 9/2, m_F = 7/2 >$ and $|^7S_3, F = 9/2, m_F = 9/2 > \rightarrow |^7P_4, F = 11/2, m_F = 11/2 >$ degenerate [39, 50]. A slight σ^- component in the Zeeman slower beam is sufficient to accumulate atoms in the state $|^7S_3, F = 7/2 >$ as shown in Fig. 2.3. These atoms will no longer be sensitive to the cooling beam and will be lost. The frequency of the repumper needed is very close to the ^{52}Cr ZS beam frequency and we will use that beam to repump the atoms back into the cooling transition.

To slow efficiently the atomic flux of ^{53}Cr we will use a ^{53}Cr ZS beam and the ^{52}Cr ZS beam acting as a repumper.

2.2.3 Transverse Cooling

To increase the atomic flux which reaches the MOT capture region we implemented horizontal and vertical transverse cooling beams as for the bosonic setup. Their role

[2]Schäfter+Kirchhoff PMC-E-460Si-4.0 (transmission efficiency of typically 75%) and Thorlabs 973-579-7227FTO30 transmission efficiency of typically 60%

[3]Actually, the magnetic field profiles crosses B=0 along the ZS. The ZS is first σ^+ and then σ^-. To simplify the discussion, I consider that the laser light is σ^+ along the ZS but the discussion remains correct.

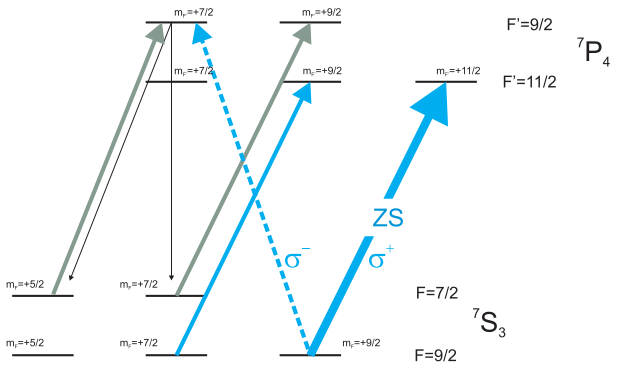

Figure 2.3: ^{53}Cr Zeeman slower mechanism for the magnetic field which makes the two atomic transitions $|^7S_3, F = 9/2, m_F = 9/2 > \rightarrow |^7P_4, F = 9/2, m_F = 7/2 >$ and $|^7S_3, F = 9/2, m_F = 9/2 > \rightarrow |^7P_4, F = 11/2, m_F = 11/2 >$ degenerate. A small σ^- component in the ZS beam can accumulate atoms in F=7/2 where they will no longer be resonant with the ZS beam. These atoms can be repumped back into $|F = 9/2, m_F = 9/2 >$ using the ZS 52 beam (grey arrows). Image taken from [50].

is to collimate the atomic beam and increase the number of atoms which reach the MOT capture region. Contrarily to the bosonic case, the beams for the MOT and transverse cooling are independent and optimization of their frequencies and power was performed. We found that 100 mW of light red-detuned by 6 MHz from resonance optimizes the TC process at the B field used to optimize the ^{52}Cr MOT in the transverse cooling setup. For the same reason as for the fermionic MOT (which I describe in the next section), a repumper is needed and the bosonic transverse cooling beam is used to perform that task.

2.2.4 The MOT

The main difference in atomic structure between the bosonic and fermionic isotope comes from the fact that the fermionic isotope has a non zero nuclear spin ($I = 3/2$) which leads to a hyperfine structure, see Fig.2.2. This hyperfine structure introduces an extra "leak" in the cooling cycle compared to the boson. Indeed, there is a non-zero probability that an atom in $|^7S_3, F = 9/2 >$ will absorb a photon of the cooling light and be promoted to $|^7P_4, F = 9/2 >$. From there on the atom can decay to $|^7S_3, F = 7/2 >$ and exit the cooling cycle. We repump these atoms back into the cooling transition by applying a laser, called Repumper 1 (R1), on the $|^7S_3, F = 7/2 > \rightarrow |^7P_4, F = 9/2 >$ transition. Atoms can no longer accumulate in $|^7S_3, F = 7/2 >$, and can only accumulate in $|^7S_3, F = 9/2 >$ or $|^7S_3, F = 5/2 >$. We can then again use a repumper beam to prevent atoms from accumulating in $|^7S_3, F = 5/2 >$, this time the beam (Repumper 2) is resonant with the $|^7S_3, F = 5/2 > \rightarrow |^7P_4, F = 7/2 >$ transition. The presence of the R1 beam for a MOT is essential: without it we do not have a MOT. The R2 beam increases the number of atoms by 20%. We did

not implement a third repumper beam on the $|^7S_3, F = 3/2 > \rightarrow |^7P_4, F = 5/2 >$ transition, since we believe its contribution should be marginal given that the effect of R2 is modest.

The frequency of the R1 beam is very close to the frequency for the ^{52}Cr MOT frequency, therefore we use the same laser beam for the ^{52}Cr MOT and for the R1 of the ^{53}Cr MOT. R2 is not very close to any of the pre-existing beams and is obtained with a set of AOMs (Fig. 2.1). The R1 repumper beams are overlapped to the fermionic MOT beam, and are eventually separated in 6 beams. The fact that the R1 beams are overlapped with the MOT beams helps produce an optimum MOT. Indeed, a configuration with only one vertical beam for R1 pushes the MOT and a retro-reflection of this vertical beam produces only a small MOT. Our interpretation is that overlapping R1 with the MOT beams is optimum for two reasons: (i) the intensity of R1 is large[4] and a MOT configuration ensures a mechanical balance and (ii) because R1 contributes to cooling due to the small hyperfine structure of $|^7P_4 >$.

2.2.5 MOT characteristics

To monitor and optimize the MOT parameters, we use fluorescent imaging with our Pixelfly camera. The camera counts the number of photons received during its integration time τ_{int}. To observe the MOT continuously, we use a commercial program called "CamWare" which enables a false color representation of the fluorescence.

The number of atoms N in the MOT is related to the number of photons N_{ph} received by the camera through the scattering rate R_{Scat}. The scattering rate gives the number of photons scattered in all directions by an atom under radiation:

$$R_{Scat}(\Omega, \delta) = \frac{\Gamma}{2} \frac{C^2 \frac{\Omega^2}{2}}{C^2 \frac{\Omega^2}{2} + \frac{\Gamma^2}{4} + \delta^2} \tag{2.1}$$

where Γ is the width of the excited state, δ is the detuning between the frequency of the MOT laser beams and the atomic resonance, $\Omega = \Gamma \sqrt{\frac{I}{I_{Sat}}}$ is the Rabi frequency, and C^2 is the averaged squared Clebsch Gordan coefficient over all the Zeeman sublevels of the ground state for a given light polarization.

The number of photons received by the camera is not directly proportional to the number of atoms in the MOT. At constant N, the photon number can increase just by reducing $|\delta|$ or increasing Ω. We fixed the resonance frequency to be the frequency of the absorption pulse which maximizes the optical denisty of the MOT.

We then optimized the number of atoms in the MOT to 1.2×10^5. This number is slightly lower than the one obtained in 2006 (see Table 2.1), but the fraction of $N_{^{52}Cr}/N_{^{53}Cr}$ is similar which makes us confident that we have optimized the MOT and the global Chromium flux is just lower. It also must be considered that at the time

[4] because it is also the ^{52}Cr MOT beam

of the double MOT experiment [39] it was the number of atoms in the MOT which was optimized, whereas now it is the number of boson atoms loaded in the 1D FORT which is optimized. This suggests that the number of bosons $N_{^{52}Cr}$ in the MOT could be larger and therefore we would have closer $N_{^{52}Cr}/N_{^{53}Cr}$ values to the historical value. For comparison I list the number of atoms in the MOT of the different isotopes for the different years:

	2006	2013
$N_{^{52}Cr}$	$(4 \pm 0.4\ ) \times 10^6$	$(1.2 \pm 0.2\ ) \times 10^6$
$N_{^{53}Cr}$	$(2 \pm 0.2\ ) \times 10^5$	$(1.2 \pm 0.2\ ) \times 10^5$
$N_{^{52}Cr}/N_{^{53}Cr}$	20 ± 4	10 ± 2

Table 2.1: Comparison of the number of atoms in the MOT of different species with the time when the team first produced a double MOT

2.2.6 Optimal trapping laser parameters

We indicate in Table 2.2 the parameters of the blue laser beams we use to produce the fermionic MOT: maximal intensity, waist, and detuning from the ^{53}Cr atomic resonance $|F = 9/2 > \rightarrow |F = 11/2 >$ at zero magnetic field. These values correspond to an optimization of the number of atoms loaded in the 1D FORT (see below), based on the following procedure. The sizes of the bosonic beams were optimized for the production of the BEC, we optically shaped their fermionic counterparts to reach the same size. The size of R2 has been optimized. The repartition of power between the three bosonic beams (MOT, ZS and TC) is the one optimizing BEC production. The repartition of power between the four fermionic beams (MOT, ZS, TC and R2) has been optimized to maximize the 1D FORT loading. As for the frequencies, all of them have been optimized for fermionic loading except the one of ZS 52, which provides best BEC production.

2.2.7 Overlapping fermionic beams on the bosonic beams

There are, to my knowledge, three standard ways to perfectly overlap two beams together: with a dichroic mirror, a 50/50 plate, or with a Polarization Beam Splitter. A dichroic mirror works when the wavelength of the different beams are different. A 50/50 plate works when you are ready to lose half of your optical power. A PBS is a good way of overlapping beams when the polarization of the beam is not an important issue.

Here we want to align the fermion beam on the boson beam. They have almost the same frequency and a dichroic mirror is out of the question.

Beam	δ	I_0(mW·cm^{-2})	w (mm)
MOT 53	-12 MHz	189	4.5-5.2
R1 MOT 53	-324 MHz	140	4.2-4.5
R2 MOT 53	-530 MHz	23	3.8-4.1
ZS 53	-453 MHz	430	Not collimated
ZS 52	-766 MHZ	180	Not collimated
TC53	-6 MHz	80	2.8-14
TC52	-324 MHz	16	2.8-14

Table 2.2: Summary of the different beams, with their waist w, peak intensity I_0 (defined as $I_0 = \frac{2P}{\pi w^2}$ with P the beam power) and detuning δ from the ^{53}Cr atomic resonance at zero magnetic field, leading to the best fermionic 1D FORT loading.

For the ZS and transverse cooling, the polarization of the beam is crucial, therefore a PBS wouldn't work. A 50/50 plate would make us lose power for the boson and the fermion and we can't spare to lose any optical power. The solution used here was to align the fermionic beams with a slight angle compared to the boson beam.

The MOT beam is recombined with the bosonic beam on a 50/50 mirror. There was already a 50/50 mirror on the bosonic MOT path to separate the beam in two: one for the horizontal plane and one for the vertical plane. We therefore recombined the fermion beam with the boson beam on the 50/50 mirror. Finally, as the polarization of the R2 beam is not relevant we therefore recombined this beam with the fermionic MOT beam on a PBS.

2.2.8 Need of light protected reservoirs

Our experiment produces independently a ^{52}Cr MOT of a few 10^6 atoms at approximatively 120 μK ($\approx T_{Doppler}$) and a ^{53}Cr MOT of 1.2×10^5 atoms presumably at the same temperature. The typical number of atoms trapped in both MOTs is quite small compared to other species (such as Rb or Na where MOTs can have up to 10^{10} atoms see for example [70]), due to large light assisted collisions between atoms in the ground state and atoms promoted to an excited state by light [50]. The light assisted collision rates are estimated at 6×10^{-10}cm^3·s^{-1} for the boson and 5×10^{-9}cm^3·s^{-1} for the fermion [50] which is typically one to two orders of magnitude worse than for alkalis.

Direct accumulation of atoms in the ground state $|^7S_3>$ from a MOT into a conservative trap where evaporation could be performed is inefficient and leads to typically 1×10^4 fermions loaded in the 1D FORT. This is due to light assisted collisions. We use dark metastable states as reservoirs where atoms can be accumulated in the 1D FORT. Atoms in metastable states are not sensitive to the MOT light and are protected from light-assisted inelastic collisions. After the loading of the 1D FORT with metastable atoms is complete, repumping to the electronic ground state $|^7S_3>$ defines the starting

point for evaporation.

In addition to the light force from the 1D FORT, atoms in metastable states are sensitive to magnetic forces created by the MOT gradients. As described in [42], cancellation of these forces by use of fast radio frequency sweeps allows to significantly increase the number of atoms loaded in the 1D FORT. This technique provides the same benefit in the fermionic case, typically a factor two in the number of atoms loaded in the 1D FORT.

The next section describes our study of the loading of the 1D FORT with ^{53}Cr atoms.

2.3 Loading metastable ^{53}Cr atoms in the 1D FORT

To produce a BEC, the use of $|^5D>$ metastable dark states as a reservoir was not sufficient. A large inelastic collisions rate between atoms in $|^5D>$ of the order $\beta^{(52)}_{^5D-^5D} = 3.5 \times 10^{-11}\text{cm}^3\cdot\text{s}^{-1}$ [54] prevents from accumulating enough atoms to reach degeneracy with evaporation cooling. The solution was to use another metastable state as a reservoir, $|^5S_2>$, more favorable for accumulation. Atoms can be accumulated in $|^5S_2>$ through leaking from the excited state $|^7P_3>$. This was a real breakthrough in increasing the atomic number since the inelastic collision rate is smaller than in $|^5D>$: $\beta^{(52)}_{^5S-^5S} = 1.6 \times 10^{-11}\text{cm}^3\cdot\text{s}^{-1}$. In addition, the light shift for this state is larger than for the $|^5D>$ states for the wavelength of the 1D FORT which results in a deeper trap [43]. Using accumulation in state $|^5S_2>$ allows us to load about 10^6 bosonic atoms in the 1D FORT, where evaporation can be performed and BECs of a few 10^4 atoms are produced.

To reach fermionic degeneracy with sympathetic evaporative cooling, we first have to accumulate as many ^{53}Cr atoms as possible in the same 1D FORT where ^{52}Cr atoms were successfully loaded. For that we followed the same strategy as for the boson, that is to accumulate metastable dark states in the 1D FORT, and then repump them into the ground state. In this section we first describe the repumping laser systems that we use. We then present our measurement of the frequencies of the different ^{53}Cr repumping lines of interest, which were unknown.

2.3.1 Repumping lines of metastable states of ^{53}Cr

Repumping of the different metastable states is performed through the excited state $|^7P_3>$ (see Fig.2.2). We use three different red laser diodes, with an extended cavity scheme using a grating to ensure selective retro-reflection, and a monomode regime. The wavelengths are respectively 663.183 nm, 653.973 nm, and 633.183 nm for repumping the bosonic $|^5D_4>$, $|^5D_3>$ and $|^5S_2>$ states.

From the $|^7P_3>$ state, population of the $|^5D_2>$ state is possible, but the study in [54] showed that repumping this state does not lead to better loading of the 1D FORT

with ^{52}Cr. We therefore assumed that the gain would be marginal as well with ^{53}Cr and we did not study repumping from this state.

The first step to optimize the 1D FORT loading was to find the repumping lines of ^{53}Cr atoms. The transition frequencies for repumping the atoms from metastable states to the ground state are isotope-dependent because of the hyperfine structure of ^{53}Cr, and isotopic shifts. The isotopic shift is the difference in frequency for a given transition between the two isotopes assuming a zero hyperfine splitting. For the fermionic isotope, the value of the isotopic shift is deduced from the shift between the bosonic and fermionic transition and the HF splitting of the fermionic isotope.

Frequency stabilization of the three laser diodes is obtained by locking on a Fabry Pérot (FP) cavity. For the 663 and 633 nm laser diodes, we use the FP cavity on which Ti:Sa1 is locked: once this cavity is locked using saturation absorption, it defines an absolute reference. For the 654 nm diode, we use the FP on which Ti:Sa2 is locked. For all diodes, we use an AOM in a double-pass scheme, which provides a frequency shift as large as the free spectral range of the locking cavities, to set the frequency of the repumper beams at resonance of the bosonic lines.

For each transition, we split the boson repumping beam into two separate beams, and shifted in frequency one of those beams by a set of AOMs to probe the fermionic repumping transition. The two beams are then recombined and aligned on the atoms. In the following section we present our measurement of the frequency transitions for ^{53}Cr between the different metastable states and the excited $|^7P_3>$. The measurement of the frequency difference between a given bosonic and fermionic transition is directly given by the AOMs frequency shifts Δf. We can then calculate the isotopic shift associated to each transition (see below).

Repumping $|^5D>$ states

In Fig.2.4 (Fig.2.5) we show the optical system we used to produce beams for the $|^5D_3, F = 9/2>$ ($|^5D_4, F = 11/2>$)$\rightarrow$ $|^7P_3, F = 9/2>$ transition.

From the MOT, ^{53}Cr atoms naturally leak towards $|^5D_3, F = 9/2>$, $|^5D_4, F = 11/2>$ and $|^5D_4, F = 9/2>$, and can accumulate in the 1D FORT. Therefore, atoms of the 1D FORT are mainly in states $|^5D_3>$ or $|^5D_4>$. We then turn off all cooling lights and shine a repumper on the $|^5D_3, F = 9/2>$ (or $|^5D_4, F = 11/2>$)$\rightarrow$ $|^7P_3, F = 9/2>$ transition to repump atoms in the electronic ground state $|^7S_3, F = 9/2>$, and we measure the atomic number by absorption imaging on that state. The frequency which maximizes the atomic number is deduced to be the frequency which is resonant for the given transition. The result of this experiment for the $|^5D_3, F = 9/2> \rightarrow |^7P_3, F = 9/2>$ transition can be seen in Fig.2.6.

Atoms can leak from $|^7P_4, F = 11/2>$ towards $|^5D_4, F = 11/2>$ and $|^5D_4, F = 9/2>$. We indeed measured two resonances in the case of $|^5D_4>$ and we attributed the resonance which gave the maximum atomic number to be the $|^5D_4, F = 11/2> \rightarrow |^7P_3, F = 11/2>$. The frequency difference of 250 MHz which we found between the

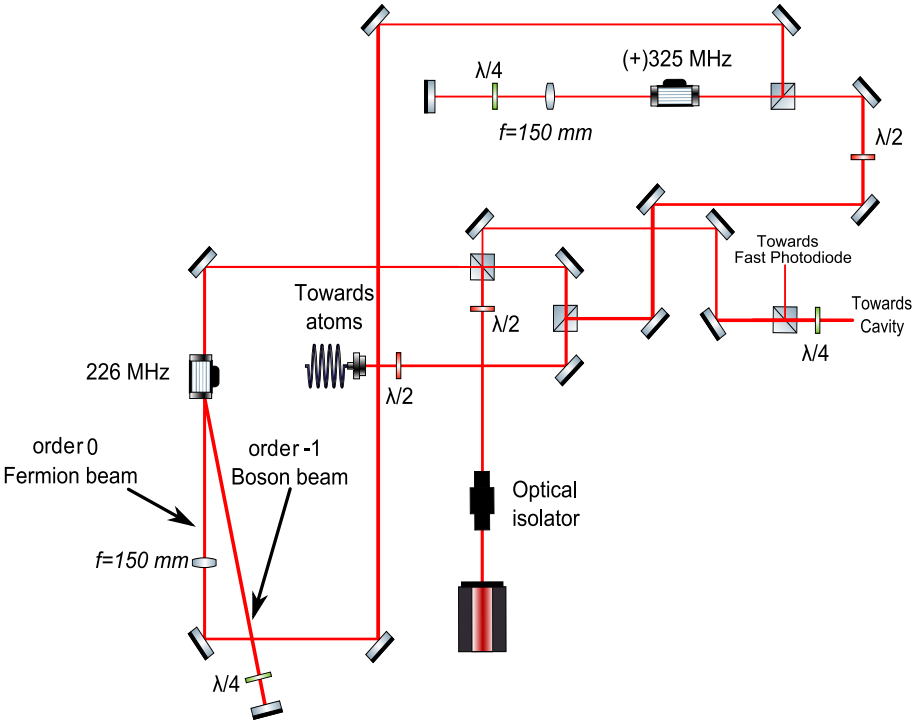

Figure 2.4: Optical setup for the $|^5D_3, F = 9/2 > \rightarrow |^7P_3, F = 9/2 >$ transition. The fermionic frequency is shifted by 1244 ± 10 MHz.

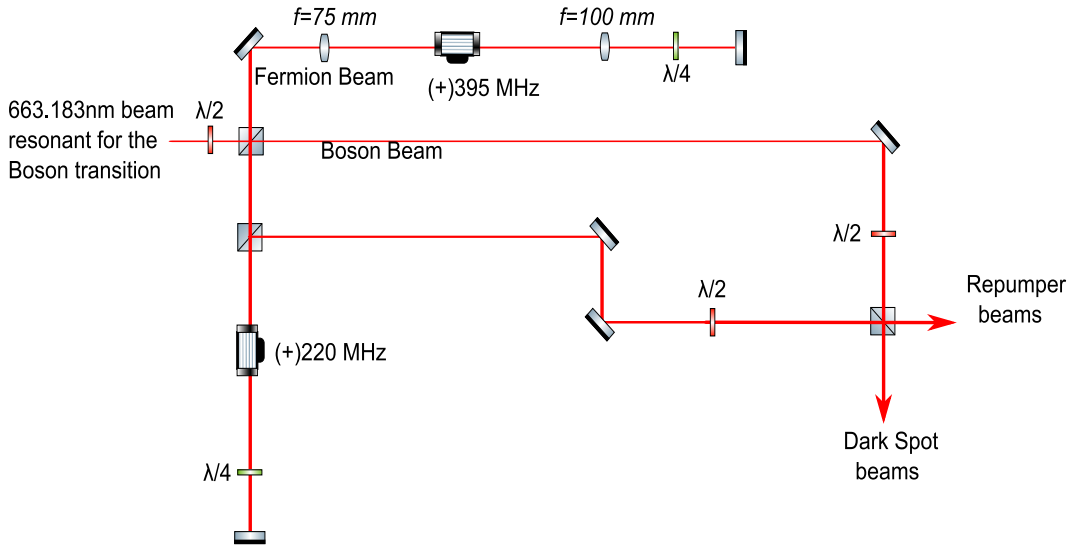

Figure 2.5: Optical setup for the $|^5D_4, F = 11/2 > \rightarrow |^7P_3, F = 9/2 >$ transition. The fermionic frequency is shifted by 1102 ± 10 MHz.

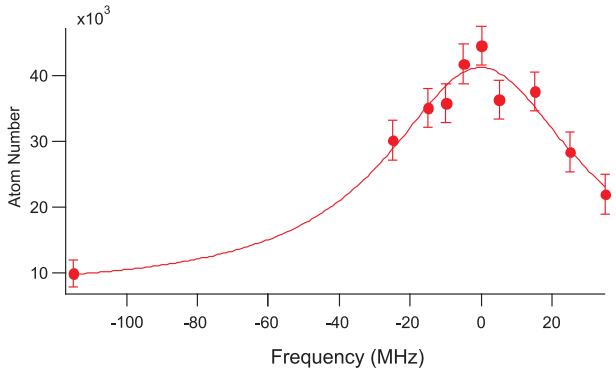

Figure 2.6: Optimisation of the $|^5D_3, F = 9/2 > \rightarrow |^7P_3, F = 9/2 >$ transition. Full line is a Lorentzian fit to the data. The width of this resonance is larger than the expected width of $|^7P_3 >$. We attribute this to the saturation of the transition due to a long repumper pulse which leads to a broadening of the resonance.

two experimental transitions is in good agreement with the energy splitting between $|^5D_4, F = 11/2 >$ and $|^5D_4, F = 9/2 >$ which can be found in [71].

We measured a frequency difference Δf of 1244±10 MHz (1102±10 MHz) between the boson and fermion frequency for the $|^5D_3, F = 9/2 >$ ($|^5D_4, F = 11/2 >$)$\rightarrow$ $|^7P_3, F = 9/2 >$ transition. The hyperfine structure of $|^7P_3 >$ can be calculated from [72], and the ones for $|^5D_4 >$ and $|^5D_3 >$ are obtained from [71]. The hyperfine spectrum is shown in Fig.2.7. From the available data and our measurements, we can deduce the isotopic shifts for each transition.

Isotopic shift calculation

In the following, I describe how we extracted the different isotopic shifts of interest.

Table 2.3 summarizes up spectroscopic measurements between hyperfine states of different fine levels.

For an isotopic shift measurement, the level considered is a virtual level defined as the barycenter of the hyperfine levels [74]. Let us call x the frequency difference between the barycenter and the hyperfine level with the highest F. The barycenter of $|^5D_4 >$, for example, can be explicitly calculated:

$$\begin{aligned} \frac{11}{2} \times 2 \times x \;\; &+ \;\; \frac{9}{2} \times 2 \times (x + 224.827) + \frac{7}{2} \times 2 \times (x + 224.827 + 234.593) \\ &+ \;\; \frac{5}{2} \times 2 \times (x + 224.827 + 234.593 + 213.970) = 0 \qquad (2.2) \\ \rightarrow x \;\; &= \;\; -276.8 \text{ MHz}. \qquad (2.3) \end{aligned}$$

The values of x for each fine level are summarized in Table 2.4.

For the excited fine level of the transition considered here (i.e. $|^7P_3 >$), spectroscopic data [72] provide the values of the magnetic dipole moment interaction (A) and of

Fine level	Investigated transition $F \rightarrow F$	Transition frequency ν_{exp} (MHz)
$^5D_4$	11/2 - 9/2	224.827
	9/2 - 7/2	234.593
	7/2 - 5/2	213.970
$^5D_3$	9/2 - 7/2	148.900
	7/2 - 5/2	130.339
	5/2 - 3/2	100.881
$^5S_2$	7/2 - 5/2	608.375
	5/2 - 3/2	434.547
	3/2 - 1/2	260.727

Table 2.3: Zero field RF transition frequencies between hyperfine states for different fine levels. Data extracted from [71, 73].

Fine level	x
$\|^5D_4>$	-276.777
$\|^5D_3>$	-156.683
$\|^5S_2>$	-521.462

Table 2.4: Values of x, the distance between the barycenter of the hyperfine levels and the hyperfine level with the highest F.

the electric quadrupole moment interaction (B) coefficients: $A = -1.5 \pm 2$ MHz and $B = -2\pm^5_1$ MHz.

The distance between the virtual transition considered for the isotopic shift and the level with highest F is given by:

$$\Delta E = \frac{1}{2}AK + hB\frac{3/2K(K+1) - 2I(I+1)J(J+1)}{2I(2I-1)2J(2J-1)} \tag{2.4}$$

where $K = F(F+1) - I(I+1) - J(J+1)$ and A and B are two coefficients accounting for the hyperfine interaction. For $|^7P_3, F = 9/2>$ we calculate ΔE=6.25 $\pm$ MHz.

Then the isotopic shift (IS) is simply given by:

$$IS = \Delta F - x - \Delta E. \tag{2.5}$$

We therefore deduce from all these data an isotopic shift of 1095$\pm$28 MHz (833$\pm$28 MHz) for the $^5D_3(^5D_4) \rightarrow {}^7P_3$ transition.

The different frequencies and isotopic shifts related to metastable states are summarized in Table 2.5 and Fig. 2.7.

^{53}Cr Transition	^{52}Cr Transition	Freq Shift	Isotopic shift
$^5D_4$F=11/2 $\rightarrow$ $^7P_3$ F=9/2	$^5D_4 \rightarrow {}^7P_3$	1242$\pm$ 10 MHz	819 $\pm$28 MHz
$^5D_3$F=9/2 $\rightarrow$ $^7P_3$ F=9/2	$^5D_3 \rightarrow {}^7P_3$	1088 $\pm$ 10 MHz	670 $\pm$28 MHz
$^5S_2$F=7/2 $\rightarrow$ $^7P_3$F=9/2	$^5S_2 \rightarrow {}^7P_3$	-685 $\pm$ 35 MHz	-155 $\pm$53 MHz

Table 2.5: Values of the frequency shift between the two repumping beams and deduced isotopic shifts for each metastable states

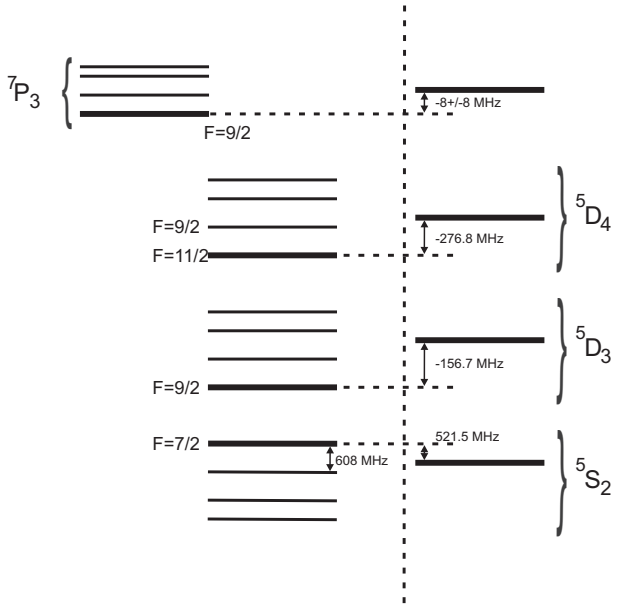

Figure 2.7: Hyperfine splitting of the fermionic metastable states of interest.

Accumulating and repumping $|^5S_2>$

Atoms of the MOT do not naturally leak towards $|^5S_2>$ because the excited state is a $|^7P_4>$ state Fig.2.2. In order to accumulate atoms in $|^5S_2, F = 7/2>$, we transfer atoms in $|^7P_3, F = 9/2>$ where they can decay to $|^5S_2, F = 7/2>$; they also decay in $|^5D>$ states but the transition rate for $|^7P_3> \rightarrow |^5S_2>$ is expected to be significantly larger than the one for $|^7P_3> \rightarrow |^5D>$ [44]. We call the beam exciting the $|^7S_3> \rightarrow |^7P_3>$ transition at 427.6 nm the Depumper since it depumps atoms from $|^7S_3>$ to $|^5D_2>$. However, being a $J \rightarrow J$, the transition will also serve for optical pumping purposes (see subsection 2.3.3). For the boson, both tasks are performed by the same beam. Due to the hyperfine structure of the fermionic isotope, a beam for each task is necessary (see below). Fig.2.8 shows the optical table dedicated to the 427 nm laser. The laser beam is first split into two: one is used for the boson, the other one is dedicated to the fermion. The fermionic beam is then split into two, one beam serves for depumping atoms in $|^5S_2, F = 7/2>$ and the other beam optically pumps

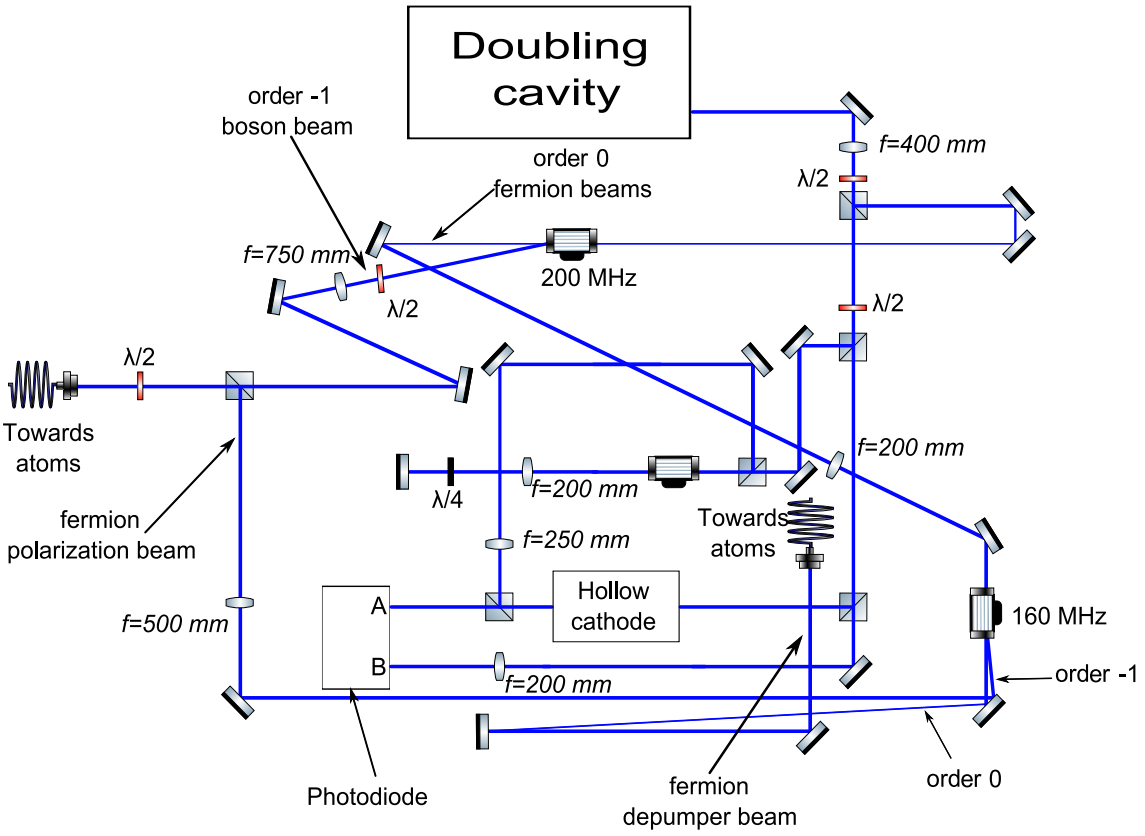

Figure 2.8: Optical setup for the 427 nm laser. It provides depumper and polarization beams for both isotopes.

$|^7S_3, F = 9/2>$ atoms into $|^7S_3, F = 9/2, m_F = -9/2>$.

We produce a ^{53}Cr MOT, and shine $|^7S_3, F = 9/2> \rightarrow |^7P_3, F = 9/2>$ light on the MOT. The resonance frequency of this transition was optimized by minimizing the MOT fluorescence: the more resonant the transition, the more atoms will be promoted to $|^7P_3>$ and exit the MOT fluorescence cycle (see Fig.2.9). We measured a frequency difference of 382±5 MHz between the bosonic $|^7S_3> \rightarrow |^7P_3>$ and fermionic $|^7S_3, F = 9/2> \rightarrow |^7P_3, F = 9/2>$ transitions. The corresponding isotopic shift is deduced from the hyperfine structure of $|^7S_3>$ [75] and $|^7P_3>$ [72] (see Fig.2.7), and is equal to 18±23 MHz. This value is in good agreement with a previous study [76].

We have also measured the $|^5S_2, F = 7/2> \rightarrow |^7P_3, F = 9/2>$ transition. We produce a ^{53}Cr MOT in presence of the Depumper beam. Atoms in states $|^5S_2, F = 7/2>$ are thus loaded in the 1D FORT. We then turn off all cooling lights and shine a repumper beam on the $|^5S_2, F = 7/2> \rightarrow |^7P_3, F = 9/2>$ transition to repump atoms in the electronic ground state $|^7S_3, F = 9/2>$ (see Fig.2.10). We finally measure the number of repumped atoms by absorption imaging. The frequency which maximizes the atomic number is assumed to be the frequency which is resonant with the transition.

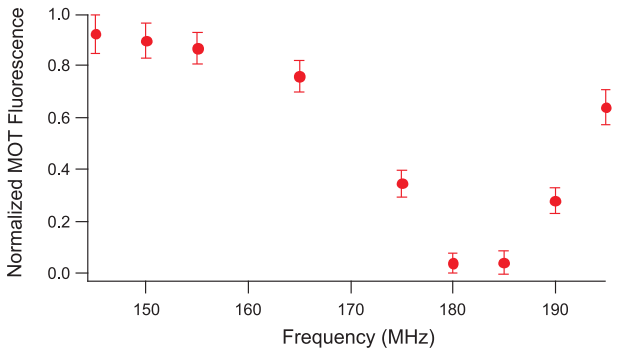

Figure 2.9: Optimization of the $|^7S_3, F = 9/2 > \rightarrow |^7P_3, F = 9/2 >$ transition. The laser frequency for which the MOT is the most depleted is considered the resonant frequency.

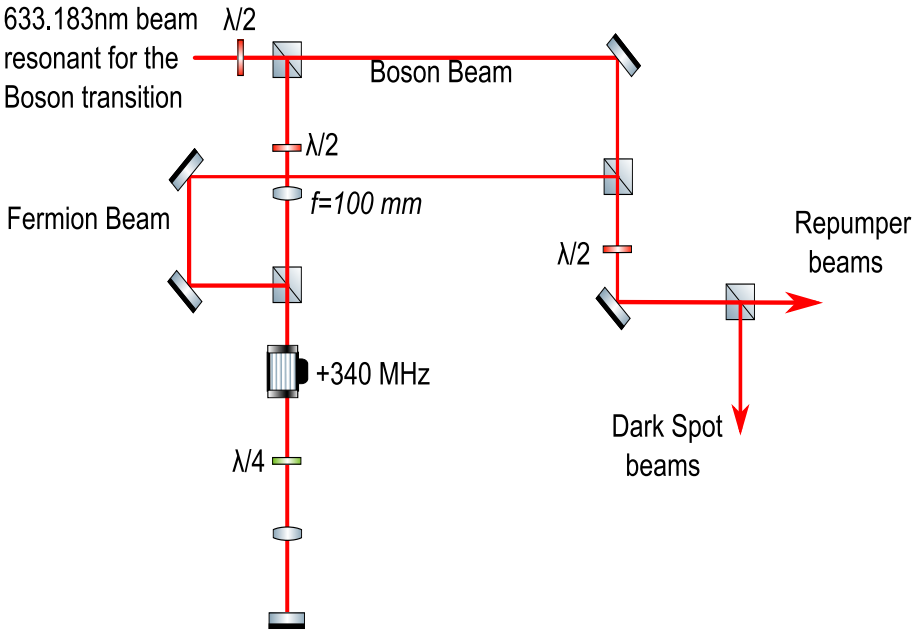

Figure 2.10: Optical setup for the $|^5S_2, F = 7/2 > \rightarrow |^7P_3, F = 9/2 >$ transition. The fermionic frequency is shifted by 685 $\pm$ 35 MHz.

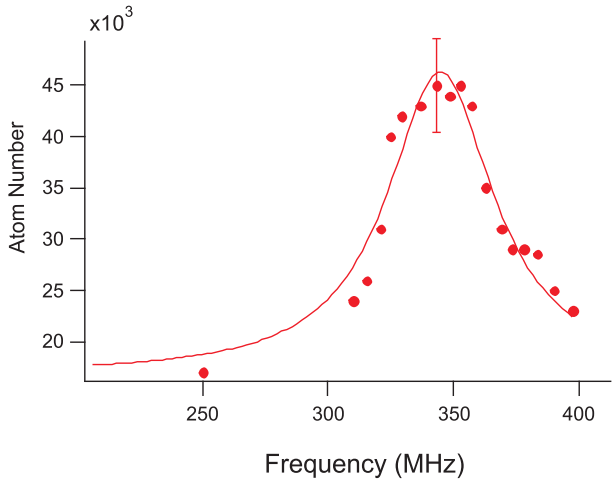

Figure 2.11: Optimisation of the $|^5S_2, F = 7/2 > \rightarrow |^7P_3, F = 9/2 >$ transition. Full line is a Lorentzian fit of width 55 ± 9 MHz. The width of this resonance is larger than the expected linewidth for $|^7P_3 >$. Again, we attribute this broadening to the saturation of the transition due to a long repumper pulse.

The result of this experiment is shown Fig.2.11.

We measured a frequency difference of -685±35 MHz between the bosonic $|^5S_2 > \rightarrow |^7P_3 >$ and fermionic $|^5S_2, F = 7/2 > \rightarrow |^7P_3, F = 9/2 >$ transitions. From the hyperfine structure of $|^5S_2 >$ given in [73] (and summarized Table 2.3), we deduce an isotopic shift of -155±53 MHz.

We observe another signal from repumping ^{53}Cr in $|^5S_2 >$, shifted in frequency by 610 MHz, which is compatible with the frequency difference expected between the $|^5S_2, F = 7/2 > \rightarrow |^7P_3, F = 9/2 >$ and $|^5S_2, F = 5/2 > \rightarrow |^7P_3, F = 7/2 >$ transitions see Table 2.3 and [72, 73]. It is very likely that the $|^5S_2, F = 5/2 >$ state is populated too by the Depumper beam, as the hyperfine structure of the excited state $|^7P_3 >$ is very small. Indeed, coupling of the ground state $|^7S_3, F = 9/2 >$ with the excited state $|^7P_3, F = 7/2 >$ leads to leakage towards $|^5S_2, F = 5/2 >$. The signal ratio of the two repumping signals in $|^5S_2 >$ is about 10% so we decided not to repump both hyperfine levels.

2.3.2 Optimal loading sequence of the 1D FORT

Depumper beams

The bosonic and fermionic depumper beams, resonant on the 427.6nm $|^7S_3 > \rightarrow |^7P_3 >$ transition, are produced from a doubling cavity using a LBO crystal, pumped by a monomode diode laser. They create a leak towards $|^5S_2 >$ metastable states as discussed above. The boson and fermion depumper beams have the same $1/e^2$ waist of 1.5mm, and are retroreflected (see below). Their optimal power, equal to 100 (140) μW

for the bosonic (fermionic) beams, results from a compromise: the higher this power the larger the depumping rate towards the favourable $|^5S_2>$ state, but the smaller the MOT atom number [54].

Repumping configuration

Let us recall the repumping configuration which optimizes the BEC production: while atoms in $|^5D_3>$ states are continuously repumped in the MOT, atoms are free to accumulate in $|^5D_4>$ and $|^5S_2>$ states in the 1D FORT. Nevertheless we use a dark-spot repumping scheme from these two states in order to maintain atoms not captured in the 1D FORT in the MOT trapping transition.

We found that the same pattern optimizes as well the accumulation of fermionic atoms in the 1D FORT. Due to power limitations for the diodes repumping $|^5D_4>$ and $|^5S_2>$ states, a global optimization had to be found to balance power between bosonic and fermionic transitions, and between repumper and dark spots beams. Table 2.6 summarizes the power of the different repumper beams.

Transition	Isotope	Type[5]	Power
$^5D_3$F=9/2 $\rightarrow$ $^7P_3$ F=9/2	^{53}Cr	Repumper	1mW
$^5D_3 \rightarrow {}^7P_3$	^{52}Cr	Repumper	2mW
$^5D_4$F=11/2 $\rightarrow$ $^7P_3$ F=9/2	^{53}Cr	Repumper	70 μW
$^5D_4$F=11/2 $\rightarrow$ $^7P_3$ F=9/2	^{53}Cr	Dark Spot	130 μW
$^5D_4 \rightarrow {}^7P_3$	^{52}Cr	Repumper	225 μW
$^5D_4 \rightarrow {}^7P_3$	^{52}Cr	Dark Spot	225 μW
$^5S_2$F=7/2 $\rightarrow$ $^7P_3$ F=9/2	^{53}Cr	Repumper	50 μW
$^5S_2$F=7/2 $\rightarrow$ $^7P_3$ F=9/2	^{53}Cr	Dark Spot	90 μW
$^5S_2 \rightarrow {}^7P_3$	^{52}Cr	Repumper	65 μW
$^5S_2 \rightarrow {}^7P_3$	^{52}Cr	Dark Spot	45 μW

Table 2.6: Power of the different beams addressing metastable atoms.

2.3.3 Polarization of the ^{53}Cr atoms

Once repumped $|^7S_3, F = 9/2>$, atoms are distributed in all Zeeman sub-levels. Polarizing atoms in the absolute Zeeman ground state ($|^7S_3, m_s = -3>$ and $|^7S_3, F = 9/2, m_F = -9/2>$ for the boson and fermion respectively) is necessary to prevent dipolar relaxation collisions [56]. If the atomic sample is not well polarized before the evaporation ramp, dipolar relaxation induces heating which prevents from reaching degeneracy. Polarization is performed through optical pumping with the J$\rightarrow$J transition of the depumper beam. A high quality for the optical pumping is required: the

[5] I recall here the difference between what I call the Dark Spot beam and the repumper beam. The Dark Spot beam is continuously on during the MOT and repumps atoms not loaded in the ODT. The repumper beam is on once the MOT process and the loading of the ODT is over, it repumps atoms of the ODT into the electronic ground state.

alignment between the σ^- lasers and the magnetic field is critical at a few degrees. Furthermore, a carefully aligned intensity-equilibrated retro-reflected scheme is required in order to limit the diffusion in momentum space [74].

For the boson, we use a short 5 μs pulse of the depumper beam. For the fermion, we find that using a resonant depumper pulse does not allow to suppress heating. Rate equation calculation shows that indeed a resonant polarizing beam also populates the $|^7S_3, F = 7/2>$ hyperfine level, and no more than 2/3 of the atoms can be accumulated in $|^7S_3, F = 9/2, m_F = -9/2>$. This is due to the small energy shifts between hyperfine levels of $|^7P_3>$ (a few MHz).

In order to perform an efficient fermionic polarization, we split the fermionic depumper beam into two (see Fig 2.8). One is left resonant and used during the 1D FORT loading as the depumper beam, while the other one is frequency shifted to the red of the transition by 180 MHz, and used for polarization. For the polarization stage, we use a power of 25 μW and a pulse time of 200 ms. Then rate equation calculations show that more than 98% of the atoms can be accumulated in $|^7S_3, F = 9/2, m_F = -9/2>$.

To check the quality of the polarization of the atoms, we measured the lifetime in the 1D FORT with and without a polarization pulse. The experimental protocol is the following. We load ^{53}Cr metastable atoms in an 1D FORT, repump them in their electronic ground state and shine, or not, the polarization beam for 500 ms. We then measure the number of atoms by absorption imaging after a time t_{wait}. The result of this experiment is shown Fig.2.12. The light absorption cross section of atoms not in the lowest Zeeman state is smaller than the one for polarized atoms because the imaging beam polarization is σ^-. However at short times we measure as many atoms with and without the polarizing beam. We interpret this result by the fact that our imaging pulse is long enough that the gas is polarized by the imaging beam. For longer times t_{wait}, there are more atoms left in the 1D FORT when the sample is initially polarized. Our interpretation is that here atom losses come from collisions with the background gas. A fit to the data yields a 1/e time of 15 s, compatible with the lifetime for polarized bosons. On the other hand, the non-polarized sample suffers also from 2 body collisions which results in losses but also cooling. It is clear from this experiment how important the polarization process is since after 20 s in the ODT there is approximatively a factor of 2 difference in atom number and an experimental run that produces BEC lasts typically 15 s.

2.3.4 Final steps before Fermi sea production

The loading of the 1D FORT from the MOTs is achieved respectively in 1000 ms for ^{53}Cr and 100 ms for ^{52}Cr.

Once the 1D FORT is loaded, the repumping from metastable states towards the electronic $|^7S_3, F = 9/2>$ ground state is performed in 200 ms. However, when the power of the repumper beams has to be shared between the bosons and the fermions (as discussed below bosons and fermions will be loaded in the same 1D FORT) the optimal

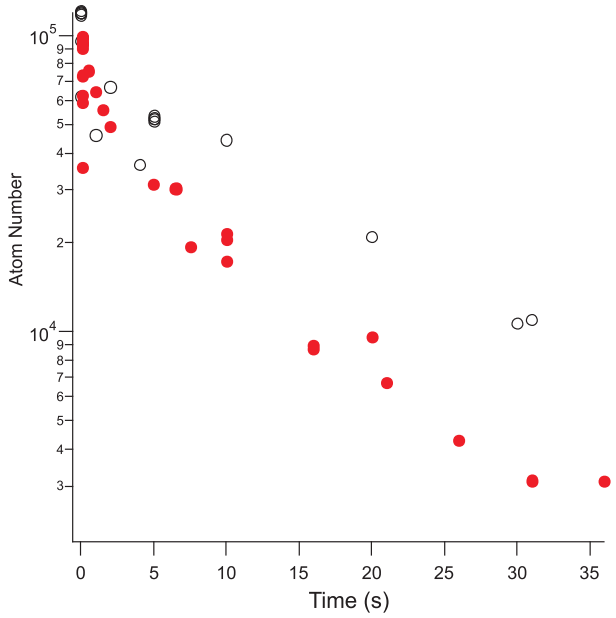

Figure 2.12: Number of atoms as a function of t_{wait} with an unpolarized sample (filled circles) or with a polarized sample (empty circles). The non-polarized sample has a reduced lifetime compared to the polarized case, which we interpret as a result of dipolar relaxation.

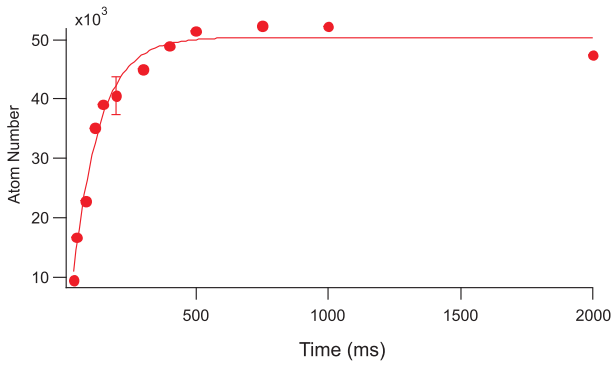

Figure 2.13: Loading of the 1D FORT with only fermionic atoms: number of atoms in the 1D FORT as a function of the loading time.

repumping time is 500 ms. This shows that more power in the repumper beams would be interesting in order to efficiently pump both isotopes into the electronic ground state $|^7S_3>$.

Evaporation strategy

Fermi statistics leads to vanishing s-wave collisions due to Van der Waals interactions at low temperatures for polarized fermions. Therefore, evaporative cooling to degeneracy, which requires efficient thermalization, has been achieved either with a mixture of two fermionic spin states [22] for which s-wave collisions are allowed, or for a Bose-Fermi mixture [77, 78]. We are able to load $(1.0 \pm 0.2) \times 10^5$ polarized atoms at 120 μK in a 1D FORT where evaporation can be performed. This is very unfavourable for a scenario involving only ^{53}Cr atoms. This is why we chose to perform sympathetic cooling with the bosonic ^{52}Cr.

With dipolar species, low temperature collisions become possible even for identical fermions. This very peculiar effect due to the long range character of DDIs was first observed with Dy [66], and was used to produce the Er Fermi sea in a very efficient way [67]. However, for Cr the dipolar elastic cross section is 20 times smaller than for Er, as it scales with d^4m^2 (d being the permanent magnetic dipole, and m the mass). In addition, we only manage to trap in a conservative trap about 30 times less atoms than in [67]. Therefore evaporative cooling to degeneracy involving identical fermions thermalizing through DDI is unfeasible.

As noticed in [39], the ZS 53 beam strongly reduces the number of atoms in the bosonic MOT, presumably because the detuning (-150 MHz) of this intense beam with the bosonic transition is not large enough to prevent mechanical effects on ^{52}Cr atoms. We have therefore to implement a sequential scheme, with first production of the fermionic MOT in order to load the 1D FORT with ^{53}Cr MOT atoms, and second production of the bosonic MOT in order to load the same 1D FORT with ^{52}Cr atoms. Then evaporative cooling can be performed. Evaporation of the fermionic isotope and achievement of the first Fermi sea of ^{53}Cr will be described in detail in chapter 4.

Part II

Cooling and thermodynamic properties of a Cr gas

CHAPTER 3

Cold collisions and thermalization processes of external and internal degrees of freedom

A fundamental question in many-body physics is how closed quantum systems reach equilibrium. This question has been addressed with cold atoms in many topics such as thermalization at low dimension [79, 80], prethermalization [81], or for specific phase transitions (e.g. for Anderson localization [82]). A particularly interesting question is how microscopic properties, i.e. collisions between atoms, are responsible for the macroscopic properties of the gas (such as temperature and magnetization). In the following we will discuss briefly about collisions between atoms, focusing on collisions due to Van der Waals interactions and collisions due to dipole-dipole interactions. We will then study how thermalization is achieved for both the mechanical and spin degrees of freedom. We then apply our understanding to deduce from spin dynamics the first measurement of the scattering length a_0 of the $S = 0$ molecular potential of Chromium: $a_0 = 13.5^{+15}_{-10} a_B$.

3.1 Cold collisions

The interaction between two particles at large distances r is dominated by the Van der Waals potential which at low temperature is isotropic and proportional to r^{-6}. The effective potential range r_0 is defined by the distance at which the Van der Waals potential balances the kinetic energy:

$$\begin{aligned} \frac{\hbar^2}{2m_r r_0^2} &= \frac{C_6}{r_0^6} \\ \rightarrow r_0 &= \left(\frac{2m_r C_6}{\hbar^2}\right)^{1/4} \end{aligned} \tag{3.1}$$

with m_r the reduced mass of the pair of colliding atoms, $\hbar = h/(2\pi)$ with h Planck's constant, and C_6 the Van der Waals coefficient. For Chromium we have C_6=733 $\pm$70 E_h a_B^6 with a_B the Bohr radius and E_h=4.359744$\times$ 10^{-18}J is a Hartree [83]. r_0 is then approximatively 5 nm. This potential range is of the same order as the scattering length away from a Feshbach resonance [84].

On the other hand, the atomic densities n of quantum gases are in the range of $n = 10^{20}$ at·m^{-3}. Therefore the average distance between two particles is typically

$d = n^{-1/3} \approx 100$ nm. Away from a Feshbach resonance, $d >> r_0$ and we can safely consider that collisions take place only between pairs of atoms.

3.1.1 Contact collisions

a) Scattering length

We define a contact collision as a collision due to an interatomic potential $V(r)$ which decreases sufficiently fast as a function of interatomic distance r. In scattering theory, a contact collision is described by the phase shift of an incoming plane wave by a scattering potential. The cross section of a collision between two spinless distinguishable atoms can be shown to be [85]:

$$\sigma = \frac{4\pi}{k^2} \sum_{l=0}^{\infty} (2l+1) \sin^2 \delta_l(k) \tag{3.2}$$

with l the orbital quantum number of the atom pair, k the relative wave vector, and $\delta_l(k)$ the phase shift acquired by the incoming particle of orbital momentum l during the collisional process.

Atoms with orbital momentum l feel a centrifugal barrier potential $\frac{\hbar^2 l(l+1)}{m_r r^2}$. The Van der Waals potential and the centrifugal potential lead to a barrier height that is $E_l = \frac{2}{3}\frac{\hbar^2 l(l+1)}{m_r b^2}$ where b is the distance to the top of the centrifugal barrier preventing atoms with energy smaller than E_l from colliding. In our experiment for l=1,

$$\begin{aligned} b(l=1) &= \left(\frac{3C_6 m_r}{\hbar^2 l(l+1)}\right)^{1/4} = \left(\frac{3}{2l(l+1)}\right)^{1/4} r_0 = 4.5 \pm 0.2 \text{ nm} \\ \rightarrow E_{l=1} &= (1.7 \pm 0.1) \times 10^{-27} \pm \text{ J} \\ \text{and } E_{l=1} &= \frac{3}{2} k_B T \rightarrow T = 820 \pm 40 \ \mu\text{K}. \end{aligned} \tag{3.3}$$

For $l > 0$, E_l is greater than the temperature of our gas at all times (at the start of the experiment $T = 120$ μK and is typically ≤ 1 μK for the experiments presented in this thesis). In the following we shall therefore only consider s-wave collisions ($l = 0$) between pair of atoms.

$\delta_0(k)$, the phase shift acquired for an s-wave collision, is defined as [85]:

$$-a = \lim_{k \to 0} \frac{\delta_0(k)}{k} \tag{3.4}$$

with a the scattering length. Therefore in the limit of low energies ($k \to 0$), the cross section takes the following simple form:

$$\sigma = 4\pi a^2 \tag{3.5}$$

For symmetry reasons, polarized fermions (bosons) cannot collide through $l = 0$ ($l = 1$) collisions. Therefore the cross section associated with low energy colliding fermions is 0. This comment is not valid for fermions in different spin states since two fermions of different spin states can collide through an s-wave collision channel. For identical bosons, a factor 2 must be added in eq.(3.5) to account for their indistinguishability [85].

b) Effective potential

The real form of the potential between two atoms is complicated and not well known. This motivated the use of a pseudo potential with a simple mathematical form which must keep the characteristics of the Van der Waals interactions: isotropic and short-range[1] character ($\propto 1/r^6$). Interactions between atoms are strong but only occur when atoms are close together. This is rare in the case of dilute gases. To avoid having to deal with the real form of the potential in order to describe a collision between two atoms, the concept of effective interaction was introduced [86]. This effective interaction must take into account the physical properties of the real Van der Waals interaction. As described above, the collision of a pair of particles with small total energy in the center of mass frame is dominated by the s-wave contribution to the wave function. To first order in the interaction potential, one can then derive the following expression for the scattering length [85]:

$$a = \frac{m_r}{2\pi\hbar^2} \int_0^\infty d^3r \; U(r) \tag{3.6}$$

with $U(r)$ the real interaction potential which often has a complicated form. Eq.(3.6) is difficult to compute and is never used in practice. Since we are interested in the value of a and are not concerned by the real form of $U(r)$, we will therefore replace the real potential by an effective potential U_{eff} which we can compute and gives the same scattering length in the Bprn approximation (eq.(3.6)). The simplest effective potential respecting the physical properties of the Van der Waals interaction is:

$$U_{eff}(\vec{r} - \vec{r}') = g\delta(\vec{r} - \vec{r}') \tag{3.7}$$

where $g = 2\pi\hbar^2 a/m_r$ is the interaction strength and $\delta(\vec{r})$ denotes the Dirac delta function.

c) Spin dependent collisions

In this thesis, we will be particularly interested in collisions involving atoms in different Zeeman sublevels. We adapt eq.(3.7) in order to take into account this possibility. In

[1] The distinction between short-range and long-range interactions depends on the dimensionality of the system D. Formally, a potential is defined to be short-ranged if it decreases with distance faster than $1/r^D$.

the treatment elaborated above, it was convenient to treat the collision in the center of mass frame as center of mass motion R is not modified by the collision. We found that the interaction through a molecular potential can be completely characterized by the scattering length a. When dealing with internal spin degrees of freedom we use the spin molecular basis which is particularly appropriate in order to describe a spin collision since it is the total spin of the colliding atoms which is conserved for isotropic interactions. S therefore plays a similar role to R in our analogy. The spin projection of the atom, as the relative motion of colliding atoms r, can however evolve.

Let us consider two atoms of spin s with spin projection m and m' along the quantization axis. This pair of atoms can be written as $|s, m; s, m' >_A$ in the atomic basis and $|S, M_S >_M$ in the molecular basis, with $M_S = m + m'$ and $0 \leq S \leq 2s$. A collision between two atoms in different spin states can happen through different molecular channels. Each molecular channel has its own scattering length. We define a_S as the scattering length associated to atoms colliding through the molecular channel S.

The total wavefunction describing the collision has a spatial part and a spin part. The spatial wavefunction associated to an s-wave collision is symmetric. For bosons (fermions), the total wavefunction is symmetric (antisymmetric) and therefore the spin wavefunction must be symmetric (antisymmetric). For even S states, the spin wavefunction of bosons (fermions) is symmetric (antisymmetric) under the exchange of the spin of two atoms. For odd S states, it is the contrary: the spin wavefunction of bosons (fermions) is antisymmetric (symmetric) under the exchange of the spin of two atoms. To respect the global symmetry of the particles, only molecular channels with even S must therefore be considered both for bosons and for fermions. To illustrate this, let us consider the stretched states of 2 bosonic and 2 fermionic atoms. The stretch state of two bosons of spin s=1 is:

$$|s = 1, m_s = 1; s = 1, m_s = 1 >_A = |S = 2, M_S = 2 >_M . \tag{3.8}$$

This ket is an even S state and is symmetric. Similarly, for fermions with spin s=3/2 we have:

$$|s = 3/2, m_s = 3/2; s = 3/2, m_s = 3/2 >_A = |S = 3, m_S = 3 >_M . \tag{3.9}$$

This ket is an odd S state and is symmetric. The effective pseudo potential taking into account spin states can then be written:

$$\begin{aligned} U_{eff}(r - r') &= \delta(r - r') \sum_{S=0}^{2s} g_S P_S \\ &= \delta(r - r') \sum_{S=0}^{2s} g_S |S, M_S >< S, M_S| \end{aligned} \tag{3.10}$$

with the sum holding for even S only, $g_S = 2\pi\hbar^2 a_S/m_r$ is the strength of the interaction for atoms colliding through the molecular potential S, and P_S is the operator which projects the atomic spin of the pair of atoms onto the molecular basis.

This interaction is invariant under rotations in coordinate space. This implies that this collisional process conserves orbital angular momentum and the total electronic spin angular momentum. Therefore L, M_L, S and M_S are conserved quantities during a collision where L is the total angular momentum of projection M_L. However, the spin projection of an individual atom can change (for example by flipping one spin up and the other one down). These collisions are called contact spin exchange collisions.

For ^{52}Cr with $s = 3$, there are four scattering channels. Three of them were measured previously ($a_6 = 102.5 \pm 0.4\ a_B$, $a_4 = 64 \pm 4\ a_B$, $a_2 = -7 \pm 20\ a_B$ [83, 87]). The last scattering length, a_0, was measured during my PhD studies and is the focus of the last part of this chapter.

3.1.2 Dipole-dipole collisions

One important feature of Chromium resides in its relatively strong magnetic dipole moment $\mu = 6\ \mu_B$ with μ_B Bohr's magneton. Each atom can be seen as a magnet which creates a B field acting on the other dipoles. The dipole-dipole interaction (DDI) potential between two atoms of magnetic moment $\vec{\mu_i} = g_{Landé}\mu_B\vec{s_i}$ separated by $\vec{r}$ is:

$$V_{DDI}(\vec{r}) = \frac{\mu_0(g_{Landé}\mu_B)^2}{4\pi r^5}\left(r^2\vec{s}_1.\vec{s}_2 - 3(\vec{s}_1.\vec{r})(\vec{s}_2.\vec{r})\right) \tag{3.11}$$

with μ_0 the vacuum permeability and $g_{Landé}$ the Landé factor. The DDI operator is given by:

$$\hat{V}_{DDI} = \frac{\mu_0(g_{Landé}\mu_B)^2}{4\pi r^5}\left(r^2\hat{\vec{S}}_1.\hat{\vec{S}}_2 - 3(\hat{\vec{S}}_1.\hat{\vec{r}})(\hat{\vec{S}}_2.\hat{\vec{r}})\right). \tag{3.12}$$

with $\hat{\vec{S}}$ the spin operator and $\hat{\vec{r}}$ the position operator. This expression is invariant under simultaneous rotations in coordinate space and electronic spin space. It is not invariant under separate rotations. It is the total angular momentum J which is conserved in a dipole-dipole collision.

The DDI is anisotropic (it depends on $\vec{s_i}.\vec{r}$ and can be attractive or repulsive see Fig.3.1), and long-range[2] ($\propto 1/r^3$). Following pioneering experiments in the group of T.Pfau which demonstrated how a dipolar BEC elongates along the axis of the dipoles to minimize energy [88], early experiments in the group have highlighted the anisotropic character of the DDI by measuring the dependence of collective excitations [89] and the speed of sound [90] upon different magnetic field orientations. The long range character of DDI has been observed through the interaction between atoms,

[2]for a 3D system. In 2D and 1D, DDI is considered as a short-range potential.

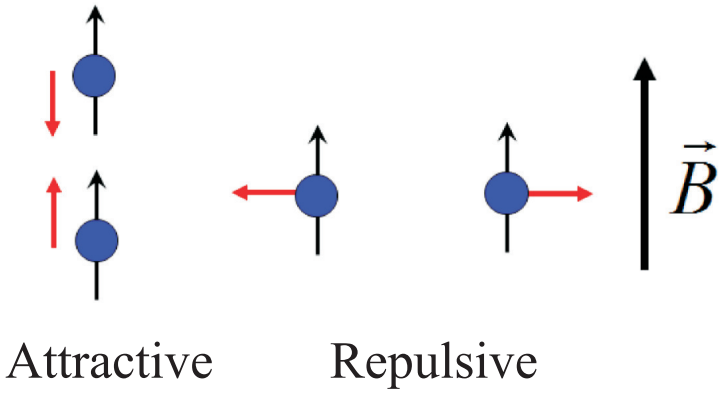

Figure 3.1: Sketch illustrating the anisotropy of Dipole Dipole Interactions. Two dipoles in a head to tail configuration attract each other where as two dipoles side by side repel each other.

molecules, or Rydberg atoms in different lattice sites [31, 34, 91]. The strength of this interaction is proportional to $\vec{\mu}^2$. Therefore, for $s = 3$ chromium, this interaction is 36 times stronger than for $s = 1/2$ alkalis. The relative strength of the DDI compared to contact interaction is given by the factor ϵ_{DD} which, in a spherical trap, is equal to

$$\epsilon_{DD} = \frac{4\pi}{3}\frac{s^2 d^2}{g_S} = \frac{2\pi}{3}\frac{s^2 d^2 m_r}{\pi\hbar^2 a_S} \tag{3.13}$$

with $d^2 = \frac{\mu_0 (g_{Landé}\mu_B)^2}{4\pi}$; $\epsilon_{DD} > 1$ corresponds to the limit at which a dipolar BEC collapses under the effect of the attractive part of the DDI. In this limit, the repulsive contact interaction is too weak to stabilize the BEC [92]. For Chromium, $\epsilon_{DD} \approx 0.16$ far away from a Feshbach resonance. This value can take any desired value by tuning the scattering length a_S accross a Feshbach resonance. Experiments in the Stuttgart group studied the collapse of a BEC of Chromium as a function of ϵ_{DD} and trap geometry [93, 94]. Recently, Dy and Er with larger dipole moment (respectively $\vec{\mu}$= 10 μ_B and $\vec{\mu}$= 7 μ_B) and larger mass have been cooled to degeneracy [17, 18, 66, 67].

Developing eq.(3.12) yields:

$$\begin{aligned}
\hat{V}_{DDI}(\vec{r}) &= \frac{d^2}{r^3}\left(\frac{1}{2}(\hat{S}_{1+}\hat{S}_{2-} + \hat{S}_{1-}\hat{S}_{2+}) + \hat{S}_{1z}\hat{S}_{2z}\right) \\
&- 3\frac{d^2}{r^5}\Bigg(\hat{S}_{1z}\hat{S}_{2z}\hat{z}^2 \\
&+ (\hat{S}_{1z}\hat{S}_{2-}\frac{\hat{z}\hat{r}_+}{2} + \hat{S}_{1-}\hat{S}_{2z}\frac{\hat{r}_+\hat{z}}{2}) + c.c. \\
&+ \hat{S}_{1+}\hat{S}_{2+}\frac{\hat{r}_-^2}{4} + c.c. \\
&+ (\hat{S}_{1+}\hat{S}_{2-}\frac{\hat{r}_-\hat{r}_+}{4} + c.c)\Bigg)
\end{aligned} \tag{3.14}$$

where $\hat{S}_\pm = \hat{S}_x \pm i\hat{S}_y$ are the spin raising/lowering operators, $\hat{r}_\pm = \hat{x} \pm i\hat{y}$, and $\hat{x}$, $\hat{y}$, $\hat{z}$ are normalized coordinates.

Let us consider an external magnetic field $\vec{B}$ aligned along $\hat{z}$. We can distinguish 3 different types of collisions due to dipolar interactions.

- Terms involving $\hat{S}_{1z}\hat{S}_{2z}$ are collisions where each atom conserves its spin and are often called **Ising terms**. These collisions are elastic and long range. The Ising terms are multiplied by $(1 - 3\hat{z}^2)$ due to the interaction anisotropy, which leads to a deformation of the BEC. This phenomenon called magnetostriction has been observed for Chromium [95, 96].

- Long range dipolar **spin exchange** collisions $(\hat{S}_{1+}\hat{S}_{2-} + \hat{S}_{1-}\hat{S}_{2+})$. These collisions do not conserve the spin of an individual atom but only the longitudinal magnetization. These collisions have been observed with Chromium atoms loaded in an optical lattice prepared out of spin equilibrium [91]. Again, the exchange terms are multiplied by $(1 - 3\hat{z}^2)$. In Part III, we will be particularly interested in spin exchange processes due to these terms.

- Finally, there are collisions for which the magnetization is not conserved, for example $\hat{S}_{1-}\hat{S}_{2-}$. They have drastic consequences for the properties of a BEC since they **free magnetization** [87, 97, 98, 99]. These collisions will be essential in the cooling mechanism using the spin degrees of freedom which we demonstrate in chapter 5. This property is specific to dipolar collisions, since contact collisions conserve the total electronic spin and thus conserve magnetization. This change in magnetization is necessarily accompanied with a change in orbital angular momentum, which is given by terms involving $\hat{r}_-$ or $\hat{r}_+$, as the total orbital momentum J is a good quantum number. This spin-orbit coupling is particularly appealing. In particular, dipole-induced spin relaxation may lead to a transfer of spin into angular momentum. This process could lead to a rotation of the ensemble and would be similar to the well-known Einstein-de Haas effect [100, 101, 102].

Dipolar cross section

In the following section, I will give the results of the cross sections associated to the possible dipolar collision channels which were established in [103].

Let us consider two atoms in spin state $m_s = +3$. There exists three different dipolar collision channels:

$$
\begin{aligned}
|m_s = +3, m_s = +3> &\rightarrow |m_s = +3, m_s = +3> \\
|m_s = +3, m_s = +3> &\rightarrow \frac{1}{\sqrt{2}}(|m_s = +3, m_s = +2> + |m_s = +2, m_s = +3>) \\
|m_s = +3, m_s = +3> &\rightarrow |m_s = +2, m_s = +2> .
\end{aligned}
$$

The first channel conserves magnetization whereas the two others do not. When magnetization is not conserved, the pair of atoms gains a kinetic energy of $\Delta E^i = i g_{Landé} \mu_B B$ with B the magnetic field, and i is a number equal to the change in magnetization after the collision. The cross sections associated to the different dipolar collisional channels in the framework of the first-order Born approximation are [87]:

$$\sigma_{dip}^{(0)} = \frac{16\pi}{45} s^4 \left(\frac{\mu_0 (g_{Landé}\mu_B)^2 m}{4\pi\hbar^2} \right)^2 h(1) \tag{3.15}$$

$$\sigma_{dip}^{(1)} = \frac{8\pi}{15} s^3 \left(\frac{\mu_0 (g_{Landé}\mu_B)^2 m}{4\pi\hbar^2} \right)^2 h(k_f/k_i) \frac{k_f}{k_i} \tag{3.16}$$

$$\sigma_{dip}^{(2)} = \frac{8\pi}{15} s^2 \left(\frac{\mu_0 (g_{Landé}\mu_B)^2 m}{4\pi\hbar^2} \right)^2 h(k_f/k_i) \frac{k_f}{k_i} \tag{3.17}$$

with $s = 3$ the spin of a Chromium atom, μ_0 the vacuum permeability, μ_B the Bohr magneton, $g_{Landé}$ the Landé factor, k_i and k_f are the moduli of the initial and final wave vectors. The final wavevector k_f is not the same depending on the considered collisional channel. $h(x)$ is a monotone function defined for $x \in [1, +\infty[$ by:

$$h(x) = \begin{cases} 1 - \frac{1}{2}\epsilon & \text{if } x = 1 \\ 1 + \epsilon\big(- \frac{1}{2} - \frac{3}{8} \frac{(1-x^2)^2}{x(1+x^2)} \log_e \frac{(1-x)^2}{(1+x)^2} \big) & \text{if } x > 1 \end{cases}$$

where $\epsilon = 1$ for bosons and $\epsilon = -1$ for fermions.

3.2 Thermalization processes

In this thesis we will be interested in the thermalization of the spin degrees of freedom and the mechanical degrees of freedom which can be treated using the same formalism. To thermalize a degree of freedom, different states must be coupled to each other and there has to be irreversible energy redistribution processes. Irreversible energy redistribution in a closed system is in practice provided by coupling an initial state to a large number of output channels. This coupling is ensured by collisions. In the following we shall distinguish two types of collisions: one which does not lead to thermalization of any degrees of freedom which we label as "coherent collision" and one which ensures thermalization and that we call "incoherent collision".

The following discussion applies to the case of a thermal gas. A BEC can be immersed in the thermal gas, which alters the density of the gas which enters in thermalization processes.

3.2.1 Thermalization of a polarized gas

Let us first consider the case of a polarized gas and discuss how the mechanical degrees of freedom may be thermalized.

a) Coherent collisions

We denote a collision to be coherent if it is a forward scattering process where the incoming waves of momenta $\vec{k}_1$ and $\vec{k}_2$ scatter in the same direction: $(\vec{k}_1,\vec{k}_2) = (\vec{k}'_1,\vec{k}'_2)$ with $\vec{k}'_i$ the outgoing wavevector of particle i (see Fig.3.2). There exists only one output channel which conserves the momenta of both particles. No energy exchange takes place, therefore there is no energy redistribution, and thermalization cannot happen. Coherent collisions do not thermalize the gas.

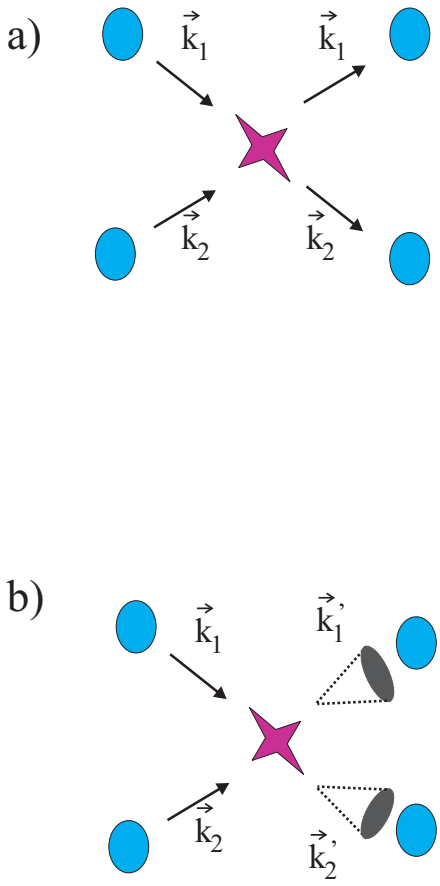

Figure 3.2: Sketch illustrating coherent and incoherent collisions. a) Coherent collisions: the incoming waves of momenta $\vec{k}_1$ and $\vec{k}_2$ scatter in the same direction: $(\vec{k}_1,\vec{k}_2) = (\vec{k}'_1,\vec{k}'_2)$. These collisions are reversible, they do not redistribute energy and do not thermalize the mechanical degrees of freedom. b) Incoherent collisions: the incoming states are coupled to many possible momentum states (represented here by a cone):$(\vec{k}_1,\vec{k}_2) \neq (\vec{k}'_1,\vec{k}'_2)$. Incoherent collisions are irreversible, redistribute energy between particles and thermalize the mechanical degrees of freedom. Here in the sketch we did not account for the symmetrization of the problem.

Although forward scattering collisions do not redistribute energy between colliding

particles, the phase shift acquired due to collisions with a medium of density n modifies the energy of the particles. This gives rise to the the mean field interaction shift $E = \frac{4\pi\hbar^2}{m} n a_S = n g_S$ with $g_S = \frac{4\pi\hbar^2}{m} a_S$ the interaction strength. Such a formula is given by the Bogoliubov dispersion relation at high momenta [23]: an excitation over a BEC, in the limit k $\to \infty$, has an energy $\epsilon(k) = \frac{\hbar^2 k^2}{2m} + n g_S$ with n the BEC density.

We introduce for these coherent processes a frequency Γ_{coh} such as:

$$\Gamma_{coh} = \frac{1}{h} \frac{4\pi\hbar^2}{m} n a_S \tag{3.18}$$

Therefore we interpret contact interactions as a result of contact coherent collisions in the weakly interacting limit $n a_S^3 << 1$.

b) Incoherent collisions

When the collision couples the incoming states to many possible momentum states $(\vec{k}_1, \vec{k}_2) \neq (\vec{k}'_1, \vec{k}'_2)$, even though each collision is reversible by themselves, many collisions which do not evolve in phase take place, irreversible energy redistribution is then ensured. These collisions are branded as incoherent. The coupling between different states is then set by the Fermi Golden rule and yields the collision rate $\Gamma_{inc} = n\sigma v$ with σ the atomic cross section and v the relative mean velocity of the pair of colliding atoms. For pure s-wave collisions of undistinguishable bosons in the low energy limit we have $\sigma = 8\pi a_S^2$. For a dilute Boltzmann gas, it has been shown that typically three collisions are sufficient to randomize velocities and ensure thermalization of the mechanical degree of freedom [104].

c) Comparison of the collisional rates

Both collisional processes take place in any gas but on timescales set by different parameters. In order to evaluate which collisional process dominates, one needs to compare

$$\Gamma_{coh} = \frac{1}{h} \frac{4\pi\hbar^2}{m} n a_S \tag{3.19}$$

$$\text{and } \Gamma_{inc} = n\sigma v. \tag{3.20}$$

Both collisional processes cannot be measured in the same way. Indeed forward scattering results in a phase shift and may be probed by e.g. an interferometric set up [105]. On the other hand, incoherent processes can be probed by measuring thermalization of the velocity distribution [106].

Physical insight can be gained by dividing equations eq.(3.19) and eq.(3.20). If one looks at the ratio between coherent and incoherent rate, one obtains:

$$\frac{\Gamma_{coh}}{\Gamma_{inc}} \sim \frac{\lambda_{dB}}{a_S} \tag{3.21}$$

with $\lambda_{dB} = \sqrt{\frac{2\pi\hbar^2}{mk_BT}}$ the de Broglie wavelength and k_B is the Boltzman constant. A wavepacket remains coherent for a long time when its size (λ_{dB}) is large compared to the scatterer (a_S). In the extreme case of the BEC, where $\lambda_{dB} \to \infty$, we have $\frac{\Gamma_{coh}}{\Gamma_{inc}} \to \infty$: there are interactions among particles, but "no collisions".

This ratio, can be recast using eq.(3.4) and yields:

$$\frac{\Gamma_{coh}}{\Gamma_{inc}} = \frac{2\pi}{16}\frac{1}{\delta_0(k)}. \tag{3.22}$$

$\Gamma_{coh} >> \Gamma_{inc}$ means that very little phase shift is acquired during a collision. Many collisions may take place and evolve in phase, which is consistent with the fact that coherence is conserved. In the opposite limit when $\Gamma_{coh} << \Gamma_{inc}$, a collision induces a large phase shift. Many collisions take place but they do not evolve in phase, and the coherence of the sample is destroyed.

We have now gained insight into the meaning of the thermodynamics of a "non interacting BEC". Here it is assumed that collisions take place and are fast enough for thermal equilibrium to be reached: Γ_{inc} is large enough to ensure thermalization. However, interactions are weak enough that they do not modify the thermodynamics: $h\Gamma_{coh}$ is small.

3.2.2 Thermalization of an unpolarized gas

The discussion in subsection 3.2.1 may sound tautological. Indeed, forward scattering, leading to a mean field interaction, does not lead to a change in momentum. It is therefore obvious that it does not lead to thermalization of momentum states. We now extend this discussion to the case of an unpolarized gas. We will follow the same line of thought, and show that one can have both coherent and incoherent spin dynamics [107, 108, 109].

a) Coherent collisions

In the coherent case, we discussed that a forward collision through a molecular potential with spin S introduces a phase shift linked to the mean field energy $E = \frac{4\pi\hbar^2}{m}na_S$. Now we consider a collision where the pair of atoms is in a superposition of molecular states $|S>$ and $|S'>$. We can write the spin part of the incoming wave as:

$$|\psi_{in}>= \alpha|S,m> +\beta|S',m> \tag{3.23}$$

with α and β complex numbers satisfying $|\alpha|^2 + |\beta|^2 = 1$. After the collision, the outgoing wavefunction takes the form:

$$|\psi_{out}(t)>= \alpha e^{ig_S nt/\hbar}|S> +\beta e^{ig_{S'} nt/\hbar}|S'> \tag{3.24}$$

with t the interaction time. The phase associated with each molecular state undergoes a phase shift proportional to the interaction strength of the corresponding molecular

potential. Thus, a pair of atoms in a linear superposition of two molecular states will undergo beating which will result in spin dynamics. The rate associated with coherent spin dynamics results from a difference in scattering lengths Δa between different spin molecular potentials:

$$\Gamma_{coh}^{Spin} \sim \frac{1}{h}\frac{4\pi\hbar^2}{m}n\Delta a \tag{3.25}$$

More precisely, using eq.(3.10) the rate of a $(m_s = i,\ m_s = j) \rightarrow (m_s = k,\ m_s = l)$ coherent spin collision channel of an atom of spin s is:

$$\begin{aligned}\Gamma_{coh}^{Spin} &= \Gamma_{i,j}^{k,l} = \frac{1}{h}\frac{4\pi\hbar^2}{m}n \\ &\times \sum_{S=0,even}^{2s} a_S < s,i;s,j|S,M_S = i+j >< S,M_S = k+l|s,i;s,j > \end{aligned}\tag{3.26}$$

where the sum holds for even S values. For example, the rate associated with the forward collision $(m_s = 0,\ m_s = 0) \rightarrow (m_s = 1,\ m_s = -1)$ of an s=1 atom is:

$$\Gamma_{0,0}^{-1,1} = \frac{1}{h}\frac{4\pi\hbar^2}{m}n \times \frac{1}{3}(a_2 - a_0). \tag{3.27}$$

b) Incoherent collisions

In the incoherent case, we calculate the cross section associated to a spin changing collision by applying scattering theory to two atoms in different spin states interacting through U_{eff} (eq.(3.10))[85]. The idea of the calculation is to evaluate, within Born approximation, the probability to change momentum and spin. Although the number of spin states is reduced, the number of available momentum states is large and energy redistribution is possible. The cross section associated with the collision $(m_1, m_2) \rightarrow (m_1', m_2')$ of spin s atoms is [85]:

$$\begin{aligned}\sigma_{(m_1,m_2)\rightarrow(m_1',m_2')} &= \sigma^{Spin} \\ &= 4\pi\Big|\sum_{S=0,even}^{S=2s} \gamma_{(m_1,m_2)} c_{S,M_S;m_1,m_2} c^*_{S,M_S;m_1',m_2'} a_S\Big|^2 \end{aligned}\tag{3.28}$$

with $c_{S,m_S;m_1,m_2}$ the Clebsch-Gordan coefficient associated between an atom pair $|s,m_1;s,m_2>_A$ and a molecule $|S,M_S>_M$. $\gamma_{(m_1,m_2)}$ is a symmetrization factor which ensures the normalization of the spin part of the incoming wavefunction. For $m_1 = m_2$ we have $\gamma = 1$, and for $m_1 \neq m_2$ we have $\gamma = \sqrt{2}$. The cross section associated with spin dynamics results from the sum squared of the different possible scattering lengths weighted by the appropriate Clebsch-Gordan coefficients. The rate associated with incoherent spin dynamics is thus:

$$\Gamma_{inc}^{Spin} = n\sigma^{Spin}v. \tag{3.29}$$

For example, the rate associated with an incoherent ($m_s = 0$, $m_s = 0$) $\rightarrow$ ($m_s = 1$, $m_s = -1$) collision of an s=1 atom is:

$$\Gamma_{0,0}^{-1,1} = nv \times 4\pi \left(\frac{a_2 - a_0}{3} \right)^2. \tag{3.30}$$

Both coherent and incoherent collisional processes change the population in a spin state (as shown by the sketch Fig.3.3) and can be measured by monitoring the population of each spin state. In section 3.3, to illustrate these two different processes we shall describe two experimental results obtained in the laboratory.

c) When do we have which process?

Again, to assert which process dominates, one compares:

$$\Gamma_{coh}^{Spin} = \frac{1}{h} \frac{4\pi\hbar^2}{m} n\Delta a \tag{3.31}$$

$$\text{and } \Gamma_{inc}^{Spin} = n\sigma^{Spin} v. \tag{3.32}$$

If $\Gamma_{coh}^{Spin} > \Gamma_{inc}^{Spin}$, we may observe spin oscillations before thermalization. The damping rate of the oscillations will then be of the order of Γ_{inc}^{Spin}. However, there exists additional damping processes which occur on different timescales than the one set by the thermalization of the spin degrees of freedom. For example Γ_{inc}, which ensures thermalization of the mechanical degrees of freedom, may damp coherent spin oscillations on a faster timescale [108]. A very important point to consider when dealing with spin dynamics is that incoherent scattering is not the only possibility to provide dissipation in the spin sector: environment inhomogeneities such as fluctuations of the magnetic field or residual magnetic gradients may introduce inhomogeneous phase shifts (an additional position and spin state dependent phase shift) which will decohere the sample.

3.3 Experimental realization of coherent and incoherent spin dynamics

In the following, to illustrate our discussion we shall present two different experiments performed in our laboratory for which coherent and incoherent spin dynamics were observed.

3.3.1 Coherent process

To illustrate an experiment with coherent collisions, I will briefly present an experiment performed during Aurélie de Paz's thesis [37].

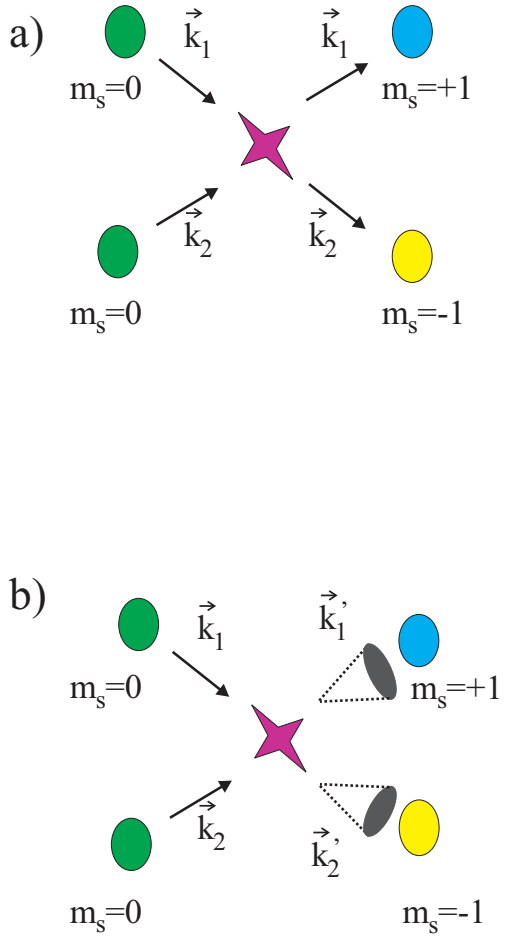

Figure 3.3: Sketch illustrating coherent and incoherent collisions when including the spin degrees of freedom. a) Spin changing coherent collisions: two atoms in spin state $m_s = 0$ may change spin state after a coherent collision. These collisions are reversible and do not lead to thermalization b) Spin changing incoherent collisions: two atoms in spin state $m_s = 0$ may change spin state after an incoherent collision. These collisions, by themselves, are reverisble but they are many and they do not evolve in phase and are thus irreverisble. These collisions lead to the thermalization of the spin degrees of freedom. Here in the sketch we did not account for the symmetrization of the problem.

In this experiment, a BEC of spin polarized $m_s = -3$ atoms is loaded into a 3D lattice to produce a Mott state [110] with on average 2 atoms per site. These atoms are then excited to $m_s = -2$ and we measure spin dynamics (see chapter 8 or [37, 91] for more experimental details). The evolution of the fractional populations in $m_s = -3, -2, -1, 0$ are shown Fig.3.4. They observe damped coherent oscillations for each spin state. The dynamics is interpreted as spin changing collisions due to contact interactions in doubly occupied sites.

Assuming a perfect preparation of an initial state of two atoms per lattice site of

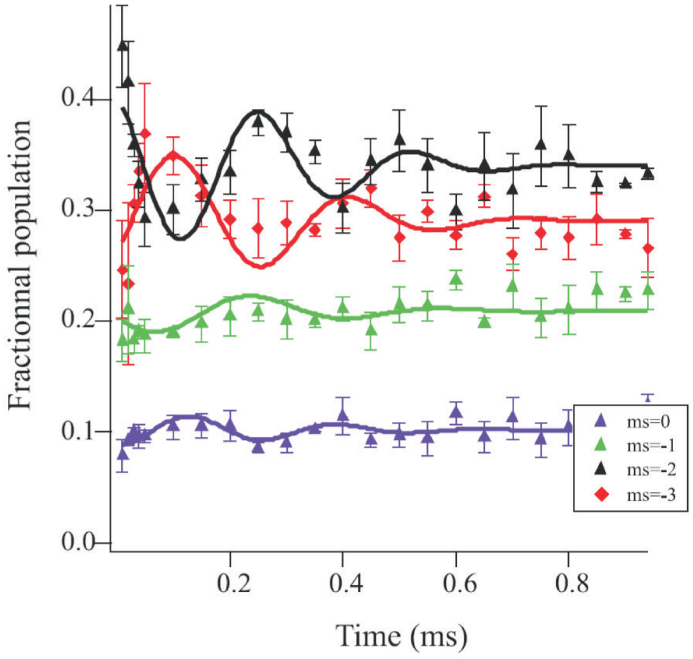

Figure 3.4: Evolution of the fractional populations in $m_s = -3, -2, -1, 0$ as a function of time after spin preparation in an excited spin state through a coherent Raman process. Error bars show statistical uncertainties. Full lines are fits to the data. We observe coherent spin oscillations. The dynamics is interpreted as driven by spin changing collisions due to contact interactions in doubly occupied sites of an optical lattice. Image adapted from [91].

spin $s = 3$ in spin state $m_s = -2$, in the molecular basis we can write:

$$|\Psi(t=0)>=\alpha|S=6, M_S=-4>_M+\beta|S=4, M_S=-4>_M \tag{3.33}$$

with $\alpha = \sqrt{\frac{6}{11}}$ and $\beta = -\sqrt{\frac{5}{11}}$ the appropriate Clebsch-Gordan coefficients. The interaction part of the Hamiltonian $\hat{H}_{int}$ will drive the evolution of the system and after a time t at the beginning of the evolution we have

$$\begin{aligned} |\Psi(t)> &= e^{i\hat{H}_{int}t/\hbar}|\Psi(t=0)> \\ &= \alpha e^{ig_6t/\hbar}|S=6, m_s=-4>_M+\beta e^{ig_4t/\hbar}|S=4, m_s=-4>_M \end{aligned} \tag{3.34}$$

because $|S = 6, m_s = -4 >_M$ and $|S = 4, m_s = -4 >_M$ are eigenstates of $\hat{H}_{int}$ with respective eigenvalues g_6 and g_4. The population in $m_s = -2$, $\Pi_{-2}(t)$, is:

$$\begin{aligned} \Pi_{-2}(t) &= |<m_s=-2, m_s=-2|\Psi(t)>|^2 \\ &= \frac{61}{121}+\frac{60}{121}\cos(\phi(t)) \end{aligned} \tag{3.35}$$

with $\phi(t) = \frac{(g_6-g_4)t}{\hbar}$. The population evolution in $m_s = -2$ can thus be seen as a beating set by the difference in interaction energies between molecular potentials.

The theoretical period of this oscillation, which can be extracted from the experimental details given in [91], is T=$\frac{h}{g_6-g_4}$ = (280±30) μs. This is in good agreement with the experimentally measured oscillation period (320±50) μs.

3.3.2 Incoherent process: determination of a_0

In this section, I will describe an experiment performed during my PhD in which we measured spin dynamics resulting from incoherent collisions between atoms in different spin states. The analysis of our data provides the first measurement of the scattering length of the S=0 molecular potential of Chromium. I will purposely omit experimental preparation details in order to concentrate on collisional processes. The experimental preparation is an extension of the experimental preparation detailed in chapter 7, and can also be found in [37, 111].

Experimental situation

We load 10^4 chromium atoms in spin state $m_s = -3$ in a double well trap. Each well contains half of the atoms. We selectively prepare the atoms of one well in spin state $m_s = +3$. The double well trap is then removed (for more experimental details on spin preparation or the double well trap see chapter 7. However the double well trap is no longer of use and one should not need to focus on the preparation of the initial conditions to understand the message of this section). The initial condition is

the following: we have 10^4 thermal atoms at T=(1.2± 0.1) μK in an ODT of trapping frequencies $\nu_{x,y,z} = (520, 615, 400)$ Hz. At $t = 0$, the initial fractional populations are:

$$\begin{aligned}
\frac{N_{-3}}{N_{Tot}} &= 0.40 \pm 0.08 \\
\frac{N_{-2}}{N_{Tot}} &= 0.08 \pm 0.02 \\
\frac{N_{-1}}{N_{Tot}} &= 0.02 \pm 0.01 \\
\frac{N_{0}}{N_{Tot}} &= 0.00 \pm 0.01 \\
\frac{N_{+1}}{N_{Tot}} &= 0.02 \pm 0.01 \\
\frac{N_{+2}}{N_{Tot}} &= 0.08 \pm 0.02 \\
\frac{N_{+3}}{N_{Tot}} &= 0.40 \pm 0.08.
\end{aligned}$$

We let the system evolve for a time t, turn off the ODT and then spatially separate the different spin components with a Stern-Gerlach technique to measure the number of atoms in each spin state.

Even though spin states with opposite spin projections should have the same atom number due to the way we prepare the sample, we find a reduced signal for atoms with $m_s > 0$ due to our imaging procedure. Even though a spin dependent coefficient can be introduced to account properly for the number of atoms in each spin state, our best signal to noise ratio is obtained for spin states with $m_s \leq 0$ and we focus our analysis only on these spin states.

We show in Fig.3.5 the evolution of the fractional populations for $m_s = -2, -1, 0$. We observe an increase of the $m_s = -2, -1, 0$ populations with no spin oscillations. The observed spin dynamics is, to within our signal to noise ratio, at constant magnetization for the first 200 ms.

Incoherent dynamics

We first estimate the timescale associate with coherent and incoherent spin dynamics:

$$\frac{1}{n}\Gamma_{Coh}^{Spin} \sim 3 \times 10^{-17}\mathrm{m}^3 \cdot \mathrm{s}^{-1} \tag{3.36}$$

$$\frac{1}{n}\Gamma_{inc}^{Spin} \sim 3 \times 10^{-18}\mathrm{m}^3 \cdot \mathrm{s}^{-1} \tag{3.37}$$

with n the density, $\Delta a = a_6 - a_4 = 2.1$ nm (a_6 and a_4 are the scattering lengths associated to the molecular potentials S=6 and S=4), and $v = 4\sqrt{\frac{k_B T}{\pi m}} = 3.1$ cm·s^{-1} at T= 1.2 μK.

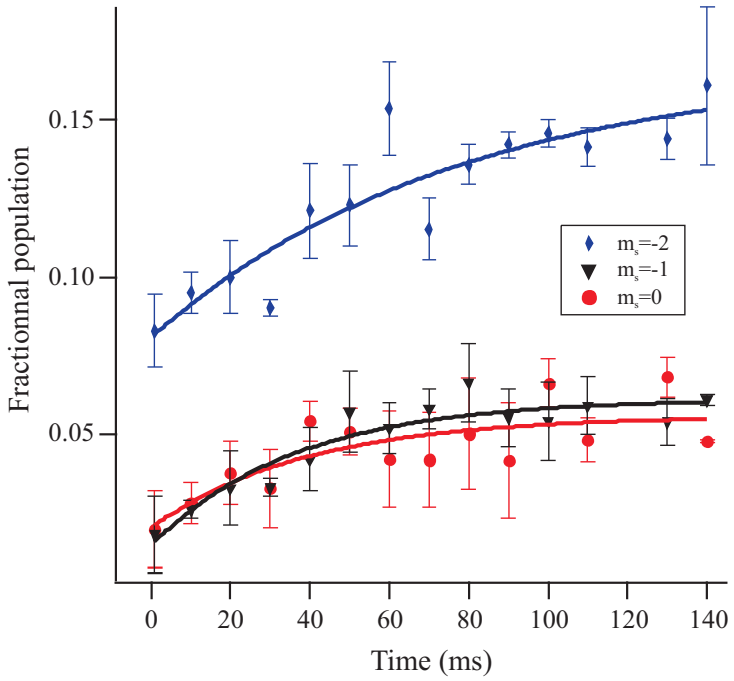

Figure 3.5: Evolution of the fractional populations in $m_s = -2, -1, 0$ as a function of time after spin preparation (see chapter 7 for more details on the spin preparation). Error bars show statistical uncertainties. Full lines are guides for the eye.

We find $\Gamma_{Coh}^{Spin} \geq \Gamma_{inc}^{Spin}$, however we do not observe any coherent spin oscillations in Fig.3.5. This is due to the fact that the different spin states are initially in an incoherent mixture. The time t_{merge} between spin preparation and the moment the two gases are merged is long: $t_{merge} \approx 20$ ms. Assuming a thermal distribution for the $m_s = +3$ gas, the peak density is:

$$n_{+3}^0 = N_{+3}\left(\frac{m\bar{\omega}^2}{2k_BT}\right)^{3/2} \tag{3.38}$$

$$= 3.5 \times 10^{18}\ \mathrm{m}^{-3} \tag{3.39}$$

with N_{+3} the number of $m_s = +3$ atoms, $\bar{\omega}=(\omega_x\omega_y\omega_z)^{1/3}$ the mean trapping frequency, and k_B is Boltzmann's constant. The timescale τ for an incoherent collision between $m_s = +3$ atoms is estimated to be:

$$\begin{aligned}\tau &= \frac{2\sqrt{2}}{n_{+3}^0 8\pi a_6^2 v} \\ &\approx 30\ \mathrm{ms} \\ &\sim t_{merge}.\end{aligned} \tag{3.40}$$

The m_s= +3 cloud has therefore lost its coherence by the time the traps are merged and we do not observe any spin oscillations.

Moreover, the magnetic field at each trap position is different, which leads to a relative phase between the $m_s = -3$ atoms and $m_s = +3$ atoms. Due to fluctuations in magnetic field between experimental realizations, the relative phase between the spin components fluctuates. Most likely, within the mean field picture [112], spin dynamics are highly sensitive to the relative phase between spin components. Because the relative phase is not well defined, coherent oscillations may not be sustained.

Fixed magnetization

We interpret that magnetization is constant by the fact that dipolar magnetization changing collisions do not intervene in the observed dynamics. Indeed the Zeeman splitting is much larger than the thermal energy (as B = 50 mG and T= 1.2 μK, we have $E_{Zeeman} = h\times$ 140 kHz and $E_{Thermal} = h\times$ 25 kHz) therefore dipolar "promotion" events where thermal kinetic energy is transferred into magnetic energy (such as the collisions involved in demagnetization cooling in [113]) which would lead to production of $m_s = -2$ atoms can safely be ruled out.

Also, the cross section associated to a dipolar relaxation collision, e.g. $(m_s = +3, m_s = +3) \rightarrow (m_s = +3, m_s = +2)$ at B=50 mG and T=1.2 μK, is [87]:

$$\sigma_{dip}^{(1)} \sim 1.5 \times 10^{-17}\mathrm{m}^2 \tag{3.41}$$

where we used eq.(3.16). The timescale τ associated with a dipolar relaxation event is of the order of:

$$\begin{aligned} \tau &\sim \frac{2\sqrt{2}}{n^0_{+3}\sigma^{(1)}_{dip}v} \\ &\sim 1.7 \text{ s} \end{aligned} \tag{3.42}$$

for $v = 4\sqrt{\frac{k_BT}{\pi m}} = 3.1$ cm.s^{-1}. τ is much larger than the experiment timescales, therefore dipolar magnetization changing collisions can be safely omitted to understand the dynamics for the experimental times considered.

The observed spin dynamics therefore results from spin exchange interactions, which can be triggered either by dipolar interactions or by spin dependent contact interactions.

Analysis of $m_s = -2$ population: exclusion of dipolar dynamics

As a first study, in order to deduce the relevant timescales of dynamics, we focused on the time evolution of $m_s = -2$ population. Since only the $m_s = -3$ and $m_s = +3$ spin states are macroscopically occupied, in this first model we assume that the production of an $m_s = -2$ atom is set by the timescale of the spin conserving (-3,+3)→ (-2,+2) collisions which consists of a dipolar term and a contact term:

$$\frac{dn_{-2}(t)}{dt} = \sigma_{(-3,+3)\to(-2,+2)} v n_{-3}(t) n_{+3}(t) \tag{3.43}$$

with $\sigma_{(-3,+3)\to(-2,+2)}$ the collision cross section associated to a (-3,+3)→ (-2,+2) event, $v = 4\sqrt{\frac{k_BT}{\pi m}}$ the average atomic relative velocity, and n_i the density of atoms in state $m_s = i$. Assuming a Gaussian distribution for the density of state $n_i(r) = n^0_i e^{-\frac{1}{2}m\bar{\omega}^2r^2/(k_BT)}$ and that $n_i(t)$=$n_{-i}(t)$, integrating eq.(3.43) over space yields

$$\frac{dN_{-2}(t)}{dt} = \frac{\sigma_{(-3,+3)\to(-2,+2)}v}{2\sqrt{2}} n^0_{+3} N_{-3}(t) \tag{3.44}$$

with N_i the number of atoms and n^0_i the peak density of $m_s = i$ atoms. In this model, the time constant τ for the time evolution of the $m_s = -2$ is given by:

$$\frac{1}{\tau} = \frac{\sigma_{(-3,+3)\to(-2,+2)}v}{2\sqrt{2}} n^0_{+3}. \tag{3.45}$$

A linear fit to the data based on the first 50 ms dynamics yields an experimental cross section of $\sigma_{exp} = (1.25 \pm 0.5 \pm 0.4) \times 10^{-17} m^2$ where we indicate successively statistical and systematic errors.

The cross section for spin exchange interactions due to dipolar interactions is estimated (see eq.(3.15) or [87]) to be:

$$\sigma_{dip}^{(0)} \approx 3 \times 10^{-18}\ \mathrm{m}^2. \tag{3.46}$$

The associated timescale for spin dynamics given our experimental parameters is $\tau \sim 7$ s: such a cross section is insufficient to account for the observed spin dynamics. We therefore attribute spin exchange dynamics due to spin-dependent contact interactions. To account for the spin dynamics, we shall consider only spin exchange interactions mediated by contact interactions.

A first estimate of a_0 extracted from the main collisional channels

In our experiment, m_s=-3 and m_s=+3 are the most populated spin states and it is collisions between atoms of these two spin states which will mostly drive the dynamics.

There are three collision channels for a (-3,+3) collision: (-3,+3)→ (-2,+2), (-3,+3)→ (-1,+1), (-3,+3)→ (0,0). From eq.(3.28), we can extract the contact scattering cross section for each of these channels within the Born approximation:

$$\sigma_{(-3,+3)\to(-2,+2)} = 8\pi(\frac{1}{77}a_6 + \frac{3}{11}a_4 - \frac{2}{7}a_0)^2, \tag{3.47}$$

$$\sigma_{(-3,+3)\to(-1,+1)} = 8\pi(\frac{5}{154}a_6 + \frac{6}{154}a_4 - \frac{5}{14}a_2 + \frac{2}{7}a_0)^2, \tag{3.48}$$

$$\sigma_{(-3,+3)\to(0,0)} = 16\pi(\frac{5}{231}a_6 - \frac{9}{77}a_4 - \frac{5}{21}a_2 - \frac{1}{7}a_0)^2.$$

For chromium, all scattering lengths are now well established except for a_0 [87, 83]. Therefore we can extract from our simulations the value of a_0 which fits best the experimental data shown Fig.3.5.

As a first analysis, we plotted $\sigma_{(-3,+3)\to(-2,+2)}$ as a function of a_0 (red line in Fig.3.6). Due to the parabolic dependence of this collisional cross section upon a_0, there are two values of a_0 which match with the experimentally measured cross section $\sigma_{exp} = (1.25 \pm 0.5 \pm 0.4) \times 10^{-17}$ m^2 deduced from the evolution of the $m_s = -2$ population (red shaded area in Fig.3.6).

The time evolution of the $m_s = -1$ and $m_s = 0$ populations are similar (Fig.3.5), and a linear fit to the first 50 ms gives $\sigma_{(-3,+3)\to(-1,+1)} \approx \sigma_{(-3,+3)\to(0,0)} \approx \sigma_{(-3,+3)\to(-2,+2)}$. As seen from Fig.3.6, only values of a_0 close to 0 lead to comparable rates for the three dynamics. We infer from our experimental data that $a_0 = 12 \pm^{15}_{10} a_B$ which is obtained from the three main collisional channels at play.

Model with all possible collision channels

Since our initial experimental conditions shows non-negligible fraction of atoms in other spin states than $m_s = \pm 3$, we established a more refined model in order to compare

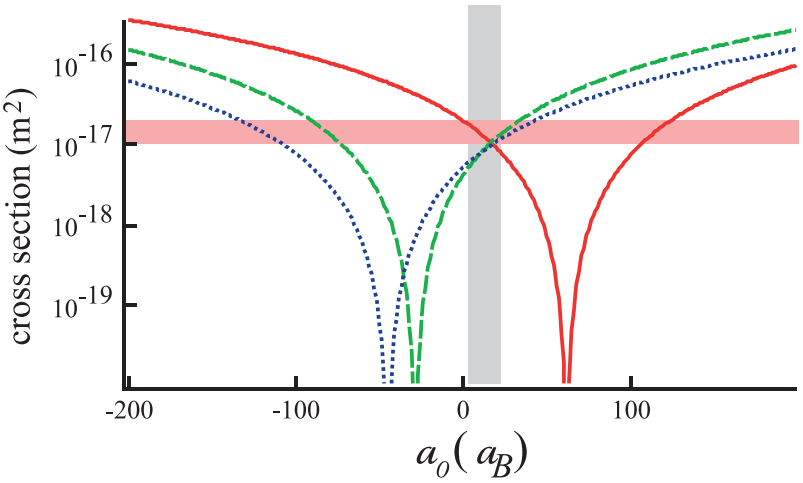

Figure 3.6: Cross sections for processes (i)$\sigma_{(-3,+3)\to(-2,+2)}$ (full line, red), (ii) $\sigma_{(-3,+3)\to(-1,+1)}$ (dashed, green), and (iii) $\sigma_{(-3,+3)\to(0,0)}$ (dotted, blue) as a function of a_0 . Red shaded area corresponds to the experimental outcome.

experimental data and numerical simulations. In our numerical simulation, we consider that the evolution of the fractional population in a given spin state m is solely governed by spin changing contact collisions:

$$\frac{dn_m}{dt} = v \sum_{m1,m2} \sigma_{(m_1,m_2)\to(m,m')} n_{m_1} n_{m_2} - \sigma_{(m,m')\to(m_1,m_2)} n_m n_{m'}, \tag{3.49}$$

with v the mean relative velocity, n_m the density of spin state m, and m' fixed by $m' = m_1 + m_2 - m$ in order to conserve the spin during the collision.

Using our initial experimental parameters, we simulated eq.(3.49) for different values of a_0 and compared them to the experimental data. The value of a_0 which best fits the data was then determined via a χ^2 *test* (see chapter 9 for more information).

Determination of a_0

Independant fits for each spin population of the experimental data for population dynamics during the first 50 ms in m_s = -2,-1,0 leads to $a_0 = 13^{+15}_{-10} a_B, 13.5^{+10.5}_{-13.5} a_B, 1.5^{+7.5}_{-9.5} a_B$, respectively with error bars denoting a 68.3% statistical confidence level. These values are all compatible with each other. As absolute population measurements in $m_s = 0$ may be underestimated due to a less efficient absorption process, we believe that there is a slight bias for the corresponding inferred value of a_0 towards the negative side. Therefore, we rely on the data for m_s = -2 to make our final estimate (the spin state which we measure best). We therefore have $a_0 = 13.5^{+15}_{-10} a_B$.

This scattering length is small, and most likely positive. As we shall see in chapter 5, this value of a_0 has an important consequences for the spinor ground state properties

of a Chromium BEC at very low magnetic field since it means the ground state of Chromium is expected to be cyclic [100].

3.4 Conclusions

In this chapter, we established the different collisional processes which can take place in our gas. We distinguished two types of collisions: coherent collisions and incoherent collisions. Incoherent collisions ensure thermalization of the different degrees of freedom. For a gas with a spin degree of freedom, these collisions lead to spin dynamics due to differences in the scattering lengths of different molecular potentials. An analysis of such spin dynamics led to the first measurement of a_0 for Chromium, the scattering length of the S=0 molecular potential. Coherent collisions on the other hand do not thermalize any degrees of freedom. They introduce phase shifts, which can also produce spin dynamics.

In the next chapter, we will present experimental results of the co-evaporation of ^{52}Cr and ^{53}Cr which led to the production of a ^{53}Cr Fermi sea. We analyze the thermalization of the mechanical degrees of freedom during evaporation and are able to extract the inter-isotope scattering length.

Then in chapter 5, we derive the thermodynamic properties of a Bose gas with a spin degrees of freedom and present two experiments. In the first experiment we explore an intriguing between spin dynamics and Bose condensation dynamics as a thermal multi-spin component gas is rapidly cooled across the Bose Einstein phase transition. In the second experiment, we take advantage of the thermalization of the spin degrees of freedom with temperature at low magnetic field in order to perform a spin selective cooling experiment.

CHAPTER 4

A ^{53}Cr Fermi sea

In this chapter, we present experimental results of the co-evaporation of ^{52}Cr and ^{53}Cr. We produce a fermionic gas ^{53}Cr at temperatures below the degeneracy temperature: a ^{53}Cr Fermi sea. We analyze the thermalization processes of the mechanical degrees of freedom during evaporation and are able to extract the inter-isotope scattering length a_{BF}=80 ± 10 a_B.

4.1 Introduction

The first degenerate Fermi gas was realized with ^{40}K [22], and was produced significantly after the first degenerate Bose gases [6, 7] despite the similarities in cooling techniques employed to produce them. The success of producing Bose Einstein Condensate came from the very efficient evaporative cooling techniques. Evaporative cooling relies on removing the most energetic atoms, and letting the atomic ensemble thermalize at a lower temperature. One of the main difficulties in cooling polarized fermions to degeneracy is the incapability of polarized fermionic atoms to collide (and therefore thermalize) through s-wave contact interactions at low energy, rendering evaporative cooling to degeneracy of polarized fermions colliding through short wave potentials impossible. To circumvent this problem and cool fermionic atoms to degeneracy, two major strategies are employed. The fermionic ensemble can be prepared in two distinct spin states. This enables s-wave collisions. Then thermalization processes between atoms of different internal states are possible and evaporating fermions is no longer inefficient. This strategy is commonly used and has produced degenerate Fermi gases of e.g. ^{40}K [22] and ^{6}Li [114]. Another strategy is to evaporate together a mixture of bosons and fermions. This technique is called sympathetic cooling. Here, fermions collide with bosons and thermalize. This also is a commonly used technique and has allowed to produce Bose-Fermi mixtures of ^{40}K-^{87}Rb, ^{6}Li-^{7}Li,^{6}Li-^{23}Na [78, 115]

Early experiments studied the thermodynamic properties resulting from Fermi statistics [77]. Attention was then brought to creating Fermi systems with tunable interactions. This was achieved by preparing a degenerate Fermi gas in two internal states and then tuning the interaction with a magnetic field close to a Feshbach resonance [13]. Strongly interacting Fermi gases were observed and studied [116, 117, 118, 119]. Ultracold molecules were then produced from a cold Fermi gas [120, 121, 122, 123] and successfully condensed [124, 125, 126]. The BEC-BCS crossover was experimentally

achieved [127, 128], and evidence of superfluidity in a strongly interacting Fermi gas demonstrated [129].

Fermi gases have also been loaded in optical lattices, a Mott insulator state was prepared [130], and have even been observed with a Quantum gas microscope [131]. The recent production of new cold gases of species with SU(N) symmetry (such as Sr or Yb [132, 133]) will allow for the exploration of exotic magnetism [134, 135].

Although this is a very active area of research, only a few ultracold Fermi gases with long range interactions have been cooled to degeneracy. Such systems are extremely appealing since long-range interaction are the leading interaction terms for the polarized case. Cold molecules with a strong electric dipole moment have been produced [32, 136], along with degenerate dipolar Fermi gases of Dysprosium [66] and Erbium [67]. With dipolar species, low temperature collisions become possible even for identical fermions. The long range potential leads to an elastic cross section independent of energy, where antisymmetric orbitals contribute to the total cross section even at zero temperature.

This very peculiar consequence of DDIs, first observed with Dy [66], was used to produce an Er Fermi sea [67]. However for Cr the dipolar elastic cross section is $\simeq 20$ times smaller than for Er, as it scales as d^4m^2 (d being the permanent magnetic dipole, and m the mass). In addition we only manage to trap in a conservative trap about 30 times less atoms than in [67] and at considerably low phase space density, which renders direct evaporative cooling of spin polarized ^{53}Cr atoms very challenging, if not unfeasible. This is why we chose to perform sympathetic cooling of ^{53}Cr fermions with the bosonic ^{52}Cr.

4.2 Thermodynamic properties of a gas of fermions

4.2.1 An ideal polarized Fermi gas

a) General description of a Fermi gas based on [137]

Polarized fermions cannot occupy the same quantum mechanical state. This is in stark contrast with polarized bosons. The distribution of spinless fermions follows the Fermi-Dirac distribution. The probability that a fermion, at thermal equilibrium with a large reservoir at temperature T and chemical potential μ, has an energy ϵ is:

$$f_\mu(\epsilon, T) = \frac{1}{e^{\frac{\epsilon-\mu}{k_B T}} + 1}. \tag{4.1}$$

A gas of N fermions at zero temperature, will have each energy level filled by an atom up until the Fermi energy, which is the energy of the N^{th} atom. The Fermi energy, which is the relevant energy scale when dealing with a fermionic gas, can be determined and has the following explicit form in a 3D harmonic trap:

$$E_f = \hbar\bar{\omega}(6N)^{1/3} \tag{4.2}$$

with $\bar{\omega}$ the mean trapping frequency. To this energy scale, we can associate the Fermi temperature T_f through $E_f = k_B T_f$. A gas of fermionic atoms is considered degenerate when the temperature T of the gas is smaller than T_f ($T < T_f$) and is considered completely degenerate in the ideal limit when $T = 0$.

The chemical potential μ of a gas is the energy one needs to give to the system, at constant temperature and entropy, in order to add a particle and for the system to keep it and remain at thermal equilibrium:

$$\mu = \left.\frac{\partial F}{\partial N}\right|_{S,T} \tag{4.3}$$

with F the free energy.

For a Fermi gas at a temperature T, there is no analytical expression for the chemical potential (since it involves computing Dirac integrals) but we can compute $\mu(T)$ numerically as shown Fig.4.1 for a 3D harmonic trap. For T=0, one retrieves the fact that $\mu(T = 0) = E_f$. The physical picture being that to add a new particle to a completely degenerate gas, the energy of the particle must be equal to the Fermi energy (since all lower energy states are occupied). $\mu(T)$ then decreases for increasing T/T_f and cancels for $T/T_f \approx 0.55$.

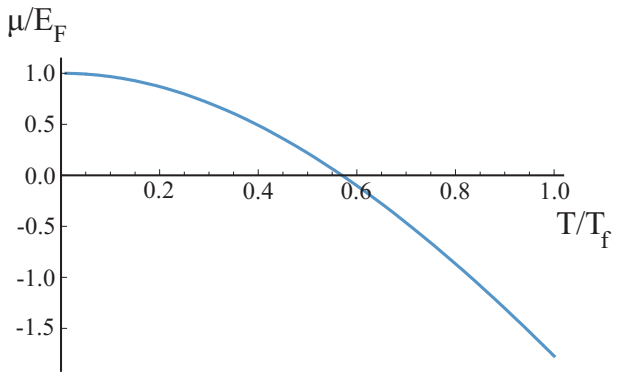

Figure 4.1: Chemical potential of a Fermi gas as a function of T/T_f.

b) Extracting experimental quantities

In our experiment, we perform absorption images of our gas in order to extract physical quantities. In the following, we will discuss how we measure the temperature of our Fermi gas and its size.

Temperature measurement

To extract thermodynamic quantities such as temperature, we acquire absorption images after turning off the trapping potential and letting the gas ballistically expand. If

the size of the gas after expansion is much larger than the initial size of the Fermi gas, the atomic distribution after expansion reflects the initial in trap momentum distribution [23].

The momentum distribution of a fermionic gas in an isotropic 3D harmonic trap is [138]:

$$n_{FD}(p) = -\frac{1}{(2\pi)^{3/2}\hbar^3}\left(\frac{k_B T}{m\bar{\omega}^2}\right)^{3/2} g_{3/2}(-e^{\frac{\mu}{k_B T}} e^{-\frac{p^2}{2mk_B T}}) \tag{4.4}$$

with $\bar{\omega}$ the mean geometric trapping frequency, T the temperature of the gas, and g_n the polylogarithmic function of order n defined as $g_n(z) = \sum_{k>0} z^k/k^n$. In the high temperature limit, this expression is equivalent to the expression obtained with a classical gas:

$$n_{Cl}(p) = \frac{N}{(2\pi)^{3/2}(mk_B T)^3} e^{-\frac{p^2}{2mk_B T}}. \tag{4.5}$$

with N the total atom number.

In the experiment, we measure the doubly integrated signal n_{dd}. We calculate the exact doubly integrated distribution expected for a gas at temperature T/T_f=0.50 (eq.(4.4)), and we fit this distribution by the doubly integrated classical distribution (eq.(4.5)). The fit yields T/T_f=0.525, overestimating the real temperature by 5%. The result of this procedure is shown Fig.4.2a.

In our experiment, we obtain temperatures as low as $T = 0.6T_f$. In this regime, fitting temperatures with the classical distribution or the exact distribution leads to differences in measured temperatures less than 5%. In the following, we will therefore use eq.(4.5) in order to determine the temperature of our gas.

Size measurement

To determine the characteristics of our Fermi gas, we measured the size of the gas *in situ*. From Fermi-Dirac statistics, the distribution of a Fermi gas in an isotropic harmonic trap at temperature T is:

$$n(r) = -\frac{(mk_B T)^{3/2}}{(2\pi)^{3/2}\hbar^3} g_{3/2}\big(-e^{\frac{\mu}{k_B T}} e^{-\frac{m\bar{\omega}^2}{2k_B T}r^2}\big) \tag{4.6}$$

with $\bar{\omega}$ the mean geometric trapping frequency, and g_n the polylogarithmic function of order n ($g_n(z) = \sum_{k>0} z^k/k^n$). In the high temperature limit, this expression is equivalent to the expression obtained for a classical gas:

$$n_{Cl}(r) = N\left(\frac{m\bar{\omega}^2}{2\pi k_B T}\right) e^{-(\frac{m\bar{\omega}^2}{2k_B T}r^2)} \tag{4.7}$$

with N the atom number. Using Mathematica, we calculate the doubly integrated distribution expected with Fermi-Dirac statistics (eq.(4.6)) at $T/T_f = 0.6$ and 1000

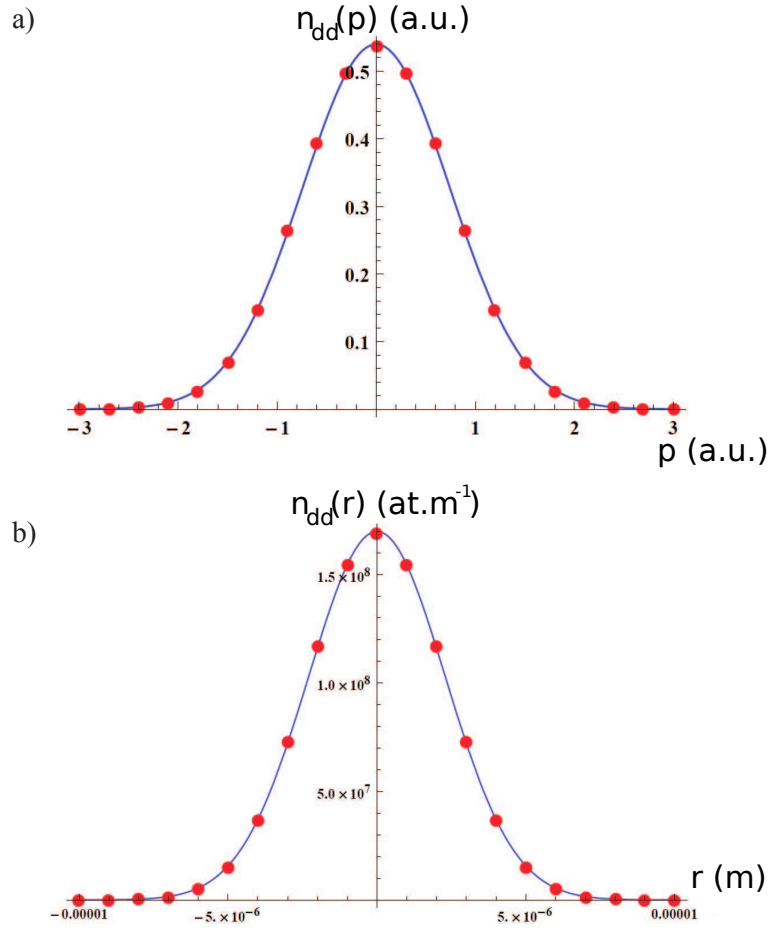

Figure 4.2: a) In red dots, doubly integrated momentum distribution of a gas at temperature $T/T_f = 0.50$ using Fermi-Dirac statistics. In blue, a gaussian fit to the points. In this regime, the fit yields the same temperature with an error less than 5%. b) In red, doubly integrated density distribution of a gas of 1000 atoms at a temperature $T/T_f = 0.60$ using Fermi-Dirac statistics. In blue, a gaussian fit to the points. The fit yields the same gas size with an error less than 5%.

atoms, and fit the calculated points with the doubly integrated classical distribution. The width of the classical fit matches the width of our gas down to the percent level. The result of this procedure is shown Fig.4.2b. We will therefore use eq.(4.7) in order to extract the size of our gas.

4.2.2 The Bose-Fermi mixture of ^{52}Cr and ^{53}Cr in metastable states

As mentioned at the end of subsection 2.3.4, the ZS 53 beam strongly reduces the number of atoms in the bosonic MOT. As we chose to cool ^{53}Cr atoms employing

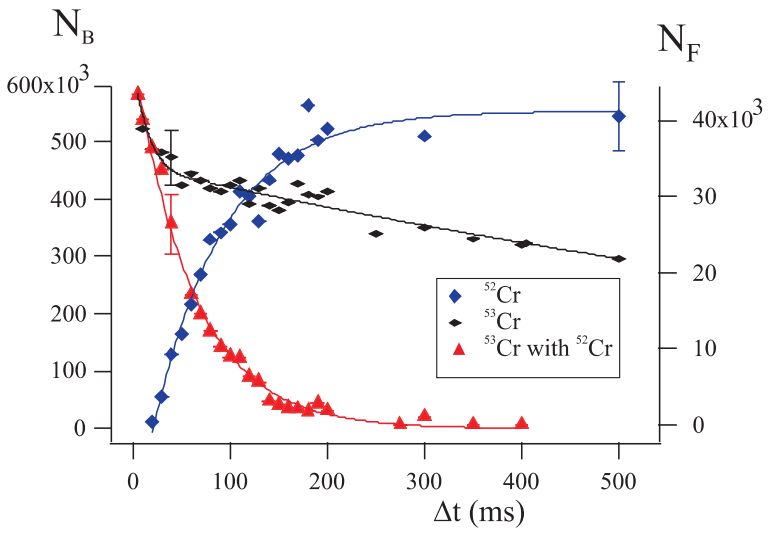

Figure 4.3: Evolution of bosonic and fermionic atom number as a function of the bosonic loading time Δt (see text). We load fermionic atoms in metastable states in a 1D FORT. We then turn off all fermionic lights. We then make a bosonic MOT and load the same 1D FORT with bosonic atoms for Δt. We measure the evolution of the fermionic atom number (red triangles) and bosonic atoms (blue diamonds). We also measure the fermionic atom number as a function of Δt when no bosonic atoms are present (black diamonds). The presence of bosonic atoms leads to extra fermionic losses which we attribute to inelastic collisions between metastable bosons and fermions.

the most abundant ^{52}Cr cloud as a coolant, it is important to store as many bosons as possible in the 1D FORT. We therefore implement a sequential scheme: we first produce a fermionic MOT and load a 1D FORT with ^{53}Cr metastable atoms for 800 ms (accumulated from a MOT, see subsection 2.3.4). We then turn off all fermionic lights (MOT, ZS, TC, R2), make a bosonic MOT and accumulate ^{52}Cr MOT atoms in the dipole trap.

In Fig.4.3 we show the evolution of the number of bosons (blue diamonds) and fermions (red triangles) as a function of the loading time Δt of boson atoms in the 1D FORT. We also show the number of fermions as a function of Δt but without making a bosonic MOT (black diamonds). Clearly, the presence of both isotopes in the 1D FORT trap leads to extra fermionic losses. We attribute these losses to inter-isotope inelastic collisions. In order to extract properly the inter-isotope contribution in the loss processes, we first analyse the losses when no bosons are present (black diamonds in Fig.4.3), then the loading of the bosons (blue diamonds), and finally we focus on the losses when both isotopes are present (red triangles).

Metastable fermion-fermion collisions

When no bosons are present, fermionic losses result from collisions with background atoms and from collisions between unpolarized metastable fermions. The evolution of fermionic density is:

$$\frac{dn_F}{dt} = -\beta_{F-F} n_F^2 - \gamma n_F \tag{4.8}$$

with $n_F(r,t)$ the fermionic density profile, β_{F-F} the two-body metastable inelastic collision rate and γ the one-body background collision rate estimated[1] at $\gamma = 0.1$ s^{-1}. Assuming a thermal gaussian density profile for n_F, eq.(4.8) can be integrated over space yielding:

$$\frac{dN_F}{dt} = -\underbrace{\frac{\beta_{F-F}}{2\sqrt{2}}\left(\frac{m\omega^2}{2\pi k_B T}\right)^{3/2}}_{\tilde{\beta}_{F-F}} N_F^2 - \gamma N_F \tag{4.9}$$

where N_F denotes the fermionic atom number, ω the mean trapping frequency, and T the temperature of the gas. The solution of eq.(4.9) is:

$$N_F(t) = \frac{-N_{0,F}\gamma}{\tilde{\beta}_{F-F}N_0 - (\gamma + \tilde{\beta}_{F-F}N_0)e^{\gamma t}}. \tag{4.10}$$

with $N_{0,F}$ the initial number of fermionic atoms. A fit to the first 100 ms of the data yields $\tilde{\beta}_{F-F}$= 8.4 $\times$ 10^{-5} s^{-1}, from which we could deduce β_{F-F} as long as we know the trapping frequencies and temperature. However, we did not measure the trapping frequencies of the 1D FORT trap at the time. Since our trap actually consists of two "parallel traps" (see Fig.1.6), it is difficult to estimate them *a posteriori*. We therefore will only compare the fermion-fermion inelastic rate to the boson-fermion one.

Boson loading

The evolution of the bosonic atom number is considered not to be affected by the presence of the fermionic isotope since we are rapidly in a situation where $N_B >> N_F$. The evolution of the boson atom number is then given by the loading of the 1D FORT which we fit with:

$$N_B(t) = N_{B,max}(1 - e^{-t/\tau}). \tag{4.11}$$

We obtain $N_{B,max} = (6.45 \pm 0.6) \times 10^5$ atoms and a loading time $\tau = 73 \pm 7$ms. These values show that the loading was not performed in an optimal situation because in the "normal" situation we have $N_{B,max}$=1.2 $\times$ 10^6 and $\tau \approx 60$ ms. In these conditions, a 100 ms loading time gives approximatively 1 $\times$ 10^6 atoms in the optical dipole trap.

[1] We measured the same one-body loss rate for the bosonic isotope.

Metastable boson-fermion collisions

When bosons are loaded in the 1D FORT, an extra loss mechanism for the fermions is introduced. We attribute these fermionic losses to two-body metastable inelastic collisions between fermions and bosons in metastable states. The evolution of the fermionic density is thus given by:

$$\frac{dn_F}{dt} = -\beta_{B-F} n_B n_F - \beta_{F-F} n_F^2 - \gamma n_F \tag{4.12}$$

with β_{B-F} the two-body boson-fermion metastable inelastic collision rate and $n_B(r,t)$ the bosonic density. Assuming that both isotopes share the same temperature, the evolution of the fermionic atom number is then:

$$\frac{dN_F}{dt} = -\underbrace{\beta_{B-F}\left(\frac{m_r^{52-53}\omega^2}{2\pi k_B T}\right)^{3/2}}_{\tilde{\beta}_{B-F}} N_B N_F - \underbrace{\frac{\beta_{F-F}}{2\sqrt{2}}\left(\frac{m\omega^2}{2\pi k_B T}\right)^{3/2}}_{\tilde{\beta}_{F-F}} N_F^2 - \gamma N_F \tag{4.13}$$

with m_r^{52-53} the Bose-Fermi reduced mass and $N_B(t)$ the bosonic atom number. There is no analytical solution to eq.(4.13). However, Mathematica can solve this differential equation numerically. A fit of the first 100 ms (see Fig.4.4) gives $\beta_{B-F} = (0.29 \pm 0.04) \times \beta_{F-F}$. This collision parameter is smaller than the Fermi-Fermi collision parameter. However in practice, due to large differences in atom number between fermions and bosons boson-fermion collisions are as detrimental as fermion-fermion collisions.

The starting point for evaporative cooling is therefore a trade-off. When Δt increases, N_B increases, but N_F decreases. We fix the loading time to be the shortest possible (leading to lower initial bosonic numbers before evaporation) but still allowing the production of BECs of $(1.0 \pm 0.1) \times 10^4$ atoms. Experimentally this corresponds to Δt =90 ms. In these conditions, we obtain the following optimal mixture before evaporation: $N_F = (3.0 \pm 0.5) \times 10^4$ and $N_B = (1.0 \pm 0.1) \times 10^6$. This corresponds to the situation where we have the minimum number of ^{52}Cr atoms required in order to produce a BEC with as many ^{53}Cr atoms as possible.

4.3 Evaporation of a Bose-Fermi mixture of ^{52}Cr and ^{53}Cr

4.3.1 A ^{53}Cr Fermi sea

a) Evaporation

Once atoms are optically pumped to their absolute ground state ($|s = 3, m_s = -3>$ and $|F = 9/2, m_F = -9/2>$, respectively), the crossed dipole trap is implemented by transferring 80% of the IR power to the vertical beam in 9 s. The total IR power is

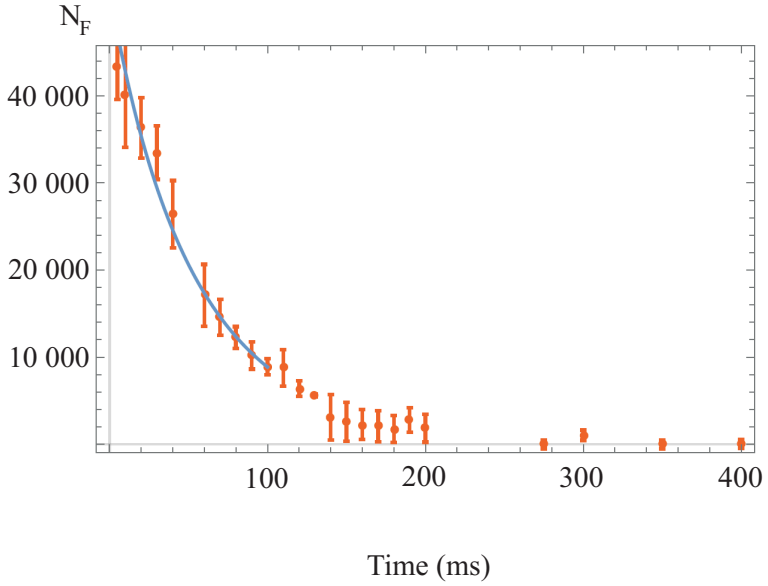

Figure 4.4: Evolution of the fermionic atom number as a function of the bosonic loading time (same evolution as the red triangles in Fig.4.3). The fit corresponds to the solution of eq.(4.13) with $\tilde{\beta}_{B-F} = (0.29 \pm 0.04) \times \tilde{\beta}_{F-F}$

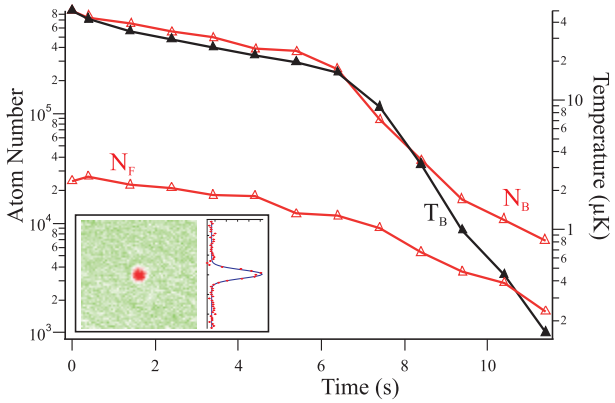

Figure 4.5: Time evolution of ^{52}Cr temperature (T_B) and atom number of both isotopes during evaporation. The crossed dipole trap is fully loaded at t=7 s. The evaporation ends at t=12 s. Inset: *in-situ* absorption image of a degenerate fermionic ^{53}Cr cloud of 10^3 atoms, with corresponding integrated optical depth.

then reduced to 1 W (starting from P= 40 W at t=4 s in Fig.4.5) in 8 s. We actually use the same form for the evaporation ramp as shown in Fig.1.8.

Throughout the evaporation ramp, we monitor for each isotope the atom number and cloud size through an absorption imaging process after a time of flight expansion t_{TOF}. The experimental determined temperatures are obtained by fitting the momentum distributions imaged after a ballisitc expansion by a bimodal distribution for ^{52}Cr

(see section 1.4), and by a Boltzmann distribution[2] for ^{53}Cr.

Fig.4.5 shows the evolution of the boson temperature T_B and atom numbers for both isotopes. Thermalization between the two isotopes is relatively good during the whole evaporation process as shown by Fig.4.6. Consequently, the boson-fermion cross section σ_{BF} has to be relatively large. On the other hand, thermalization is not perfect: the fermion temperature T_F is measured to be about 20% higher than T_B during the whole evaporation ramp (Fig.4.6). We thus infer that σ_{BF} is smaller than the bosonic cross section σ_{BB}. At the end of the ramp, a ^{52}Cr BEC is obtained with typically $(1.0\pm0.1) \times 10^4$ atoms at $T_B = (180 \pm 20)$nK, while N_F ranges between 500 and 1000 with $T_F = (220 \pm 20)$nK.

b) Evidence for the achievement of a Fermi sea

In order to characterize the fermionic gas at the end of evaporation, we need to compare the fermion temperature T_F to the Fermi temperature T_f.

At the end of evaporation, the power of the IR laser is rapidly ramped up (to 5 W) to obtain a tighter trap and freeze evaporation. We measured through parametric excitations the following trapping frequencies: $\omega_{x,y,z} = 2\pi\times(430,510,350)$Hz (with 5% uncertainty for each axis).

With these values, we calculate the associated Fermi temperatures (using eq.(4.2)):

$$\begin{aligned} T_f^{max} &= 370 \pm 20 \text{ nK for 1000 atoms} \\ T_f^{min} &= 294 \pm 16 \text{ nK for 500 atoms} \end{aligned}$$

with the uncertainties resulting from the trapping frequency measurement.

We therefore obtain $T_F/T_f = 0.66 \pm 0.08$ and a Chromium Fermi sea of $N_F = 500 - 1000$ atoms (see inset of Fig 4.5).

c) Fermi sea characteristics

We measure the *in situ* size of the fermion ensemble: $R_y = (6.3 \pm 0.6)\mu$m and $R_z = (6.7 \pm 0.7)\mu$m using a gaussian fit. This is not perfectly compatible with the expected size of our gas, where we expect a theoretical size $R_y^{(th)} = (4.5 \pm 0.2)\mu$m and $R_z^{(th)} = (6.6 \pm 0.3)\mu$m. We attribute this to the difficulty of *in situ* measurements: the probe affects the distribution (e.g by heating the sample) and the resolution of the imaging system broadens the measurement. Moreover, interactions with the Bose gas deform the Fermi gas.

The theoretical peak density n_0 of a gas of 1000 atoms at $T/T_f = 0.6$ is on the order of $n_0 \sim 5\times 10^{18}$ at·m^{-3}.

[2] as discussed in subsection 4.2.1, for $T/T_f > 0.6$ it is expected that fitting the Fermi-Dirac distribution by the Boltzmann statistics leads to the same value of temperature within 5% at maximum.

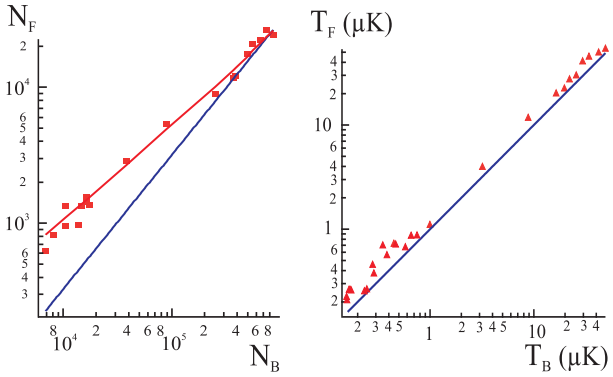

Figure 4.6: Comparison between the behaviour of the two isotopes during evaporation. Left: Atom numbers showing the smaller losses for fermions. The (red) curve is the prediction from eq.(4.30), the straight (blue) line assumes constant ratio between atom numbers. Right: Temperature of the fermionic isotope as a function of the bosonic isotope. High temperature represent the start of the evaporation ramp, low temperatures the end of the ramp. The temperature of the fermion remains about 20% higher than that of the boson during the whole sequence. The straight (blue) line corresponds to identical temperatures.

d) Getting rid of bosons

To have a pure Fermi gas, we need to get rid of the bosons without affecting the fermions. One must be careful when the two species are isotopes as they experience approximatively the same trapping potential and their optical transitions are very close. To get rid of the bosons, we adopted the strategy of performing a light pulse resonant with the bosonic isotope. During a resonant absorption pulse of $t_{pulse} = 70$ μs at $I/I_{sat} = 0.08$, the number of photons absorbed by bosonic atoms N^b_{ph} is:

$$N^b_{ph} = R_{Scat} \times t_{pulse} \approx 50 \tag{4.14}$$

with R_{Scat} given in eq.(2.1). This pulse is non retro-reflected, therefore the expected heating ΔT is of the order of

$$\Delta T \sim (N^b_{ph})^2 E_{Rec}/k_B \sim 5 \text{ mK}$$

where E_{Rec} is the recoil energy. This energy scale is much greater than the trap depth which is estimated to be in the μK regime at the end of evaporation. We do not expect any bosonic atoms to remain in the trap after such a pulse.

We produced a Fermi sea, and applied or not the bosonic resonant pulse. We observed that without the pulse we had temperatures of 210 $\pm$ 20 nK. When the pulse was applied we measured temperatures of 260 $\pm$ 20 nK. The temperature of the Fermi gas is increased by about 10 % of the Fermi temperature when we apply a resonant bosonic pulse.

We do not attribute this heating to the fact that fermions absorbed photons during the bosonic resonant pulse. Indeed, the bosonic resonant light is detuned 305 MHz away from the fermionic resonance (see Table 2.2). We estimate that the number of photons absorbed by fermionic atoms during a resonant light pulse on the bosonic transition is $N_{ph}^{f} \propto 10^{-3}$. The heating induced is smaller than 1 nK. This is negligible when compared to the temperature of the gas and cannot explain the increase in temperature.

We attribute the heating of the fermion due to fermion-boson collisions as the bosons escape the trap. In principle the energy of a bosonic atom is so large ($\Delta T \sim$ 5 mK) that most of the collision should lead to fermionic losses. Most likely, a small number of collisions produce hot fermionic atoms which remain trapped and heat the sample.

In conclusion, we have developed a method to get rid of bosons. However, this protocol induces a heating of the order of 10% of T/T_f. We attribute this heating to boson-fermion collisions as the bosons are expelled from the trap.

4.3.2 Evaporation analysis

a) Efficiency

For approximatively the same gain in temperature, there are less evaporative losses for ^{53}Cr atoms than for ^{52}Cr atoms (Fig.4.6). This results in very efficient evaporative cooling of the fermion.

The initial peak fermionic phase space density PSD_{ini} is $n_0\lambda_T^3$ with n_0 the peak atomic density and λ_T the deBroglie wavelength. At the start of evaporation, we can safely assume a gaussian atomic distribution and PSD_{ini} reads:

$$PSD_{ini} = N\left(\frac{\hbar\bar{\omega}}{k_B T}\right)^3. \tag{4.15}$$

with $\bar{\omega}$ the geometrical averaged trapping frequency. Again, having not estimated the initial trapping frequencies it is difficult to be quantitative. However, the initial phase space density for a bosonic gas of about 1×10^6 atoms was evaluated to be 5×10^{-7} when BEC was first obtained in the group [43]. We believe that the initial phase space density of the boson is not drastically different now, therefore we estimate that the initial phase space density of a fermionic gas with 3×10^4 atoms is $PSD_{ini} \sim 1.5 \times 10^{-8}$.

At the end of evaporation a degenerate gas is produced so $PSD_{fin} \approx 1$. This gain in phase space is of the same order of magnitude than that of the boson. However, this gain is achieved by losing a factor of 30 in fermionic atom number, compared to a factor 100 for the bosonic atom number. Therefore, although only 3×10^4 ^{53}Cr atoms are loaded in the optical dipole trap at 120 μK before evaporation, degenerate Fermi gases of up to 10^3 atoms can be produced. The evaporation efficiency γ, which is defined as:

$$\gamma = -\frac{d\log PSD}{d\log N} \tag{4.16}$$

is therefore 3 times larger for the fermion than for the boson and is equal to ≈ 4.5 even though each isotope sees the same optical potential. Typical reported evaporation efficiencies lie between 2.5 and 3.5 [58]. Our co-evaporation scheme is therefore very efficient in cooling the fermionic isotope if we only consider fermionic losses. However, if we consider the total atomic losses (i.e. fermionic and bosonic losses) in the definition of the evaporation efficiency, then the evaporation of the fermion is as efficient of the boson evaporation.

b) Determination of a_{BF}

In the following section, we analyze our evaporation scheme and outline the decisive role played by the numerical value of the inter-isotope scattering length a_{BF} in order to ensure thermalization of the fermionic gas. For that we develop the following theoretical model based on the scaling laws for evaporation first introduced in [139]. These scaling laws reproduce the evolution obtained with a rather more complex analysis based on the Boltzmann equation [59]. Moreover, the scaling laws were shown to be accurate even for small atom number [140].

For quantitative predictions, these scalings suffer from an exponential dependence on $\eta = U/k_B T$, where U is the trap depth which is experimentally difficult to calibrate. The main idea of our theoretical analysis is to greatly reduce this sensitivity on η by performing differential measurements.

α) Assumptions

In our model, the main assumption is that polarized ^{53}Cr atoms only collide with ^{52}Cr atoms.

This assumption is first motivated by the fact that the centrifugal barrier for the $p-$wave collisional channel is of the order of 800 μK (see eq.(3.3)), much larger than the initial temperature of the cloud. As a consequence, collisions between polarized fermions can be safely neglected.

As shown in Fig.4.5, thermalization between both isotopes is good, meaning that the inter-isotope scattering length a_{BF} should be comparable to the boson-boson scattering length $a_{BB} = 103 \pm 4 a_B$ with a_B the Bohr radius. Hence the contact inter-isotope cross section σ_{BF} is expected to be of the order of

$$\begin{aligned} \sigma_{BF} &\sim 4\pi a_{BB}^2 \\ &\sim 10^{-16} \mathrm{m}^2. \end{aligned} \tag{4.17}$$

The expected scattering cross-section between identical fermions due to DDIs is estimated to be (see eq.(3.15)):

$$\sigma_{dip}^{(0)} \approx 1.0 \times 10^{-17}\ \mathrm{m}^2. \tag{4.18}$$

This is much smaller than the estimated cross-section for boson-fermion collision σ_{BF} and we shall consider that fermions only collide with the more abundant ^{52}Cr atoms, through contact interactions. Due to large differences in atom numbers, we can also assume that evaporative losses of bosons comes solely from collisions between bosons.

Furthermore, in order to appreciate the importance of bosons during evaporation we can compare the rate of dipolar fermion-fermion collisions τ_{DDI} to contact boson-fermion collisions $\tau_{Contact}$. The collision rate τ scales as

$$\tau = \frac{1}{n_i \sigma v} \tag{4.19}$$

with v the relative velocity of the colliding atoms, n_i the atomic density of the isotope i, and σ is the contact or dipole-dipole cross section. For fermion-fermion collisions, n is simply n_F. For boson-fermion collisions, n is the bosonic density n_B. Due to the large difference in atom number, the fermionic density is roughly 30 times lower than the bosonic density. This leads to a large difference in timescales associated with a collision due to dipole-dipole interaction between fermions or contact interaction between bosons and fermions:

$$\tau_{DDI} \approx 300 \times \tau_{Contact}. \tag{4.20}$$

The rate associated with dipolar fermion-fermion collisions is negligible compared to Bose-Fermi contact collisions. The presence of bosons during the evaporation is crucial in order to assure efficient cooling and thermalization.

β) A differential measurement

One major difficulty in applying this model to quantitatively describe evaporation is that the rate of evaporation depends exponentially on η and is given for $\eta > 4$ by [141]:

$$f(\eta) \approx \frac{2\sqrt{2}[e^{-\eta}(2\eta - 6) + e^{-2\eta}(\eta^2 + 4\eta + 6)])]}{1 - e^{-2\eta}(2\eta^2 + 2\eta + 1)}. \tag{4.21}$$

Fig.4.7 shows a plot of eq.(4.21). It is usually difficult to precisely measure the trap depth in an experiment (e.g. due to uncertainties in estimating waists of laser beams *in situ*). However, the trap depth is almost identical for the two isotopes (the isotopic shifts are much smaller than the detunings of the IR laser for all optical transitions). In our analysis, we therefore strongly reduce the sensitivity to the trap depth by comparing the rate of evaporation of fermions to that of bosons.

γ) Evaporation rate equations

During evaporation, both the number of bosons and fermions diminish. This is due to (i) one-body losses with the background gas and (ii) evaporation losses due to collisions

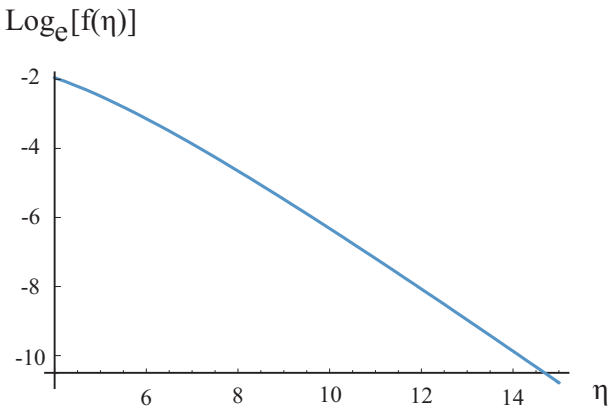

Figure 4.7: Plot of $\log_e f(\eta)$ for $\eta \in$ [4,15] (eq.(4.21)). As explained in the text calibrating $f(\eta)$ correctly is crucial due to its exponential dependence on η.

with bosons. Given these assumptions, the evolution of the number of bosons and fermions read:

$$\frac{dN_B}{dt} = -\sigma_{BB} n_B \bar{V}_{BB} f(\eta_B) N_B - \gamma N_B \tag{4.22}$$

$$\frac{dN_F}{dt} = -\sigma_{BF} n_B \bar{V}_{BF} f(\eta_F) N_F - \gamma N_F \tag{4.23}$$

where N_i is the atom number, n_i the average density, and $i = B, F$ stands for boson or fermion; $\bar{V}_{ij} = (8k_B(m_i T_j + m_j T_i)/\pi m_i m_j)^{1/2}$ is the mean of the relative velocity for particle i and j, γ is the one-body loss coefficient, independently measured to be $\gamma = 0.1\ \mathrm{s}^{-1}$. η is the ratio between the trap depth U and the thermal energy $k_B T$ ($\eta = \frac{U}{k_B T}$), and $f(\eta)$ is the average evaporation fraction for the trapped ensemble (discussed in more detail below). For a large η very few atoms are evaporated and $f(\eta)$ is close to 0 whereas it is the contrary for small η. The first term of eq.(4.22) accounts for evaporation losses due to collisions with bosons, and the second term represents background losses.

In thermal equilibrium, the kinetic energy and the potential energy in a 3D harmonic trap with N atoms are $E_{kin} = E_{pot} = \frac{3}{2} N k_B T$. The total energy E is thus given by:

$$\begin{aligned} E &= E_{kin} + E_{pot} \\ &= 3N k_B T \end{aligned}$$

Since the total atom number changes during evaporation, the total energy of the system varies accordingly. Its evolution reads:

$$\frac{d(3N_B T_B)}{dt} = -\sigma_{BB} n_B \bar{V}_{BB} f(\eta_B)(\eta_B + 1) N_B T_B - 3\gamma N_B T_B \tag{4.24}$$

$$\frac{d(3N_F T_F)}{dt} = -\sigma_{BF} n_B \bar{V}_{BF} f(\eta_F)(\eta_F + 1) N_F T_F - 3\gamma N_F T_F \tag{4.25}$$

The second term in eq.(4.24) and eq.(4.25) accounts for the energy removed from the sample once an atom has collided with the background gas. This atom has a typical energy equal to the mean atom energy $3k_BT$. The first term accounts for the energy carried away by an evaporated atom, where $(\eta_i + 1)k_BN_iT_i$ corresponds to the energy per evaporated particle of isotope i [142].

Dividing eq.(4.22) (eq.(4.23)) by the boson (fermion) atom number one obtains:

$$\frac{d\log_e N_B}{dt} + \gamma = -\sigma_{BB} n_B \bar{V}_{BB} f(\eta_B) \tag{4.26}$$

$$\frac{d\log_e N_F}{dt} + \gamma = -\sigma_{BF} n_B \bar{V}_{BF} f(\eta_F) \tag{4.27}$$

and dividing eq.(4.26) and eq.(4.27) together gives the following differential equation:

$$\frac{\frac{d\log_e N_B}{dt} + \gamma}{\frac{d\log_e N_F}{dt} + \gamma} = \frac{\sigma_{BB} n_B \bar{V}_{BB} f(\eta_B)}{\sigma_{BF} n_B \bar{V}_{BF} f(\eta_F)}. \tag{4.28}$$

To solve eq.(4.28), we first of all consider that $\bar{V}_{BB}/\bar{V}_{BF}$ is time independent. This is a good approximation, since the ratio depends on time only if the temperatures of each isotope evolve independently. As shown in Fig.4.6, the fermionic temperature is always 20 % higher than the bosonic temperature but the temperature evolution seems similar. If we assume $T_F = 1.2\ T_B$, we obtain:

$$\frac{\bar{V}_{BB}}{\bar{V}_{BF}} = \sqrt{\frac{2m_F}{m_B + 1.2m_F}} \approx 0.96 \tag{4.29}$$

where m_F (m_B) is the mass of fermionic (bosonic) isotope. If we also assume that η_i is constant in time (this assumption is justified *a posteriori* by the measurement of η_B see Fig.4.8), we can now integrate eq.(4.28) which gives for any values of t_1 and t_2:

$$\frac{\log_e\left(\frac{N_B(t_2)}{N_B(t_1)}\right) + \gamma(t_2 - t_1)}{\log_e\left(\frac{N_F(t_2)}{N_F(t_1)}\right) + \gamma(t_2 - t_1)} = \frac{\sigma_{BB}}{\sigma_{BF}} \times \frac{\bar{V}_{BB}}{\bar{V}_{BF}} \times \frac{f(\eta_B)}{f(\eta_F)}. \tag{4.30}$$

As seen from eq.(4.30), the sensitivity to trap depth is not completely suppressed by the relative measurement, because the temperatures of both clouds are slightly different, leading to values of η_B and η_F differing by up to 20 %. We therefore first estimate the value of η_B by comparing the measured loss rate of bosons and the cooling rate. From eq.(4.22) we obtain the following equation for n_B:

$$n_B = -\frac{\frac{d\log_e N_B}{dt} + \gamma}{\sigma_{BB} V_{BB} f(\eta_B)}. \tag{4.31}$$

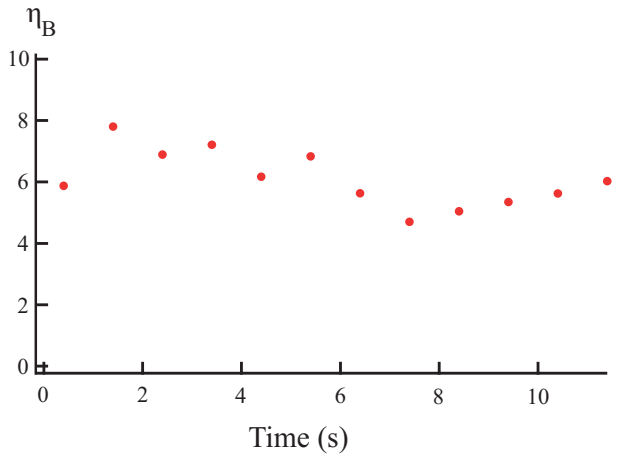

Figure 4.8: Experimental value of η_B as a function of t_2. The value of η_B is computed using eq.(4.33) and the experimental points are the same ones as for Fig.4.5. We find that η_B is approximatively constant during evaporation and obtain a mean value of $\eta_B = 6.1 \pm 0.5$.

Developing the left hand side of eq.(4.24) and eq.(4.25), dividing each side by $N_B T_B$ and substituting n_B using eq.(4.31) gives the following equation with η_B the only unknown parameter:

$$\log_e\left(\frac{T_B(t_2)}{T_B(t_1)}\right) = \frac{2-\eta_B}{3}\left[\log_e\left(\frac{N_B(t_1)}{N_B(t_2)}\right) - \gamma(t_2-t_1)\right]. \tag{4.32}$$

We therefore obtain:

$$\eta_B = -3\log_e(\frac{T_B(t_2)}{T_B(t_1)}) \times [\log_e\left(\frac{N_B(t_1)}{N_B(t_2)}\right) - \gamma(t_2-t_1)]^{-1} + 2. \tag{4.33}$$

The analysis of our data using eq.(4.33) leads to Fig.4.8 for $t_1 = 0$ and t_2 spanning over all evaporation times.

We find that η_B is approximatively constant throughout evaporation. This justifies *a posteriori* the assumption we made on η_i in order to establish eq.(4.30). Our experimental estimate is $\eta_B = 6.1 \pm 0.5$. Using T_F =(1.2±0.1) T_B, we find:

$$\frac{f(\eta_B)}{f(\eta_F)} = 2.4 \pm 0.3. \tag{4.34}$$

δ) Determination of $|a_{BF}|$

We can now use our experimental data of Fig.4.5, and estimate from eq.(4.30) the value for the cross-section σ_{BF}. We can use different sections of the whole evaporation ramp to measure the ratio σ_{BF}/σ_{BB} as shown in Fig.4.9. In practice, we span the times t_1 and

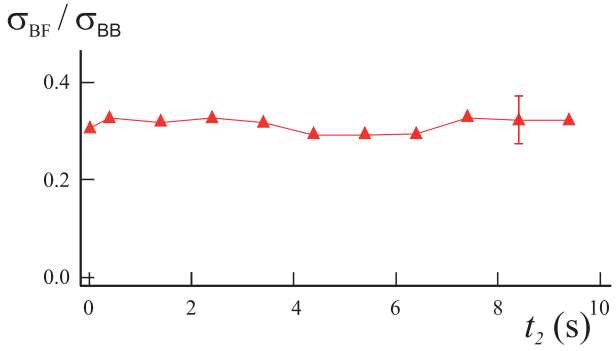

Figure 4.9: Experimental measurements of the ratio of the boson-boson and inter-isotope cross sections obtained using eq.(4.30), with $t_1 = 10$ s (see text). The error bars show the systematic uncertainty associated with $\eta_{B,F}$, which dominates over statistical uncertainties (for clarity, only one error bar is shown).

t_2 over the range of experimental times. Experimental values of σ_{BF}/σ_{BB} all lie in the interval 0.31 ± 0.05 regardless of the choice of t_1 and t_2. This indicates that σ_{BF}/σ_{BB} is insensitive to temperature within signal-to-noise. This is in good agreement with the assumption that atoms collide mostly through $s-$wave and short-range interactions, and with theoretical predictions [143].

An outcome of this analysis is the first measurement of the boson-fermion scattering length $|a_{BF}|$ when both atoms are in the stretched state of lowest energy. Indeed, $\sigma_{BF} = 4\pi a_{BF}^2$ describes collisions between (distinguishable) bosons and fermions, while the value of the boson-boson scattering length which sets the cross section between undistinguishable bosons $\sigma_{BB} = 8\pi a_{BB}^2$ has been measured to be $a_{BB} = 102.5 \pm 0.4\ a_B$ [87]. We are therefore able to provide an experimental value of $|a_{BF}|$:

$$\begin{aligned} \frac{\sigma_{BF}}{\sigma_{BB}} &= \frac{4\pi a_{BF}^2}{8\pi a_{BB}^2} = 0.31 \pm 0.05 \\ \rightarrow |a_{BF}| &= (80 \pm 10) a_B \end{aligned} \tag{4.35}$$

ϵ) Mass scaling analysis

In principle, our analysis does not give insight on the sign of a_{BF}. Nevertheless, in the following we present a mass scaling analysis [144] applied to the case of Chromium. The good agreement of the theory with our measured value and to the scattering length value associated to collisions between ^{50}Cr atoms allows us to conclude on quite solid grounds that $a_{BF} > 0$.

Gribakin and Flambaun established a simple analytic formula for the scattering length a in an atomic collision [84]:

$$a(\Phi) = \bar{a}[1 - \tan(\frac{\pi}{n-2}) \tan(\Phi - \frac{\pi}{2(n-2)})]. \tag{4.36}$$

Here, $\bar{a}$ is the mean scattering length determined by the asymptotic behavior of the potential $U(r) \sim -C_n/r^n$ with n= 6 for atom-atom scattering, and Φ is the semi-classical phase acquired during a collision. The expression of the mean scattering length is [84]:

$$\bar{a} = \cos(\frac{\pi}{n-2})\left(\frac{\sqrt{2m_r^{(i,j)}C_n}}{\hbar(n-2)}\right)^{2/(n-2)}\frac{\Gamma(\frac{n-3}{n-2})}{\Gamma(\frac{n-1}{n-2})} \tag{4.37}$$

where Γ are the Euler functions and $m_r^{(i,j)}$ is the reduced mass associated with an isotope i and an isotope j ($m_r^{i,j}$= $\frac{m^{(i)}\times m^{(j)}}{m^{(i)}+m^{(j)}}$).

Φ can be determined through the knowledge of the form of the real potential $U(r)$:

$$\Phi = \int_0^\infty \sqrt{-2m_r^{(i,j)}U(r)}dr. \tag{4.38}$$

However, eq.(4.38) is not easy to compute because $U(r)$ are often complicated and unknown functions. We determine Φ using another method. The semi-classical phase shift is related to the number of vibrational levels with zero orbital angular momentum N_s through [84]:

$$N_s = \left[\frac{\Phi}{\pi} - \frac{n-1}{2(n-2)}\right] + 1 \tag{4.39}$$

where $\left[\ \cdot\ \right]$ is the integer part. For Cr_2, N_s is measured to be 29 [145]. We then determined an interval for the semi-classical phase: $\Phi \in$[89.9;93.1] rad.

Using eq.(4.36) and eq.(4.38), we may set Φ_{52-52} (the semi-classical phase acquired during a ^{52}Cr-^{52}Cr collision) to give the experimentally measured $a_{BB} = 102.5\ a_B$ [87] and verifies $\Phi \in$[89.9;93.1] rad. We find Φ_{52-52}=90.76 rad. Finally, we performed a mass scaling operation and obtained the semi-classical phase shift for a ^{53}Cr-^{52}Cr collision Φ_{53-52}:

$$\Phi_{53-52} = \sqrt{\frac{m_r^{53,52}}{m_r^{52,52}}}\Phi_{52-52} \approx 90.995 \text{ rad}. \tag{4.40}$$

We can calculate $a(\Phi_{53-52})$ through eq.(4.36). We find a mass scaled inter-isotope scattering length $a_{BF}(\Phi_{53-52}) \approx 68\ a_B$. This value is at the limit of our error bars. A similar protocol was applied for a ^{50}Cr-^{50}Cr collision. In Fig.4.9 we report the measured value of $a_{BB} = 102.5\ a_B$ for ^{52}Cr [87], the less well known value for ^{50}Cr [83], as well as our newly measured value for $a_{BF} = 80(\pm 10)\ a_B$. In both cases, the measured scattering length is larger than the theoretical predictions based on mass scaling. The good agreement with predictions based on mass-scaling [84, 144] indicates that $a_{BF} > 0$.

In our model, we did not consider Bose-Fermi dipolar collisions. Therefore in our experimental value of a a_{BF} there is a slight contribution of dipolar collisions. A full investigation is however necessary in order to account properly for dipolar collisions. Here we just suggest that there is a slight bias of the measured scattering lengths towards larger values, due to dipolar collisions.

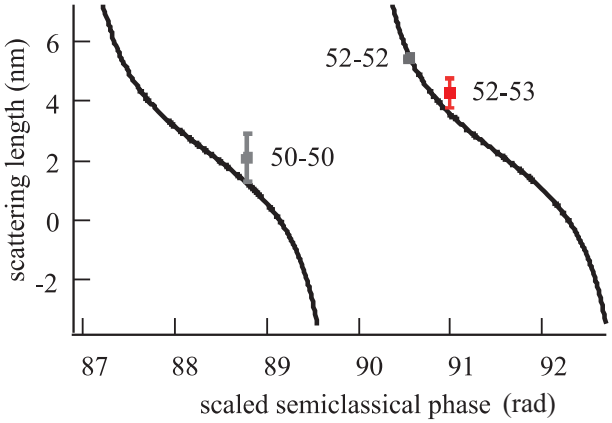

Figure 4.10: Scattering lengths of Cr as a function of the semi-classical phase. The solid line is the predicted scattering length using mass scaling of semi-classical phase (see text). The points represent experimental values of a_{BB} for ^{52}Cr [87], for ^{50}Cr, as well as our newly measured value for $a_{BF} = 80(\pm 10)\ a_B$. The good agreement with predictions based on mass-scaling [84, 144] indicates that $a_{BF} > 0$.

ζ) Analysis conclusion

Our calculations therefore confirm that $\sigma_{BF} < \sigma_{BB}$. As evaporation is optimized to be achieved as fast as possible for the boson, it is not surprising that the Fermi cloud lags slightly behind in terms of temperature. This analysis shows that our strategy to cool fermions is efficient because (i) σ_{BF} is sufficiently large to (almost) ensure inter-isotope thermal equilibrium; (ii) σ_{BF} is small enough to reduce evaporative losses of fermions, which leads to a gradual increase in the ratio of the number of fermions to the number of bosons as evaporation proceeds (see Fig.4.6). This ratio increase is essential for the positive outcome of our experiment. If we had $a_{BF} = a_{BB}$, the ratio between isotope atom number would remain constant and we would have about 300 fermionic atoms at the end of evaporation at $T_F = (220 \pm 20)$ nK. In these conditions, the Fermi temperature is 250 nK and we would have $T/T_f \approx 1$. If $a_{BF} > a_{BB}$, there would be no fermions left at the end of the evaporation sequence.

In other experiments where the fermionic isotope is cooled sympathetically with the boson, the inter-isotope cross-section is tuned using a Feshbach resonance to a value slightly smaller than the boson-boson cross section in order to optimize evaporation (as for example in [146]).

4.4 Conclusion and perspectives

In conclusion, we have produced a ^{53}Cr degenerate Fermi gas at $T_F/T_f = 0.66 \pm 0.08$, with up to 10^3 atoms, together with a BEC of 10^4 ^{52}Cr atoms by co-evaporating a Bose-Fermi mixture. The Fermi sea is produced in an efficient way due to a favourable

value of the inter-isotope cross-section σ_{BF}. It is worth pointing out that for most sympathetic cooling experiments, where evaporated atoms are mostly bosons, the size of the bosonic gas is reduced faster than the size of the fermionic gas. Cooling can then cease to be efficient because thermalization relies on a good spatial overlap between the two gases. We should not suffer from this loss in efficiency since we evaporate bosons and fermions in almost the same manner and we should always have a good overlap. Moreover, since $a_{BF} < a_{BB}$ and our number of fermions is small enough, the entire fermion distribution resides like a fermionic "core" within the Bose cloud (i.e. no phase separation) [147]; smaller temperatures could then be obtained if evaporation could proceed. Our procedure to produce ^{53}Cr Fermi seas seems optimized and it will be difficult to load more fermionic atoms in the 1D FORT in order to have larger and colder Fermi gases. Since the production of the degenerate Fermi gas is closely linked to the production of BEC, one route would be to produce BEC in a more efficient way. For example, we could implement a sub-doppler cooling scheme in gray optical molasses in order to start evaporation at lower temperatures [148].

This boson-fermion degenerate mixture might have peculiar properties, due to the strong imbalance in atom numbers. Fermions will experience a mean field potential $E_{int} = g_{BF} n_B(\vec{r})$ from the interaction with bosonic atoms of density distribution $n_B(\vec{r})$. g_{BF} is the boson-fermion coupling constant:

$$g_{BF} = \frac{2\pi\hbar^2}{m_r} a_{BF} \tag{4.41}$$

with m_r^{BF} the interisotope reduced mass. In our experiment, we estimate E_{int} ≈0.15 E_f for n_B in the order of 10^{20} at.m^{-3}; the spatial mode of the Fermi sea should be deformed by repulsive interaction with the BEC. This effect should be amplified close to an inter-isotope Feshbach resonance, which are predicted to be large (> 40 Gauss) and at fields of a few 100 Gauss (experimentally achievable) [143].

We tried to reveal the dipolar nature of the Cr Fermi sea by studying Pauli paramagnetism at low magnetic field [137]. Quantum statistics is expected to lead to a very different picture than that obtained for ^{52}Cr. For the boson, as long as the magnetic field is different from zero, a ^{52}Cr BEC is polarized at equilibrium: only the $m_s = -3$ spin component is occupied. Here DDI prevents the other spin states from condensing [97]. For the fermion, at zero magnetic field all spin states are equally populated. When the magnetic energy difference between two Zeeman states is lower than the Fermi energy, atoms with an energy larger than this magnetic energy difference will populate spin excited states through dipolar collisions(in order to minimize total energy). This would be very exciting because it would be a way of measuring the Fermi energy directly and to observe an effect due to Fermi-Dirac statistics. Moreover the physics involved in this experiment is non trivial since it is dictated by the competition between magnetic energy and the Fermi energy. Contact interactions between fermions of different spin states may even play a role. This experiment would be an exploration of the phase diagram of a degenerate dipolar Fermi gas. However, we did

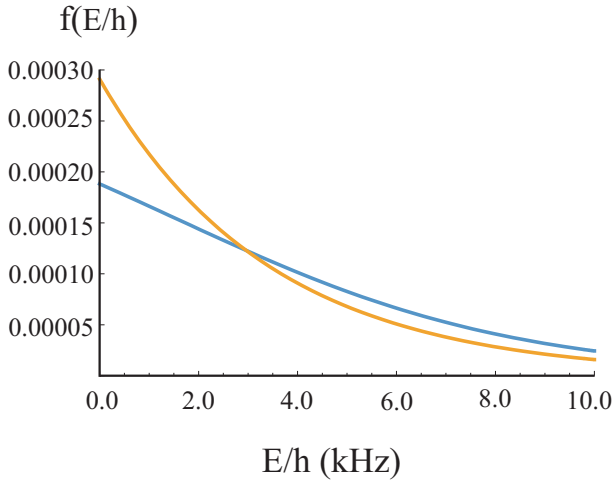

Figure 4.11: Fermi-Dirac (blue) and Boltzmann (orange) distribution for a gas at a temperature T = 0.55 T_f (slightly lower than our experimental temprature) as a function of E/h. When the magnetic field is reduced, it is energetically favourable for fermions with energy larger than the Zeeman energy to change spin state. In order to observe this effect due to the quantum nature of the gas, one must apply external magnetic fields as low as 2 kHz.

not proceed with this experiment because at $T_F/T_f = 0.6$, the Fermi-Dirac distribution and the Boltzmann distribution differ very little (see Fig.4.11). The distributions differ substantially for E/h $\leq$ 2 kHz. This requires that in order to observe a substantial difference between the depolarization expected from a thermal gas or a degenerate gas, we need to control the magnetic energy to the kHz regime which is experimentally challenging. Depolarization due to Boltzmann statistics takes place when the magnetic energy is of the same order as the thermal energy (which depends on the temperature). Depolarization due to Fermi-Dirac statistics takes place when the magnetic energy is of the same order as the Fermi Energy. In our experiment, the Fermi energy and the thermal energy are of the same order. To perform this experiment and observe a clear signature of quantum statistics, lower temperatures (in the $T/T_f \sim 0.2$ regime) are necessary.

In a 3D optical lattice, ^{53}Cr should provide a good platform to study non-equilibrium dynamics, even at relatively high T/T_f. Indeed at low B-field, the XYZ Hamiltonian could be realized [149]. Moreover, due to the quadratic Zeeman shift, the spacing in energy between different spin states is non-degenerate and it would be possible to prepare many different initial, well defined, spin states. This is not the case for the boson where the spacing in energy between different spin states is the same and limits the initial preparation. In an experiment with the boson presented in chapter 8, by introducing an optical quadratic shift, approximately 80% of the atoms in $m_s = -3$ were successfully transferred in $m_s = -2$. For the fermion, with a simple Radio-Frequency

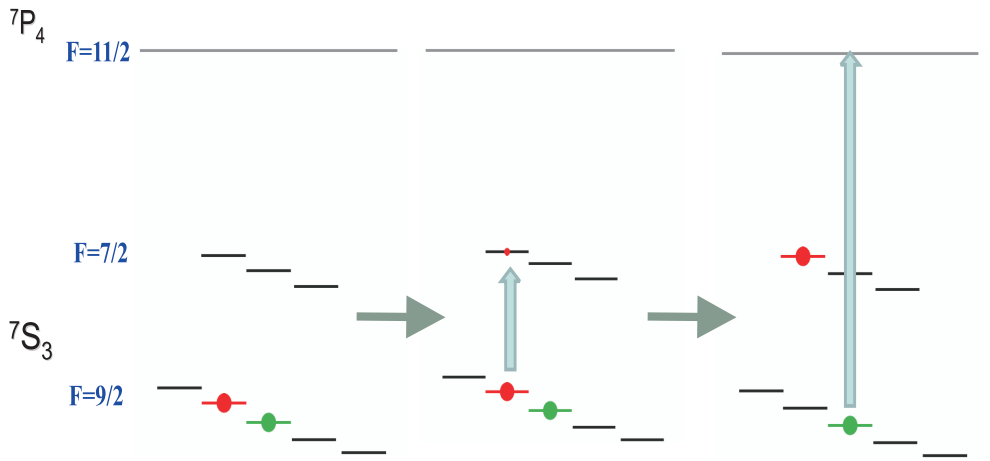

Figure 4.12: Scheme of the experimental procedure to selectively measure a given spin state. In this example, there are two spin states in the electronic ground state. In order to image the "green" spin state, we must first transfer the atoms in the "red" spin state to an other hyperfine state and then apply the imaging pulse.

(RF) pulse, it would be possible to promote approximately 100 % of the atoms in $|F = 9/2, m_F = -9/2 >$ towards $|F = 9/2, m_F = -7/2 >$. From there on, the dynamics from this out-of-spin equilibrium situation should be very intriguing and different from the bosonic case. Here magnetism and transport are coupled due to the Pauli principle (which implies that atoms cannot be in the same site with the same spin state): the tunneling of an atom to a neighbouring occupied site depends on the spin state of the atom pair. If the atoms are in the same spin state, the Pauli principle inhibits this tunneling process.

To perform such an experiment, due to our low atom number we need to be able to measure atoms of a given spin state *in situ*. We are not actually capable of such a procedure. However this could be performed with an RF field. With a well calibrated RF pulse, the desired spin state can be transferred into another hyperfine state which is not resonant with the imaging beam. For imaging a given spin state we could use the following scheme summarized in Fig.4.12: after performing an experiment involving several spin states, one could transfer all atoms of the "unwanted" spin state through a RF pulse to the $|^7S_3, F = 7/2 >$ hyperfine state. Then one can shine the imaging beam on the $|^7S_3, F = 9/2, m_F = -9/2 > \rightarrow |^7P_4, F = 11/2, m_F = -11/2 >$ transition and image only atoms in the spin state not perturbed by the RF pulse. A RF antenna has been installed and characterized recently as part as Lucas Gabardos' master's project [150], and loading fermions in a lattice promises to be an exciting avenue for the group. However, for the remainder of my thesis, we did not perform any more experiments with the fermionic isotope. We focused our attention solely on the bosonic isotope. In the following I will present experiments where we were interested in the thermodynamic properties of a Bose gas with a spin degree of freedom.

CHAPTER 5

Cooling a spinor Bose gas

In this chapter I first recall general results for the thermodynamic properties of a Bose gas with a spin degree of freedom. I then present two experiments. In the first experiment, we rapidly cool a thermal multi-spin component gas across the phase transition for Bose Einstein Condensation. We then study the interplay between internal and external degrees of freedom in order to define which spin state may condense. In the second experiment, we cool a polarized BEC using the spin degree of freedom to store and remove entropy from the BEC.

5.1 Introduction

There is a wide selection of atoms and molecules which have been produced in the ultracold regime. These particles are characterized by both their internal and external degrees of freedom. The first BEC experiments were performed with gases in one internal state and are referred to as scalar BECs. Very soon after, BECs in different internal states were produced and are referred to as spinor BECs. The interplay between the external and internal degrees of freedom in the multi-component systems leads to physics out of reach for scalar BECs. Not all cold gases can be easily adapted to study spinor physics. In order to study the physics of different internal states, the lifetime of each internal state has to be long compared to thermalization processes and the experiment time. Furthermore, the confinement potential must be the same for all the internal states.

Our Chromium gas is particularly well suited for the study of spinor physics. Its relatively large electronic spin s=3 yields the possibility of having a gas in the electronic ground state in 2s+1 different internal spin states. The lifetime of atoms in spin excited states are limited by dipole-dipole relaxation processes which were intensively studied and they can be negligible for sufficiently fast experiments [87]. As for Van der Waals interactions, there are 4 different collision scattering lengths which have the peculiarity of being very different, which lead to intriguing collision dynamics as shown in chapter 3. Here the internal degree of freedom is the projection of the electronic spin (i.e. associated to a Zeeman state). In addition, the confinement potential cannot be a magnetic trap because they are spin dependent. We therefore will use an optical dipole trap.

In this chapter we will first discuss general thermodynamic properties of a Bose

gas with an internal spin degree of freedom. We will then present two experimental results. We first study the interplay between internal and external degrees of freedom of a Bose gas across the BEC transition. We then discuss how we can cool a polarized BEC by storing entropy in spin excited states which are then removed from the trap, thus cooling the sample.

5.2 Thermodynamic properties of a spinor Bose gas

5.2.1 An ideal polarized Bose gas

a) Bose distribution

The quantum statistical description of a non interacting Bose gas is a common subject well described in many books (see for example [137]). The thermodynamic properties of bosons may be derived from the Bose Einstein distribution. Consider a system of N bosons at thermal equilibrium at a temperature T, the Bose Einstein distribution quantifies the average number of atoms $\bar{n}_i$ in state i of energy E_i:

$$\bar{n}_i(\mu, T) = \frac{1}{e^{(E_i-\mu)/k_B T} - 1} \tag{5.1}$$

with μ the chemical potential of the gas. The total atom number satisfies $\sum_i n_i = N$. For a given temperature and atom number, μ is fixed with eq.((5.1)).

In state i, the average occupation necessarily verifies $\bar{n}_i \geqslant 0$. This imposes $\mu \leq E_0 \leq E_i$ where E_0 is the lowest energy level. For the case of an ideal gas we set the energy scale so that E_0=0.

b) Saturation of the thermal gas and critical temperature for BEC

For a fixed value of temperature T, the function describing the number of atoms in excited states ($\sum_{i\neq 0} \bar{n}_i = N_T$) increases with μ and reaches a maximum $N_{T,Max}$ for $\mu = E_0 = 0$. There is an upper limit, for a given temperature, to the number of atoms in excited states. A thermal gas cannot have more than $N_{T,Max}$ atoms. In contrast, there is no upper limit to the number of atoms in the lowest energy level. If a particle is added to a gas with $N = N_{T,Max}$ atoms in excited states, it will necessarily occupy the lowest energy level $i = 0$ (since the number of excited atoms is already maximum). A macroscopic occupation of this state takes place if more particles are added. The macroscopic occupation of the lowest energy state of the system is called Bose Einstein Condensation. When a BEC is present, the chemical potential is μ=0, meaning that it does not cost any energy to add a particle to the BEC.

In literature, the situation when $N_T = N_{T,Max}$ is referred to as *saturation of the thermal distribution*. For a given T, the thermal gas is not saturated if $N_{T,Max} > N \approx N_T$ and a macroscopic occupation of state i =0 cannot take place. On the

other hand, for a given T where $N_{T,Max} < N$, the thermal gas is saturated and $\mu = E_0$=0. There will be $N_T = N_{T,Max}$ particles occupying excited states and $N - N_{T,Max}$ particles occupying the ground state. The critical situation $N_{T,Max} = N$ corresponds to $N_{T,Max} = N_T(T = T_C, \mu = E_0)$ where T_C is the critical temperature. In the case of N non interacting bosons in a 3D harmonic trap (which in practice will apply to most of the experiments presented in this manuscript), the critical temperature has the following form:

$$k_B T_C = \hbar\bar{\omega}\left(\frac{N}{\zeta(3)}\right)^{1/3} \tag{5.2}$$

where $\zeta(s) = \sum_{i=1}^{\infty} \frac{1}{i^s}$ is the Riemann Zeta function, and $\bar{\omega} = (\omega_x\omega_y\omega_z)^{1/3}$ is the geometrical average trapping frequency. In the experiments presented in this thesis, we cross the phase transition for $T_C \sim 400$ nK with typically $N = 10^4$ atoms and $\bar{\omega} = 2 \times \pi$ 330 Hz. For temperatures below T_C in a 3D harmonic trap, the condensate fraction f of N non interacting bosons evolves in the following way with temperature [23]:

$$f = \frac{\bar{n}_0}{N} = 1 - \left(\frac{T}{T_C}\right)^3. \tag{5.3}$$

c) BEC and phase space density

Another description of BEC is through the concept of phase space density. In a de Broglie picture, an atom can be seen as a wave of wavelength the thermal de Broglie wavelength $\lambda_{dB} = \sqrt{\frac{2\pi\hbar^2}{mk_BT}}$ where m is the mass of the atom and k_B is the Boltzman constant. The lower the temperature the longer λ_{dB}. When atoms are cooled to a temperature for which λ_{dB} is comparable to the inter-atomic distance, the atomic waves overlap. At this temperature, the atoms undergo the BEC phase transition. The temperature T_c of this phase transition in a 3D harmonic trap is obtained from solving:

$$n\lambda_{dB}^3 = \zeta(3) \approx 1.202. \tag{5.4}$$

where n is the atomic density. By developing this expression, one retrieves eq.(5.2). This ratio can be seen as the ratio between the particle density and the number of significantly occupied states per unit volume. If this ratio is large, this means that there are lot of particles for a small number of available states. The number of accessible states is proportional to $1/n\lambda_{dB}^3$. Assuming equiprobability of each accessible state, $n\lambda_{dB}^3$ represents the probability of occupying one of these states (the ground state for example). When a BEC forms, $n\lambda_{dB}^3 \sim 1$ and only one state becomes accessible, the ground state of the trap.

d) Critical entropy for BEC

It is interesting to recast the phenomenon of BEC in terms of the existence of a critical entropy Σ_c. The entropy per particle Σ/N of a mono-atomic classical gas of N particles at $T > T_C$ is:

$$\frac{\Sigma}{Nk_B} = \frac{3}{2} - \log(n\lambda_{dB}^3). \tag{5.5}$$

This classical expression for entropy is called the Sackur-Tetrode equation [137]. Even though this is a classical expression, we can already notice that a different behaviour of entropy takes place depending on the relative sign of $\log(n\lambda_{dB}^3)$. Entropy has two regimes: it can be larger or smaller than 3/2.

For an ideal gas of N particles in a box, the entropy Σ of a gas at $T < T_C$ is inversely proportional to the phase space density [137]:

$$\frac{\Sigma}{N} = \frac{5}{2}k_B \frac{1}{n\lambda_{dB}^3} g_{5/2}(1) \tag{5.6}$$

where $g_n(1)$ is the polylogarithmic functions defined as $g_n(z) = \sum_{k>0} z^k/k^n$. From eq.(5.6), we see that Σ =0 at T=0, in agreement with the third law of thermodynamics. This means that the condensed phase has no entropy. At any finite temperature, the total entropy is entirely due to particles in excited states. The fraction of particles in excited states (or thermal fraction) is $f_{th} = \frac{N_T}{N} = (\frac{T}{T_C})^3$. For $T < T_C$, we can write the entropy for a 3D harmonic trap in the following way [23]:

$$\begin{aligned} \frac{\Sigma}{N} &= 4 \times \frac{g_4(1)}{g_3(1)} k_B \left(\frac{T}{T_C}\right)^3 \\ &= \underbrace{4 \times \frac{g_4(1)}{g_3(1)} k_B}_{\Sigma_c} f_{th} \\ &= \Sigma_c f_{th} \\ &\simeq 3.6 k_B f_{th} \end{aligned} \tag{5.7}$$

with Σ_c homogeneous to an entropy and that we shall now identify as the critical entropy. At $T < T_C$, each thermal atom carries an entropy equal to Σ_C. A gas with entropy $\Sigma < N\Sigma_c$ has necessarily a condensed phase. On the other hand, a gas with $\Sigma > N\Sigma_c$ has no condensed phase. It is interesting to realize that Σ_c has a universal character since it depends only on the dimensionality of the gas, and is independent of temperature or trapping parameters such as the trapping frequency ω. In that sense, entropy is the correct figure of merit in order to characterize a gas.

5.2.2 An ideal multicomponent Bose gas

The existence of an internal spin degree of freedom modifies the thermodynamic properties of a Bose gas. We shall call N_i the population in spin state $m_s = i$ and N_{Tot} the

total atom number. For a gas of spin s we have:

$$N_{Tot} = \sum_{i=-s}^{s} N_i. \tag{5.8}$$

We denote as n_0^i and N_{th}^i the number of condensed and thermal atoms in spin state i:

$$N_i = n_0^i + N_{th}^i. \tag{5.9}$$

The magnetisation M of the gas is related to how the different spin states are occupied. The relative magnetization of the BEC and of the thermal gas read respectively:

$$\begin{aligned} M_{BEC} &= \sum_{i=-s}^{s} \frac{i n_0^i}{n_0^{Tot}} \\ M_{th} &= \sum_{i=-s}^{s} \frac{i N_{th}^i}{N_{th}^{Tot}} \end{aligned} \tag{5.10}$$

with n_0^{Tot} the total number of condensed atoms and N_{th}^{Tot} the total number of thermal atoms ($n_0^{Tot} = \sum_{i=-s}^{s} n_0^i$ and $N_{th}^{Tot} = \sum_{i=-s}^{s} N_{th}^i$). We can then define the total relative gas magnetization as:

$$M = \sum_{i=-s}^{s} \frac{i N_i}{N_{Tot}}. \tag{5.11}$$

The interaction between the spin and the magnetic field gives rise generally to a Zeeman energy term which comprises a linear term and a quadratic term. For an atom of spin s and quadratic shift q_B in a magnetic field B, the Zeeman energy term writes:

$$E_Z(m_s) = m_s g_{Landé} \mu_B B + q_B m_s^2 B^2 \tag{5.12}$$

with $g_{Landé}$ the Landé factor and μ_B the Bohr magneton. The quadratic Zeeman shift arises from the interaction between the nuclear spin and the electronic spin. Thus atoms with no nuclear spin, such as ^{52}Cr, do not have a magnetic quadratic Zeeman effect. However, an optical quadratic effect can be induced by the optical trapping potential. This optical quadratic term can be particularly large for Chromium[1] due to its specific fine structure [151]. The strongest contribution term of the AC Stark shift is scalar and for large detunings is the well known light shift term responsible for optical dipole traps [152]. The following contributions to the optical potential are tensorial. For large magnetic fields, we may consider only the diagonal contributions which are of the form $q_{LS} m_s^2$. In the following we will write the quadratic contribution to the energy as $q m_s^2$ which can be either of magnetic or optical origin.

[1] For the experiments presented in this chapter with Chromium, we estimate that $q_{LS} \sim 10$ Hz and will not play a significant role.

The scalar Bose distribution (i.e. bosons with just one spin state eq.(5.1)) for non-condensed atoms can be generalized to include different Zeeman states in the following way:

$$N_{th}^{ms} = \sum_{i \neq 0} \frac{1}{e^{\beta(E_i + E_z(m_s) - \mu)} - 1} \tag{5.13}$$

with $E_i + E_z(m_s)$ the energy of a particle in excited state i, which depends on the spin state m_s with $E(m_s) = m_s g_{Landé} \mu_B B + q m_s^2$.

In the following, we shall discuss the general thermodynamic properties of an ideal spinor gas depending on the existence of the quadratic term[2] q and the fact that total magnetization M is constant or not. In the next section we will discuss how the presence of interactions modify the ideal picture presented below. For each situation, it is important to pinpoint the constraints on the system. Each constraint will be fixed via a Lagrange multiplier (as was the case for μ which is related to the constraint on the total atom number). When magnetization is fixed the Lagrange multiplier will be identified as a magnetic chemical potential. We then may derive properties for each spin component at thermodynamic equilibrium.

The reader must not be confused about neglecting interactions but still discussing thermodynamic equilibrium properties. Based on the discussion in chapter 3, we are considering the case $\Gamma_{inc} > \Gamma_{coh}$, for which collisions occur on a timescale much faster than that required for interaction energy terms to play a significant role.

a) Fixed magnetization

The constraint of fixed magnetization can be taken into account by setting a Lagrange multiplier. This Lagrange multiplier sets the magnetization and fixes an effective magnetic field B_{eff} which gives to the atoms an effective Zeeman energy [153]:

$$E_i^{Mag} = i g_{Landé} \mu_B B_{eff} \tag{5.14}$$

$$\text{so that } \mu_i = \mu - E_i^{Mag}. \tag{5.15}$$

In the following, we will discuss the behaviour of an ideal multi-spin component gas of spin $s = 1$, with fixed magnetization at spin equilibrium[3]. Here the only spin changing process are associated to (m_s=0,m_s=0) $\longleftrightarrow$ (m_s=+1,m_s=-1). The Zeeman energy does not intervene when dealing with magnetization collisions and we may omit the Zeeman energy when at fixed magnetization.

We will now discuss which are the different processes which will define which spin state may condense, when no quadratic shift is present and then with a quadratic shift.

[2] Even if q can be negative, we will only discuss $q \geq 0$ which leads to a larger qualitative difference than $q < 0$

[3] In order to simplify the discussion we do not explicitly discuss the example of a $s = 3$ gas, which has the same general behaviour in the ideal case than the $s = 1$ gas.

α) No quadratic shift (q=0)

Let us consider the case with no quadratic shift and a negative magnetization. The energy necessary to add a particle in state $m_s = 0$ is μ_0 the chemical potential of spin state $m_s = 0$. The energy necessary to add a particle in state $m_s = -1$ is the chemical potential μ_{-1}, and differs from μ_0 by the effective Zeeman energy:

$$\mu_{-1} = \mu_0 + g_{Landé}\mu_B B_{eff}. \tag{5.16}$$

In the same manner to add a particle in state $m_s = +1$, one needs the energy:

$$\mu_{+1} = \mu_0 - g_{Landé}\mu_B B_{eff}. \tag{5.17}$$

In general for a spin s we have:

$$\mu_i = \mu_{-s} - (i+s)g_{Landé}\mu_B B_{eff} \tag{5.18}$$

for $i \in [-s, s]$. As the gas is cooled the internal chemical potential of each spin state will grow and μ_{-s} will reach 0 first for a critical temperature (referred to as T_{C1}). Thus a BEC in $m_s = -s$ forms. As the gas is cooled further, the chemical potential of the second-to-lowest spin state will reach zero (B_{eff} is free to evolve in order to fix the total magnetization) for a second critical temperature (referred to as T_{C2}). Eq.(5.18) then imposes that all chemical potential must be zero (B_{eff} is equal to zero): all other spin states condense simultaneously [153]. There are two phase transitions, even if $2s + 1$ spin states are present.

In the case $M = 0$ at thermal equilibrium, all spin states are equally occupied. It costs the same energy for a particle to be in any spin state, $B_{eff} = 0$ and each spin state has the same chemical potential. In that case, as the gas is cooled the chemical potential of each spin state will reach zero simultaneously and there will be a BEC in each spin state (the two phase transitions coincide).

β) Quadratic shift q>0

Most atoms, and in particular alkali atoms, have a nuclear spin, and therefore a non zero magnetic quadratic shift (q≠0). It is interesting to study how the introduction of the quadratic shift changes the result above. When the nuclear spin $\hat{I}$ is different from 0, it is convenient to work in the total angular momentum basis $\hat{F}$ defined as:

$$\hat{F} = \hat{I} + \hat{J} \tag{5.19}$$

where $\hat{J}$ is total electron angular momentum.

Let's discuss the example of a spin F=1 gas, with fixed magnetization. The presence of the quadratic energy changes the equality eq.(5.18). The energy to add a particle in spin state $m_F = 0$ is μ_0. The energy necessary to add a particle in state $m_F = -1$ is equal to the energy to add a particle in $m_F = 0$ minus the effective Zeeman and

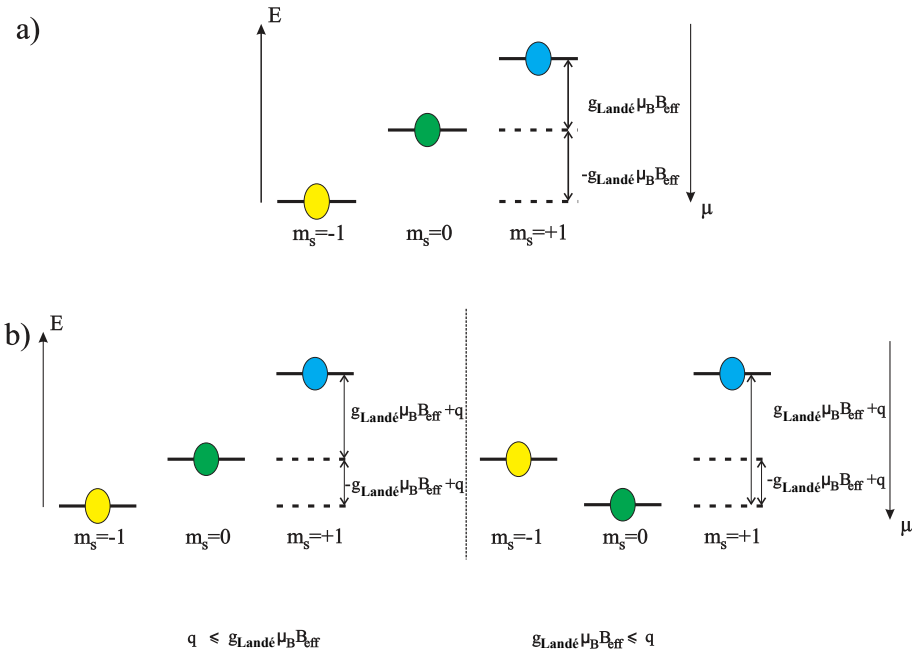

Figure 5.1: Sketch illustrating the energy scale for a spin $s = 1$ atoms, at fixed magnetization which introduces an effective magnetic field B_{eff} (see text), for a) no quadratic shift, b) a non zero quadratic shift.

quadratic energy difference between the two. We may then write the chemical potential of each spin state:

$$\begin{aligned} \mu_0 &= \mu_0 \\ \mu_{-1} &= \mu_0 + g_{Landé}\mu_B B_{eff} - q \\ \mu_{+1} &= \mu_0 - g_{Landé}\mu_B B_{eff} - q. \end{aligned} \tag{5.20}$$

To make predictions on which states may condense, we will distinguish two scenarios depending on the relative values of $g_{Landé}\mu_B B_{eff}$ and q.

In a first scenario, let us consider the case where the most populated thermal state is $m_F = -1$: set by $q \leq g_{Landé}\mu_B B_{eff}$. Here, it is $m_F = -1$ which has the largest chemical potential, then $m_F = 0$ (see eq.(5.20)). As the gas is cooled the internal chemical potential of each spin state will grow and μ_{-1} will reach 0 first for a critical temperature T_{C1}. Thus a BEC in $m_F = -1$ forms. Reducing the temperature further, there will be a second critical temperature T_{C2} where $\mu_0 = 0$ and the $m_F = 0$ component will condense. As soon as $\mu_0 = 0$, eq.(5.20) imposes:

$$\mu_{+1} = -2q < 0. \tag{5.21}$$

The chemical potential of spin state $m_F = +1$ will never reach zero (we considered $q > 0$), therefore a BEC will not form in m_F=+1 even if cooling proceeds.

In a second scenario, let us consider the most populated thermal state to be $m_F = 0$: set by $q \geq g_{Landé}\mu_B B_{eff}$. Here, it is $m_F = 0$ which has the largest chemical potential, then $m_F = -1$ (see eq.(5.20)). As the gas is cooled the internal chemical potential of each spin state will grow and μ_0 will reach 0 first for a critical temperature T_{C1}. Thus a BEC in $m_F = 0$ forms. Reducing the temperature further, there will be a second critical temperature T_{C2} where $\mu_{-1} = 0$ and the m_F = -1 component will condense. As soon as $\mu_{-1} = 0$, eq.(5.20) imposes:

$$\mu_{+1} = -2q < 0. \tag{5.22}$$

A BEC will not form in m_F=+1: μ_{+1} will never reach zero even if cooling proceeds.

If we had considered the case $M > 0$, we find the same results under the exchange of $m_F = -1$ with $m_F = +1$.

This result differs substantially from the case q=0, there underneath the second critical temperature all spin components condensed simultaneously. For $q \neq 0$ not all spin components will condense and depending on the relative values of $g_{Landé}\mu_B B_{eff}$ and q it is not the same spin state which will condense first.

b) Free magnetization

We now consider the case where magnetization is not conserved. As illustrated in subsection 3.1.2, Dipole Dipole collisions have collisional channels which allow the magnetization of the gas to vary. There is no effective magnetic field which fixes magnetization, which is instead fixed by the real external magnetic field B and the temperature T of the gas.

α) No quadratic shift (q=0)

Let us first consider the case $q = 0$ for an $s = 1$ atom. Here magnetic energy consists only of the linear Zeeman term. The energy to add a particle in state $m_s = 0$ is simply μ_0. The energy necessary to add a particle in state $m_s = -1$ is the chemical potential μ_{-1}, and differs from μ_0 by the Zeeman energy. We have for each spin state:

$$\begin{aligned} \mu_0 &= \mu_0 \\ \mu_{-1} &= \mu_0 - g_{Landé}\mu_B B \\ \mu_{+1} &= \mu_0 + g_{Landé}\mu_B B \end{aligned} \tag{5.23}$$

where B is the external magnetic field. For a spin s, we therefore have:

$$\mu_i = \mu_{-s} - (i+s)g_{Landé}\mu_B B \tag{5.24}$$

for $i \in [-s, s]$.

If the external magnetic field is exactly zero, the chemical potentials of each spin states are equal. As the gas is cooled, all chemical potentials will increase in the same

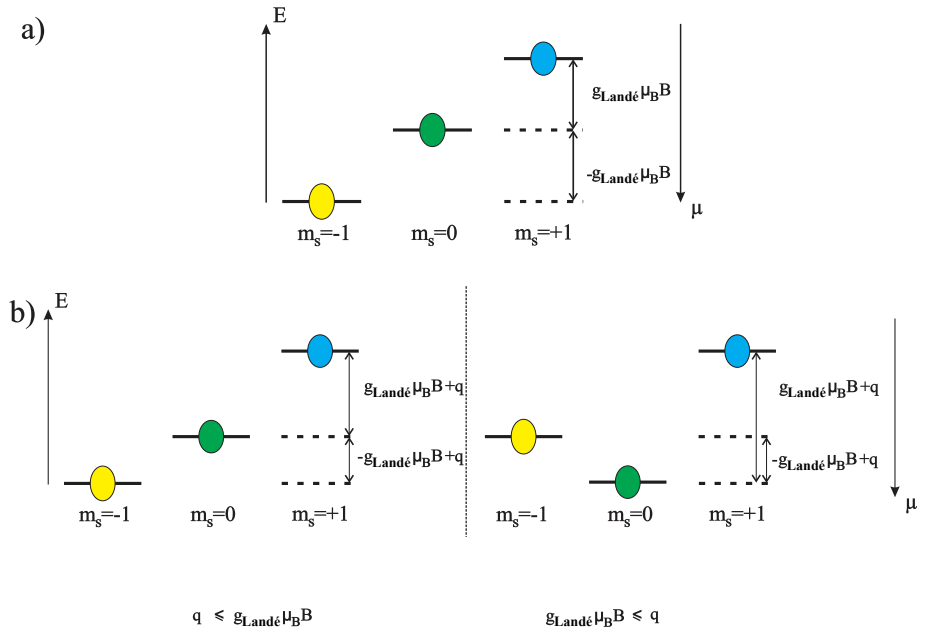

Figure 5.2: Sketch illustrating the energy scale for a spin s=1 atoms, at free magnetization, for a) no quadratic shift, b) a non zero quadratic shift. It is the same as for Fig.5.2 except that here B is the external magnetic field and not an effective magnetic field (see text).

manner and reach zero simultaneously: a BEC will form simultaneously in all spin states.

In experiments, B is always finite and imposes that μ_{-s} is the highest chemical potential. As the gas is cooled, μ_{-s} will reach zero at a certain temperature and $m_s = -s$ will condense. However eq.(5.24) reveals that for a finite B, the other chemical potentials will never reach zero: there is no second phase transition. The BEC remains polarized.

β) Quadratic shift q>0

Let us now consider the case $q \neq 0$. We must now take into account the quadratic energy term. Even though Chromium has no magnetic quadratic Zeeman energy, it is sensitive to the optical quadratic effect induced by the optical dipole trap. Again, μ_0 is the energy to put a particle in spin state $m_s = 0$. We may then write the chemical potentials associated to all spin states:

$$\begin{aligned} \mu_0 &= \mu_0 \\ \mu_{-1} &= \mu_0 + g_{Landé}\mu_B B - q \\ \mu_{+1} &= \mu_0 - g_{Landé}\mu_B B - q. \end{aligned} \tag{5.25}$$

To make predictions on which states may condense, we will distinguish two scenarios depending on the relative values of $g_{Landé}\mu_B B$ and q.

In a first scenario, let us consider the case where the most populated thermal state is $m_s = -1$. We then have $q < g_{Landé}\mu_B B$. Here, it is $m_s = -1$ which has the largest chemical potential, then $m_s = 0$ (see eq.(5.25)). As the gas is cooled the internal chemical potential of each spin state will grow and μ_{-1} will reach 0 first for a critical temperature. Thus a BEC in $m_s = -1$ forms. However eq.(5.25) reveals that for a finite B, the other chemical potentials will never reach zero: there is no second phase transition. For a spin s gas, we have the same behaviour except that it is in spin state $m_s = -s$ that the BEC forms.

In a second scenario, let us consider the case where the most populated thermal state is $m_s = 0$. We then have $q > g\mu_B B$. Here, it is $m_s = 0$ which has the largest chemical potential, then $m_s = -1$ (see eq.(5.25)). As the gas is cooled the internal chemical potential of each spin state will grow and μ_0 will reach 0 first for a critical temperature. Thus a BEC in $m_s = 0$ forms. For a finite B, the other chemical potentials will never reach zero: there is no second phase transition. For a spin s gas, we have the same behaviour.

In the case of free magnetization, only one spin state may condense. The presence of q may however alter which spin state condenses.

5.2.3 Ground state in presence of interactions

The ideal picture presented above is modified by the inclusion of interactions between atoms. When dealing with interactions, one can distinguish two parts: one spin dependent and one spin independent. In the following we shall focus only on the spin dependent interactions and on how the ideal picture is modified.

a) Fixed magnetization

The mean field ground state spinor wave function of an F=1 with fixed magnetization gas is found by minimizing the free energy [154]:

$$K = \int d^3rn[V + \frac{c_0 n}{2} + \frac{c_2 n}{2} < \vec{F} >^2 + < H_q > -\tilde{p} < F_z >] \tag{5.26}$$

where the kinetic energy was neglected here, V is the trapping potential, n is the density, $< \vec{F} >=< \xi|\vec{F}|\xi >$ where $\vec{F}$ is the angular momentum per atom and ξ is the spinor part of the wavefunction, and $< \xi|H_q|\xi >$ is the quadratic Zeeman energy in an external magnetic field. $\tilde{p}$ is a Lagrange multiplier which accounts for conservation of magnetization ($\tilde{p} = g_{Landé}\mu_B B_{eff}$). The mean field energy in eq.(5.26) consists of a spin independent part proportional to c_0 and a spin dependent part proportional to $c_2 < \vec{F} >^2$ with $c_2 = \frac{4\pi\hbar^2}{m}\frac{a_2 - a_0}{3}$. The ground state of a spinor gas will minimize K for a given $\tilde{p}$, $< H_q >$ and c_2. The minimization of eq.(5.26) will drastically depend on the sign of c_2.

α) Anti-ferromagnetic interactions $a_2 > a_0$

Let us discuss the results for a mean field ground state at $T = 0$ in the case $q = 0$ and $a_2 > a_0 > 0$. If $a_2 > a_0$, collisions through the $S = 0$ molecular potential will be energetically favourable (because they lead to less repulsion) which corresponds to anti-ferromagnetic interactions. In zero magnetic field, the condensate lowers its energy by minimizing its average spin, i.e. by making $| < \vec{F} > | = 0$. This can be achieved for a spinor $\xi = (0, 1, 0)$. All spinors obtained by a rotation of ξ minimize also eq.(5.26). ξ corresponds to a degenerate set of spinors, the polar states, corresponding to all possible rotations of the hyperfine state $|m_F >= 0$: $\xi = U(\alpha, \beta, \tau) \begin{pmatrix} 0 \\ 1 \\ 0 \end{pmatrix}$ with $U(\alpha, \beta, \tau) = e^{-iF_x\alpha} e^{-iF_y\beta} e^{-iF_z\tau}$ where (α, β, τ) are the Euler angles [154].

Let us now discuss the cooling of a thermal gas at non zero magnetic field. For $M < 0$, below the first critical temperature a condensate will appear in the most populated state, namely $m_F = -1$ as in the ideal case. Below the second critical temperature, a condensate will also appear in $m_F = +1$. The $m_F = 0$ condensate component never shows up in the limit $a_0 + 2a_2 >> a_2 - a_0$. This is a different result from the ideal Bose system where all three components appear at lower T [153].

The presence of a quadratic shift q changes this picture since it tends to advantage the condensation of $m_F = 0$ spin component. The phase diagram here is dependent on q and the magnetization of the gas [155, 156, 157].

β) Ferromagnetic interactions $a_0 > a_2$

If $a_2 < a_0$, collisions through the $S = 2$ molecular potential will be energetically favoured which corresponds to ferromagnetic interactions. Even in the case of zero field, the condensate lowers its energy by maximizing its average spin, by making $| < \vec{F} > |=1$ [154].

Within the assumption that all spin states share the same spatial wave function (this approximation is called the Single Mode Approximation), below the first critical temperature a condensate will appear in the most populated state namely $m_F = -1$. Below the second critical temperature, the condensate will form in state $|m_F = -1 >_\theta$, which is $m_F = -1$ in the basis associated to any angle θ fixed in order to have the right magnetization. It is also proposed that below the second critical temperature a phase separation could take place between the existing $m_F = -1$ condensate and the "new" $m_F = +1$ condensate [153] and maybe then lead to triple condensation [158].

b) Free magnetization: the case of Cr

Due to its large spin, Chromium features non negligible dipole-dipole interactions which free the magnetization, no magnetic quadratic Zeeman effect, and 4 different scattering lengths. This leads to a very rich phase diagram. Santos and Pfau [100] (as well as

Ho and Diener [159]) studied the phase diagram for Cr shown Fig.5.3. The different regions show the possible phases, depending on the B-field (represented by $\tilde{p}$ in their study) and on the g_0/g_6 ratio (unknown at the time). In addition to the ferromagnetic and polar phases also predicted for spin 1 atoms, new phases such as the cyclic phase are predicted. A large variety of cyclic phases are predicted, each with different spin components which may condensed (indices represented in Fig.5.3) and with a specific phase relations between the condensed spin components (see also [155]). We will discuss

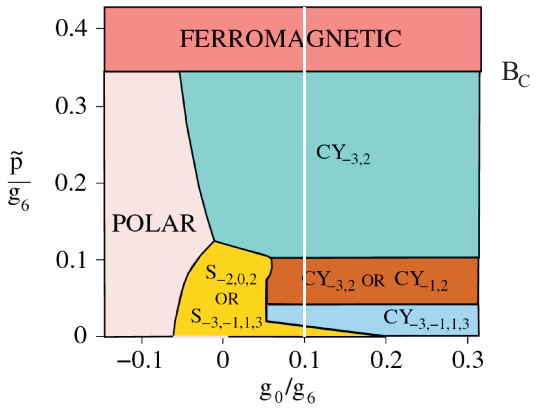

Figure 5.3: Chromium phase diagram adapted from [100]. It gives the ground state for a spinorial Cr BEC, depending on the value of a_0 (unknown at the time the diagram was performed) and the magnetic field relative to contact interaction through the S=6 molecular potential $\tilde{p}/g_6$. The white solid line corresponds to the value deduced from our experimental measurement of a_0 in chapter 3. Here $\tilde{p} = g_{Landé}\mu_B B$.

in the following that depending on the relative value of the Zeeman energy compared to spin dependent energy terms, two different behaviours are obtained.

We define a critical magnetic field B_C for which the Zeeman energy is equal to the spin dependent contact energy. For Chromium, the critical magnetic field has a complicated expression and involves a linear combination of several scattering lengths (namely a_6, a_4,and a_2) [160]. Typical experimental values lead to $B_c \approx 200$ μG and it is challenging to achieve lower experimental magnetic fields.

α) High magnetic field (B >> B_C)

At high magnetic field (i.e $B >> B_C$), the ground state is a ferromagnetic state (Fig.5.3). Therefore below a critical temperature the lowest Zeeman energy state condenses, and no other spin state will condense. The BEC is polarized. Atoms in excited spin states are necessarily thermal atoms and a second phase transition is avoided. This result is similar to what would be expected from Bose thermodynamics at free magnetization section 5.2.2b)α).

β) Low magnetic field (B << B_C)

Now let us consider the case of an experiment performed at low magnetic fields (i.e $B < B_c$).

After the first phase transition, we have a BEC in m_s = -3. However, the ground state is no longer a ferromagnetic state (Fig.5.3) and the gas has no reason to remain polarized. If cooling is continued, below a second critical temperature the gas enters a spinorial phase where different spin states condense. With our newly measured value of $a_0 = 13.5 \pm 11 a_B$, we have $g_0/g_6 \approx 0.13 \pm 0.1$: the ground state is expected to be Cyclic.

c) Previous experimental study of the chromium phase diagram

The phase diagram with free magnetization has been studied with Chromium by our group before my thesis work and the explored phase diagram will help us illustrate the different phenomena [97]. The phase diagram of a spin s=3 gas is shown Fig.(5.4). There are 3 distinct phases. Phase A corresponds to a thermal gas in each Zeeman component; Phase B to a BEC only in $m_s = -3$; Phase C to a BEC in all spin states[4].

The vertical line corresponds to an exploration of the phase diagram at very low magnetic field. In that case for high enough temperature the magnetization M remains close to zero. At high temperature, we have a thermal gas in each Zeeman component. As the temperature is reduced, the chemical potential of the lowest Zeeman state reaches 0 at a first critical temperature: a BEC is formed in $m_s = -3$. As the temperature is further lowered, below a second critical temperature we enter phase C where all other spin components condense simultaneously [99]. This double phase transition was not clearly observed in the experiment (and could be investigated in future studies) however a multi-spin component BEC was produced.

The second line corresponds to the case of $B > B_C$. At high temperature, phase A is obtained with a thermal gas in each Zeeman component. As the temperature is reduced, a BEC is formed in $m_s = -3$ as the first critical temperature is crossed. The gas then spontaneously polarizes itself. And even if cooling proceeds, the second phase transition is avoided and phase C is avoided [97].

d) Experimental study performed in this thesis

In the following we will present two experiments motivated by our understanding of the thermodynamic properties of a Chromium gas.

As mentioned above, it is experimentally difficult to enter phase C of the phase diagram since it requires working with $B < B_c$. One route we will explore in the next chapter is to prepare a multi-spin component gas with magnetization M > -3 in

[4]In this chaper, we will abusively call this transitory state with a BEC in all spin states as a phase even though it is not a stable phase. For Chromium, we expect the ground state stable phase at $T = 0$ to be cyclic.

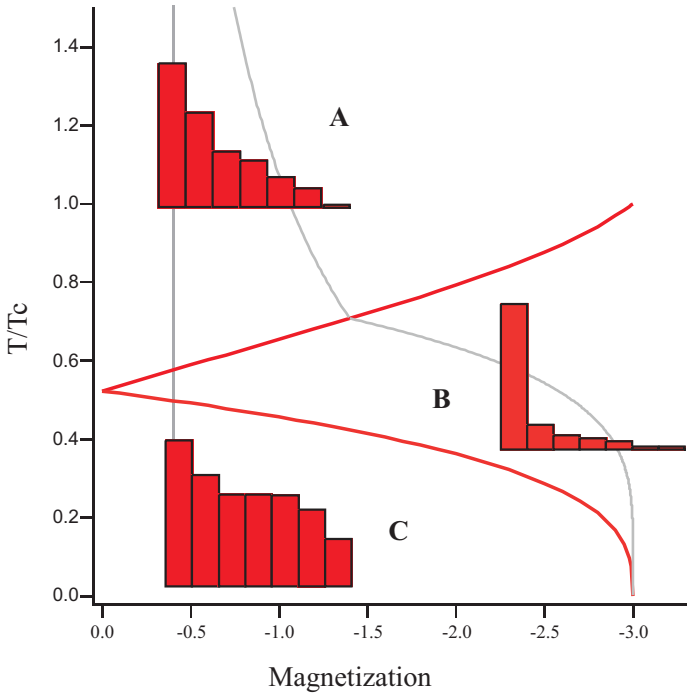

Figure 5.4: Phase Diagram of a Spin 3 gas. The solid lines delimitate the 3 phases predicted for a non interacting gas of bosons. Phase A: thermal gas in each Zeeman component. Phase B: BEC only in $m_s = -3$. Phase C: BEC in all Zeeman components. The histograms represent typical experimental population distributions. The vertical gray line corresponds to an experiment performed with $B < B_C$. In that case, in practice, the magnetization M is always close to zero. The other gray line corresponds to the case with $B > B_C$, then magnetization is free. Image adapted from [97]

phase A with $B > B_c$, and reduce the temperature quickly compared to magnetization dynamics. The goal is to determine whether it is possible to enter phase C, and therefore to obtain a metastable spinorial BEC.

In section 5.4, we will take advantage of the fact that at $B > B_C$, BEC occurs only in $m_s = -3$: any atom in a spin state $m_s \neq$-3 is necessarily a thermal atom (whereas atoms in $m_s =$-3 can be thermal or condensed atoms). Thermal atoms carry all the entropy of the gas. We therefore implemented a trap loss mechanism specific to $m_s \neq$-3 atoms in order to remove efficiently entropy from the gas and thus purify the $m_s = -3$ BEC.

5.3 Shock cooling a multi-component gas

In the following section, we present a joint experimental and theoretical effort to understand the spin dynamics resulting from a rapid quench across the Bose Einstein transition of a multi spin component gas.

5.3.1 Motivation

This work studies the dynamics of BEC in presence of a spin degree of freedom, and it is closely related to early research on the dynamics of BEC for a polarized gas. After the first Bose-Einstein condensates were obtained, Miesner et al. investigated how the BEC nucleates [161]. They measured in real time the formation of the BEC as the temperature was reduced across the phase transition. They found that the formation of the condensate is a Bose stimulated process. More recently, in a quasi-two-dimensional box trap experiments performing a temperature quench below the superfluid transition investigated the dynamics of spontaneous symmetry breaking and revealed the production of long-lived topological defects [162, 163]. The number of topological defects created as a function of the quench parameters is predicted to follow universal laws.

This work extends the dynamical studies of Bose-Einstein condensation to the case of a multi-component Bose gas, in order to establish the mechanisms to reach both superfluid and magnetic orders. We present an experiment aiming to study the out-of-equilibrium properties of a spin 3 gas and determine if a multicomponent BEC can be produced. To do so, we prepare a thermal multi-spin component gas at a given magnetization and rapidly cool the gas across T_C at a magnetic field B $> B_C$. At fixed magnetization, a spinor BEC should be produced. At free magnetization, the BEC is polarized (phase B). If the cooling is performed fast compared to magnetization dynamics, the experiment could show how the gas may relax from phase C to phase B due to dipole-dipole interactions (see Fig.5.4).

We find that the dynamics of Bose-Einstein condensation is affected by spin-changing collisions arising from relatively strong spin-dependent interactions. Thermalization of the spin degrees of freedom is influenced by the occurrence of BEC, and in turns influences which multi-component BECs can be produced. In practice, phase C is barely reached. This is not due to dipole-dipole interactions (as was the case in [97]) but to spin exchange mechanisms and a lack of spin thermalization.

5.3.2 Experimental protocol for a multi-component gas with M=-2.50±0.25

a) Preparation of a thermal multi-spin component gas

Our experiment starts with a thermal gas of 1.5×10^4 ^{52}Cr atoms in an ODT, at $T = 1.1 \times T_c = (440 \pm 20)$nK. The trapping frequencies are $\nu^i_{x,y,z}$=(288,335,410) Hz.

The thermal gas is initially polarized in the Zeeman lowest energy state $m_s = -3$. The initial magnetisation is M=-3. To prepare a mixture of thermal gases in different spin states, we adiabatically reduce the magnetic field B to a small value such that the Zeeman energy is of the same order as the thermal kinetic energy of the gas. The magnetic field is calibrated by Radio-Frequency spectroscopy. Experimentally the field is reduced to B_{exp}= 1.5 ± 0.3 mG. Depolarization of the cloud is spontaneously driven by magnetization-changing collisions associated to dipole-dipole interactions as shown in Fig.5.5 [97, 113]. The initial peak density is $n_0 \sim 10^{19}$ at.m^{-3} and we estimate the

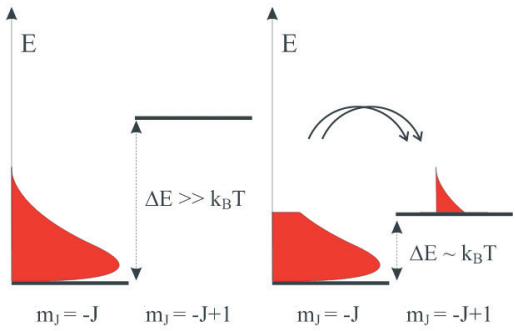

Figure 5.5: Sketch illustrating spin preparation. Image adapted from [113]. We prepare a thermal gas in $m_s = -3$ at high magnetic field ($g_{Landé}\mu_B B >> k_B T$). The magnetic field is then reduced so that $g_{Landé}\mu_B B \sim k_B T$. $m_s > -3$ atoms are spontaneously produced by magnetization-changing collisions associated to dipole-dipole interactions. In the figure, the final step where atoms of each spin state rethermalize.

timescale τ_{dip} associated to dipole-dipole collisions to be:

$$\begin{aligned} \tau_{dip} &\sim \frac{1}{n_0 \sigma_{dip} v} \\ &\sim 1 \text{ s} \end{aligned} \tag{5.27}$$

Once $B = B_{exp}$, we wait for 1.5 s for dipole-dipole collisions to take place in order to obtain a gas at spin equilibrium. Magnetization is a function of the applied external magnetic field and temperature. Using eq.(5.10) and eq.(5.13), we can express $M(B,T)$:

$$M(B,T) = \frac{1}{N_{tot}} \sum_{i=-s}^{s} i \times N_{th}^{i}(B,T) \tag{5.28}$$

with N_{th}^{i} the number of thermal atoms in spin state i and $N_{tot} = \sum_{i=-s}^{s} N_{th}^{i}$ the total atom number. At a magnetic field of B = 1.5 mG, we expect a magnetization of M = -1.6. This is far from our experimentally measured magnetization of $M = -2.50 \pm 0.25$.

We ascribe such a difference to an underestimation of the atom number in spin states $m_s >$ -3 and that spin was not completely thermalized. We know that our imaging process is only perfectly resonant for m_s =-3. When we performed this experiment, we did not calibrate the efficiency of our measurement of higher excited spin states. Therefore we do not know how to count efficiently the number of atoms in spin excited states. We focused our analysis on the populations in m_s = -3, m_s = -2 and m_s = -1. In a later experiment (discussed in chapter 8), the absorption coefficient for each spin state was measured. This coefficient was very close to 1 for m_s = -2 and typically 1.4 for m_s = -1. Therefore our measurement of the absolute population in m_s= -1 is probably underestimate by 40 %, however the population in m_s=-2 is well accounted for. In the following, our analysis will focus on spin states $m_s = -3$ and $m_s = -2$, for which no corrective absorption coefficients are needed. The initial (uncorrected) measured populations are:

$$\begin{aligned} N_{-3} &= 7000 \pm 700 \\ N_{-2} &= 5000 \pm 500 \\ N_{-1} &= 2000 \pm 200. \end{aligned}$$

The initial population in states $m_s > -1$ are negligible.

b) Shock cooling and measurement

We then quickly and adiabatically reduce the trap depth to the final trap frequencies $\nu^f_{x,y,z}$=(166,195,235) Hz. In a normal evaporation sequence, this would correspond to the "end of evaporation" see Fig.1.8. The trap depth is reduced by applying a linear ramp to the voltage control of the trapping laser AOM. Due to the AOM transfer function, the trapping frequency ramp is not perfectly linear. However, for our experimental parameters, there are barely any differences between a linear ramp and the actual ramp. In the following we shall therefore consider the ramp as linear.

The laser intensity is reduced so that the trapping frequencies go from ν^i to ν^f in a time t_S, resulting in fast forced evaporative cooling of all Zeeman states. In the following, we will refer to this evaporation ramp as "shock cooling" (see Fig.5.6) because (i) in a normal evaporation sequence there is 2 s between the two values of trapping frequencies ν^i and ν^f, whereas here we will be dealing with shorter times, and (ii) because the cooling process is non adiabatic with respect to magnetization physics as long as the experiment time $t \leq \tau_{dip}$.

After a time t (which can be smaller than t_S), we turn off the dipole trap and study spin dynamics and condensation by measuring both the spin and momentum distributions after a 6 ms Time Of Flight (TOF). The different spin components are separated via a magnetic field gradient pulse present during the TOF (as explained in subsection 1.5.2). As an example, we show in Fig.5.7 the total atom number as a function of time for a shock cooling time t_S = 500 ms. The final total atom number

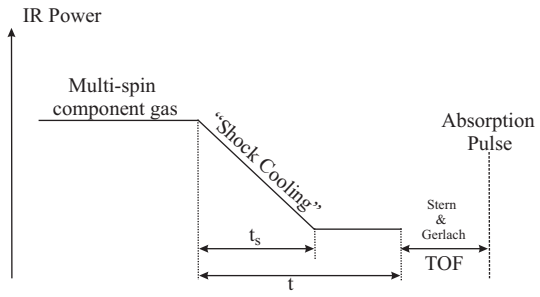

Figure 5.6: Experimental sequence showing the reduction of the ODT intensity in a duration t_S. An absorption image is taken after a time t (which can be smaller than t_S) and Stern-Gerlach separation.

($\sim$ 5000) is about twice lower than one would expect with a "classic" evaporation sequence.

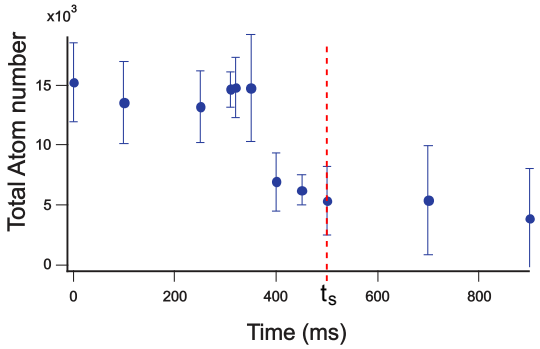

Figure 5.7: Total atom number as a function of time for a shock cooling time t_S = 500 ms. Dashed (red) vertical line highlights the end of the shock cooling evaporation ramp. The final total atom number ($\sim$ 5000) is about twice lower than one would expect with an optimal evaporation sequence of 2 s.

5.3.3 Results

a) A BEC in m_s = -3

We performed three shock-cooling experiments with different t_S in order to evaluate the impact of the speed of the shock cooling procedure on the external degrees of freedom of the gas (see Fig.5.8). After a time t (which can be smaller than t_S), the $m_s = -3$ gas reaches the same condensed fraction for t_S equal to 250 ms, 500 ms, and 1 s. We infer that the external mechanical degrees of freedom (characterized by the temperature) reach the same equilibrium for the three shock cooling experiments.

Fig.5.9 shows a typical absorption picture taken at $t = t_S$ for t_S = 500 ms. It reveals a BEC in $m_s = -3$, and a thermal gas in spin excited states. We extract the

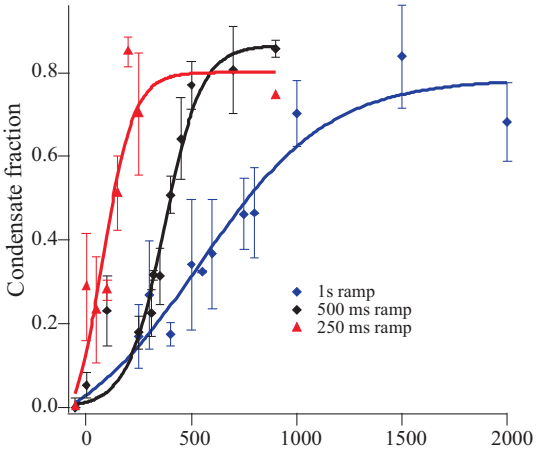

Figure 5.8: Evolution of the BEC fraction in $m_s = -3$ for three shock-cooling times t_S as a function of time t. At the end of the shock cooling procedure, the external degrees of freedom of the gas reach about the same thermal equilibrium for the three shock-cooling times, as the final BEC fraction is about the same. Lines are guide to the eyes.

number of thermal and condensed atoms of a given spin state through bi-modal fits accounting for Bose statistics: a Thomas-Fermi fit accounts for condensed atoms and a gaussian fit for thermal atoms. We plot in Fig.5.10 the thermal atom numbers as well as the condensate fractions in $m_s = (-3, -2)$ as a function of time t for a shock cooling time $t_S = 500$ ms. We found similar results for $t_S = 250$ ms and $t_S = 1$ s. For $t_S > 1$ s ($= \tau_{dip}$), the gas should spontaneously polarizes itself in m_s= -3 as in [97] due to dipolar non conserving magnetization collisions.

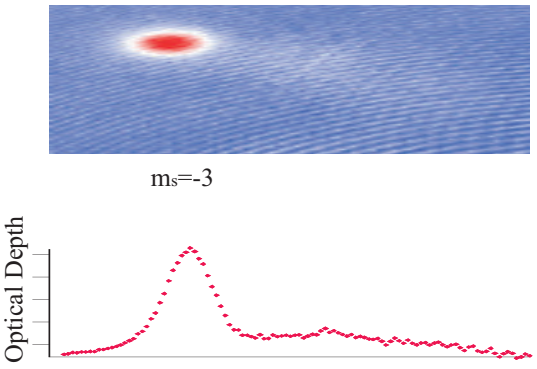

Figure 5.9: Typical absorption picture taken at $t = t_S = 500$ ms with the corresponding optical density along the axis of the Stern-Gerlach. We can see a BEC in m_s = -3 and thermal gases in spin excited states.

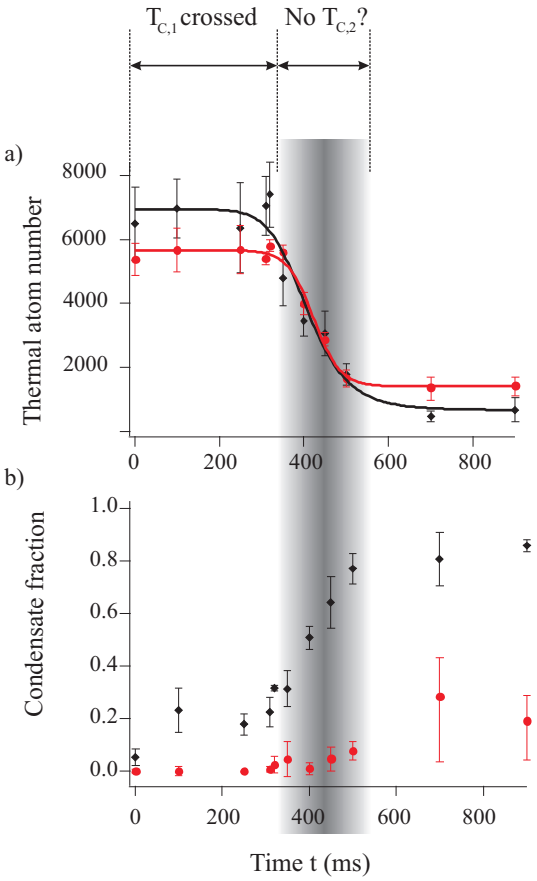

Figure 5.10: Experiment for a shock cooling time $t_S = 500$ ms. a) Number of thermal atoms in $m_s = -3$ (black diamonds) and $m_s = -2$ (red circles) as a function of time t. As soon as cooling starts, $m_s = -3$ and $m_s = -2$ share the same thermal atom number. b) Condensate fraction in $m_s = -3$ (black) and $m_s = -2$ (red) as a function of time. A large BEC in $m_S = -3$ is obtained but condensation in $m_s = -2$ remains small. The shaded region highlights the moment when cooling takes place.

b) A saturated m_s= -2 thermal gas

The gray area in Fig.5.10 highlights a relatively long cooling time during which the $m_s = -3$ and $m_s = -2$ gases hold the same number of thermal atoms, and during which there is a BEC in the lowest state $m_s = -3$ but only a small one in $m_s = -2$. The presence of a BEC in spin state m_s =-3 signals that the thermal m_s= -3 gas is saturated. The $m_s = -2$ and $m_s = -3$ thermal atoms have the same measured mechanical temperature (within our 5% experimental uncertainty) and experience the same optical trapping potential. If dealing with ideal gases, this is enough evidence to claim that the m_s = -2 gas is also saturated. The inclusion of interactions slightly modifies this discussion since repulsive interactions between the BEC and the thermal gas reduces the density of the thermal gas and affects saturation condition (see [164]

for an experimental study of the effect of interactions on saturation). However, both the $m_s = -2$ and $m_s = -3$ thermal atoms interact exclusively through the S=6 molecular potential with the existing $m_s = -3$ BEC. Therefore we can assess that the $m_s = -2$ cloud is saturated even taking into account interactions, and should condense for further cooling.

However, BEC does not occur in this state until t $\leq$ 700 ms. Only for t $\approx$ 700 ms do we distinguish a small BEC also in $m_s = -2$. The error bars are then large because it is difficult to differentiate between a BEC and a thermal cloud due to small number of remaining atoms. This experimentally demonstrates that a BEC in $m_s = -2$ hardly forms, although the $m_s = -2$ thermal gas is saturated and cooling proceeds.

5.3.4 Interpretation

a) Initial incoherent dynamics

The first point to clarify is whether the spin dynamics is set by coherent or incoherent collisions. The initial preparation of the thermal gas reaches spin equilibrium through incoherent collisions. The thermal gas is then in an incoherent mixture of spin states and, initially, the dynamics will be set by incoherent processes. For an incoherent mixture the spin dynamics rate Γ_{inc} is set by the density of the cloud through $\Gamma_{inc} = n\sigma v$ with n the atomic density, v the average relative atomic velocity and $\sigma_{i,j}^{k,l}$ the cross section of the spin changing collision $(i, j) \rightarrow (k, l)$ (see eq.(3.28)) associated *a priori* to contact or dipole dipole collisions.

b) Fixed magnetization

Magnetization is constant, within our signal to noise ratio, over the experimental times (see Fig.5.11). We therefore may consider only magnetization conserving dynamics which in principle can result either from dipole-dipole interaction or contact interaction.

However, the timescale associated to dipolar collisions (eq.(5.27)) is larger than that of shock cooling dynamics and can be neglected[5]. Spin dynamics is therefore entirely controlled by spin exchange interactions at *constant magnetization*, driven by spin dependent contact interactions. The spin dynamic rate $\Gamma_{inc} = n\sigma v$ is extremely sensitive to the presence of a BEC (which enhances n). Therefore, the emergence of a BEC in a spin-excited state should trigger faster spin dynamics.

c) Emergence of coherent dynamics

Once a small BEC in m_s = -2 is formed, coherent processes are possible. Therefore, in addition to energy redistribution through spin-exchange processes, the formation of BEC also triggers coherent spin oscillations due to forward scattering. The typical rate

[5] it is actually the whole point of the experiment to cool the gas on a faster timescale than the timescale associated with dipole-dipole interactions

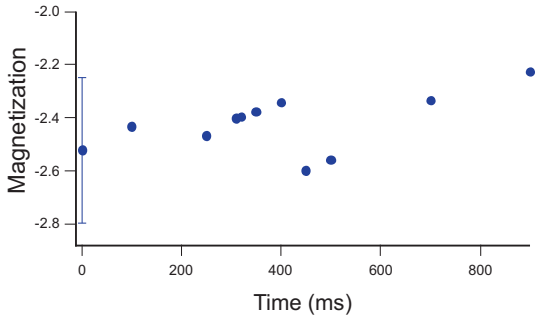

Figure 5.11: Magnetization as a function of time t for a shock cooling time t_S = 500 ms. The measured initial magnetization, set by the temperature of the gas and the external magnetic field, is 2.5 ± 0.25. Magnetization is roughly conserved during the experiment. We therefore may consider only magnetization conserving dynamics resulting mostly from contact interaction.

of a $(m_s = i, m_s = j) \rightarrow (m_s = k, m_s = l)$ coherent spin collision channel of an atom of spin s is:

$$\begin{aligned}\Gamma_{i,j}^{k,l} &= \frac{1}{h}\frac{4\pi\hbar^2}{m}n \\ &\times \sum_{S=0,even}^{2s} a_S < s,i;s,j|S,m_S = i+j >< S,m_S = k+l|s,k;s,l > \end{aligned} \quad (5.29)$$

where the sum holds for even S, and spin projection is conserved ($i + j$=$k + l$).

d) Timescales of the main collisional processes

α) Thermal gas timescales

The full rate equation for each spin state would be similar to eq.(3.49). In the following, to grasp the timescales at play we will only consider the main collisional channels. For an m_s = -2 gas, the main collisional channels are $(-2,-2) \rightarrow (-1,-3)$ and $(-2,-2) \rightarrow (-2,-2)$. The first process accounts for spin exchange collisions. Both ensure thermalization of spin state m_s= -2.

Spin exchange rate from $m_s = -2$

The main rate equation for spin exchange in m_s= -2 reads:

$$\frac{dn_{-2}}{dt} = -\sigma_{-2,-2}^{-3,-1} v n_{-2}^2(t). \quad (5.30)$$

For a thermal distribution, integrating eq.(5.31) over space yields:

$$\frac{dN_{-2}}{dt} = -\frac{n_{0,m_s=-2}^{Therm}(t)}{2\sqrt{2}}\sigma_{-2,-2}^{-3,-1} v N_{-2}(t) \quad (5.31)$$

where $n^{Therm}_{0,m_s=-2}(t) = N_{-2}(t)(\frac{m\bar{\omega}^2(t)}{k_BT})^{3/2}$. The initial peak density in $m_s = -2$, assuming a thermal distribution and N_{-2}= 5000 atoms, is $n^{Therm}_{0,m_s=-2}(0) = 7.7 \times 10^{18}$ at·m^{-3}.

The rate of the dominant spin exchange term is thus:

$$\begin{aligned} \Gamma_{inc,1} &= \frac{n^{Therm}_{0,m_s=-2}\sigma^{-3,-1}_{-2,-2}v}{2\sqrt{2}} \\ &\sim 2 \text{ s}^{-1}. \end{aligned} \tag{5.32}$$

for a thermal gas at $T = T_C$= 400 nK, with relative velocity $v = 4\sqrt{\frac{k_BT}{\pi m}} = 1.8$ cm·s^{-1}, and $\sigma^{-3,-1}_{-2,-2} = 8\pi\frac{15}{121}(a_6 - a_4)^2 = 3.4 \times 10^{-17}$ m^2. Therefore a typical timescale of a few seconds is thus necessary in order to reach spin equilibrium.

Mechanical thermalization rate of $m_s = -2$

The rate of the dominant thermalization rate of the mechanical degrees of freedom of an m_s= -2 gas is

$$\begin{aligned} \Gamma_{inc,2} &= \frac{n^{Therm}_{0,m_s=-2}\sigma^{-2,-2}_{-2,-2}v}{2\sqrt{2}} \\ &\sim 20 \text{ s}^{-1} \end{aligned} \tag{5.33}$$

with $\sigma^{-2,-2}_{-2,-2} = 8\pi\frac{1}{121}(6a_6 + 5a_4)^2 = 4.76 \times 10^{-16}$ m^2.

$\Gamma_{inc,2} >> \Gamma_{inc,1}$ insures that the mechanical degrees of freedom thermalize faster than the spin degree of freedom. Therefore without other collisional processes a small m_s=- 2 BEC can in principle be formed faster than it is depleted by spin exchange mechanisms.

Mechanical thermalization rate of $m_s = -3$

The dominant thermalization rate of the mechanical degrees of freedom of m_s= -3 is associated to $\sigma^{-3,-3}_{-3,-3} = 8\pi a_6^2$= 7.39 $\times 10^{-16}$ m^2, and has a rate $\Gamma_{inc,3} \sim 40$ s^{-1}. We find that $\Gamma_{inc,3} \sim \Gamma_{inc,2}$. Since the thermalization rate of $m_s = -3$ is large enough to produce a BEC in $m_s = -3$, the thermalization rate of m_s = -2 should be large enough to produce a BEC also.

β) BEC timescales

In the Thomas-Fermi approximation [23], a BEC has an inverted parabola distribution. This is very different from the thermal gaussian distribution and leads to a different expression for the average atomic density.

Incoherent spin exchange rate

For a Thomas Fermi distribution, integrating eq.(5.31) over space yields:

$$\frac{dN_{-2}}{dt} = -\underbrace{\frac{15^{2/5}}{14\pi}\Big(\frac{m\bar{\omega}}{\hbar\sqrt{\frac{1}{11}(6a_6+5a_4)}}\Big)^{6/5}}_{n^{BEC}_{0,m_s=-2}} N_{-2}^{2/5}\,\sigma^{-3,-1}_{-2,-2} v N_{-2}(t). \tag{5.34}$$

Once the m_s=- 2 BEC is formed, it takes only 120 condensed atoms in order to have the same averaged atomic density than 5000 thermal atoms at $T = T_C$ (then $n^{BEC}_{0,m_s=-2} \approx n^{Therm}_{0,m_s=-2}$). However, for a BEC of 100 atoms the Thomas-Fermi approximation is at the limit of being valid ($R_{TF} \sim a_{HO}$ where a_{HO} is the length of the harmonic oscillator). For 500 atoms in the condensate, we have $\Gamma^{(BEC)}_{inc,1} \approx 7$ s^{-1} which is of the same order as the the thermalization rate $\Gamma_{inc,2}$. Therefore the mechanical degrees of freedom and spin exchange process from $m_s = -2$ take place on similar timescales (mechanical thermalization is still three times faster).

Coherent spin exchange rate

Once a m_s=- 2 BEC is formed, two m_s = -2 atoms can undergo a forward scattering event. The rate associated to a coherent $(-2,-2) \rightarrow (-1,-3)$ is:

$$\Gamma_{coh} = \Gamma^{-3,-1}_{-2,-2} = \frac{1}{h}\frac{4\pi\hbar^2}{m} n^{BEC}_{0,m_s=-2}\frac{\sqrt{30}}{11}(a_6 - a_4). \tag{5.35}$$

For 500 atoms in the condensate, we obtain $\Gamma^{-3,-1}_{-2,-2} \approx 60$ s^{-1}. The rate of coherent spin exchange, for this condensed atom number, becomes three times larger than the mechanical thermalization rate (eq.(5.33)).

e) Our scenario

Our scenario is the following and is summed up in the sketch Fig.5.12. We rapidly cool thermal gases in different spin states. The rate associated to thermalization of the external degrees of freedom is here larger than any spin exchange rate. Almost no spin exchange takes place initially, and a BEC in m_s = -2 can form. However, as soon as the BEC is formed, spin exchange processes (such as $(-2,-2) \rightarrow (-1,-3)$) are of the same order as thermalization processes and take place, preventing formation of a large $m_s = -2$ BEC. Since the $m_s = -3$ gas is saturated, any "new" atom in m_s=-3 will directly be added to the existing condensate. In m_s=-1 the thermal gas is not saturated, and any added atom in that state, originating from a BEC or not, will become a thermal atom.

Thus spin exchange collisions deplete the m_s= -2 BEC as fast as it is created and a multi-component BEC cannot be sustained due to fast spin dynamics emptying m_s= -2 and to the lack of saturation of the m_s=-1 thermal gas.

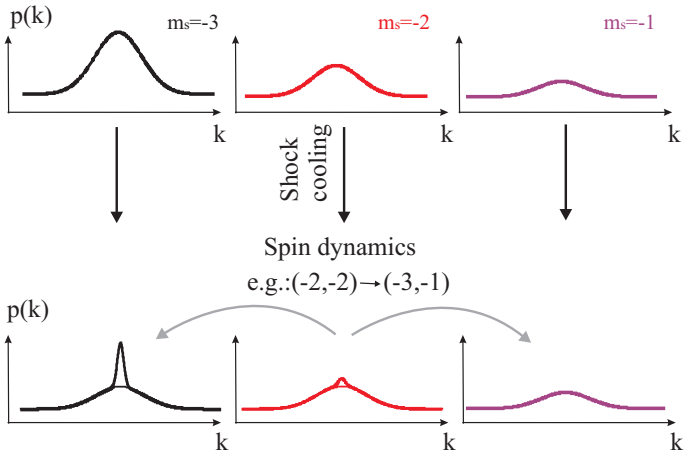

Figure 5.12: Sketch illustrating our interpretation. Before shock cooling, we have thermal distribution in each spin states. As shock cooling proceeds, a BEC in m_s= -3 is formed. Even though the thermal m_s = -2 is saturated, a BEC cannot be sustained in this state because fast spin-exchange processes $(-2,-2) \rightarrow (-1,-3)$ deplete the BEC as soon as it is produced.

5.3.5 Numerical simulations

a) Classical Field Approximation

The Gross Pitaevskii equation (GPE) describes well the properties of the condensate at zero temperature. However, the dynamics of a Bose gas at non-zero temperature remains a challenge from the theoretical point of view. One successful approach relies on two-gas models [165]. In these models, one assumes that the system at finite temperatures consists of two distinct components: the condensate and the thermal cloud.

To simulate data relative to our non zero temperature experiment, we started a collaboration with Mariusz Gajda from Warsaw and Miroslaw Brewczyk from Bialystok. They use the Classical Field Approximation (CFA) in order to numerically simulate data for T $\neq$ 0. In this approximation, the bosonic field operator is replaced by a classical field. The classical field describes the condensate in dynamical equilibrium with the thermal cloud. According to CFA, the GPE determines the evolution of the classical field which is a complex function carrying the information on both the condensed and thermal atoms [166, 167, 168] (this model is thus intrinsically different to the two-gas models). Once the time evolution is obtained, the condensate is defined as the dominant term in the spectral decomposition of the time-averaged single particle density matrix associated to the classical field.

In Fig.5.13, we illustrate this process. Once the evolution of the classical field is performed, a time averaged single particle density matrix is constructed. If there is a dominant term in the spectral decomposition of the density matrix it is defined as the

condensate. Here the population of different spin states is plotted as a function of the mode number. We read that, for this experimental sequence, there is a BEC in m_s= -3 of $\sim$ 2500 atoms and a thermal gas with typically 100 atoms per mode. No BEC is obtained in m_s= -2 or m_s= -1.

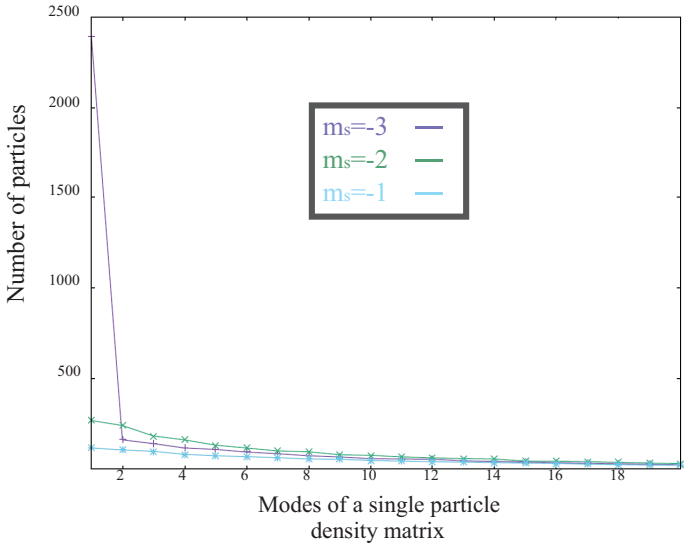

Figure 5.13: Illustration of the classical field approximation. Here, a classical field is associated to each spin state. Once the evolution of the classical field is performed, a time averaged single particle density matrix is constructed. If there is a dominant term in the spectral decomposition of the density matrix it is defined as the condensate. Here the population of different spin states is plotted as a function of the mode. We read that, for this experimental sequence, there is a BEC in m_s= -3 of $\sim$ 2500 atoms and thermal gas with typically 100 atoms per mode and no BEC in m_s= -2 or m_s= -1.

b) Simulation of the experiment

The initial classical field corresponds to about 13.10^3 of ^{52}Cr atoms at equilibrium at the critical temperature of about 400 nK and with the experimental Zeeman distribution. To describe such a sample, M. Brewczyk and M. Gajda followed the prescription given in Ref.[168].

Evaporative cooling is mimicked by adding a purely imaginary potential to the GPE simulations at the edge of the numerical grid which discretizes space. This purely imaginary potential accounts for evaporation and acts as a cut off: it defines a boundary for removing atoms from the system. Simulations use the same trap geometry as the one in the experiment, and more specifically the same time-dependent trap frequencies. The temperature of the system is very sensitive to the choice of the cut-off for evaporation. The value of the cut-off was fixed empirically in order to match best the experimental sequence (i.e. atom number evolution in time).

Numerical simulations were performed with and without including dipole-dipole interactions. The simulations show that dipole-dipole interactions play a negligible role (as expected), except when the magnetic field is well below 1 mG where they then play an important role for the spinor phase (and therefore well below the experimental situation).

The simulations of M.Gajda and M.Brewczyk confirm the absence of a significant condensate in $m_s = -2$ and the formation of a large BEC in m_s =-3 (see Fig.5.14). Their simulations also show that the $m_s = -3$ and m_s = -2 thermal gases hold the same atom number and temperature. Thus, as in the experiment, m_s= -2 is a saturated thermal gas.

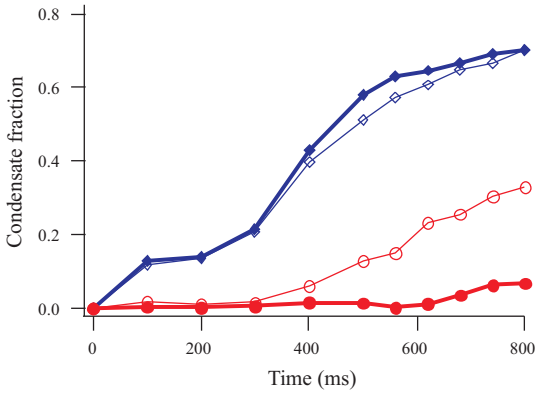

Figure 5.14: Numerical Simulation. Evolution in time of the condensate fraction of $m_s = -3$ and $m_s = -2$ for different values of a_4 after a cooling duration time t_S= 500 ms and a final temperature of $T = 120$ nK. The data in blue diamonds corresponds to the BEC fraction in $m_s = -3$ where as the data in red circles is $m_s = -2$. Filled markers correspond to simulations where a_4 was set to its true value i.e. $a_4 = 64a_B$ where a_B is the Bohr radius. Empty circles correspond to simulations where a_4 was set equal to a_6. The impact of the value of $a_6 - a_4$ on the dynamics is striking since by setting this value to 0, a macroscopic BEC in $m_s = -2$ is enabled.

c) Simulation with $a_4 = a_6$

To evaluate the impact of spin-exchange processes on the dynamics of condensation, they reproduced these simulations with a modified value of a_4 such that $a_4 = a_6$. In this case, all the rates associated to spin-exchange processes $(-2, -2) \rightarrow (-1, -3)$ vanish ($\Gamma_{inc,1}$ and $\Gamma^{-3,-1}_{-2,-2}$ scale respectively as $(a_6 - a_4)^2$ and $(a_6 - a_4)$). As shown in Fig.5.14, a large BEC then forms in the spin excited state $m_s = -2$. At $T = 0$, we expect the same condensate fraction in each spin state (all atoms are condensed). The lower condensate fraction of the $m_s = -2$ compared to $m_s = -3$ is interpreted as being due to the initial spin distribution: the $m_s = -2$ condenses for a lower temperature than

$m_s = -3$ and the condensate fraction of $m_s = -2$ is "behind in time" compared to the condensed fraction of $m_s = -3$.

These simulations confirm the crucial role of spin-dependent interactions in order to understand the dynamics of BEC.

5.3.6 Thermodynamics interpretation

Let us recall the accepted scenario for the thermodynamics of non-interacting multi-component Bose gases at low temperature, fixed magnetization, and no quadratic Zeeman effect (see [153] or subsection 5.2.2). In this picture, a ferromagnetic BEC, polarized in the most populated state ($m_s^{min} = -3$ in our case), forms below a first critical temperature. Due to the absence of a quadratic Zeeman effect, the chemical potentials of all spin states are linearly spaced

$$\mu_i - \mu_{-s} = -b(i+s) \; \forall \; \mathrm{i} \; \in \; [-\mathrm{s}, \mathrm{s}]. \tag{5.36}$$

As a consequence, once a second component m_s saturates (i.e. $\mu_{m_s} = 0$) $b = 0$ is required, and all the other thermal spin states saturate simultaneously. In our situation, both the experiment and the numerical simulation indicate that the external degrees of freedom have reached equilibrium after shock cooling.

We observe the production of a BEC in the most populated lowest energy state below a critical temperature. This temperature is obtained shortly after shock cooling starts (see Fig.5.10 for $t_S = 500$ ms). However, as shock cooling proceeds and lower temperatures are obtained, although the thermal clouds of the lowest two spin components are saturated, the other thermal clouds ($m_s > -2$) are not saturated. This is in contradiction with the basic prediction of the Bose thermodynamics of large spin atoms with no interaction, which shows that the spin degrees of freedom in our experiment remain *out of thermal equilibrium*.

This lack of thermal equilibrium in the spin degree of freedom results from the fact that spin exchange processes *for the thermal gas* are slow in regards of condensation dynamics. In the experiment, we cannot wait for spin thermal equilibrium due to incoherent collisions to take place since magnetization changing collisions take place on a similar timescale. Indeed the timescale associated to spin thermalization is of the order of several $1/\Gamma_{inc,1}$ (eq.(5.33), similar to τ_{dip}.

Besides, if exchange rates in the thermal gas were larger or equal than thermalization rates, collisions at fixed magnetization would lead complex dynamics where at the end all spin states could saturate simultaneously.

In our experimental conditions, non-saturated spin-excited states thus act as a reservoir into which population may be dumped, thus preventing BEC but in the stretched state, the only one which is collisionally stable. Indeed, let us consider a $(-2,-2) \rightarrow (-1,-3)$ process between two condensed atoms. Since the thermal gas in m_s = -1 is not saturated, the condensed atom produce in $m_s = -1$ will de-condense and occupy an excited state. However, since a BEC is present in m_s = -3, the atoms

produced in $m_s = -3$ will be added to the existing condensate. It is only when all spin states are saturated that a multi-component BEC can be sustained.

5.3.7 Experiment for a gas with $M = -2.00 \pm 0.25$

To deepen our understanding of the combined effects of Bose-Einstein condensation and spin dynamics, we performed a second series of shock cooling experiments, this time with a lower gas magnetization $M = -2.00 \pm 0.25$.

a) State preparation

In this set of experiments the initial spin distribution is prepared by applying a Radio-Frequency pulse (the effect of a RF pulse on a BEC is explained in detail in section 8.4.1. Here we performed a $2\pi/7$ RF pulse.) to a $m_s = -3$ thermal gas of 1.8×10^4 atoms at T= 1.1 T_C and letting the different spin components decohere. The initial fractional population in $m_s = -3$, -2, -1 and 0 states are:

$$\begin{aligned} \frac{N_{-3}}{N_{Tot}} &= 0.31 \pm 0.03 \\ \frac{N_{-2}}{N_{Tot}} &= 0.40 \pm 0.04 \\ \frac{N_{-1}}{N_{Tot}} &= 0.21 \pm 0.02 \\ \frac{N_0}{N_{Tot}} &= 0.06 \pm 0.01. \end{aligned}$$

The initial population in states $m_s > 0$ are negligible. We did not rely on magnetization changing collisions for the spin preparation as in the first experiments for two reasons. First, lower magnetization requires lower experimental magnetic fields, with associated technical difficulties. Second, depolarization via a small RF pulse allows for a more balanced population between spin populations in m_s = -3, -2, -1. When depolarization is obtained via magnetization changing collisions, equal population in each state requires $g_{Landé}\mu_B B/k_B T \to 0$ which is experimentally difficult and also results in 7 spin states, each with low population. Here with a RF pulse, we can reach an interesting situation where saturation may be reached more or less simultaneously for 3 spin states.

b) Experiment

After the RF pulse, we then perform a shock cooling ramp between the initial and final trap frequencies ν^i and ν^f. For shock cooling times similar to the one in the first experiment (t_S = 250 ms, 500 ms, 1 s), we do not observe any condensed fraction in any spin state. However for shock cooling times $t_S \leq$ 100 ms, we observe the

production of small condensates in all three lowest energy states (a typical absorption picture of the multi-component condensates is shown in Fig 5.15). In Fig.5.16 we show magnetization and total atom number as a function of time for $t_S = 50$ ms. We observe that magnetization is constant, and that the total atom number is significantly reduced after approximatively 30 ms of the 50 ms shock cooling ramp.

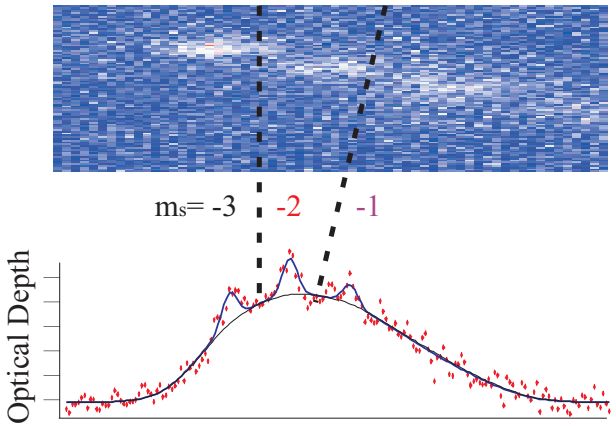

Figure 5.15: Typical absorption picture taken at $t = t_S = 50$ ms with the corresponding optical density along the axis of the Stern-Gerlach for an initial magnetization $M = -2$. We can see very small condensates in m_s= -3, -2, and -1.

We define the total condensate fraction of the gas as the total number of condensed atoms over the total atom number (i.e. $\sum_{i=-s}^{s} n_i/N_{Tot}$ with n_i the condensate fraction in spin state i). We plot in Fig.5.17 the total condensate fraction of the gas at $t = t_S$ as a function of t_S.

c) Interpretation

Since the effect of the shock cooling ramp on atom number lags (this can be seen by the delay in decrease of atom number Fig.5.16), it takes several tens of ms before any dynamics takes place. Assuming a thermal atom distribution, the initial peak density is $n_0 \sim 10^{19}$ at.m^{-3}. The timescale τ_{inc} associated with an incoherent $(-3,-3) \rightarrow (-3,-3)$ collision at a temperature $T = 1.1 \times T_c$ is:

$$\begin{aligned} \tau_{inc} &= \frac{2\sqrt{2}}{n_0 \sigma_{(-3,-3)}^{(-3,-3)} v} \\ &\sim 25 \text{ ms} \end{aligned} \tag{5.37}$$

with v the relative velocity. In practice, along with the presence of magnetic gradients (which dephase the different spin components), τ_{inc} is short enough to ensure that all the different spin components have decohered (see section 3.2).

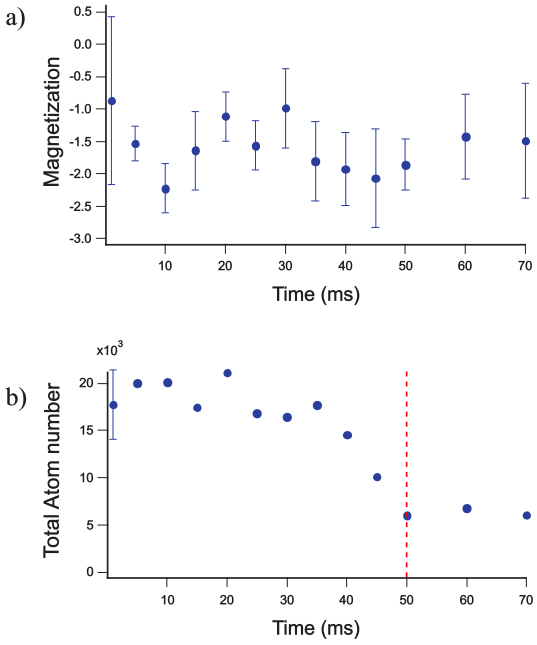

Figure 5.16: a) Magnetization as a function of time for a shock cooling time $t_S = 50$ ms. Spin preparation is performed by a RF pulse. The experimental magnetization is 2.0 ± 0.25. b) Total atom number as a function of time for a shock cooling time $t_S = 50$ ms. The total atom number is significantly reduced after approximatively 30 ms of the 50 ms shock cooling ramp. Dashed (red) vertical line highlights the end of the shock cooling evaporation ramp.

We observe that the average magnetization is roughly conserved during the timescale of the experiment (Fig.5.16).

We interpret the observation of multi-component BECs by the fact that shock cooling is now performed on a similar timescale as the rate of exchange processes. Each component is cooled very fast. Spin dynamics is slow enough that a spinor BEC is first produced in $m_s = -3, -2, -1$. However, spin excited states with $m_s \geq 0$ are not saturated so that spin dynamics then tends to populate the non saturated states and empty the condensates. The condensates are thus only metastable. Spin-dynamics has again a very profound influence on the dynamics of condensation.

d) Magnetization fluctuations

An important observation regarding the multi-component condensates which are obtained is that their magnetization shows strong fluctuations. From shot to shot, we see that the condensed fraction in a given spin state fluctuates. We measure fluctuations of the magnetization of the condensate fraction at the end of a shock cooling experiment with t_S= 50 ms about twice larger than fluctuations of the magnetization of the thermal gas (Fig.5.18). Unfortunately, due to our relatively low signal to noise ratio a

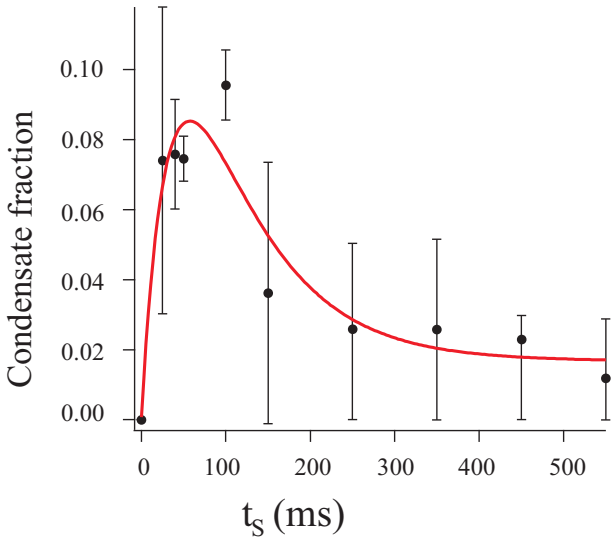

Figure 5.17: Total condensate fraction of the multi spin component gas (i.e. $\sum_{i=-s}^{s} n_i/N_{Tot}$) at $t = t_S$ ms as a function of time t_S. We observe small short lived multi-component condensates only in the 3 lowest energy states. The line is a guide to the eye.

full experimental investigation of magnetization fluctuations has not been performed.

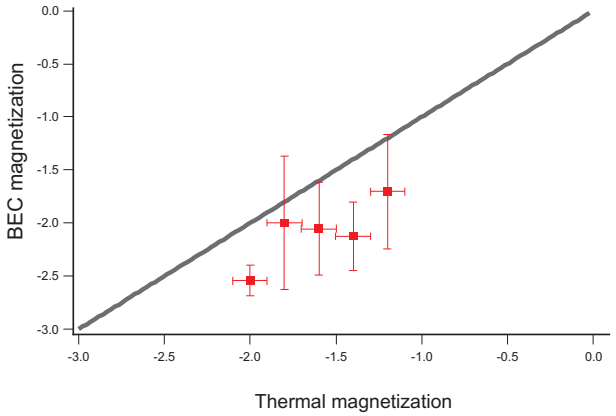

Figure 5.18: Magnetization of the condensate fraction as a function of the magnetization of the thermal gas at the end of a shock cooling experiment with t_S= 50 ms. The gray straight solid line (of unity slope, crossing the origin) is given for reference. Although the data is noisy, the general trend suggest that the error bars along the vertical direction are about twice larger than the error bars along the horizontal direction. This suggests that magnetization fluctuations of the BEC are larger than fluctuations of the thermal gas.

To give a first insight into why shock cooling might lead to magnetization fluctua-

tions in the BEC phase, we first write the mean-field equations of the spin dynamics for the multi component BECs. For pedagogical reasons, since we are not interested in solving this problem but to illustrate the different contributions of the different terms, we will only write terms which involve the three lowest spin states:

$$\begin{aligned} i\hbar\dot{\Psi}_{-3} &= g_{-3,-1;-2,-2}\Psi^*_{-1}\Psi_{-2}\Psi_{-2} + \sum_{j=1}^{3} g_{-3,-j;-3,-j}(\Psi^*_{-j}\Psi_{-j})\Psi_{-3} \\ i\hbar\dot{\Psi}_{-2} &= 2g_{-3,-1;-2,-2}\Psi^*_{-2}\Psi_{-3}\Psi_{-1} + \sum_{j=1}^{3} g_{-2,-j;-2,-j}(\Psi^*_{-j}\Psi_{-j})\Psi_{-2} \\ i\hbar\dot{\Psi}_{-1} &= g_{-3,-1;-2,-2}\Psi^*_{-3}\Psi_{-2}\Psi_{-2} + \sum_{j=1}^{3} g_{-1,-j;-1,-j}(\Psi^*_{-j}\Psi_{-j})\Psi_{-1} \end{aligned} \tag{5.38}$$

where $\Psi_i = \sqrt{n_i}_i e^{i\phi}$ is the classical field associated to spin state i with phase ϕ_i and population n_i, and $g_{i,j,k,l}$ is the interaction strength associated to a coherent (m_s=i,m_s=j) $\rightarrow$ (m_s=k,m_s=l) collision. The first term describes spin exchange collision, whereas the second term represents collisions where the spin of each atom is conserved but affects the phase ϕ_i of Ψ_i. The key point in eq.(5.38) is that spin dynamics depends on the phases of the different spin components.

Our interpretation for magnetization fluctuations is that Bose-condensation of the different spin-excited states introduce a spontaneous symmetry breaking as the phase of each condensate (in a given m_s) is built up randomly. Phase fluctuations lead to fluctuations in spin dynamics (eq.(5.38)) [112], and therefore in the magnetic state which is eventually obtained. Since spin dynamics may lead to populations in non saturated states, spin dynamics at constant total magnetization may lead to a modification of the magnetization of the BEC. Therefore fluctuations in spin dynamics may lead to BEC magnetization fluctuations.

Numerical simulation

M.Gajda and M.Brewczyk performed numerical simulations to test this scenario. As the CFA does not provide a direct way to provide symmetry breaking at the BEC transition, they applied a random relative phase to the wave-functions describing the thermal atoms in different spin components before condensation. This provides an empirical way to simulate symmetry breaking. They performed a series of numerical simulations for different sets of relative phases between the Zeeman components. They then obtained small condensates with fluctuating magnetization. Furthermore, we also observe that spin and condensation dynamics are also significantly modified by the applied random phases. Due to large computational time for each run, a systematic study of BEC magnetization as a function of initial phases has not yet been performed and remains to be thoroughly investigated. However, while the magnetization fluctuations obtained in the numerical simulations are typically three times smaller than

the experimental measurements, these preliminary results support the scenario that the combined effect of spontaneous symmetry breaking and spin dynamics lead to the observed spin fluctuations.

5.3.8 Conclusion and perspectives

We performed fast cooling across the BEC transition starting with a multi-component spin thermal gas. We were expecting to obtain multi-BEC components and then observe how the system polarizes itself towards its ferromagnetic ground state. Actually, in the first set of experiments we found that even though the first thermal spin excited state was saturated, the other spin components were not, and a BEC in m_s = -2 was difficult to form due to a strong interplay between Bose condensation and spin dynamics. In a second series of experiments, we started with larger populations in the first spin excited states and produced small short-lived BECs which decay due to spin changing collisions. Our experiments show that even though the mechanical degree of freedom is thermalized, it is difficult to thermalize the spin degrees of freedom. This effect has to be taken into account for large spin systems (such as Dy [17] and Er [18] which have 17 and 13 spin states respectively), where all spin states must be fully saturated for a stable multi-component BEC to be produced at thermal equilibrium. Finally, we point out that when a multi component BEC is dynamically produced, spontaneous symmetry breaking leads to independent phases within the BEC components which triggers spin fluctuations. Although these experiments only focused on the collisional aspect of the interplay between spin dynamics and condensation, we believe that the subject could be further explored. Law, Pu, and Bigelow showed that anti-ferromagnetic coupling leads to a unique ground-state which has super-Poissonian fluctuations in the population of each spin state [169]. It would be interesting to deepen the study of fluctuations in the experiments. A larger atomic sample could also allow saturation for all spin states. Then we would have an experiment where the condensation of a given spin state would result from an interplay between superfluid order and magnetic order.

5.4 Removing entropy of a polarized BEC through spin filtering

In the following section we propose a cooling mechanism where the spin degree of freedom is used to store and remove entropy from a polarized BEC. We develop a non interacting model which accounts well for the data and suggests that this cooling mechanism should work for non dipolar species as well.

5.4.1 Introduction

Current cooling limitations

Evaporation has proven to be a very efficient way of cooling atomic gases. When the temperature T of the gas is greater than the interaction energy $g_S n$ (with n the density and g_S the interaction strength), most of the energy carried by an atom is thermal. Therefore removing the most energetic atoms results in an efficient cooling of the sample. When $k_B T < \mu$, the cooling efficiency reduces owing to the fact that the chemical potential accounts for a non negligible part of the energy carried away by each evaporated atom. This reduction in efficiency of evaporation was recently observed [170]. They showed that evaporation still continues despite the reduction of efficiency, and extremely low entropies of $\Sigma/N \sim 10^{-3} k_B$ were produced. This reported value of entropy represents a huge leap since, for comparison, reported entropies for a 500 pK BEC are $\Sigma/N \sim 1.5 k_B$ [171].

Why a new cooling mechanism?

In a lattice, when the internal degree of freedom is included in the thermodynamic picture, such as spin, a critical value of entropy Σ_{Mag} exists below which quantum magnetic ordering and magnetic correlations become accessible. For example, an atom of spin s pinned to a lattice site can be in $2s+1$ spin states. The entropy per atom associated to accessible independent magnetic states is

$$\Sigma_{Mag} = k_B \log(2s+1). \tag{5.39}$$

If the sample has an entropy lower than Σ_{Mag}, it is necessarily in a correlated magnetic regime where exotic quantum phases are expected. Despite impressively cold temperatures achieved (sometimes ranging in the pK regime [171]), only recent experiments have been able to observe short range magnetic correlations in optical lattices with fermions [172, 173, 174].

The hope to study magnetic correlations of atoms in optical lattices, and the possible connections to exotic superconductivity are major motivations to obtain systems with lower entropies than currently available [175]. It is therefore important to find

new ways to remove entropy in degenerate quantum Bose or Fermi gases loaded in optical lattices [176, 177].

Most cooling techniques involve only the mechanical degrees of freedom. It is likely that the difficulty to reach low spin entropy is associated to the fact that most cooling schemes are spin insensitive. This motivates the need to implement a cooling mechanism which directly involves the spin degrees of freedom. Here, we propose to use the spin degrees of freedom to efficiently store and remove entropy from a polarized Bose-condensed gases to reach temperatures below the current limitations set by evaporative cooling. This experimental campaign was performed before the extremely low entropies reported in [170]. Our cooling mechanism is expected to lead to even lower entropies, if ever even lower entropies turned out to be necessary.

Principle of the experiment

Our cooling mechanism takes advantage of the thermodynamic properties of spinor gases. As discussed earlier, the non interacting phase diagram for a large spin and barely any quadratic shift, like in Chromium, predicts three phases. Phase A corresponds to a thermal gas in each spin component. Under a first critical temperature, we enter phase B: a BEC forms in the lowest Zeeman energy state. Population of other spin states are necessarily thermal. Under a second critical phase transition, all spin states condense simultaneously (phase C). When magnetization is free, such is the case for Chromium, the second phase transition is avoided as long as the magnetic field B is greater than a critical magnetic field B_C, which is predicted in the 100 μG regime with the given experimental parameters.

Our cooling mechanism takes place in phase B. There, we induce a selective loss specific to atoms in $m_s \neq$ -3. These atoms are necessarily thermal and an efficient gain in condensed fraction and therefore a reduction of entropy is possible, even at large trap depths.

5.4.2 Experimental protocol

a) Initial starting point: a BEC in m_s =-3

Our experiments starts with preparing a ^{52}Cr BEC in the absolute ground state $m_s = -3$ with an initial condensate fraction f_i of typically $1 - 2 \times 10^4$ atoms. The initial condensate fraction is set by varying the final value of the IR power of the evaporation ramp, thus defining an initial thermal population and an initial number of condensed atoms. See Step 1 of Fig.5.19.

b) Preparing atoms in $m_s \neq$-3

The magnetic field, which is initially B_i=40 mG, is then lowered in 50 ms to a final value B_f, low enough to trigger depolarization of the thermal gas ($g\mu_B B_f \simeq k_B T$). See

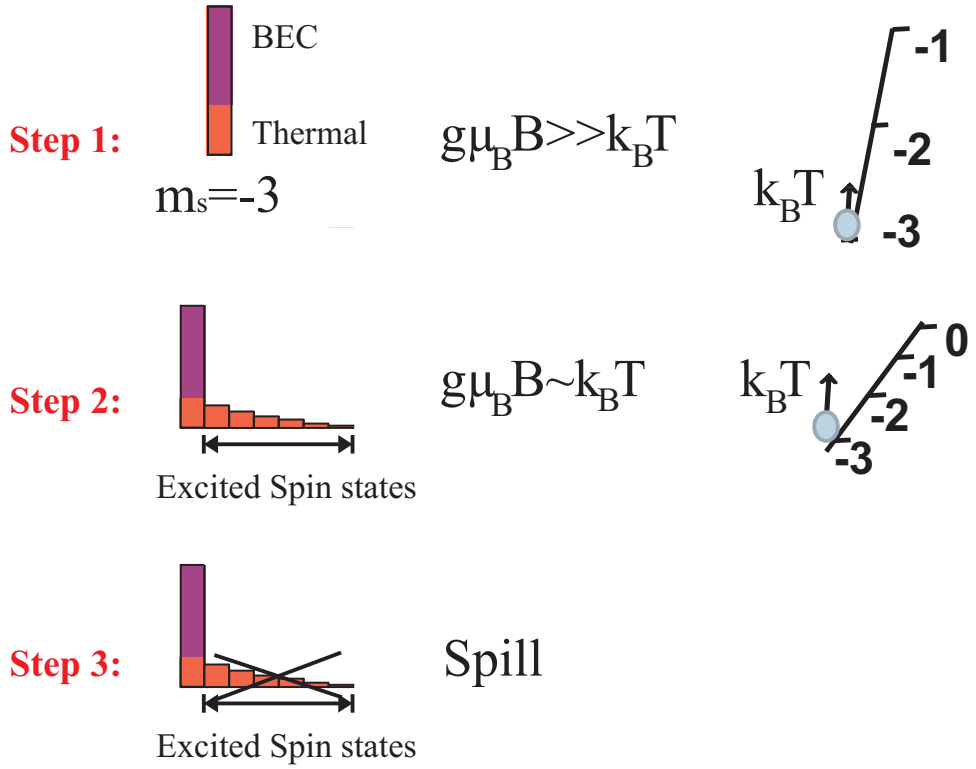

Figure 5.19: Sketch of the experimental procedure. Step 1: Produce a BEC in $m_s = -3$ at high B field (i.e. $g\mu_B B_f >> k_B T$). Step 2: Lower the magnetic field so that $g\mu_B B_f \simeq k_B T$. Dipolar collisions between thermal atoms spontaneously take place and populate spin excited states. Step 3: Get rid of atoms in spin excited states.

Step 2 of Fig.5.19 but high enough that a BEC may form only in $m_s = -3$ (we remain in phase B). For $T = 400$ nK, $g_{Landé}\mu_B B = k_B T$ leads to a B field of approximatively 3 mG.

We then let the cloud evolve at B_f for t_{wait}=150 ms. This timescale is long enough for inelastic dipolar collisions to ensure depolarization. Indeed, the typical peak density associated to a thermal gas of 2×10^4 atoms at $T = 250$ nK with a mean geometrical trap frequency $\bar{\omega} = 2 \times \pi$ 250 Hz is $n_0 \sim 2 \times 10^{19}$ at·m^{-3}. The typical rate for these collisions for a magnetic field in the 1 mG range is 15 s^{-1} and it takes several dipolar collisions to thermalize the spin degrees of freedom (see [87] or eq.(3.16)).

B_f is calibrated by use of RF spectroscopy, and it can be controlled to the 100 μG level (see [178] for magnetic field stabilization).

c) Removing atoms in $m_s \neq$-3

We then proceed to remove atoms in spin excited states (see Step 3 of Fig.5.19). This spin filtering procedure consists of i) raising the magnetic field to 30 mG (this ensures

that we go away from the low magnetic field region in a controlled way so that we do not cross B_c); ii) changing the trap in order to spill out atoms with $m_s > -3$. For that we reduce the trap depth and add a vertical B field gradient (of about 1 G·cm^{-1}) as illustrated by the sketch Fig.5.20. During this experimental sequence only $m_s = -3$ atoms remain trapped while $m_s > -3$ atoms are lost. $m_s > -3$ atoms fall out of the trap because optical and magnetic forces are insufficient to compensate gravity. In Fig.5.21, we illustrate the form of the potential at the point of minimum IR power (see Fig.5.20) along the vertical direction for 3 different spin states, and a magnetic gradient of 0.8 G·cm^{-1}. We can see that under these conditions, $m_s = -3$ atoms can still be trapped, whereas $m_s >$ -3 are expelled from the trap.

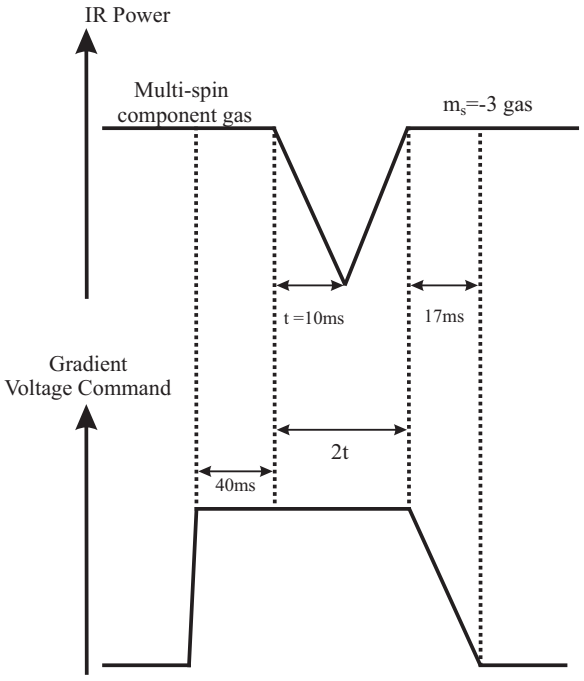

Figure 5.20: Sketch of the experimental filtering procedure. We apply a magnetic field gradient along the vertical direction. We then reduce the trap depth up to a certain value where optical and magnetic forces are insufficient to compensate gravity for $m_s > -3$ atoms. We then recover the initial optical trap, remove the magnetic field gradient and recover the initial trapping conditions. The 40 ms time between applying the magnetic gradient and the beginning of the reduction of the IR intensity is set by the induction time of the coils. This times typically sets the timescale for spin filtering. The IR ramp time of 10 ms is the shortest possible allowed by the voltage control of the AOM and in practice is long enough to allowing for spin filtering.

We checked that no evaporation is induced by the filtering procedure. We performed a spin filtering protocol without depolarization (i.e. an experiment performed at $g_{Landé}\mu_B B_f >> k_B T$ see Fig.5.22). We measure a 5% difference in condensed frac-

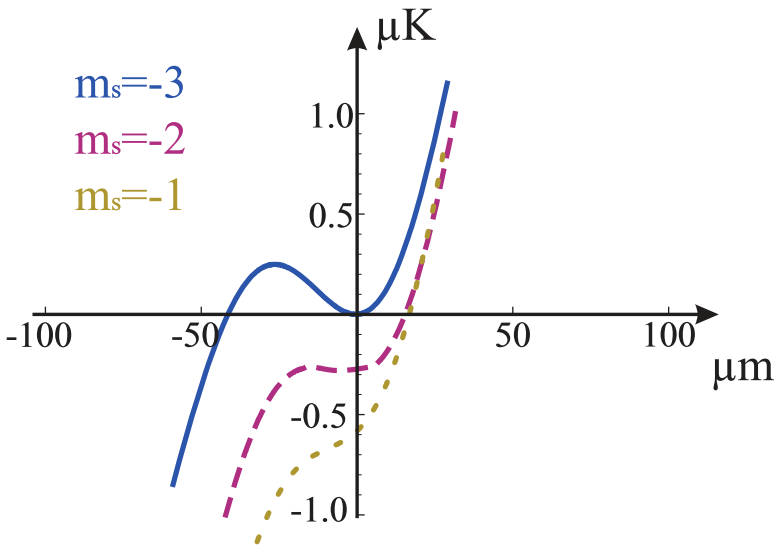

Figure 5.21: Illustration of the form of the potential along the vertical direction at the point of minimum IR power (see Fig.5.20) for 3 different spin states, and a magnetic gradient. The trap depth in these conditions is estimated to be 1.4 μK and the IR beam waist is estimated to be 50 μm. The gradient creates (in the calculation taken to be 0.8 G·cm^{-1}) a force maximally opposite to gravity for $m_s = -3$ atoms. We can see that under these conditions, $m_s = -3$ atoms are still be trapped (full blue curve), whereas $m_s >$ -3 are expelled from the trap (for clarity reasons, an energy offset between the potentials is introduced and we only represent $m_s = -2$ and $m_s = -1$ in dashed magenta and dotted gold respectively).

tion (within our signal to noise ratio) for a procedure performed at relatively high initial temperature, which we expect to be sensitive to any extra evaporation. In addition, we measured through Stern-Gerlach analysis that indeed the losses induced by the new trap are almost total for $m_s > -3$.

The spin filtering is performed rapidly, as fast as possible actually (in 60 ms), to ensure that no dipolar relaxation occurs. This would correspond to typically one dipolar collision with the timescale calculated above. However, 60 ms is the total amount of time to raise the magnetic field, apply magnetic gradients, and lower the trap confinement. The whole process decreases density and separates in situ the different Zeeman components. As a consequence it is difficult to assess precisely the time for dipolar relaxation. Experimentally, we observe no heating of the BEC which would be a consequence of dipolar relaxation. Finally, we recover the initial (purely) optical trap at B_i, and measure the new BEC fraction.

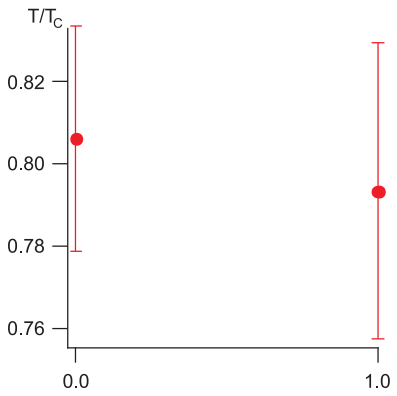

Figure 5.22: Measured T/T_C for a BEC in $m_s = -3$ with the spin filtering method (abscise 0) or without (abscise 1). We measure the same temperature within our experimental error bars. We conclude that our spin filtering protocol does not introduce any extra cooling or heating. Any cooling observed will thus be attributed to our cooling mechanism.

d) The thermodynamic operations

Fig.5.23 shows a sketch of the experiment in the (M, T) diagram and qualitatively describes the thermodynamic operations of our cooling mechanism. Fig.5.23a represents our initial conditions. We have a BEC in m_s= -3 and all the thermal atoms are in m_s=-3. We then lower the magnetic field to a value of the magnetic field B_f. B_f is low enough that sufficient thermal atoms may change spin states, but high enough so that $B_f > B_c$ and that phase C is avoided. The gas is cooled and magnetization increases (see Fig.5.23b). Atoms in $m_s >$ -3 are then selectively removed. The total atom number is lowered, thus the critical temperature for condensation is lowered also. This process can result in a gain of condensate fraction (Fig.5.23c).

5.4.3 The experimental results

We performed the cooling mechanism for different values of the magnetic field B_f and for different initial condensate fractions. As mentioned above, the initial condensate fraction is set by varying the final value of the IR power of the evaporation ramp resulting in different trap frequencies parameters.

a) Measuring condensate fractions

To accurately measure BEC fractions is not an easy task, especially for high BEC fractions due to small thermal component. Here, we release the atoms from the trap by switching off the IR trap and take an absorption picture after a time of flight of 5 ms. The difficulty of accurately measuring condensate fractions resides in the fact that temperature sets both the width of the gaussian describing thermal atoms and the BEC

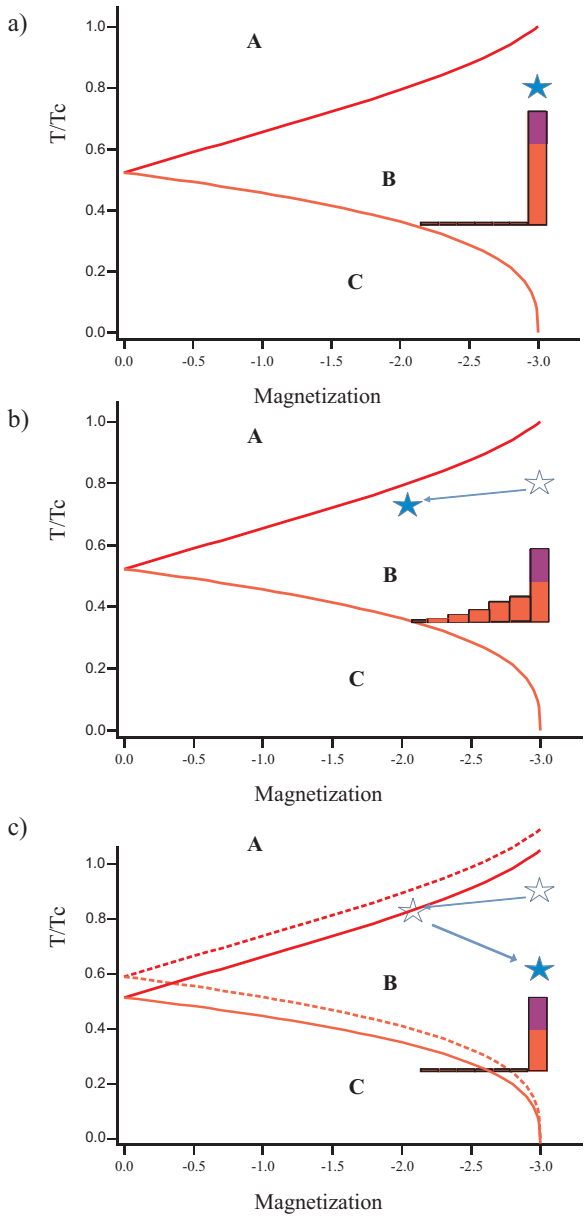

Figure 5.23: Sketch of our cooling mechanism represented on the phase diagram of a spin 3 atom. a) Representation of our initial conditions. We have a BEC in m_s= -3 and all the thermal atoms are in m_s=-3. b) We then lower the magnetic field to a value of the magnetic field B_f low enough that sufficient thermal atoms may change spin states, but high enough so that $B_f > B_c$ and that phase C is avoided. c) Atoms in $m_s >$ -3 are then selectively removed. The total atom number is lowered, thus the critical temperature for condensation is lowered also, thus the vertical scale is modified. The dashed line represents the "old" critical temperature. This process can result in a gain of condensate fraction provided the "new" T/T_c is lower than the initial one.

fraction. We perform a two-stage analysis of the images. A first fit is used to measure the total number of atoms, and with the knowledge of the trapping frequencies we can deduce the critical temperature T_c (eq.(5.2)). A second bi-modal fit is then performed where the temperature is a free parameter and the total atom number and critical temperature are fixed by the first fit (a Thomas-Fermi profile fits the condensate and a gaussian fits the thermal atom distribution). This procedure was optimized in order to ensure good measurements of thermal fractions down to ten percent, or BEC fraction up to 90%.

b) Proof of principle

We first performed a proof of principle experiment, where we did not filter the thermal excited spin states and checked if the BEC fraction becomes larger or not in the $m_s = -3$ component after a Stern-Gerlach separation.

The experiment starts with a thermal gas in m_s= -3 at B_i. We then cool the gas and produce a BEC in m_s= -3. The initial condensed fraction is:

$$f_i = 1 - \left(\frac{T_i}{T_{c,i}}\right)^3. \tag{5.40}$$

We then lower the field to B_f= 1 mG. After a time t_{wait}, we turn off the dipole trap and measure both the spin and momentum distributions after a 5 ms TOF. The different spin components are separated via a magnetic field gradient pulse of approximatively 3.5 G·cm^{-1} present during the TOF (as explained in subsection 1.5.2). We define $(T_f/T_{c,f})$ as the temperature of the gas divided by the critical temperature which is calculated by considering only the number of atoms in m_s= -3:

$$T_{c,f} = \left(\frac{N_{-3,f}}{N_{tot,i}}\right)^{1/3} \tag{5.41}$$

This is not the real critical temperature of the gas, since it does not consider the total final atom number, but would be if the $m_s > -3$ atoms were removed.

In Fig 5.24, we show $(T_f/T_{c,f})$ as a function of $(T_i/T_{c,i})$ for B_f= 1 mG. The black curve represents $(T_f/T_{c,f}) = (T_i/T_{c,i})$. We find that our cooling mechanism produces a BEC polarized in the lowest energy state with an increased condensate fraction, provided the initial thermal fraction is low enough: this marginally demonstrates that our cooling mechanism works, however error bars remain large due to magnetic field fluctuations.

c) Spin filtering a polarized BEC

We now use the whole experimental protocol to filter the excited spin states. The experiment starts with a thermal gas in m_s= -3 at B_i. We cool the gas and produce a BEC in m_s= -3. The initial condensed fraction is f_i. We then lower the field to B_f.

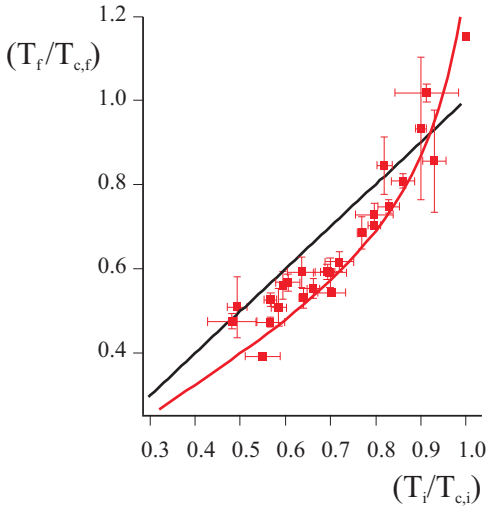

Figure 5.24: Proof of principle for purification of a ^{52}Cr BEC. After depolarization occurring at a B field of B_f=1 mG, we measure the final condensate fraction in m_s=-3 and hence the effective final reduced temperature (red squares), as a function of the initial reduced temperature. Error bars show statistical uncertainties. The (red) solid line is the result of our model. The (black) straight solid line (of unity slope, crossing the origin) is a reference (i.e. no cooling). Data follows the general trend given by the model. However experimental error bars are large due to magnetic field fluctuations.

After a time t_{wait}, we perform the spin filtering protocol which is sketched Fig.5.20. At the end of the filtering process, we turn off the IR trap and let the gas expand for a TOF of 5 ms, after which we perform an absorption pulse imaging sequence. In Fig.5.25 we show the final condensate fraction, f_2, as a function of B_f for different initial condensate fraction f_i. In full lines we show the result of our non-interacting model (see subsection 5.4.5).

When B_f is large, we find $f_2 = f_i$: the cooling protocol has no effect on the condensed fraction. For the smallest initial condensate fractions f_i, f_2 gets smaller than f_i at the lowest B_f. On the other hand, when f_i is large enough, f_2 gets significantly larger than f_i. There also seems to be an intermediate regime where f_2 first increases as B_f is lowered, and then decreases. These features are present in the non-interacting model we established (see subsection 5.4.5).

d) First interpretation

Our experiments shows that increased condensed fractions can be observed after our cooling process as long as the initial condensate fraction is large enough.

To gain insight on the physics at stake, we plot in Fig.5.26a the number of thermal and condensed atoms, as a function of B_f for a relatively high initial condensate fraction f_i. Fig.5.26b shows the measured final condensed fraction f_2 for an other set of data

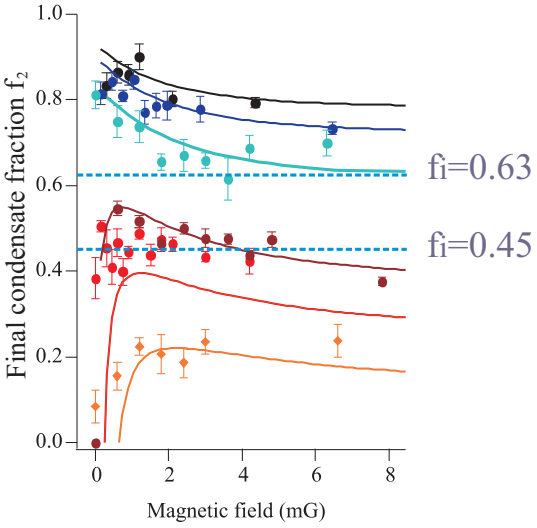

Figure 5.25: Experimental results for spin spilling with an $s = 3$ ^{52}Cr BEC, for different initial BEC fractions f_i (represented by different colours). For each initial BEC fraction, the BEC fraction after spilling (i.e. f_2) is plotted as a function of B_f. When B_f is large, we find $f_2 = f_i$: the cooling protocol has no effect on the condensed fraction. For the smallest initial condensate fractions f_i, f_2 gets smaller than f_i at the lowest B_f. On the other hand, when f_i is large enough, f_2 gets significantly larger than f_i. Full coloured lines are predictions of our non-interacting model (see subsection 5.4.5). Dashed blue lines seperate, based on our non-interacting model, three regions where different behaviours may be observed depending on the initial condensed fraction.

but shows the same behaviour and helps illustrate the discussion.

For large values of B_f we measure $f_2 = f_i$: the procedure has no effect on the condensed fraction, which makes sense since for large B_f all thermal atoms stay in $m_s = -3$. For small values of B_f, we measure a reduction in the number of thermal atoms and condensed atoms. For this particular value of f_i, the losses result in an increase of the condensate fraction. We interpret this behaviour as the consequence of the competition between three effects. (i) As population in spin-excited states is purely thermal, spin filtering leads to purification of the BEC. The number of thermal atoms is reduced therefore the condensed fractions has increased. (ii) As the thermal gas in m_s=-3 depolarizes and populates spin excited states, the number of thermal atoms in m_s=-3 decreases. The BEC must "melt" to maintain saturation of the thermal $m_s = -3$ gas. (iii) As BEC atoms have zero energy [23], this cools the thermal gas which can then be saturated at a lower temperature, as already observed in [179] and [180]. Competition between these effects can lead to an increase in condensate fraction, provided the initial BEC atom number is large enough. However, if the initial condensed fraction is too small, depolarization can lead to a complete melting of the BEC in order to re-saturate the thermal gas. In the case shown here, the initial condensate fraction is large enough

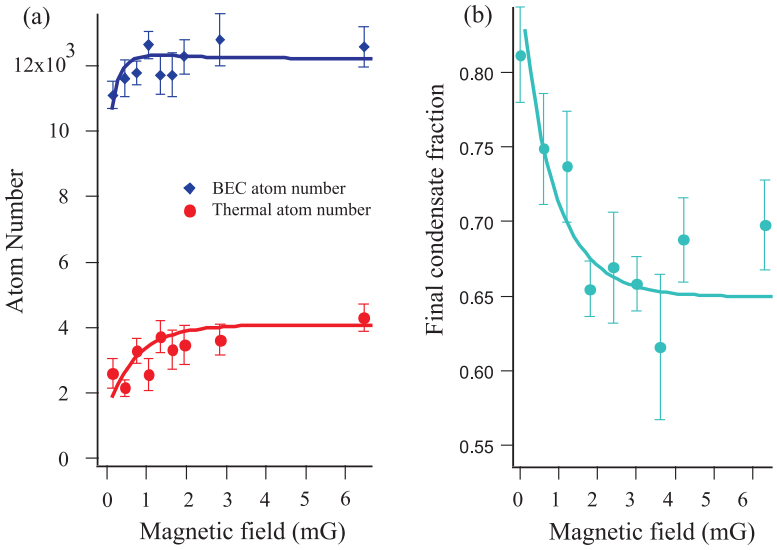

Figure 5.26: Experimental results for spin spilling with an $s = 3$ ^{52}Cr BEC. a) Number of atoms after spin spilling: in the BEC (top), in the thermal component (bottom). Lines are guide to the eye. b) Final condensate fraction as a function of B_f, for an initial BEC fraction of f_i =0.67±0.05. The solid line for the condensed fraction results from our theoretical model (see subsection 5.4.5).

so that spilling results in an increase of the condensate fraction.

5.4.4 Applicability to non dipolar gases

We have shown that our experimental protocol can result in an increased condensate fraction. In our experiment, population in spin excited states is provided by dipolar collisions. However, there are only two criteria necessary for our cooling mechanism: (i) a BEC in only one spin state and (ii) thermalization of the spin degree of freedom in order to populate spin excited states. Therefore our cooling scheme should work for non dipolar gases with contact spin changing collisions.

For example let us consider a spinor s=1 BEC of Rb or Na which have a non zero quadratic shift and for which only magnetization conserving collisions are allowed. Spin-changing collisions associated with the difference in scattering lengths in the molecular potentials $S = 0$ and $S = 2$ redistribute population between $m_s = 0$ and $m_s = \pm 1$ at constant magnetization. As explained in section 5.2.2, the positive quadratic Zeeman effect provides an energy shift qm_s^2 between a pair of atoms in the $m_s = 0$ state and a pair of atoms in states $m_s = \pm 1$, which favors BEC in $m_s = 0$, and it "costs" $2q$ for two atoms in $m_F = 0$ to perform a spin changing collision. The quadratic Zeeman energy can be reduced so that $q \sim k_B T$, then contact spin changing

collisions ensure populations in spin excited states with thermal atoms[6].

The process is completely analogous to the dipolar case: instead of having $(-3,-3) \rightarrow (-2,-2)$ collisions and be sensitive to the linear Zeeman energy, here $(0,0) \rightarrow (-1,+1)$ collisions ensure population of the excited spin states and the energy scale is set by the quadratic Zeeman energy.

5.4.5 Theoretical model

We elaborated a simple *non interacting model* to compare our results and estimate the efficiency of the mechanism. When magnetization is free (case of dipolar particles) the magnetic energy includes the linear Zeeman effect, whereas when magnetization is fixed (as for example for Rb and Na atoms), the linear Zeeman effect is gauged out and the magnetic energy only includes the quadratic Zeeman effect q. In both cases, we denote the lowest energy spin state m_s^{min} ($m_s^{min} = -3$ for Cr with free magnetization, $m_s^{min} = 0$ for Rb or Na at fixed zero magnetization).

a) Model principle

Let us here briefly introduce the main steps for our model. The initial state considered is a BEC in m_s^{min}, with all the thermal atoms in m_s^{min}, at an initial temperature of $T = T_i$ and magnetic field B_i. We then consider a virtual state after the magnetic field was reduced diabatically to a value B_f, but before thermalization of the spin degrees of freedom occurred. The transformation is diabatic with respect to the spin degrees of freedom: depolarization has not yet taken place. Therefore we have still a BEC in m_s^{min} with all the thermal atoms in m_s^{min} at a temperature T_i but now the external magnetic field is B_f. We then compute the equilibrium state assuming thermodynamic equilibrium is reached through a transformation with total energy and atom number conserved (no dissipation process). The gas now occupies different spin states and is at a temperature T_f. We may then remove atoms in excited spin states and compute the new condensate fraction.

b) Initial state: a BEC in m_s^{min}

We consider a polarized BEC at a finite temperature T_i in the lowest energy spin state m_s^{min}. We set the initial magnetic energy to zero. We assume that a BEC is only present in state m_s^{min}, so that $\mu_{m_s^{min}} = 0$. The initial condensed fraction f_i in a 3D harmonic trap is:

$$f_i = \frac{n_{0,i}}{N_{tot,i}} = 1 - \left(\frac{T_i}{T_{c,i}}\right)^3 \tag{5.42}$$

[6]The linear Zeeman effect plays no role in the case of a fixed magnetization since the initial linear Zeeman energy is equal to the final linear Zeeman energy.

with $N_{tot,i}$ the initial total atom number and $n_{0,i}$ the initial condensed atom number and $T_{c,i}$ the initial critical temperature for condensation given by

$$k_B T_{c,i} = \hbar\omega \left(\frac{N_{tot}}{\zeta(3)} \right)^{1/3}. \tag{5.43}$$

The initial number of thermal atoms is thus $N_{th,i}^{(m_s^{min})} = N_{tot,i} - n_{0,i}$.

The initial energy of the gas in a 3D harmonic trap with a BEC present is thus:

$$\begin{aligned} E_i &= \overbrace{E_{kin,i} + E_{pot,i}}^{E_{Trap,i}} && (5.44) \\ &= 3k_B T_i g_4(e^{-\beta\epsilon_{0,m_s^{min}}}) \left(\frac{k_B T_i}{\hbar\omega} \right)^3 \\ &= 3\frac{\zeta(4)}{\zeta(3)} N_{th,i}^{m_s^{min}} k_B T_i && (5.45) \end{aligned}$$

with E_{Trap} the sum of kinetic and potential energy, g_n the polylogarithm function of order n, $\zeta(n)$ the Riemann function ($\zeta(n) = g_n(1)$), ω the geometric average of the angular trapping frequencies and $\beta = 1/k_B T_i$. ϵ_{k,m_s} is the single-particle energy of the trap harmonic oscillator state k, thus $\epsilon_{0,m_s^{min}} = 3\hbar\omega/2$, and we make the usual assumption that $\beta\epsilon_{0,m_s^{min}} << 1$.

c) Depolarization

The magnetic field is set to a value B_f to allow depolarization. To compute the equilibrium state after depolarization, we assume thermodynamic equilibrium at temperature T_f, conservation of the total atom number, and of total energy (no dissipation).

The spin composition in the final state will be entirely characterized by the thermal atom number in spin state i, $N_{th,f}^i$, and the final condensate atom number in m_s^{min} $n_{0,f}$. We also define $N_{th,f}$ as the total thermal atom number in the final state:

$$N_{th,f} = \sum_{i=-s}^{+s} N_{th,f}^i. \tag{5.46}$$

Premise

As long as we have a BEC in m_s^{min} in the final state, the number of thermal atoms in m_s^{min} in the final state is proportional to the temperature to the power three, as the trap is a 3D harmonic trap:

$$N_{th,f}^{m_s^{min}} = A T_f^3 \tag{5.47}$$

with A a constant which depends on the trap and on the total atom number $N_{tot,i}$. This equation is valid for all values of the magnetic field B_f. In particular, it has to

be true for the case where B_f is infinite in which case we recover the initial state. All the thermal atoms are then in m_s^{min} so that:

$$N_{th,f}^{m_s^{min}} = N_{th,f} \tag{5.48}$$

$$N_{th,f} = N_{th,i}^{m_s^{min}} \tag{5.49}$$

$$T_f = T_i. \tag{5.50}$$

Therefore at the limit of condensation, $T_f = T_{c,i}$ and $N_{th,f}^{m_s^{min}} = N_{tot,i}$ so that $A = N_{tot,i}/T_{c,i}^3$, and we obtain:

$$N_{th}^{m_s^{min}} = \frac{N_{tot,i}}{T_{c,i}^3} T_f^3 \tag{5.51}$$

At high magnetic field all atoms are in m_s^{min}, there is no depolarization, and the critical temperature does not change.

Now let us use eq.(5.51) to discuss the case $B_f = 0$. In that case, the thermal populations in each spin state are equal:

$$N_{th}^{m_s^{min}} = \frac{1}{2s+1} N_{th,Tot}. \tag{5.52}$$

At the limit of condensation, we define $T_f = T_{c,f}$, with $T_{c,f}$ the final critical temperature for condensation. Using the fact that at $T_{c,f}$, $N_{th,tot} = N_{tot,i}$, eqs.(5.51) and (5.52) give:

$$T_{c,f}(B=0) = T_{c,i} \times \left(\frac{1}{(2s+1)}\right)^{1/3}, \tag{5.53}$$

which is the critical temperature at B=0 and corresponds for example to the critical temperature at $M = 0$ of Fig.5.4.

Atom conservation

We assume a BEC in m_s^{min} and conservation of the inital total atom number $N_{Tot,i}$. Eq.(5.51) allows us to relate the thermal atom number in m_s^{min} after depolarization, $N_{th,f}^{m_s^{min}}$, to the temperature T_f after depolarization:

In the thermodynamic limit, the thermal population in each spin state reads:

$$N_{th,f}^{m_s} = \sum_k f_{k,m_s}(0) \approx g_3\left(e^{-\beta\epsilon_{0,m_s}}\right)\left(\frac{k_B T_f}{\hbar\omega}\right)^3 \tag{5.54}$$

where $\epsilon_{0,m_s} = 3\hbar\omega/2 + (m_s - m_s^{min}) g_{Landé}\mu_B B$ in the case of a linear spin. Assuming again that all condensed atoms are in m_s^{min}, additional atoms are then condensed in state m_s^{min}:

$$n_{0,f} = N_{Tot} - \sum_{m_s} N_{th,f}^{m_s}. \tag{5.55}$$

where $n_{0,f}$ is the number of condensed atoms after depolarization.

Energy conservation

The energy after depolarization is:

$$\begin{aligned} E_f &= E_{\text{Trap},f} + E_{Mag,f} \\ &= \sum_{m_s} \left(3k_B T g_4(e^{-\beta\epsilon_{0,m_s}}) \left(\frac{k_B T_f}{\hbar\omega}\right)^3 + N_{th,f}^{m_s}\epsilon_{0,m_s}\right). \end{aligned} \tag{5.56}$$

$E_{Mag,f}$ is the gain in magnetic energy acquired by thermal atoms having changed spin state.

Final condensed fractions

The final temperature T_f and BEC atom number $n_{0,f}$ are thus derived and can be compared to initial values T_i and $n_{0,i}$. Any atom in spin-excited state $m_s \neq m_s^{min}$ can be removed (by means of magnetic field gradients, micro-wave transitions, and/or a resonant push laser beam). After depolarization, we define

$$f_1 = \frac{n_{0,f}}{N_{Tot,i}} \tag{5.57}$$

the BEC fraction relative to the total number of atoms, and

$$f_2 = \frac{n_{0,f}}{(n_{0,f} + N_{th,f}^{(m_s^{min})})} = \frac{n_{0,f}}{N_{Tot,f}} \tag{5.58}$$

the BEC fraction relative to atoms in state m_s^{min} with $N_{Tot,f}$ the final total atom number (i.e. after spin filtering).

These two condensed fractions correspond respectively to not filtering and spin filtering the spin excited states. In the following we will evaluate f_1 and f_2 to discuss the physics at play, first for B_f=0 and then $B_f \neq$0.

d) The case of B_f=0

Let us first discuss the case B_f=0 (although unfeasible experimentally, it will help in understanding the physical processes involved). After depolarization for B_f=0 , the thermal populations in each spin state are equal:

$$N_{th,f}^i = N_{th,f}^j = \frac{1}{(2s+1)} N_{th,f} \;\forall\; (\mathrm{i},\mathrm{j}) \;\in\; [-\mathrm{s},\mathrm{s}]. \tag{5.59}$$

Eq.(5.51) gives:

$$\frac{N_{th,f}}{N_{tot,i}} = (2s+1)\left(\frac{T_f}{T_{c,i}}\right)^3. \tag{5.60}$$

E_i is given eq.(5.45). We now compute E_f (eq.(5.56)), the energy after depolarization. There is no magnetic energy term, for $B_f = 0$. We find:

$$\begin{aligned} E_f &= (2s+1) \times 3\frac{\zeta(4)}{\zeta(3)} N_{Tot} k_B T_{c,i} \left(\frac{T_f}{T_{c,i}}\right)^4 \text{ (same thermal population in each state)} \\ E_f &= 3\frac{\zeta(4)}{\zeta(3)} N_{th,f} k_B T_f \text{ (using eq.(5.60))}. \end{aligned} \tag{5.61}$$

Conservation of energy imposes that:

$$\begin{aligned} E_i &= E_f \\ N_{th,i}^{(m_s^{min})} T_i &= N_{th,f} T_f. \end{aligned} \tag{5.62}$$

Using eq.(5.62), we have:

$$\begin{aligned} \frac{N_{th,f}}{N_{tot,i}} \frac{T_f}{T_{c,i}} &= \frac{N_{th,i}^{m_s^{min}}}{N_{tot,i}} \frac{T_i}{T_{c,i}} \\ &= (1-f_i)(1-f_i)^{1/3} \\ &= (1-f_i)^{4/3}. \end{aligned} \tag{5.63}$$

Eq.(5.60) yields

$$\begin{aligned} \frac{N_{th,f}}{N_{tot,i}} \frac{T_f}{T_{c,i}} &= (2s+1)\left(\frac{T_f}{T_{c,i}}\right)^4 \\ &= (2s+1)\left(\frac{1-f_1}{2s+1}\right)^{4/3} \end{aligned} \tag{5.64}$$

as $1 - f_1 = N_{th,f}/N_{tot,i}$ by definition.

Using eqs.(5.64) and (5.63) we may express the condensate fraction f_1 without filtering the spin excited states:

$$f_1 = 1 - (1-f_i)(2s+1)^{1/4}. \tag{5.65}$$

We may also express the condensate fraction f_2 when spin filtering is performed:

$$\begin{aligned} f_2 &= \frac{n_{0,f}}{n_{0,f} + N_{th,f}^{(m_s^{min})}} = \frac{n_{0,f}/N_{tot,i}}{n_{0,f}/N_{tot,i} + \frac{N_{th,f}}{2s+1}/N_{tot,i}} \\ &= \frac{f_1}{f_1 + \frac{1-f_1}{2s+1}} \\ &= (2s+1)\frac{1-(1-f_i)(2s+1)^{1/4}}{(2s+1) - 2s(2s+1)^{1/4}(1-f_i)}. \end{aligned} \tag{5.66}$$

We plot in Fig.5.27 f_1 and f_2 as a function of f_i for s=3.

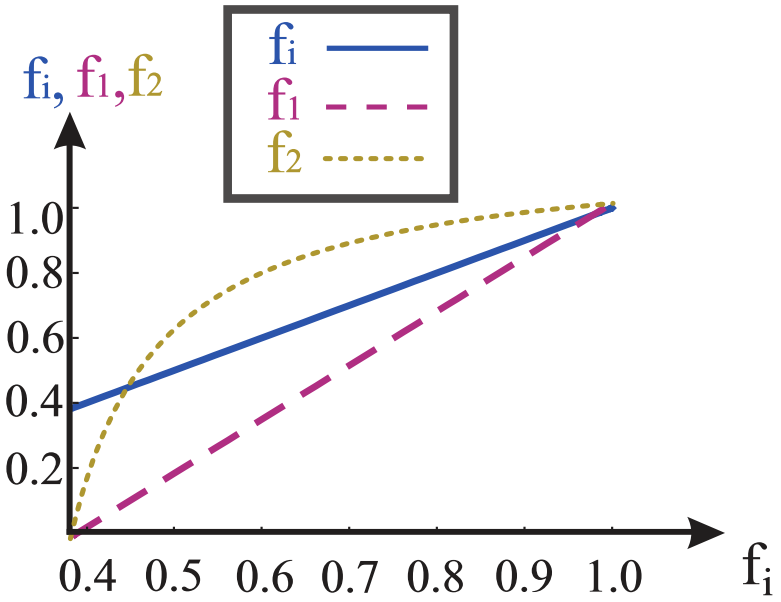

Figure 5.27: f_1 (purple dashed) and f_2 (gold dotted) for B_f=0 and f_i (blue line) as a function of f_i for s=3. When spin filtering is not performed, the final condensed fraction after depolarization is lower than before depolarization, i.e. $f_1 \leq f_i$. If $f_i \leq 0.385$, we no longer have a condensate after depolarization. When spin filtering is performed (f_2, golden line) we have $f_2 \geq f_i$ as long as $f_i \geq 0.449$. See text for more information.

Interpretation for f_1

Eq.(5.65) imposes that $f_1 \leq f_i$: when spin filtering is not performed, the final condensed fraction after depolarization is lower than before depolarization. Our interpretation is that, when depolarization occurs, the thermal gas in m_s^{min} is no longer saturated. The BEC then melts to re-saturate the thermal gas. The total number of thermal atoms increases during this process, and the number of condensed fraction is lowered. Thus the condensed fraction can only be lowered.

If $f_i <$ 1- $(2s+1)^{-1/4}$ (for s=3, this imposes that $f_i \geq$ 1- $7^{-1/4} \approx 0.385$), we have negative values for f_1. A negative condensate fraction has no physical significance and our model therefore has no meaning in that case. For $f_i <$ 1- $(2s+1)^{-1/4}$, depolarization melts completely the BEC fraction. The initial BEC fraction is too weak that the number of thermal atoms which changed spin state is larger than the number of condensed atoms to re-saturate the thermal gas. This sets a lower limit to f_i for our cooling mechanism to work, and for the model to have a meaning.

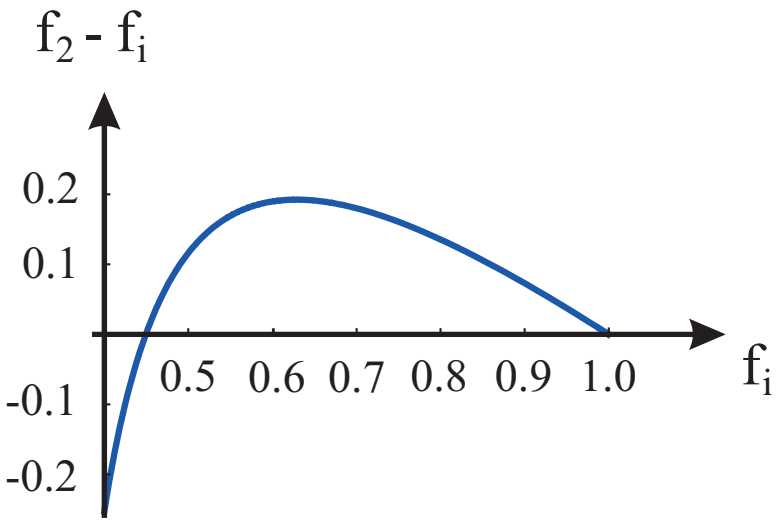

Figure 5.28: Gain in condensate fraction when spilling is performed (f_2-f_i) as a function of initial condensate fraction f_i for s=3. At best, the condensate fraction can be increased by 0.19 for $f_i = 0.63$.

Interpretation for f_2

$f_2 \geq 0$ as long as $f_i \geq$ 1- $(2s+1)^{-1/4}$. This is the same criteria than for f_1: if the initial condensate fraction is too weak, the BEC will completely melt.

We also have $f_2 \geq f_i$ as long as $f_i \geq (1 + 2s - (1 + 2s)^{3/4})/(2s)$. For s=3 this leads to $f_i \geq 0.449$. Filtering spin excited states after depolarization results in a gain in condensate fraction, provided a large enough f_i.

These results are summed up in Fig.5.27 for s=3. We also show Fig.5.28 the gain in condensate fraction when spilling is performed f_2-f_i as a function of f_i. At best, the condensate fraction can be increased by 0.19 for $f_i = 0.63$.

Melting cools

Let us now look at how temperature is affected during the cooling mechanism.

Eq.(5.63) can be expressed as $(2s+1)(\frac{T_f}{T_{c,i}})^4 = (\frac{T_i}{T_{c,i}})^4$. As long as the final condensate fraction is positive, we have the following temperature relation:

$$\frac{T_f}{T_i} = (2s+1)^{-1/4} \approx 0.61 \text{ for s } = \text{ 3.} \tag{5.67}$$

When the BEC melts to saturate the thermal gas, the number of condensed atoms lowers, however the thermalization of BEC atoms (at T=0) with the thermal atoms (at T= T_i) lead to a cooling of the gas ($T_f = (2s+1)^{-1/4} T_i < T_i$) which can then saturate at a lower temperature.

e) The case of $B_f \neq 0$

Let us now consider the case $B_f \neq 0$, and once again assume that a BEC is only formed in m_s^{min}. In the following we will consider the case of a linear Zeeman energy. We start with a gas polarized in m_s^{min}=-s, with initial condensed fraction $f_i = \frac{n_{0,i}}{N_{tot,i}}$. The magnetic field is then lowered to $B_f > 0$.

The chemical potential of spin state m_s =-s is 0 because we start with a BEC in that state. The chemical potential of each spin state is simply:

$$\mu_i = -b(i+s) \; \forall \; \mathrm{i} \; \in \; [-\mathrm{s}, \mathrm{s}]. \tag{5.68}$$

Population in each spin state

The population in spin state i relative to the one in spin state m_s^{min} is (see eq.(5.13) adapted to the case of a 3D harmonic trap):

$$\frac{N_{th,f}^{(i)}}{N_{th,f}^{(m_s^{min})}} = \frac{g_3(e^{-(i+s)y})}{\zeta(3)} \tag{5.69}$$

with $y = \frac{g_{Landé}\mu_B B_f}{k_B T_f}$, $g_{Landé}$ the Landé factor and μ_B Bohr's magneton.

The total thermal atom number can be evaluated with eq.(5.51):

$$\begin{aligned} N_{th,f}^{Tot} = \sum_{i=-s}^{s} N_{th,f}^{(i)} &= N_{Tot,i} \frac{T_f^3}{T_{c,i}^3} \frac{\sum_{i=-s}^{s} g_3(e^{-(i+s)y})}{\zeta(3)} \\ &= N_{Tot,i} \frac{T_f^3}{T_{c,i}^3} \frac{S(y)}{\zeta(3)} \end{aligned} \tag{5.70}$$

where we define S(y)= $\sum_{i=-s}^{s} g_3(e^{-(i+s)y})$.

Energy of each spin state

We now proceed to compute the energy associated to each spin state. Each spin state has a different chemical potential.

The trap energy and magnetic energy of each spin state can be expressed as:

$$E_{Trap,f}^{(Tot)} = 3N_{th,f}^{(Tot)} k_B T_f \frac{S_{Trap}(y)}{S(y)} \tag{5.71}$$

$$E_{Mag,f}^{(Tot)} = k_B T_f \frac{N_{th,f}}{S(y)} y S_{Mag}(y) \tag{5.72}$$

where $S_{Trap}(y) = \sum_{i=-s}^{+s} g_4(e^{-(i+s)y})$ and $S_{Mag}(y) = \sum_{i=-s}^{+s} (i+s) g_3(e^{-(i+s)y})$. Energy conservation leads to:

$$\zeta(4) N_{th,i} T_i = \zeta(3) N_{th,f}^{(Tot)} T_f \frac{S_{Trap}(y) + \frac{y}{3} S_{Mag}(y)}{S(y)}. \tag{5.73}$$

Final condensed fractions

Eq.(5.70) and eq.(5.73) lead to:

$$\left(\frac{T_f}{T_{c,i}}\right)^4 (S_{Trap}(y) + \frac{y}{3} S_{Mag}(y)) = (1 - f_i)^{4/3} \tag{5.74}$$

This defines an implicit equation for $\frac{T_f}{T_{c,i}}$, with $y = \frac{g_{Landé}\mu_B B_f}{k_B T_{c,i}} (\frac{T_f}{T_{c,i}})^{-1}$. This equation can be solved numerically for a given value of f_i and $\frac{g_{Landé}\mu_B B_f}{k_B T_{c,i}}$. We can then deduce the values of the condensed fraction without spin filtering or with spin filtering using eq.(5.70):

$$f_1 = 1 - \frac{S(y)}{\zeta(3)} \left(\frac{T_f}{T_{c,i}}\right)^3 \tag{5.75}$$

$$f_2 = \frac{n_{0,f}}{n_{0,f} + N_{th,f}^{(m_s^{min})}} = \frac{n_{0,f}/N_{Tot}}{n_{0,f}/N_{Tot} + N_{th,f}^{(m_s^{min})}/N_{Tot}}$$

$$= \frac{f_1}{f_1 + (\frac{T_f}{T_{c,i}})^3}. \tag{5.76}$$

We plot in Fig.5.29 f_1 and f_2 as a function of B_f for different values of the initial condensed fraction in the case of s=3.

Interpretation for f_1

Let us first discuss the case of f_1, the condensed fraction when spin filtering is not performed.

The same general behaviour is observed no matter f_i. We see Fig.5.29 that f_1 starts by increasing as the magnetic field is reduced. f_1 then decreases and becomes smaller than f_i. The lowest value of f_1 is obtained for B_f=0.

For high enough B field, depolarization of the thermal gas leads to an increase of the condensed fraction. This effect is associated with demagnetization cooling, a process previously demonstrated in the thermal regime where kinetic energy is transformed into magnetic energy as an atom occupies a spin excited state, and then is pumped back to the ground state [113]. When the experiment is performed at non-zero magnetic field, demagnetization of thermal $m_s = -3$ atoms is accompanied by cooling, as the process is endoenergetic. Therefore cooling associated with the transfer between magnetic and kinetic energy can lead to an increase in the BEC atom number *even without spin filtering*: $n_{0,f} > n_{0,i}$, and hence $f_1 > f_i$, as shown in Fig.5.29a). However, this effect is small compared to the three major effects described above.

Interpretation for f_2

Let us now discuss the case of f_2, the condensed fraction when spin filtering is performed for the case s=3.

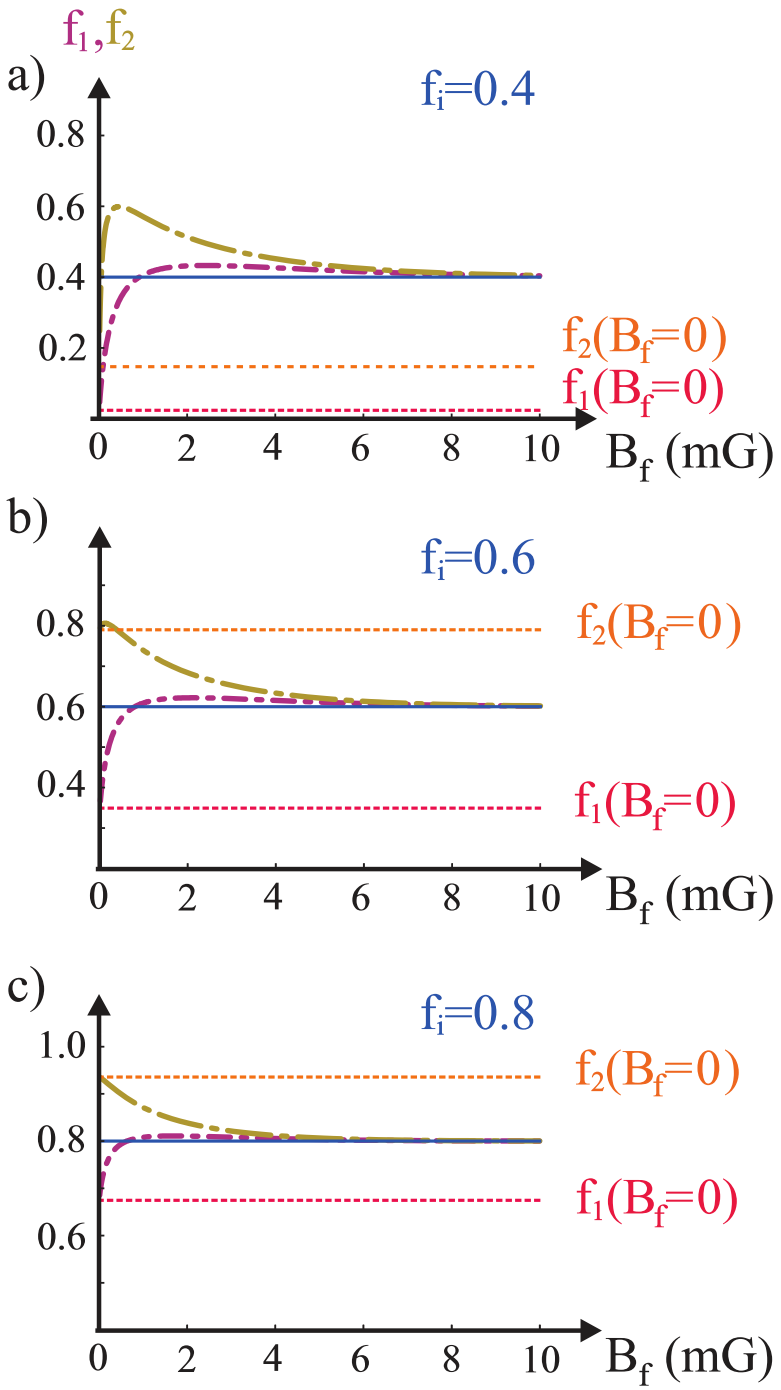

Figure 5.29: f_1 (in purple short dash-dotted line) and f_2 (gold, long dash-dotted line) as a function of B_f for s=3 and initial condensed fractions a) f_i =0.4, b) f_i =0.6,and c) f_i =0.8 (blue full line). We also indicate values of $f_1(B=0)$ and $f_2(B=0)$ for each initial condensed fraction. The same general behaviour is observed for f_1 no matter f_i. For f_2 there is three regimes depending on the value of f_i: $f_i < 0.449$, $0.449 < f_i < 0.63$, and $f_i > 0.63$.

The situation is a little bit more complex and we define three regimes depending on the value of f_i, the initial condensed fraction.

If $f_i > 0.63$, f_2 constantly increases as B_f is lowered. The maximum value for f_2 is obtained for B_f=0.

If $f_i < 0.449$, f_2 first increases as the magnetic field is lowered and a maximum value is obtained for a magnetic field $B_f > 0$, and then decreases and becomes smaller than f_i. The minimum value is obtained for $B_f = 0$.

If $0.449 < f_i < 0.63$, f_2 first increases as the magnetic field is lowered. Then a maximum value for a magnetic field $B_f > 0$ is obtained. Finally f_2 decreases but always remains larger than f_i no matter B_f.

We plot in Fig.5.29 f_2 as a function of B_f for each regime. We also indicate these regimes on our experimental data Fig.5.25.

Comparison with data

We superimpose to our data shown in Fig.5.25 and Fig.5.26 the prediction of our non-interacting theoretical model. Our model, with no free fitting parameter, accounts well for the experimental results, even if the experimental error bars are quite large. We thus are confident that it grasps the main physical processes at stake and we will rely on it for accounting for the cooling efficiency of our protocol and the limits of the cooling mechanism.

Cooling efficiency

To assess the efficiency of this cooling procedure we consider the reduction of entropy after one cooling cycle. Below T_c, all entropy is contained in the thermal fraction, and each thermal atom has a temperature-independent entropy of approximatively 3.6 k_B (see eq.(5.7)). As a consequence, selectively removing thermal atoms is an excellent way to remove entropy. With Σ_i the mean entropy per atom before depolarization, and Σ_f the mean entropy per atom after spin filtering. We have:

$$\frac{\Sigma_f}{\Sigma_i} = \frac{N_{th,f}}{N_{th,i}} = \frac{1-f_2}{1-f_i}. \tag{5.77}$$

This expression is minimal for B_f=0 and $f_i \to 1$, and reaches $\frac{1}{(2s+1)^{3/4}}$. In Fig.5.30 $\frac{\Sigma_f}{\Sigma_i}$ is shown for different values of B_f, as a function of T_i, in the case of Cr with $s = 3$. $\frac{\Sigma_f}{\Sigma_i}$ remains significantly smaller than 1 even at very low T_i, provided a low enough B_f field: a reduction of entropy by a factor of at least two is obtained until $k_B T_i \simeq g\mu_B \mathrm{B}_f$. Then, a lower B_f must be reached so that cooling may continue.

As T approaches 0, the thermal fraction gets smaller and smaller. Therefore spilling affects less and less atoms. However, the gain in entropy remains good, provided a low enough B_f. As a consequence, the efficiency of our spin cooling mechanism, defined as

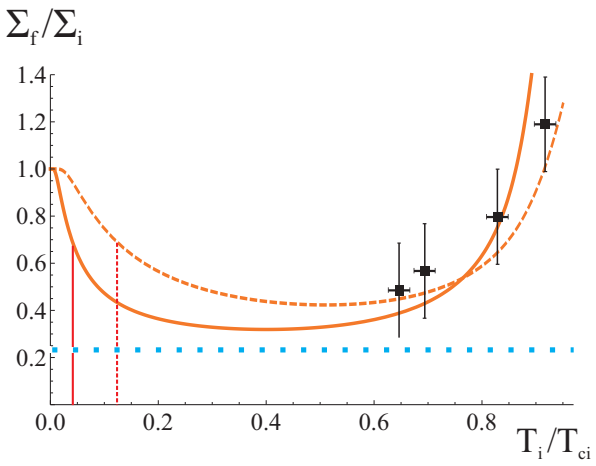

Figure 5.30: Theoretical results for the s=3 ^{52}Cr BEC. Ratio of final (after spin purification) and initial mean entropy per atom as a function of initial temperature, for B_f=0.3 mG (dashed) and B_f=0.1 mG (solid). The horizontal dotted line corresponds to the maximal gain, reached at $B_f \to 0$ and $T_i \to 0$ (given by eq.(5.66)). The vertical lines indicate the qualitative limit for cooling, set by $g\mu_B B_f \simeq k_B T$. The dots (black) correspond to experimental data taken at $B_f = 0.2 \pm 0.1$ mG, including statistical uncertainties.

the gain in phase space compared to the number of lost atoms, diverges as $T \to 0$:

$$\frac{\log(\frac{n\lambda_f^3}{n\lambda_i^3})}{\log\frac{N_{Tot,f}}{N_{Tot,i}}} = \frac{\log\frac{\Sigma_f}{\Sigma_i}}{\log\frac{N_{Tot,f}}{N_{Tot,i}}} \underbrace{\to}_{T\to 0} \infty \tag{5.78}$$

because $\frac{N_{Tot,f}}{N_{Tot,i}} \to 1$ while $\frac{\Sigma_f}{\Sigma_i} \to \frac{1}{(2s+1)^{3/4}}$ (< 1) if $B_f \to 0$.

The evolution of the efficiency of our cooling mechanism as a function of temperature is opposite to the one for evaporation. Evaporation is very efficient at high temperatures (where most of the energy carried away has a thermal origin), and in the quantum regime is not as efficient (where the chemical potential accounts for a non negligible part of the energy carried away by each evaporated atom). In contrast, the spin cooling mechanism discussed here is inefficient at high temperatures, and extremely efficient at low temperatures.

f) Limitations

Cooling limits

There are two limits in our cooling mechanism, one experimental and the other fundamental. (i) The control of the magnetic field experimentally sets a limit to the experiment. (ii) The value of the magnetic field below which the BEC is no longer in

one spin state. Indeed, our cooling mechanism assumes a BEC polarized in a well defined Zeeman state, which in general depends on conditions set by interactions between the atoms.

In the experiment reported here with Chromium which has a predicted cyclic ground state, a magnetic field larger than 100 μG is necessary in order to have a polarized BEC only in m_s =-3. This sets a limit of our cooling mechanism down to 30 nK.

For alkalis, we recall that a polar state is necessary to apply our mechanism for these non dipolar species. For Rubidium the ground state is ferromagnetic for a zero quadratic shift. At typical densities of 10^{14} at·cm^{-3}, a quadratic energy shift of typically 10 Hz, provided by a magnetic field of 380 mG, is necessary to ensure that the BEC is polar. Temperatures of the order of 500 pK could be obtained with such magnetic fields ($k_BT = h\times$ 10 Hz).

For Sodium, spin dependent interactions favor a polar $m_s = 0$ BEC. This is the most favorable scenario. Na, with a quadratic effect of 280 Hz/G^2, could achieve temperatures in the 100 pK range with B fields below $\simeq$ 100 mG. In this extreme regime, thermal population of spin-excited states is possible as long as $k_BT > q$. This limit ensures that the mesoscopic polar BECs does not suffer from spin fluctuations, so that the BEC is in a well defined spin state [181, 182]. If $q > k_BT/N$ with N the condensed atom number, spin fluctuations are a mesoscopic effect and the ground state cannot be considered polar anymore so that our cooling mechanism would not be efficient in this regime. This sets a practical limit to cooling in the pK range for sodium.

Inclusion of interactions

The effect of interactions was taken into account by including in ϵ_{k,m_s} the effect of spin-dependent contact interactions within the Bogoliubov approximation. Calculations were performed by P. Pedri. They show that interactions between particles lead to a stronger reduction in entropy at low temperature, due to a larger density of states in spin excited states.

Since the inclusions of interactions changes only quantitatively the non interacting picture, and not qualitatively, I will not discuss here these calculations. If one wants to deepen his understanding, please refer to Annexe 10.

Cooling with magnons

In parallel to this work, Olf *et al.* performed a similar cooling experiment [170]. In their experiment, they produce a polarized BEC of ^{87}Rb in state $|F = 1, m_F = -1 >$. They then perform a radio-frequency pulse and populate spin state $|F = 1, m_F = 0 >$. Immediately after the RF pulse, the population in spin state $|F = 1, m_F = 0 >$ has the same characteristics as the initially polarized degenerate Bose gas (namely it has the same condensed fraction). Thermalization leads for spin state $|F = 1, m_F = 0 >$ to a decrease in the number of condensed atoms (with zero energy) and an increase of

the number of thermal atoms (with typical energy $k_B T$). Thus the condensed fraction in $|F = 1, m_F = 0 >$ is lowered. The entire thermalization process takes place at constant energy. Therefore the increase in energy of the $|F = 1, m_F = 0 >$ component is accompanied by a lowering in energy of $|F = 1, m_F = -1 >$, and an increase of its condensate fraction.

This cooling mechanism bears strong similarities with the one presented in this chapter, it has however differences. Our loss mechanism is specific to thermal atoms. Here, the demagnetization process uses radio-frequency pulses, and therefore does not allow one to engineer a loss specific to non-condensed atoms. However, a cooling cycle with an RF-pulse does not take as much time as the one we propose here and does not need a precise control of magnetic field. It is relatively easy to perform several cooling cycles with a RF pulse. In our case, due to technical difficulties in controlling the magnetic fields, we were unable to perform spin cooling twice in an experiment.

An optimized spin cooling protocol would achieve spin filtering continuously: as atoms occupy spin excited states they are straight away lost. If performed with high enough initial condensate fraction, this could rapidly lead to very pure condensates.

Therefore, although our cooling mechanism is more efficient and has promising prospects, their process is more adapted to multiple cooling cycles and has already demonstrated its efficiency.

Measuring very cold samples

As very pure condensates are obtained, measuring small thermal fractions is a challenge. It is then advantageous to use the spin degree of freedom for thermometry, as explored in [97, 170]. At thermal equilibrium, atoms in different spin states share the same temperature. Preliminary results indicate that thermalization remains efficient even for very low temperatures [170]. Measuring the temperature or the number of thermal atoms in spin-excited states offers a background-free measurement, contrarily to the case of a bi-modal distribution when a BEC is present.

5.4.6 Conclusion and perspectives

In conclusion, we investigated an efficient cooling mechanism using the spin degree of freedom. It is based on redistribution of entropy among the spin states. Thermal atoms flow from the spin state where the BEC is present (m_s= -3 for Chromium) towards excited spin states. The BEC then melts in order to maintain saturation of the m_s= -3 thermal gas. This melting leads to a cooling of the thermal gas since condensed atoms are at $T = 0$ K. The thermal gas can then be saturated at a lower temperature.

In addition, cooling by spin filtering can be repeated an arbitrary number of times. Since each cycle leads to typically a factor of two reduction in mean entropy per atom, we foresee that this scheme could indeed be a way to reach new regimes of deep degeneracy.

Finally, one of the interesting pending questions is whether this scheme will help to remove entropy for BECs loaded in optical lattices. Indeed, even though low entropies are reached in the bulk, higher entropies are obtained in the lattice. It is accepted that most of the entropy lies in the superfluid shells surrounding the Mott plateaux characteristic of the typical wedding cake distribution [183]. If our cooling mechanism could be extended to be performed in the lattice, it could efficiently remove entropy and help the system in reaching low spin entropies.

Summary of *Part II*

In this part of my thesis, I focused my attention on thermodynamics questions. We first established how the mechanical and spin degrees of freedom can thermalize. We then analysed the co-evaporation of the fermionic isotope and extracted the scattering length of the Bose-Fermi scattering length. We then presented two experiments involving a Bose gas with a spin degree of freedom. We investigated the different dynamics for thermalization of the spin degrees of freedom and the mechanical degrees of freedom as a multi-spin component gas was cooled across the phase transition of BEC. Finally, we proposed and demonstrated a new cooling mechanism where the spin degree of freedom was used to store and remove entropy from a polarized BEC.

In the following part, we will focus our attention on spin dynamics. We will perform two experiments where the goal is to observe spin dynamics, due to dipole-dipole interactions, after our system is prepared out of spin equilibrium.

Part III

From classical to quantum magnetism using dipolar particles

CHAPTER 6

Classical and quantum magnetism

In this chapter, we will first show that a classical behaviour comes when correlations can be neglected. We then present how cold atoms are a platform to study quantum magnetism and establish how dipolar interactions may provide an interesting tool to investigate quantum magnetism. In chapter 7 and chapter 8 we present two experiments where atoms, prepared in spin excited states, interact via both contact and dipolar interactions. We hope to observe signatures of quantum correlations from the subsequent spin dynamics. We shall focus our attention primarily on dynamics due to dipolar interactions, the main originality of our system.

6.1 Classical magnetism of spins in a magnetic field

In the following we will establish the dynamics of N spins interacting in a magnetic field. Although we will talk about the spin of an atom, which has a quantum origin, the dynamics will be well described by particles which do not exhibit any spin correlations and are accounted for by classical equations (as a dipole would be).

6.1.1 One spin

Let us consider the magnetic moment of an atom due to electronic origin. For a spin s, electron charge $q_e = -q$, and electron mass m_e:

$$\vec{\mu} = -g_{Landé} \underbrace{\frac{q\hbar}{2m_e}}_{\mu_B} \frac{1}{\hbar}\vec{s} \tag{6.1}$$

with $g_{Landé} \approx 2$ the Landé factor and μ_B is the Bohr magneton. We can define the gyromagnetic factor γ such as $\gamma = g_{Landé}\mu_B/\hbar$.

If the atom is subject to an external homogeneous magnetic field $\vec{B}_{ext}$, the equation of motion reads [184]:

$$\frac{d\vec{s}}{dt} = -\gamma\vec{s} \times \vec{B}_{ext}. \tag{6.2}$$

The spin will precess at the Larmor frequency $\Omega = \gamma B_{ext}$ which is independent of the length of the spin. Therefore, the precession rate at high magnetic fields of the

electronic spin of Chromium atoms or Rubidium atoms (which have different electronic spin) will be the same.

The potential energy associated to the interaction between a spin and the magnetic field is given by

$$E = -\gamma \vec{s}.\vec{B}_{ext} \tag{6.3}$$

and the associated Hamiltonian is simply:

$$\hat{H} = -\gamma \hat{\vec{S}}.\vec{B}_{ext} \tag{6.4}$$

6.1.2 Two spins

Let us consider two classical spins of magnetic moment $\vec{\mu}_i$ in a magnetic field $\vec{B}_{ext}$. The evolution of each spin is simply:

$$\begin{aligned} \frac{d\vec{\mu}_1}{dt} &= \vec{\mu}_1 \times (\vec{B}_{ext} + \vec{B}(\vec{\mu}_2)) \\ \frac{d\vec{\mu}_2}{dt} &= \vec{\mu}_2 \times (\vec{B}_{ext} + \vec{B}(\vec{\mu}_1)) \end{aligned} \tag{6.5}$$

where $\vec{B}(\vec{\mu}_i)$ represents the field created by $\vec{\mu}_j$ and felt by $\vec{\mu}_i$. The field created at a position $\vec{r}'$ by a dipole $\vec{\mu}$ at a position $\vec{r}$ takes the following form:

$$\vec{B}(\vec{r},\vec{r}') = \frac{\mu_0}{4\pi}\Big(\frac{|\vec{r}-\vec{r}'|^2\vec{\mu} - 3(\vec{\mu}.(\vec{r}-\vec{r}'))(\vec{r}-\vec{r}')}{|\vec{r}-\vec{r}'|^5}\Big). \tag{6.6}$$

This function has the same expression under the permutation of $\vec{r}$ with $\vec{r}'$ if $\vec{\mu} = \vec{\mu}'$ which is the case if the dipoles are aligned by the external magnetic field. Each dipole therefore experiences exactly the same magnetic field and will evolve in the same manner. The two dipoles will therefore precess in synchronization and the total spin of the system will be conserved in time.

For an inhomogeneous system, for example two dipoles with different moments, each dipole will precess at different frequencies and the total spin might not be conserved even for a classical system.

6.1.3 N spins: mean field dynamics

We now extend the reasoning to N spins and adopt a quantum formalism. The Heisenberg evolution of the spin operator associated to one given spin reads:

$$\begin{aligned} \frac{d<\hat{S}>}{dt} &= \frac{i}{\hbar} <[\hat{H},\hat{S}]> \\ &= <\gamma \hat{S} \times (\vec{B}_{ext} + \sum_i \hat{\vec{B}}_i)> \end{aligned} \tag{6.7}$$

with $\vec{\hat{B}}_i$ the field created by dipole i.

If one neglects correlations in eq.(6.7), the average of the product is then equal to the product of the averages, then the equation of motion reads:

$$\frac{d < \hat{S} >}{dt} \approx \gamma < \hat{S} > \times(\vec{B}_{ext} + \sum_i < \hat{B}_i >). \tag{6.8}$$

Each dipole will precess around a magnetic field given by the sum of the external magnetic field with the one created by all the other dipoles. We recover a classical precession equation. This shows that spin dynamics is classical provided correlations are neglected. In the specific case of a BEC, neglecting correlations allows to approximate the BEC wavefunction as a product wavefunction and to retrieve the Gross Pitaevskii equation [23]. One must not be shocked at identifying the GPE to a classical equation since with the GPE we retrieve the classical Euler equations of hydrodynamics for a fluid.

6.2 Quantum correlations

Why should we go beyond this mean field approximation? Correlated states are at the heart of quantum mechanics and to overlook correlations is equivalent to overlooking some of the most fascinating aspects of quantum mechanics (e.g. entanglement cannot be understood in a classical way). Over the last decade, both theoreticians and experimentalists have been providing huge efforts towards creating and detecting N-body correlated systems.

The main approach of our work is to load atoms in an optical lattice and create a system which will evolve following a Hamiltonian under which correlated states may arise.

6.2.1 Cold atoms in optical lattices

Cold atom experiments offer a clean and controllable environment. Atoms can be loaded in an optical periodic potential. The depth of a lattice site, the tunneling between sites, the dimensionality, and the even disorder can be controlled [110].

Bosonic atoms in a lattice exhibit two distinct regimes separated by a quantum phase transition: the superfluid and the Mott regime. This phase transition was observed in 2001 in Munich [185] and is considered as the birth of the study of strongly correlated states of matter using cold atoms in optical lattices.

In the superfluid regime, the interaction strength U between particles occupying the same site is too weak compared to the atomic kinetic energy ("J" term) to keep atoms in a given site. Each atom is delocalized over the system and the gas has a global coherent phase. In the Mott phase, U/J is large enough that each atom is pinned to a

given site (because it costs too much energy to have two atoms in the same site) and the gas loses its global phase coherence.

The Hamiltonian associated to cold bosonic atoms loaded in an optical potential is very similar to the Bose-Hubbard Hamiltonian of condensed matter [110]:

$$\hat{H}_{BH} = -J \sum_{<i,j>} \hat{a}_i^\dagger \hat{a}_j + \frac{1}{2} U \sum_i \hat{a}_i^\dagger \hat{a}_i^\dagger \hat{a}_i \hat{a}_i + \sum_i (V_i - \mu) \hat{a}_i^\dagger \hat{a}_i. \tag{6.9}$$

with $\hat{a}_i$ ($\hat{a}_i^\dagger$) the bosonic annihilator (creator) operator applied to site i, and J represents the hopping of an atom between neighbouring sites. The main difference with the Bose-Hubbard Hamiltonian of condensed matter is in the third term where the energy offset between neighbouring sites due to a slowly varying external trapping potential $V(x)$ is taken into account.

6.2.2 Quantum magnetism

We have not yet addressed the question of how the spin of the atoms organize themselves. Do spins prefer aligning themselves with their neighbour or would they rather anti-align themselves? What are the magnetic properties of Mott insulator systems? How do interacting spin systems evolve? These are the questions that the field of quantum magnetism attempts to answer to and in this part of my thesis we will focus on bringing answer elements to the last of these questions.

Condensed matter systems

Let us first see how magnetism arises in condensed matter systems and consider a 1D chain of N fermions of spin $s = 1/2$ which models the behaviour of electrons in a 1D cristal. For a finite on site interaction U between fermions of different spin states, two fermions can temporarily be in the same site after one atom undergoes a tunneling event. There are then two possibilities: (i) the same atom can sucessively tunnel back, thus leaving the system unchanged, or (ii) the "other atom" can tunnel. This is depicted in Fig.6.1. This latter double tunneling event (called super-exchange) is equivalent to a spin flip of the atom pair. The rate associated to a super-exchange event is $\frac{J^2}{U}$ and the spin flip is associated to $S_i^- S_{i+1}^+$ + h.c. operators. The double tunneling event which does not result in any spin exchange is equivalent to an Ising term. Thus the total Hamiltonian of the system is equivalent to:

$$\hat{H} = \sum_i + \frac{2J^2}{U} \left(\hat{S}_i^- \hat{S}_{i+1}^+ + \hat{S}_i^+ \hat{S}_{i+1}^- \right) + \frac{4J^2}{U} \hat{S}_i^z \hat{S}_{i+1}^z \tag{6.10}$$

which can be cast under the form of the Heisenberg hamiltonian of magnetism:

$$\hat{H} = J_{ex} \sum_i \vec{\hat{S}}_i . \vec{\hat{S}}_{i+1} \tag{6.11}$$

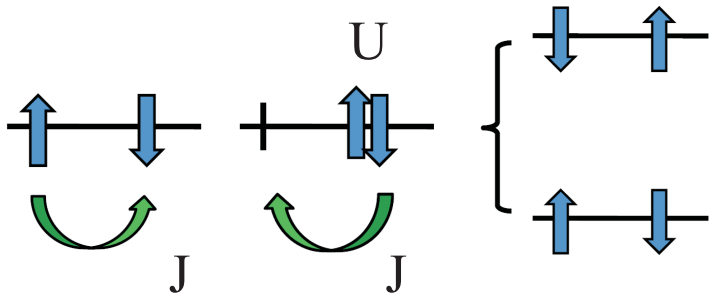

Figure 6.1: Cartoon illustrating a spin flip process mediated by super-exchange interactions. The atom in the left site can tunnel to its neighbouring site. Then the other atom has the possibility to tunnel to left site. This double tunneling process, called super-exchange, is equivalent to a spin flip process. Image adapted from [186].

with $J_{ex} = \frac{4J^2}{U}$ (see [186] for an exact derivation using perturbation theory). The super-exchange process is equivalent to an effective spin-spin interaction. Thus magnetism arises without any magnetic interaction. This super-exchange mechanism is at the origin of magnetism in insulators. There are two cases to consider: $J_{ex} > 0$ and $J_{ex} < 0$. For $J_{ex} < 0$, the interaction energy of two spins favors them to be parallel. This corresponds to the ferromagnetic case. For $J_{ex} > 0$, two spins would rather be in an antiparallel configuration. This corresponds to the anti-ferromagnetic case.

Cold atoms systems

In cold atom experiments with different spin states, super-exchange mechanisms also take place. Thus a cold atom experiment can properly engineer the Heisenberg Hamiltonian. This is very appealing system to study magnetism with effective spin systems, with Bosons or Fermions.

Numerical exploration of Fermi-Hubbard model is more complicated than for the Bose-Hubbard one, and ground state properties for fermions other than for half-filling (i.e. for an $s = 1/2$, this corresponds to the situation with one atom per site) are still not well known. One possibility explored in cold atomic systems, is to prepare fermions in a lattice and investigate the properties of the Fermi-Hubbard model. The goal of these studies is to understand the behaviour of electrons in solids. The Graal would be an explanation of high T_c superconductors. Even though no complete theory of high-temperature superconductivity exists, it is suggested (see [187] for example) that the Fermi-Hubbard model may contain its essential ingredients. For an unpolarized Fermi gas, J and U are both positive which implies that the ground state is an anti-ferromagnetic singlet state [188]. This anti-ferromagnetic order is predicted at temperatures lower than the Néel temperature $T < T_N$ for half-filling (which is the condensed matter equivalent of no doping). Properties away from half-filling remain unknown. Fig.6.2 shows a sketch of the phase diagram of a high-temperature supercon-

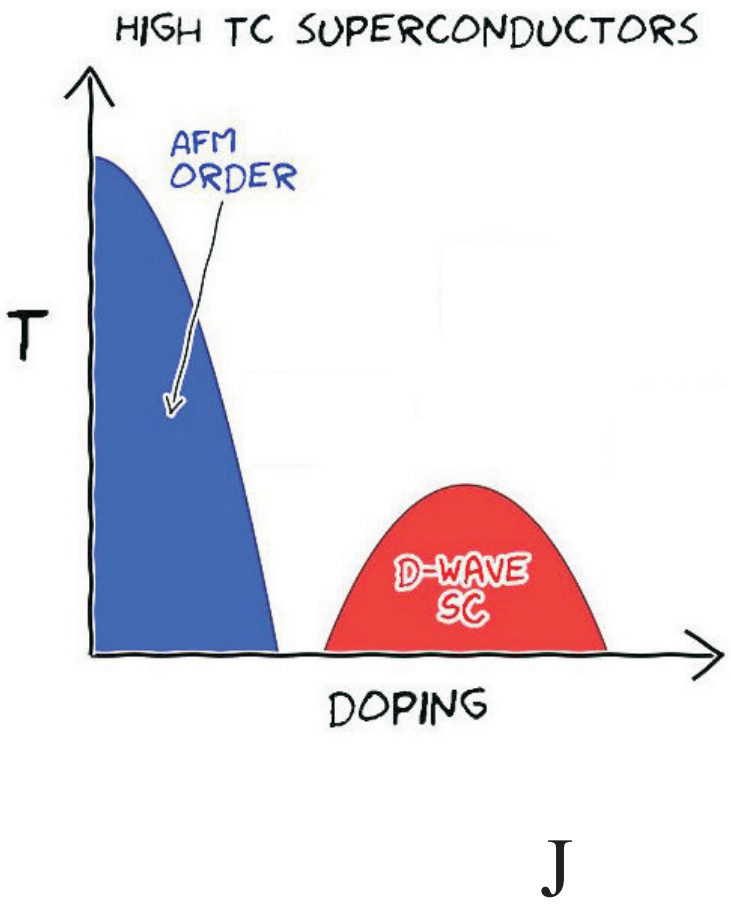

Figure 6.2: Sketch of the phase diagram of a high-temperature superconductor taken from [190]. At zero doping and low temperatures, they exhibit anti-ferromagnetic order. As hole doping is introduced, their anti-ferromagnetism disappears in favour of a superconducting state with high critical temperature.

ductor. However, it is difficult with a cold atom experiment to reach as low entropies Σ as in condensed matter systems. Indeed, the Fermi temperature T_F of a typical solid is $\sim$ 10000 K [189]. A condensed matter system at liquid Nitrogen temperature is already at $T/T_F < 0.01$ ($\Sigma \propto T/T_F$). To my knowledge, the lowest entropy systems with cold atomic Fermi gases are at best $\frac{T}{T_F}$=0.05. However, some experiments have started exploring this anti-ferromagnetic regime by cleverly redistributing entropy within the system and have observed anti-ferromagnetic correlations [172, 173]. From there on, the goal is to reach lower entropies deep in the anti-ferromagnetic regime. Then the filling can be tuned to see if the Hubbard model contains the essential ingredients in order to enter the superconducting phase. Hence the importance of working on new cooling method such as the one described in chapter 5.

The Bose-Hubbard model has been intensively studied numerically and most of the

ground state properties are known. However, out of equilibrium properties are not yet well understood and it is one of the main interests in loading bosons in a lattice and it is the interest of the experiments I will present in the following chapters.

6.2.3 Quantum magnetism with a dipolar system

As mentioned above, the effective spin-spin interactions (called super-exchange interactions) give rise to the Heisenberg Hamiltonian. However, it is possible to study magnetism with a "real" spin-spin interaction between particles. One approach is to study interactions between polar molecules. Their induced electric dipole moment being large, spin exchange processes between polar molecules loaded in a lattice have been observed [34]. Despite the challenge of producing cold molecules, it is an appealing system since one may tailor the relative contribution of the Ising and spin exchange term of the Hamiltonian. Here in Villetaneuse, we explored Quantum Magnetism driven by magnetic dipole-dipole interactions between Chromium atoms.

Effective dipolar Hamiltonian

Dipole-dipole interactions create an interaction between lattice sites nearly independent of the lattice depth. I recall the form of the dipole-dipole Hamiltonian:

$$\begin{aligned}\hat{H}_{dip} &= \frac{d^2}{r^3}\left(\frac{1}{2}(\hat{S}_{1+}\hat{S}_{2-}+\hat{S}_{1-}\hat{S}_{2+})+\hat{S}_{1z}\hat{S}_{2z}\right)\\ &- 3\frac{d^2}{r^5}\Bigg(\hat{S}_{1z}\hat{S}_{2z}z^2\\ &+ (\hat{S}_{1z}\hat{S}_{2-}\frac{zr_+}{2}+\hat{S}_{1-}\hat{S}_{2z}\frac{r_+z}{2})+c.c.\\ &+ (\hat{S}_{1+}\hat{S}_{2+}\frac{r_-^2}{4}+c.c.)\\ &+ (\hat{S}_{1+}\hat{S}_{2-}\frac{r_-r_+}{4}+c.c)\Bigg)\end{aligned} \tag{6.12}$$

where $d^2{=}\mu_0/4\pi(g_{Landé}\mu_B)^2$ (μ_0 being the magnetic permeability of vacuum, $g_{Landé}$ the Landé factor, and μ_B the Bohr magneton) and r is the distance between atoms.

The Hamiltonian has two different types of collisions: collisions which conserve magnetization and collisions which do not. Keeping in eq.(6.12) collisions which conserves transverse magnetization, the dipolar Hamiltonian then has the following form:

$$\hat{H}_{dip}^{eff}=\sum_{i,j}\frac{d^2}{|r_i-r_j|^3}\left(\hat{S}_i^z\hat{S}_j^z-\frac{1}{4}(\hat{S}_i^-\hat{S}_j^+ + \hat{S}_i^+\hat{S}_j^-)\right)[1-3\hat{z}^2] \tag{6.13}$$

This Hamiltonian is known as the secular dipolar Hamiltonian in the context of Nuclear Magnetic Resonance [191]. It shares strong similarities with the Heisenberg Hamiltonian: they have the same operators but with different relative coefficients.

The Heisenberg Hamiltonian describes an effective isotropic spin-spin interaction between spin 1/2 fermions. Here, the effective dipolar Hamiltonian describes a long range anisotropic spin-spin interactions between particles. Therefore each atom interacts with all the other atoms. Can magnetism arise in our situation? Also, the ratio of the coefficients in front of the spin operators are different (we would have +1/2 instead of -1/4). This difference breaks the rotational symmetry of the spin part of the Hamiltonian. The spin dynamics in a lattice observed in chapter 8 will be attributed to this ratio difference. Particles may also have a larger spin than 1/2, this leads to spin exchange dynamics where the population in a given spin state may evolve in time (whereas no population dynamics takes place for $s = 1/2$).

Also, large spin atoms have several scattering lengths associated to different molecular potential which, as discussed in chapter 5, leads to contact spin dynamics.

Turning off magnetization changing collisions

Despite the long range character of dipolar interactions, dipolar relaxation is a local process at the scale of the lattice [87]. The inter-particle distance $R_{RD}^{(j)}$ at which a dipolar relaxation collision takes place is:

$$R_{RD}^{(j)} = \frac{16\hbar}{3\pi\sqrt{m(j \times g_{Landé}\mu_B B)}} \tag{6.14}$$

where j denotes which dipolar relaxation canal was used (see subsection 3.1.2). In the experiments presented in chapter 8, we perform experiments in a lattice with a spacing $R_{Lat} = \lambda/2 = 266$ nm. The typical magnetic fields for each experiment is 10 mG and 360 mG. This corresponds to $R_{RD}^{(1)}(B = 10 \text{ mG}) = 140$ nm and $R_{RD}^{(1)}(B = 360 \text{ mG}) = 23$ nm.

In the first set of experiment of chapter 8, intrasite magnetization changing collision are suppressed by setting the magnetic field to a low value such that the magnetic energy released during a magnetization changing collisions is smaller than the first band excitation. In an optical lattice, dipolar intrasite magnetization changing collisions are a resonant process which can be suppressed [192]. In this experiment we have $B = 10$ mG, leading to $R_{RD}^{(1)}(B = 10 \text{ mG}) < R_{Lat}$: intersite magnetization changing collision might not be completely negligible. However the experimental magnetization is constant over the experimental timescales indicating that intersite dipolar collisions occur on a longer timescale and can in practice be neglected.

In the second set of experiments of chapter 8, the experiments were performed at high magnetic field (typically 360 mG). Here, we have $R_{RD} << R_{Lat}$: dipolar relaxation in a lattice may only occur between particles in the same lattice site. The magnetic energy released during an intrasite magnetization changing collision is transferred into kinetic energy. If the kinetic energy is much larger than the trap depth, the pair of colliding atoms are lost. Therefore, atoms remaining in the trap have only experienced magnetization conserving collisions and have evolved through $\hat{H}_{dip}^{eff}$. Losses can be

accounted for in the model independently with a spin dependent loss term. However, one must be careful when omitting dipolar relaxation events in the manner announced above since a pair of $m_s = -3$ atoms do not have any dipolar relaxation channels. Magnetization will then not be exactly conserved during the experiment due to the fact that $m_s = -3$ atoms are not lost, while atoms in other spin states suffer losses.

6.2.4 Quantum magnetism approach in our laboratory

We are interested in observing quantum correlations created by dipole dipole collisions. However, spin exchange contact collisions also take place and create correlated states.

In a first set of experiments (see chapter 7), we will load our Chromium BEC in a double well trap. Each well will be composed of atoms in a stretched spin state, with the spin of atoms in one well being in the opposite spin state of atoms in the other well, thus forming two giant dipoles of spin Ns interacting via Dipole Dipole interactions. The question we address in this part, is whether the magnetic field created by a dipole of large spin Ns may develop quantum correlations. We will be interested in looking for violations of the mean field rate equation for precession (eq.(6.8)).

In a second set of experiments (see chapter 8), atoms are prepared in an out-of-equilibrium spin state and evolve under H_{dip}^{eff} but also due to contact spin exchange collisions. These experiments are performed in a lattice with a variable depth, going continuously from the superfluid regime to the Mott regime. We want to understand if quantum correlations can develop in a system of bosons (with larger spin) interacting through a real spin-spin interaction (i.e. Dipole Dipole interaction). The spin excitation will be performed from two different techniques: (ii) with a tensor light shift which allows preparation of atoms in spin excited state m_s = -2 or (ii) with a Radio Frequency pulse tilting the spin of the atoms. We measure the evolution of population of each spin state as a function of time (a feature not possible for a s=1/2 system since there the population in a given spin state is constant in time at constant magnetization). We study if quantum correlations can take place for such a system, and if there are any conditions for there appearances.

CHAPTER 7

Classical magnetism with large ensembles of atoms

In this chapter, we present the experimental details in order to prepare a double well trap for our Chromium BEC. We load atoms in the double well trap and prepare the atoms of one well in the spin state m_s= +3 and leave the atoms of the other well in m_s= -3. We have thus prepared two giant spins interacting via DDI. We find that these giant spins behave as two classical magnets and in practice we observe no spin dynamics (which we interpret as metastability).

7.1 Introduction

In this chapter we will discuss the implementation of a new trap (referred to as double well trap) in which we will load two BECs (of N atoms each) where each well can be seen as a macroscopic object of spin $S = Ns$, with s the spin of an atom.

In the present experiment, atoms are initially prepared in both wells in opposite stretched spin states. If we consider atoms of one of the wells, two atoms locally interact only through the $S = 6$ molecular potential, and no local contact spin-exchange is possible (see chapter 3 or [193]). Therefore if the two wells are fully separated no spin dynamics associated with contact interactions is possible.

Our new trap thus enables us to create a purely dipolar system of two giant spins of 2N atoms, each interacting only via dipole-dipole interactions.

7.2 A double well trap for spin dynamics

7.2.1 Optical setup

To build a double well trap, we use an interference pattern resulting from the interference of two light beams produced by the Verdi[1] laser. In order to have a BEC loaded in just two wells, the size of the BEC must be of the same order as the fringe spacing. We measure the trapping frequencies of the IR ODT to be

$$\omega_{x,y,z} = 2\pi(520 \pm 12, 615 \pm 15, 395 \pm 12)\text{Hz} \tag{7.1}$$

[1] The same Verdi laser which pumps the Ti:Sa1

We deduce the following Thomas Fermi Radii ($R_{x,y,z} = \sqrt{\frac{2\mu}{m\omega^2_{x,y,z}}}$) for a Chromium BEC of 10^4 atoms:

$$R_{x,y,z} = (2.5, 2.1, 3.3)\mu\text{m}. \tag{7.2}$$

The fringe spacing induced by one retro-reflected lattice beams is $i = \lambda/2 \approx 260$ nm. Since $2R_{x,y,z} \sim 20 \times i$, loading the BEC with one retro-reflected lattice beam would result in the loading of about 20 wells. We cannot use a lattice beam in order to produce a double well trap and we therefore set up a new optical path shown Fig.7.1. We chose to produce the interference pattern from two beams which are separated spatially by a distance d before being focused by a lens. The lens we use (which belongs to the PixelFly imaging system) is positioned so that its focal plane matches the BEC position. The two trapping beams will then overlap at the focal plane and produce an interference pattern along $\vec{y}$ as shown on the sketch Fig 7.2. The interfringe spacing is:

$$i = \frac{\lambda}{2\sin\frac{\theta}{2}}. \tag{7.3}$$

The optical path we use (shown Fig.7.1 and Fig.7.2) imposes that the focal length of the last lens before the atoms is $f = 200$ mm. To satisfy $i \sim 2 \times R_y \sim 4.2$ μm, we need $\theta \approx 0.12$ rad and

$$\begin{aligned} \tan\frac{\theta}{2} &= \frac{d}{2f} \\ \rightarrow d &= 2.5 \text{ cm}. \end{aligned} \tag{7.4}$$

To prepare such an optical setup, an incoming beam, coupled through a polarization maintaining fibre, is split into two parallel beams spatially separated by 10 mm, using a non-polarizing lateral displacement beam splitter. The beam's waist is then 1.1 mm and their power can be varied up to 1.5 W simultaneously. A 2.5 magnification telescope increases their separation to the desired value of 2.5 cm. These beams then propagate through a dichroic mirror (with 90% transmission for light at 532 nm) and then focus on the BEC thanks to the achromatic doublet of focal length 200 mm used for imagery. One advantage of this setup is that apart from the optical path in the beam splitter, both beams go through the same optics. This allows for common-mode rejection of the phase noise. Therefore, we only need to pay attention to phase noise induced by the beam splitter. It was estimated that a variation of 1 K in the temperature of the crystal of the lateral beam splitter can induce a phase variation of 2.14 rad between the two beams [194]. We therefore stabilized the beam splitter in temperature and obtained a fluctuation of 22 mK over an hour [37, 194].

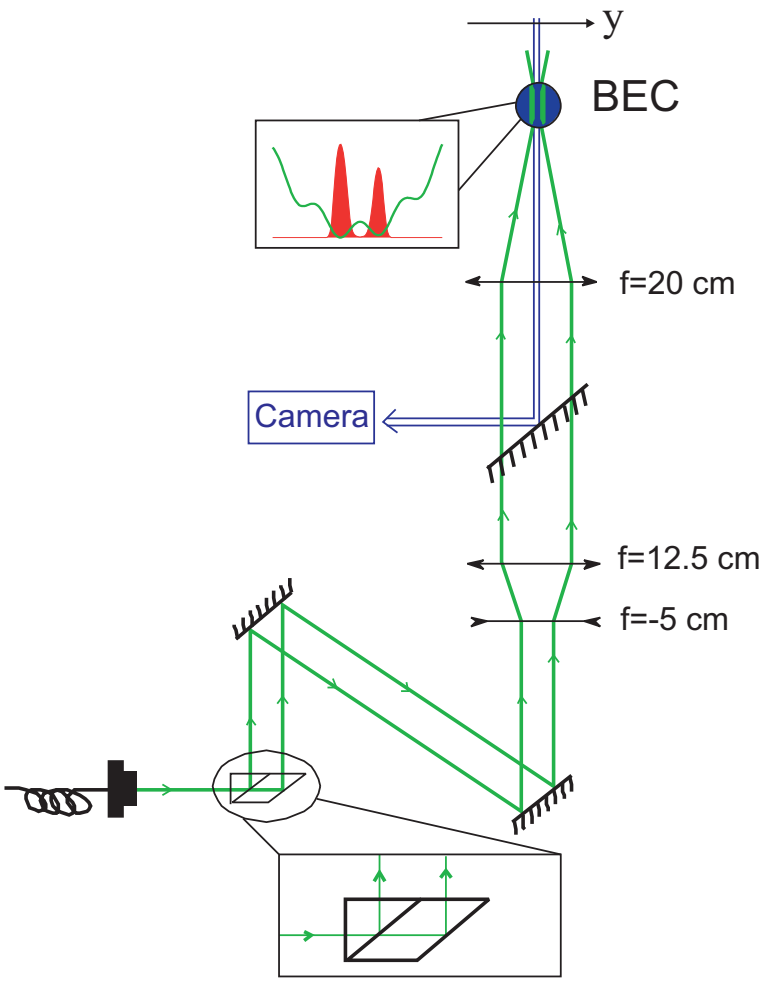

Figure 7.1: Scheme of the optical setup producing a double well trap. An incoming beam goes through an AOM which allows for control of the beams power, is coupled in a fibre, then it is split in two beams using a non-polarizing lateral displacement beam splitter. It is further separated by a 2.5 telescope to reach the separation required, goes through a mirror which reflects 425 nm light, and is then focused on the atomic plane by the first lens of the imaging setup described in section 1.4. Image adapted from [37].

7.2.2 Trap characterization

Loading the double well trap

The double well trap is aligned to form on the position of the BEC in the IR trap. Once the BEC is produced, we ramp the power of the double well trapping beams to 1.5 W in 100 ms. This time is chosen in order to be as short as possible, but still long enough that the loading is adiabatic. In Fig.7.3 we show a false color in situ image

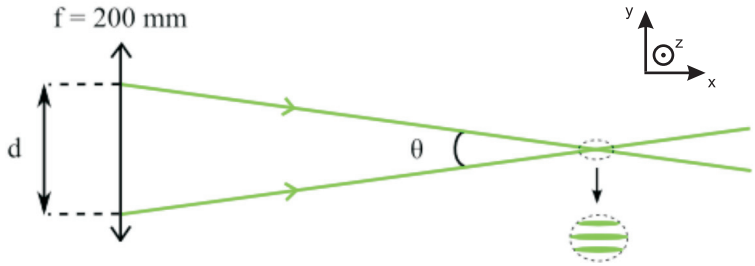

Figure 7.2: Sketch illustrating the interference pattern formed by two co-propagating beams with an angle θ. Image adapted from [37].

after having ramped up the power of the double well trap, this confirms that we load two distinct wells.

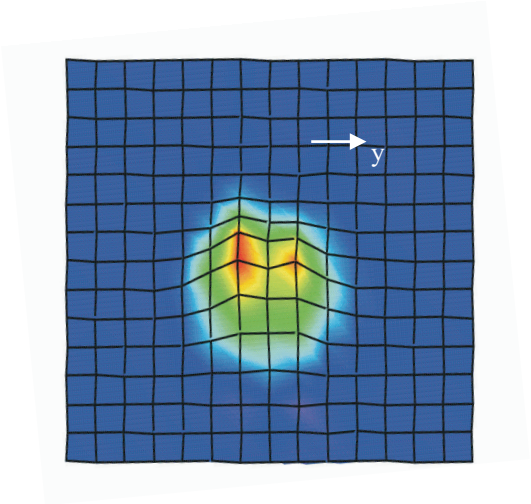

Figure 7.3: *In situ* absorption image of a the BEC loaded in the double well trap. Only two intensity maxima are observed which we interpret as that only two wells are effectively loaded. However there is an unbalance in their population.

Another way to confirm that we indeed load the BEC in two distinct wells is through the observation of matter wave interferences. Once the atoms are loaded in the double well trap, we turn off all trapping lights, let the gas expand for a time of flight of 5 ms and take an absorption image. We observe an atomic distribution with fringes (Fig.7.4). We interpret these fringes as the result of the interference between two coherent gases and we conclude that the double well was successfully loaded. As for optical interference setups, an unbalance in the intensity of the sources lead to a reduction in the contrast

of the interference pattern. A similar phenomenon takes place here: the fluctuations in the loading of the double well trap lead to a fluctuation of the observed contrast.

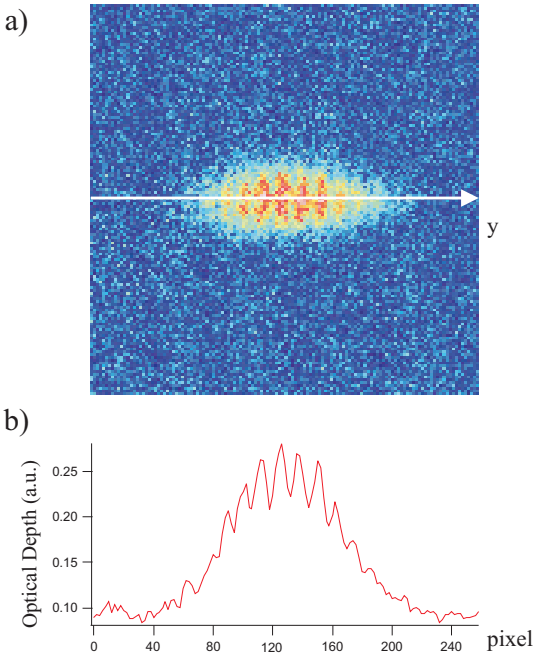

Figure 7.4: a) Absorption image after a BEC is loaded in a double well trap and expanded for a 5 ms TOF. The image shows a matter wave interference pattern revealing that the double well is indeed loaded. b) Integration along y of the absorption image, showing the interference pattern.

Trapping frequencies

We measure the trapping frequencies (by means of parametric excitation) of our double well trap to be $\omega_{x,y,z} = 2\pi(1090 \pm 70, 5630 \pm 650, 1390 \pm 100)$Hz for a total 532 nm light power of 1.5 W. For a given well loaded with 5000 atoms, we deduce a Thomas-Fermi of $R_{x,y,z} = (2.5, 0.5, 1.9)$ μm. For 5000 atoms in a well, we calculate the critical temperature to be T_c= 1.6 μK.

Potential barrier

From the trapping frequencies we can estimate the height V_0 of the barrier between the two wells. The sinusoidal potential $V(y)$ can be approximated as a harmonic potential around a minimum of the potential since the potential barrier is much greater than the

temperature T of the gas ($V_0 >> k_B T$). We can then extract V_0:

$$\begin{aligned} V(y) &= V_0 \sin^2 2\pi \frac{y}{2\Delta} \\ &\approx V_0 \left(\pi \frac{y}{\Delta}\right)^2 \\ &\approx \frac{1}{2} m\omega_y^2 y^2 \\ \rightarrow \quad \frac{V_0}{k_B} &\approx \frac{1}{k_B} \frac{m\omega_y^2 \Delta^2}{2\pi^2} \approx 6\ \mu\text{K for } \Delta = 4\mu\text{m} \end{aligned} \tag{7.5}$$

with Δ the interfringe spacing.

Trap stability

We noticed fluctuations in the loading of the double wells. To characterize the origin of these fluctuations, we produced a BEC in the IR ODT and pulsed the double-well trapping lights at the same time we pulsed the imaging light. An interference pattern is visible. It arises from the interference pattern created by the two beams of the double well trap. Atoms which were on a maximum of intensity of the interference pattern will be shifted off resonance due to the very large light shift of the $|^7P_4>$ state. This large light shift is due to the vicinity of a transition frequency from $|^7P_4>$ with the Verdi light. They will not be sensitive to the imaging light, contrarily to atoms on a minimum of intensity. For each image, we fit the doubly integrated atomic density along x and z by the following function:

$$I(y) = I_0 \sin(ky + \phi) e^{-\frac{(y-y_0)^2}{w^2}}. \tag{7.6}$$

Here we approximate the BEC spatial distribution by a Gaussian, y_0 (w) relates to the position of the center (the 1/e size of the BEC), k is the spatial frequency associated to the fringe spacing and ϕ a phase. Fluctuations of the BECs position will result in a fluctuation of y_0 whereas fluctuations of the relative phase between the two interfering trapping beams will result in fluctuations of ϕ. The result of this experiment for 45 *in situ* images is shown Fig.7.5. The stability of the position of the fringes is extremely good, the standard deviation of the fringe position is 100 nm: the phase between the interfering beams is well defined. From a fit to the Optical Density (inset Fig.7.5) we can also deduce an experimental value of the interfringe. We measure i= (3.9±0.2) μm, close to the desired value of 4.2 μm. The stability of the position of the BEC is poor. The standard deviation of the BEC position is 1 μm. Since the fluctuations of the BECs position are of the same order as its size and as the fringe spacing, we understand why the loading of the trap is not reproducible (i.e. the number of atoms trapped in each of the two wells)[2].

[2] After writing the manuscript, it was pointed out that a non-adiabatic loading may also explain instabilities.

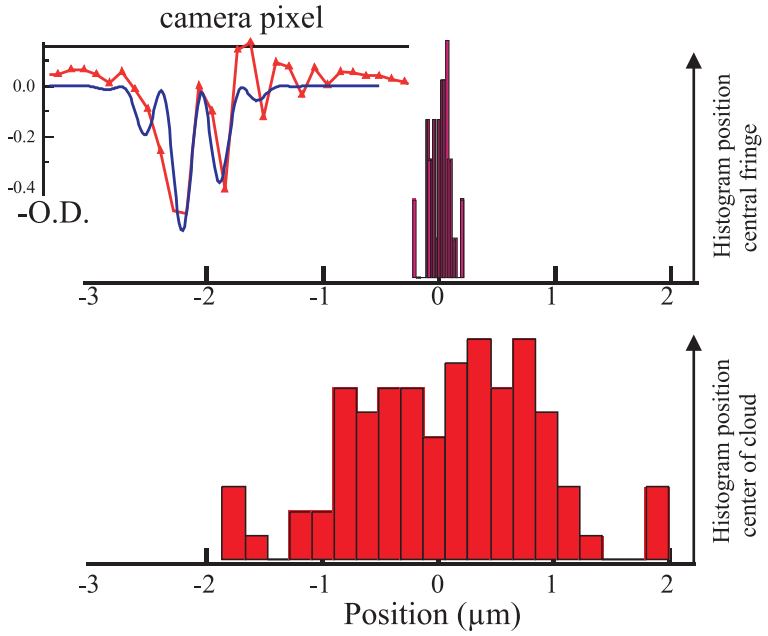

Figure 7.5: Double well trap stability. The top curve shows (red triangles) the doubly integrated optical depth revealing the density distribution. The (blue) full line is a fit using a Gaussian modulated by a sinusoidal function. From the fitted phase of the sinusoidal function, we derive a histogram of the position of the central dark fringe, which is stable to 100 nm. From the center of the Gaussian, we derive histograms of the position of the atomic distribution, which reveals that standard deviation of the BEC position is 1 μm (same order as its size).

We interpret the fluctuation of the BEC position resulting from a fluctuation of the pointing of the IR laser beam from one experiment to another. In order to increase the stability of the experiment one would need to reduce the pointing fluctuation (for example with the implementation of a pointing lock on the IR beam).

7.2.3 Spin preparation

Evaporation in the IR ODT produces a BEC in the lowest Zeeman state $m_s = -3$. We have successfully loaded the BEC in the double well trap and thus have two atomic ensembles in spin state $m_s = -3$. We are interested in spin dynamics triggered by DDI between atoms of different wells. To do so we prepare atoms of one of the wells in an excited spin state, $m_s = +3$, with a Radio-Frequency sweep. A sketch of the initial state is shown Fig.7.6.

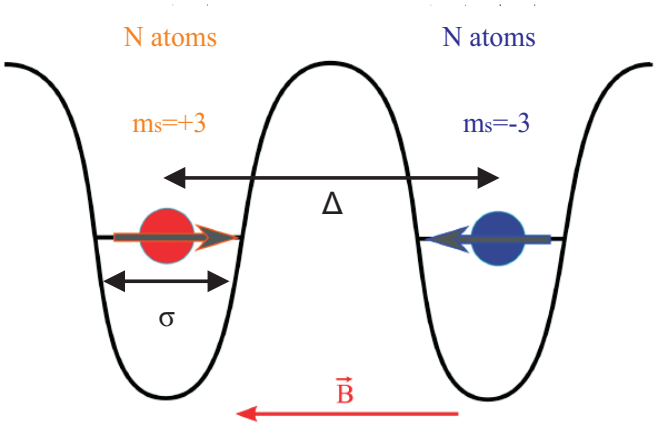

Figure 7.6: Sketch of the initial state of the experiment. Image adapted from [37].

A magnetic gradient along y

We are able to prepare atoms in $m_s = +3$ by Rapid Adiabatic Passage. To be able to prepare atoms of only one well in an excited spin state with this method, each atomic ensemble needs to experience a different magnetic field. This is achieved by applying a magnetic gradient along the direction of the wells (i.e. along $\vec{y}$).

At the start of the experiment, the magnetic field at the BEC position is $g_s\mu_B B/h$ =200 kHz. The magnetic field is mainly along the y direction. We then apply a magnetic gradient of $g\mu_B b/h$=2.5 kHz·μm^{-1} with the MOT coils. This results in a difference in magnetic field resonance of approximatively 10 kHz between two wells separated by Δ= 4.0 μm.

Radio-Frequency sweep

After the magnetic field gradient is applied, we perform an RF sweep, whose amplitude follows a Gaussian temporal profile. Such pulse shaping (similar to the Blackman window commonly used in atom interferometry [195]) is necessary in order to avoid the fast frequency components associated with instantaneous turn-on and turn-off of the RF field, which in practice are sufficient to spoil the selectivity of the RF sweep. With a 5 ms RF sweep, whose span and peak Rabi frequency are 30 and 1.5 kHz, respectively, we successfully flip the atomic spins selectively in one well, leaving unchanged the spin of the atoms in the other well. We estimate the efficiency of the sweep to be approximatively 90 %.

Turning off the magnetic gradient

No intersite spin exchange dynamics can take place until the magnetic gradients is turned off. Indeed as long as the magnetic resonance between the two wells are different, exchange mediated by DDI is then an off resonance process [91]. There is also no intra site dynamics since atoms colliding through contact interaction are in the stretch state $|s = 3, m_s = +3 >$ or $|s = 3, m_s = -3 >$ from which no spin exchange processes may take place. Thus this system is a purely dipolar system of two giant spins.

Monitoring the spin distribution of each well

To measure the evolution of the different spin populations, we turn off the vertical trapping beam and use a Stern-Gerlach procedure to separate the different spin states along the horizontal trapping beam. We apply a magnetic field gradient of 0.25 G·cm^{-1} with the MOT coils along x. We perform an absorption image using the PixelFly camera (see section 1.4) along the x direction. The details of this procedure are explained in detail in [37] and briefly in section 1.5.

We show in Fig.7.7 an absorption image taken right after spin preparation (for $t = 0$). Atoms on the left correspond to negative m_s states, whereas atoms on the right correspond to positive m_s states. The signal asymmetry is due to different efficiencies in the absorption imaging of the different m_s states. The experimental ramps are summarized in Fig.7.8.

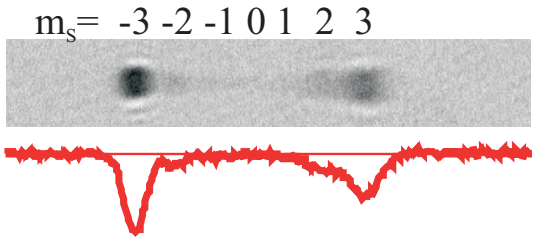

Figure 7.7: A Stern-Gerlach image taken after an RF-sweep which only addressed the atoms in one of the wells. The atoms at the left of the picture are atoms unaltered by the RF. They were at the left-well position, and they remained in $m_s = -3$. Atoms at the right of the picture have been affected by the RF, because they are in the right well. The RF sweep has promoted them to $m_s = +3$. We measure populations in spin states $m_s \neq \pm 3$. Atoms in $m_s = +2$ are attributed to atoms in the right well having experienced a dipolar relaxation process. Atoms in $m_s = -2$ are attributed to contact collisions between $m_s = -3$ atoms from the left well with atoms in $m_s = +2$ originally in the right well who suffered a dipolar relaxation and crossed the potential barrier (about 20% of the atoms of the right well have enough energy to cross the barrier).

The Stern-Gerlach image shown in Fig.7.7 was taken after an RF-sweep intended to only address the atoms in one of the wells. Our interpretation of this image is the

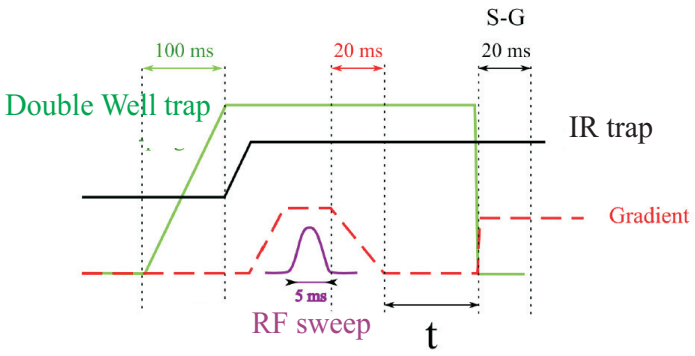

Figure 7.8: Once a BEC is produced at the end of evaporation in the ODT, we load the double well trap in 100 ms. We then apply a magnetic gradient so that the Zeeman energy of each well differs and apply an RF sweep to promote atoms in one well to $|s = 3, m_s = +3 >$. We then turn off the magnetic gradient. Once the magnetic gradient is off, spin exchange processes can take place during t ms. We then image the number of atoms in each spin state through a Stern-Gerlach imaging process. Image adapted from [37].

following. The atoms on the left of the image are atoms unaltered by the RF. They were at the left-well position, and they remained in $m_s = -3$. Atoms at the right of the picture have been affected by the RF (they are in spin state $m_s \neq$ - 3), because they are in the right well. The RF sweep has promoted them to $m_s = +3$.

Following the system preparation, contact spin mixing mechanisms do not take place, however dipolar spin mixing mechanisms can eventually populate all spin states. For a dipolar collision, the spin projection of an atom can change at most by $\Delta m_s = 1$. Therefore, for short time evolution, positive m_s states originate from the well where the spin flip was efficient (the right well), while negative m_s states originate from the left well. As long as the population in $m_s = 0$ remains negligible, this Stern-Gerlach measurement will therefore allow us to study the spin dynamics of each well separately. In the case the population in $m_s = 0$ is no longer negligible (not the case in the experiment), a site-selective Stern-Gerlach detection would be necessary in order to access the spin distribution of each well.

Spin preparation instabilities

As discussed above, our experiment suffers from loading instabilities (resulting from pointing instabilities of the IR beam) which introduce a fluctuating imbalance in population between the two wells. To suppress this instability, we proceeded to a post selection of the data. We only considered data where measured total magnetization (with no

correcting coefficients for spin states in $m_s > -3$) verified the criteria $M = -0.5 \pm 0.5$. This post selection analysis is justified by the fact that magnetization is conserved during the dynamics. We therefore are confident to have found a scheme which enables us to prepare two atomic ensembles of approximatively the same population in two different wells in two opposite spin states, and that we can monitor the spin dynamics resulting from this preparation.

It is worth noticing that after such spin preparation we can remove the green light responsible of the double well trap. This results in a mixture of $m_s = -3$ and $m_s = +3$ atoms in the IR ODT. The dynamics of such a system, dominated by contact interactions, was studied in chapter 3.

7.3 Spin dynamics

7.3.1 Metastability with respect to inter-site spin-exchange

We first discuss the spontaneous evolution of the spin distribution after the right atoms are promoted to the $m_s = +3$ state, and the magnetic field gradient is switched off.

Initial spin dynamics in a fully separated double-well trap is purely dipolar, because atoms are locally in a stretched state (see section 7.1). For an initial state $|N : L, -3; N : R, 3\rangle$ (corresponding to N atoms in the left well in state $m_s = -3$ and N atoms in the right well in state $m_s = 3$), two spin relaxation channels are possible corresponding to dipolar relaxation between atoms in the right well and dipolar spin exchange between atoms in the left and right well.

Initial fast dipolar relaxation

Let us first discuss dipolar relaxation induced by collisions between $m_s = +3$ atoms inside the right well. We do observe such phenomena (Fig.7.9 see circled area of density profile for t= 1 ms).

The density of the atoms in a well of the double-well trap is relatively high. We have a peak atomic density n_0^{BEC}= 1.41 10^{21} m^{-3} in a well for 5000 atoms. At the magnetic fields of the experiment ($g_s \mu_B B/h$ =200 kHz), this yields a sub-ms dipolar relaxation collision time:

$$\begin{aligned} \tau_{DR} &= \frac{2\sqrt{2}}{n_0^{BEC} \sigma_{dip}^{(1)} v} \\ &\approx 0.8 \text{ ms}. \end{aligned} \tag{7.7}$$

Dipolar relaxation is so fast that we cannot resolve its dynamics. Because the energy released in a dipolar relaxation event (approximatively 3 μK using $g_s \mu_B B \approx k_B T$) is smaller than the trap depth, atoms remain in the right well after dipolar relaxation. The inelastic process thus results in a rapid increase of the temperature of the right

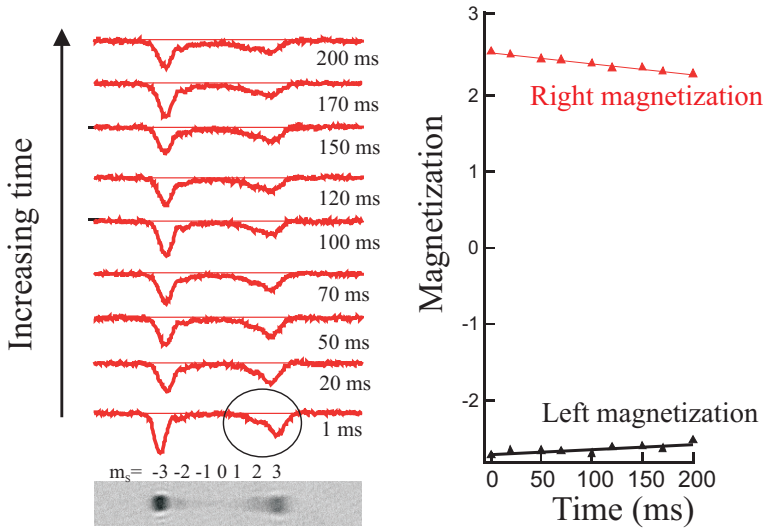

Figure 7.9: Spin dynamics in the double-well trap. Lower left panel: Absorption image after the Stern-Gerlach separation demonstrating the spin preparation with opposite polarization in the two wells. Top left panel: density profiles for increasing hold time before release and Stern-Gerlach analysis showing the evolution of the spin composition. Right Panel: Magnetization is almost constant in both wells.

cloud. The initial magnetization in the right well is approximatively 2.5 (Fig.7.9). We can therefore estimate that the released magnetic energy in the right well for a magnetic field of $g\mu_B B/h = 200$ kHz is of the order of

$$\Delta E \sim 0.5 \times 200 \text{ kHz} \tag{7.8}$$

from which we can extract an increase of temperature of

$$\Delta T \sim 1.7\ \mu\text{K}. \tag{7.9}$$

We measure the temperature of the cloud 1 ms after spin preparation to be 3 μK (see absorption image Fig.7.10), about twice larger than what our calculation gives.

The initial fast dipolar relaxation and temperature increase leads to a fast decrease of the gas density. We estimate the density at T=3 μK to be:

$$n_0 = N\left(\frac{m\bar{\omega}^2}{k_B T}\right)^{3/2} \tag{7.10}$$

$$= 6.5 \times 10^{19}\ \text{m}^{-3} \tag{7.11}$$

with $\bar{\omega} = (\omega_x\omega_y\omega_z)^{1/3}$ the geometrical average trapping frequency. The timescale associated to dipolar relaxation is then on the order of 5 s^{-1} (eq.(7.7) but with a different value for density): dipolar relaxation practically stops after 1 ms. As shown in Fig.7.9, the total magnetization (right magnetization and left magnetization) then barely decreases for times up to 200 ms.

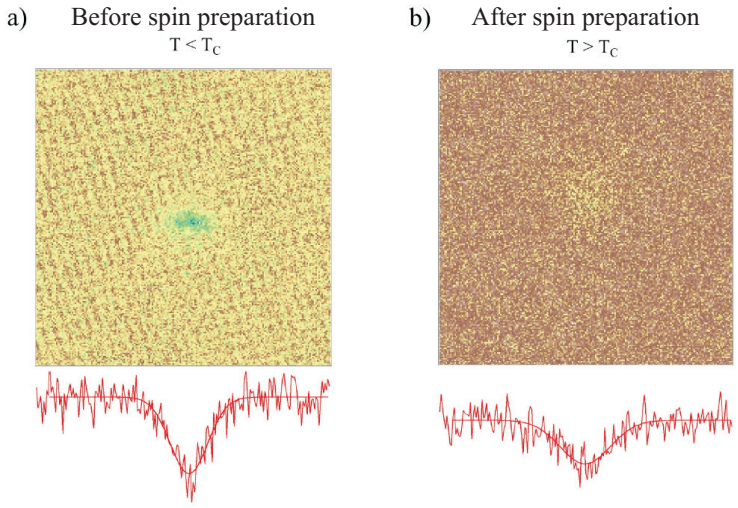

Figure 7.10: Absorption image of the gas before and after spin preparation. We measure a) a temperature of $\approx$ 400 nK before the RF-pulse ($T < T_c$)and b) a temperature of 3 μK after the RF-pulse ($T > T_c$). We attribute the heating to very fast dipolar relaxation collisions between atoms in m_s=+3.

Metastability with respect to dipolar spin exchange processes

The second process which can occur is dipolar spin-exchange between the right and the left atoms. The magnetic field generated by a single spin s at a position $\vec{r}$ from the spin location is:

$$\vec{B}(\hat{\vec{s}},\hat{\vec{r}}) = \frac{\mu_0\gamma}{4\pi}\frac{3\hat{\vec{r}}\,(\hat{\vec{r}}\cdot\hat{\vec{s}}) - \hat{\vec{s}}\,\hat{r}^2}{\hat{r}^5} \tag{7.12}$$

with $\gamma = g_s\mu_B/\hbar$ the gyromagnetic factor. The dipolar field B_D is in the 30 μG regime. The external magnetic field B_{ext} = 50 mG, is much larger than the dipolar field. Classical physics then predicts than the spin evolution is a precession around the external magnetic field. As the spins are initially aligned with the external magnetic field therefore classical physics predicts no dynamics.

In quantum mechanics spin-exchange processes mediated by dipolar interactions are possible. Let us compute the strength of the dipolar spin exchange term which couples $|L:S,-S;R:S,+S>$ (atoms in the left well in state $|S,-S>$ and atoms in the right well in state $|S,+S>$) to $|L:S,-S+1;R:S,+S-1>$ and call this spin exchange rate Γ_{exc}. We have:

$$\hbar\Gamma_{exc} = sN\frac{\mu_0}{4\pi}\frac{(g_s\mu_B)^2}{\Delta^3}. \tag{7.13}$$

For 2N=10^4 Chromium atoms separated by $\Delta = 4.2\mu$m, we find $\Gamma_{exc} = 2\pi\times 10$ Hz, with an estimated 30% uncertainty, due to the fluctuations on N (20%), and the accuracy for

the measurement of Δ (5%). This rate defines a full inversion time (corresponding to the state $|N:L,3;N:R,-3\rangle$) equal to 140 ms. As shown in Fig.7.9, we do not observe significant spin-exchange on this time scale: after the initial fast dipolar relaxation, the populations remain almost frozen in their spin states. We do not observe spin dynamics although $t > 1/\Gamma_{exc}$.

We show in the following why the timescale for a full spin inversion ($|L:S,-S;R:S,+S> \rightarrow |L:S,+S;R:S,-S>$) is much larger than $1/\Gamma_{exc}$ as N (and therefore S) is large. The metastability of the spin distribution results from a competition between exchange interactions and Ising interactions.

7.3.2 Interpretation of spin-exchange suppression

Model for dipolar dynamics between two wells

As explained above, the double well system can be described by two interacting giant spins. We therefore developed a theory to account for the dynamics observed, where the spins of the left well interact only with the spins of the right well (and vice-versa) through dipolar interactions. Within the Heisenberg picture the equation of motion (for left well spins) reads:

$$\frac{d}{dt}\hat{\vec{s}}_{L,i} = \gamma \hat{\vec{s}}_{L,i} \times \left(\vec{B}_0 + \sum_j \vec{B}(\hat{\vec{s}}_{R,j}, \hat{\vec{r}}_{i,j}) \right) \tag{7.14}$$

with $\gamma = g_s \mu_B/\hbar$ the gyromagnetic factor, and analogously for the spins of the right well. The magnetic field generated by a single spin at a position $\vec{r}$ from the spin location is given eq.(7.12).

We define the total spin of the left well as:

$$\hat{\vec{S}}_L = \sum_i \hat{\vec{s}}_{L,i} \tag{7.15}$$

and analogously for the right well ($S_L = S_R = Ns$). We obtain two simple equations of the following form:

$$\frac{d}{dt}\hat{\vec{S}}_L = \gamma \hat{\vec{S}}_L \times \left(B_0 \vec{u}_z + \vec{B}(\hat{\vec{S}}_R, \vec{\Delta}) \right) \tag{7.16}$$

$\vec{\Delta}$ being the relative position of the two wells ($\langle \vec{r}_{i,j} \rangle \simeq \vec{\Delta}$ as $\Delta > \sigma$ with σ the width of the atomic cloud).

The second term of eq.(7.16) can lead to time evolutions for the z components of the total spins, $\left\langle \hat{S}_{L,R\,z} \right\rangle$. We do not consider magnetization changing collisions (such as dipolar relaxation) in our theoretical framework thus the dipolar Hamiltonian reduces to a form similar to H_{dip}^{eff}:

$$\hat{H}_{dip}^{eff} = -2\frac{\mu_0 \gamma^2}{4\pi\Delta^3}\left(\hat{S}_L^z \hat{S}_R^z - \frac{1}{4}\left(\hat{S}_L^+ \hat{S}_R^- + \hat{S}_L^- \hat{S}_R^+ \right) \right). \tag{7.17}$$

The case s=1/2

Let us consider the case of a spin 1/2 system where each well is prepared in opposite spin states. We will consider only magnetization conserving collision (as for the experiment), thus the Hamiltonian of the system reduces to $\hat{H}_d^{eff}$. There are four different configurations to consider:

$$|L,+1/2;R,-1/2>,\ |L,-1/2;R,+1/2>,\ \underbrace{|L,+1/2;R,+1/2>,\ |L,-1/2;R,-1/2>}_{eigenstates}$$

The two last states are eigenstates of $\hat{H}_d^{eff}$ and will not drive any dynamics. Let us write $\hat{H}_d^{eff}$ in the $|L,+1/2;R,-1/2>,\ |L,-1/2;R,+1/2>$ basis. We find:

$$\hat{H}_{dip}^{eff} = 2\frac{\mu_0\gamma^2}{4\pi d^3}\hbar^2\frac{1}{4}\begin{pmatrix}1 & 1\\ 1 & 1\end{pmatrix}.$$

The diagonal terms are the same and the coupling terms are different from zero. This means that it is possible to have a complete transfer [74] from $|L,+1/2;R,-1/2>$ to $|L,-1/2;R,+1/2>$ through dipolar interactions. We show this result Fig.7.11, where the magnetization in the left well will oscillate from -1/2 to 1/2 at a rate of Γ_{exc} (and in the right well from $+1/2$ to $-1/2$).

The case s=1

Let us now discuss the case of s=1 corresponding to two spins 1/2 particles in each well. There are now $(2s+1)^2 = 9$ different possible configurations. Only 3 configurations are not eigenstates of $\hat{H}_d^{eff}$:

$$|L,+1;R,-1>,\ |L,0;R,0>,\ |L,-1;R,+1>. \tag{7.18}$$

In this basis, $\hat{H}_d^{eff}$ reads

$$\hat{H}_{dip}^{eff} = -2\frac{\mu_0\gamma^2}{4\pi d^3}\hbar^2\begin{pmatrix}-1 & 1/2 & 0\\ 1/2 & 0 & 1/2\\ 0 & 1/2 & -1\end{pmatrix}.$$

The diagonal terms are no longer equal. We can infer that dipolar interaction has "more difficulty" to transfer atoms from $|L,+1;R,-1>$ to $|L,-1;R,+1>$. Indeed, the coupling between $|L,+1;R,-1>$ and $|L,0;R,0>$ is non resonant [74], the same can be said between $|L,0;R,0>$ and $|L,+1;R,-1>$. Therefore, the transfer from $|L,+1;R,-1>$ to $|L,-1;R,+1>$ is not as efficient as in the s=1/2 case. This longer transfer time can be seen Fig.7.11.

Towards larger s

As s is increased with increasing numbers N of spins 1/2 particles in each well, the coupling between intermediate states (i.e. $|L, +m_s; R, -m_s >$ to $|L, m_s - 1; R, -m_s + 1 >$ for an initial preparation $|L, +s; R, -s >$) is progressively less efficient. Therefore the oscillation between the extreme spin state is damped, and the exchange process takes longer and longer times (as shown Fig.7.11). As N is increased, there are more and more intermediate states, each state being non resonantly coupled to the next due to the (diagonal) Ising terms which are not equal. Dynamics is inhibited for large spins.

Eq.(7.16) readily shows that the many-body evolution of $2N$ spins in two traps can be reduced to the two-body evolution of two giant spins. It can be numerically solved, and the time evolution of the left magnetization as a function of N is shown in Fig.7.11 for the case where the external magnetic field dominates the dipolar field created by the atoms of the right well, in which case eqs.(7.16) and (7.17) give identical results (this condition applies to our experiment as typical values of the external field is 50 mG and the dipolar field B_D is 30 μG). The results in Fig.7.11 show that spin-exchange due to dipole-dipole interactions between the two wells is strongly inhibited when N, and therefore the magnitude of the total spin in each well increases, which is consistent with our experimental observation (no spin dynamics).

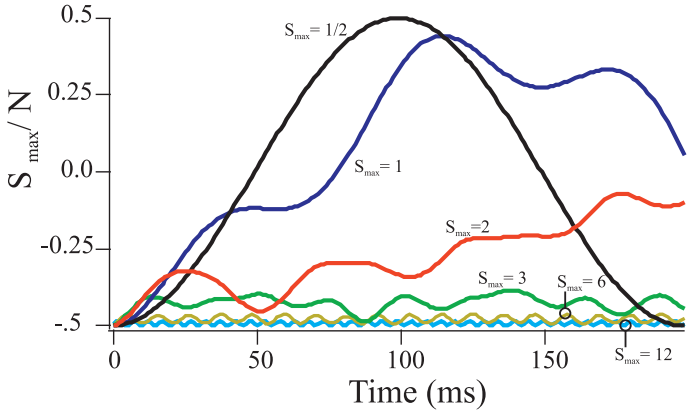

Figure 7.11: Magnetization dynamics in one well for increasing number of particles. Here we consider spin 1/2 particles; the increasing number of atoms per well create an increasing local total spin S_{max} (from 1/2 for one atom per well, to 12 for 24 particles per well). Magnetization per atom in a given well is plotted as a function of time. Increasing spin results in almost frozen spin dynamics, therefore reaching a classical behavior.

A closer look at the quantum model shows that the spin dynamics of N spins in fact does not completely vanish at short times. We numerically observe spin-exchange collisions, where two atoms undergo the transition $|L, +s; R, -s > \rightarrow |L, +s-1; R, -s+ 1 >$, within a timescale $1/\Gamma_{exc}$. However, these collisions do not proliferate, and the

spins remain roughly locked at their initial positions for extremely long times. The reason why massive spin-exchange cannot occur is that the Ising term $\hat{S}_L^z \hat{S}_R^z$ of eq.(7.17) creates an energy barrier that cannot be overcome for large spins, the exchange terms $\hat{S}_L^+ \hat{S}_R^- + \hat{S}_L^- \hat{S}_R^+$ being too small. As the size of the total spin increases, the rate for a full spin-exchange process decreases. We therefore observe in the numerical simulations a crossover between quantum magnetism and classical magnetism as N, and therefore s, is increased.

A classical interpretation

Our experimental data is also well accounted for by a classical theory of two localized interacting magnets of opposite magnetization in a large external magnetic field. In this case, magnetization dynamics is also completely frozen. Indeed, provided intersite spin correlations are neglected such that

$$\frac{d<\vec{S}>}{dt} =< \vec{S} \times (\vec{B} + \sum_j \vec{B}_j) > \approx < \vec{S} > \times (\vec{B} + < \sum_j \vec{B}_j >), \tag{7.19}$$

eq.(7.16) reduces to the simple equation of precession of classical magnets (similarly to what was discussed in chapter 6. Within this classical approximation the orientations of two classical magnetic moments of opposite directions, each almost parallel to the magnetic field, are locked. This results from dynamical stability of a system which is otherwise energetically unstable. Our experimental observations can therefore be understood within this simple classical magnetism framework.

In our classical model, the length of the spin does not intervene, therefore no matter the length of the spin we do not expect any spin dynamics. For large spins, the quantum model also predicts inhibited spin dynamics. However, as the spin is decreased, the quantum simulation predicts spin dynamics. Thus this experiment provides an example in which increasing the length of a spin drives the system from quantum to classical.

7.4 Conclusion and outlook

We have experimentally studied a chromium BEC loaded into a double-well trap. The well separation was sufficient to enable a spin preparation with opposite spin polarizations of the two atomic subsystems. We find that this spin configuration is metastable, with a lifetime greatly exceeding the timescale associated with dipole-dipole interactions between clouds. This stability arises because dipolar spin exchange interactions lead to populations of states which are non resonantly coupled to the initial state due to Ising interactions. The spin dynamics is classically suppressed by the interplay between exchange and Ising interactions. This classical behaviour arises due to the very large effective spin realized within each well. In our situation, an increased spin length leads to reduced spin fluctuations and a classical behaviour.

CHAPTER 8

Out-of-equilibrium spin dynamics mediated by contact and dipolar interactions

In this chapter we will discuss two experiments where we observed spin dynamics. The main difference between the experiments resides in the spin preparation. The experiments were performed both in the bulk in the superfluid regime and in an optical lattice deep in the Mott regime. We will compare our data with theoretical mean field and beyond mean field models. We will to understand how the different regimes and spin excitations may impact on the creation of quantum correlations or not. These experiments are preliminary results that we started during my PhD, and S. Lepoutre and L. Gabardos continued working on while I was writing this manuscript.

8.1 Introduction

In this chapter we will discuss two experiments where we observed out of equilibrium spin exchange dynamics. The trap and spin preparation are different than those described in chapter 7. Here atoms will be trapped in a single well trap or in a 3D optical lattice. I will start by presenting how we produce the trapping potentials, their features, and the experimental procedures employed in the experiments. Then, I will discuss the spin dynamics we observed after atoms are promoted to m_s= -2. The spin dynamics that follows this initial spin preparation was studied as a function of the lattice depth V_0. The data acquisition and the experiment were performed before the start of my thesis. Here, I will briefly describe the data and present our interpretation for the observed dynamics which involves a combination of short-range and long-range interactions. For low lattice depths, when the gas is in the superfluid regime, we observe that the spin dynamics is well described by an inhomogeneous mean-field theory. With the help of P.Pedri, I also developed a code simulating the evolution of the initial state through the Gross-Pitaevskii equation using the Single Mode Approximation. This approximation fails to reproduce our data which shows that an inhomogeneous mean field theory is necessary in order to describe our data. Deep in the Mott regime, mean field theory fails to properly describe our data. We find that the inclusion of beyond mean-field effects at the perturbative level is sufficient to provide a quantitative description of the data.

In the last part of this chapter, I will describe another set of spin dynamics exper-

iments which the team started at the end of my PhD studies, in the bulk and deep in the Mott regime. The spin excitation here is performed by a spin rotation induced by a Radio-Frequency pulse. Based on theory predictions obtained in collaboration with the group of A.M. Rey from JILA, we expect that such a procedure followed by spin-spin interaction could lead to quantum correlations for large rotations (i.e. $\sim \pi/2$). Here I'll present preliminary results. In the bulk, our data shows spin dynamics sensitive to the direction of the magnetic field which can be cancelled for a "magic angle", in agreement with a mean field theory. In the lattice, the evolution of different spin states is compatible with a beyond mean field theory. We are currently investigating what are the correct theoretical approaches which match best our data.

8.2 Setting up optical lattices

I will start by presenting how we produce a 3D optical lattice and the different experimental techniques performed when operating with lattices.

8.2.1 Optical lattices

A retro-reflected laser beam propagating along the, e.g., y direction of wavelength λ produces a periodic stationary wave of period $\lambda/2$. Like for most optical traps, the laser beam needs to be focused on the atoms in order to be intense enough to trap them [152]. As long as the trapping beam is homogeneous over the size of the atomic sample, the intensity profile experienced by the atoms is:

$$I(y) \propto I_{0,y} \sin^2(ky + \phi) \tag{8.1}$$

with $I_{0,y}$ the beam intensity, $k = 2\pi/\lambda$, and ϕ a phase. The associated lattice trap frequency can be much larger than in for a non retro-reflected scheme. When the trapping frequency along $\vec{y}$ of the optical potential is greater than the thermal kinetic energy or the interaction energy of the gas ($\hbar\omega >> k_B T$, gn), the motion of the atoms in that direction is frozen. We refer to such a trap as 2D systems since its motion is free in 2 dimensions. If two retro-reflected beams are applied in two orthogonal spatial directions, the atomic motion is frozen in two directions and we refer to these gases as 1D systems. When a periodic potential is applied in all three spatial directions, the motion of the atoms is frozen in all directions. Atoms will be regularly spatially separated from one another thus mimicking a perfect crystal structure. In this thesis we will only deal with a 3D lattice system.

8.2.2 Experimental setup

Our optical system which produces the 3D optical lattice is illustrated in Fig.8.1. We use 3 W of a laser Verdi V18 beam ($\lambda = 532$ nm) and separate it in two paths by a

Polarization Beam Splitter. One path is dedicated to the confinement in the vertical direction, the other path for the horizontal confinement. We dedicate 1 W of light for the vertical path, and 2 W for the horizontal path.

The vertical beam passes through an AOM[1] and is injected in a polarization maintaining optical fibre[2]. The beam is collimated with a 1.4 mm waist at the output of the fibre and passes through a PBS which defines the beam polarization. It is then focused on the atoms with an $f_1 = 300$ mm lens L1. The waist of the beam at the atom position is 40 μm. We place a second lens L2 of focal length $f_2 = 400$ mm at f_2 from the atoms, and a mirror at 0 ° at f_2 from this second lens. This ensures that the reflected beam and the incoming beam will have their focal point at the same position, and that they have the same beam mode[3]. This retro-reflected beam assures the confinement in the vertical direction. The intensity profile in this direction is given eq.(8.1).

$$\begin{aligned} I(y) &= I_{0,y}|e^{iky} + e^{-iky}|^2 \\ &= 4I_{0,y}\cos^2(ky). \end{aligned} \tag{8.2}$$

The horizontal beam passes through an AOM[4]. The difference in frequency shifts between the horizontal and vertical beams (of 190 MHz) is large enough that atoms do not feel the mechanical effect from the beatnote. The horizontal beam is then separated in two beams with equal power for each path. Each horizontal beam is injected in an optical fibre[5]. Only one of the two beams is retro-reflected (let us call this beam H1), the other beam (H2) will intersect with the retro-reflected beam at an angle of 45 ° (see Fig.8.2). The H1 beam is collimated and has a 1 mm waist at the output of the optical fibre and passes through a PBS which defines the beam polarization. It is then focused on the atoms with an $f = 250$ mm lens. The size of the beam at the atom position is 40 μm. A relay system with an $f = 250$ mm lens retro-reflects the beam. The H2 beam is collimated at the output of the fibre with an f = 15.4 mm lens and a waist of 1.4 mm. The beam passes through a PBS and is focused on the atoms with an $f = 300$ mm lens. The size of the beam at the atom position is 40 μm. The horizontal confinement is produced by the interference of 3 non orthogonal beams with the same polarization and frequency. The potential in the horizontal plane will have the following form:

$$I(x,z) = |E_1(e^{ikx} + e^{-ikx}) + E_2 e^{ik(\frac{x+z}{\sqrt{2}})}|^2 \tag{8.3}$$

with E_i the amplitude of the electric field of the beam on path H_i. The horizontal basis ($\vec{x}$, $\vec{z}$) (Fig.8.2) is not the appropriate one to account for the trapping potential.

[1] Model: MT80-A1.5VIS from Opto-electronic; coupling efficiency: 80%, frequency shifted by +80 MHz

[2] Model: Thorlabs TS0821227PMS460-HP, cut with an angle; coupling efficiency: 70%

[3] this is often referred to as a "relay system"

[4] Model: MT110-A1.5VIS from Opto-electronic; coupling efficiency: 80%, frequency shifted by -110 MHz

[5] Model: Thorlabs TS0821227PMS460-HP, cut with an angle; coupling efficiency: 70%

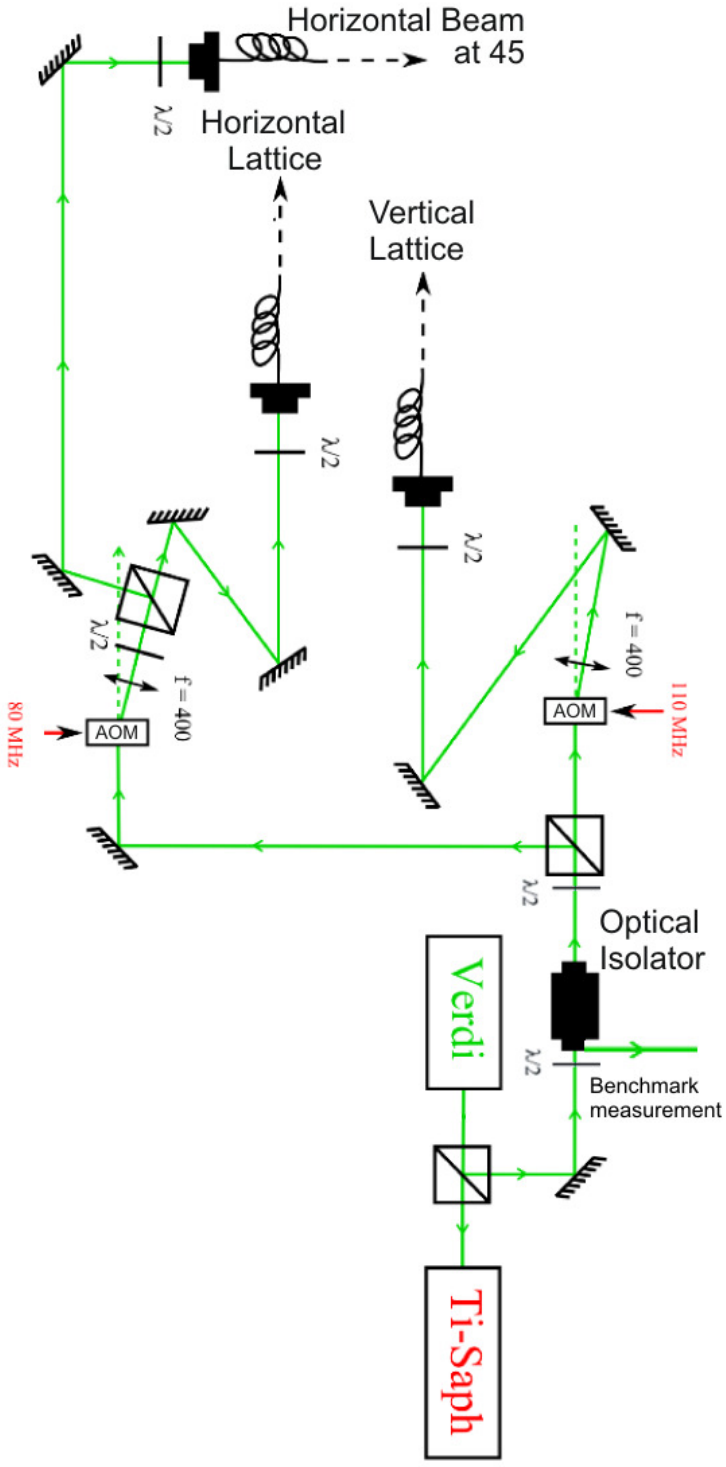

Figure 8.1: Sketch of the setup. 3 W of Verdi light are used for the optical lattices. The beam is split in two, 1 W for the vertical confinement and 2 W for the horizontal confinement. The vertical and horizontal beam go through an Acousto-Optic-Modulator with different frequency shifts. Then they are injected into optical fibres. Image adapted from [37].

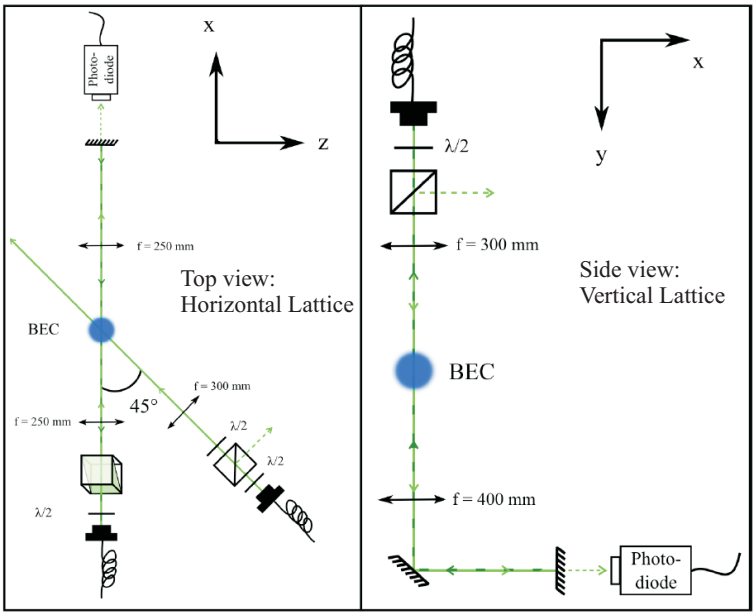

Figure 8.2: Sketch of the lattice setup. The horizontal lattice is produced by the interference of 3 non orthogonal beams. One of the beams is retro-reflected. The third beam intersects these two beams with an angle of 45 °. The vertical lattice is produced by the retro-reflection of a beam aligned close to the vertical direction (there is a 7 ° angle between the beam and the vertical axis). Image adapted from [37].

The vectors ($\vec{x}$', $\vec{z}$') constructed by rotation of 22.5 ° (i.e $\pi/8$ rad) around $\vec{y}$ yield the following intensity profile:

$$\begin{aligned} I(x',z') &= 2E_1^2 + E_2^2 \\ &+ E_1^2 \cos\left(2k(z'\sin\frac{\pi}{8} + x'\cos\frac{\pi}{8})\right) \\ &+ E_1E_2\cos\left(2kz'\sin\frac{\pi}{8}\right) \\ &+ E_1E_2\cos\left(2kx'\cos\frac{\pi}{8}\right). \end{aligned} \tag{8.4}$$

The periodicity of the potential is of $\frac{\lambda}{2\cos\frac{\pi}{8}} \sim \frac{\lambda}{2}$ along x' and $\frac{\lambda}{2\sin\frac{\pi}{8}}$ along y'.

The alignment of each beam is a two step process. We first align the incoming beam on the atoms, the retro-reflected beam being blocked (so that we can focus only on the incident beam). To align the incoming beam on the atoms we produce a BEC or a thermal gas in the crossed optical dipole trap, turn off the ODT and let the gas expand for typically 1.5 ms. We then pulse the trapping vertical/horizontal light and at the same moment we image the atoms while using the vertical/horizontal imaging system. Due to the large light shift of the $|^7P_4>$ state when the beam is aligned on the

gas, atoms absorb less light of the resonant imaging beam. Once the alignment process is complete, one must position the lens of the incoming beam so that its focal point matches the BEC position. This can be done by minimising the size of the atomic cloud affected by the light shift. When this is achieved, we may pass to step two: align the retro-reflected beam. To do so, we inject the reflected beam back into the fibre. Light will then take the same optical path but backwards, and to quantify the retro reflected beam coupling in the fiber we can measure the power of the beam reflected by the entrance PBS of the isolator. A benchmark measurement for the retro reflection is a 100 mW reflected by the second PBS of the isolator (i.e. closest to the Verdi head) for 1 W at the input of each optical fibre (see Fig.8.1).

Lattice depth calibration

To extract the trapping characteristics of our lattice beams we proceed to measure the barrier height of each lattice beam. As explained in detail in [196], by pulsing the retro-reflected light beam on the BEC for a short time before letting the gas expand (for the case of the non retro-reflected horizontal beam, we pulse the two incoming horizontal beams), the light pulse transfers quantized momenta to the gas and couples plane wave states separated by momenta $2\hbar k$. Evaluating the transfer of populations to different momenta orders enables us to characterize the optical depth of the potential.

The result of this procedure on the vertical direction can be seen Fig.8.3. From the relative population of atoms with momenta $k = 0, \pm 2\hbar k, \pm 4\hbar k$ and a numerical calculation estimating the relative populations as a function of light pulse time (a similar protocol as in [197]), we extract from these data $V_0 = 25$ E_r for each pair of interfering beams. At maximum power and alignment, we achieve $V_0 = 30$ E_r with E_r the recoil energy. The recoil energy is defined as $E_r = \frac{\hbar^2 k^2}{2m} \approx h \times 13$ kHz, where k is the wavevector associated to the lattice light. It corresponds to the energy increase associated to the emission of a photon.

8.2.3 Trapping parameters

Trapping frequencies

It is straightforward to extract the trapping frequency in the vertical direction from the depth of a lattice site since the confinement is produced by one retro-reflected beam:

$$\begin{aligned} \omega_y &= \frac{1}{\hbar}\sqrt{4V_0 E_r} \\ &\approx 2\pi \times 135 \text{ kHz for } V_0 = 25 \text{ } E_r. \end{aligned} \tag{8.5}$$

In the horizontal direction it is not as straightforward extracting the trapping frequencies from the potential depth. Here we rely on an experimental measurement. From a parametric excitation experiment we obtain $\omega_{x'} \approx 175$ kHz, $\omega_{z'} \approx 55$ kHz for $V_0 = 21$ E_r.

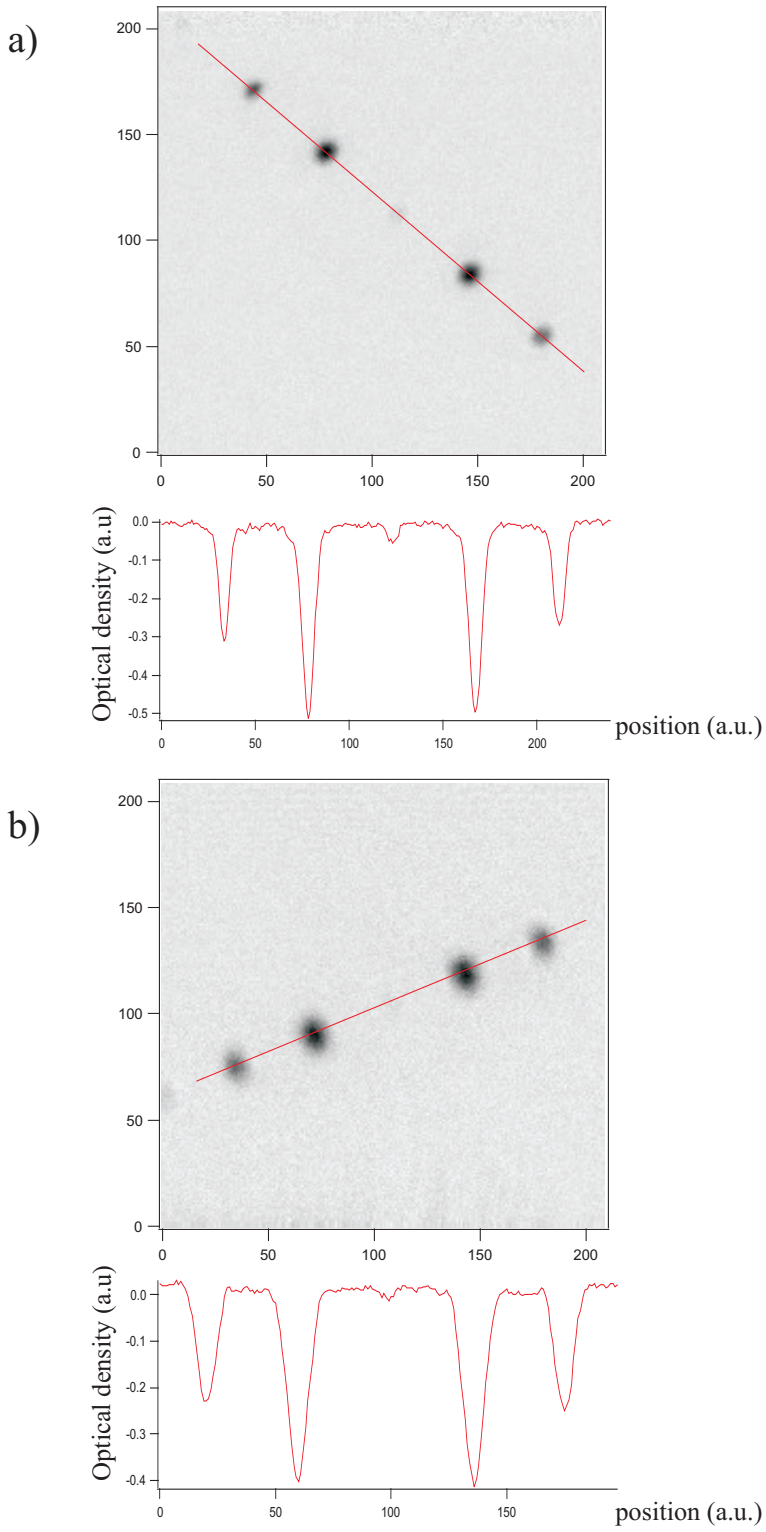

Figure 8.3: Calibration of the Horizontal Lattice Depth using the Kapitza-Dirac method. a) Absorption image and optical density of the diffraction pattern associated to the retro-reflected horizontal beam (H1). b) Absorption image and optical density of the diffraction pattern associated to the intersection of the two incoming horizontal beams. In both cases, we shine a light pulse $t_{pulse} = 2$ μs on the atoms, then let them expand and imaged using an absorption process. Atoms are successfully transferred to states of momenta $|n\hbar k>$.

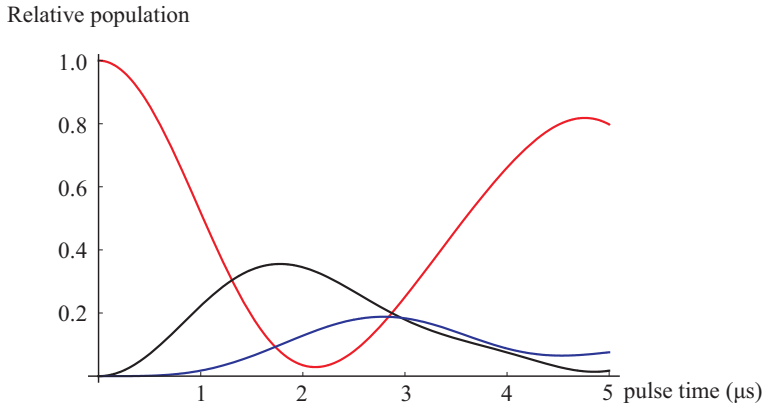

Figure 8.4: Evolution of the population of the three first diffraction orders (black: $\pm p = 0$, red: $p = \pm 2\hbar k$, green:$p = 4\hbar k$) calculated for a lattice depth $V_0 = 25E_r$ as a function of the lattice pulse time.

Interaction and tunneling energy

In the limit $V_0 >> E_r$, Wannier function $w_i(x_i)$ are an appropriate basis to describe an atom localized in a lattice site [110].

The tunneling element J between a lattice i with a lattice site j can be estimated by calculating the overlap of the Wannier functions between sites i and j [110]:

$$\begin{aligned} J &= \int d^3x w(x - x_i)^*[-\frac{\hbar^2}{2m}\Delta + V(x)]w(x - x_j) \\ &= \frac{4}{\sqrt{\pi}} E_r (\frac{V_0}{E_r})^{3/4} e^{-2\sqrt{V_0/E_r}} \end{aligned} \tag{8.6}$$

where $V(x)$ is the optical lattice potential. $4J$ is the energy width of the lowest band. The tunneling time τ is then:

$$\begin{aligned} \tau &= \frac{h}{4J} \\ &\approx 15 \text{ ms for } V_0 = 25 \ E_\text{r} \text{ along the } x \text{ or } y \text{ direction} \\ &\approx 100 \text{ ms for } V_0 = 25 \ E_\text{r} \text{ along the } z \text{ direction.} \end{aligned} \tag{8.7}$$

In the same manner, one can compute the interaction energy term between two atoms in the same lattice site:

$$\begin{aligned} U &= \frac{4\pi\hbar^2}{m} a_S \int d^3x |w(x)|^4 \\ &\approx \sqrt{\frac{8}{\pi}} k a_S E_r (\frac{V_0}{E_r})^{3/4} \\ &\approx h \times 5.6 \text{ kHz for } V_0 = 25 \ E_\text{r} \text{ and } E_r = \frac{\hbar^2}{2m}(k_x k_y k_z)^{2/3} \end{aligned} \tag{8.8}$$

It is interesting to realize from eq.(8.6) and eq.(8.8), that increasing the lattice depth reduces exponentially the tunneling time and increases (almost linearly) the interaction strength.

In the following we will be interested in quantum magnetism, and as discussed earlier in chapter 6, it is the super-exchange interaction which sets the relevant dynamics timescales. At the deepest lattice configuration, the super-exchange timescale is:

$$\begin{aligned} \tau_{ex} &= \frac{h}{J_{ex}} \\ &= \frac{hU}{4J^2} \\ &\sim 20 \text{ s.} \end{aligned} \tag{8.9}$$

In the deep lattice regime, super-exchange interaction does not play any role on the experimental timescales we shall study.

Atom distribution

In the Mott phase, the atomic distribution is determined by the competition between onsite interaction and external potential energy. In the no hopping limit, $J/U \to 0$, the Bose Hubbard Hamiltonian reduces to the sum of single site Hamiltonian:

$$H = \sum_{i=1}^{N} H_i \tag{8.10}$$

$$H_i = U n_i(n_i - 1) + (V_i - \mu) n_i. \tag{8.11}$$

The ground state is obtained by minimizing H_i with respect to the site occupation for a given $\mu - V_i$. It can be shown [198] that:

$$n - 1 < \frac{V_i - \mu}{U} < n \tag{8.12}$$

minimizes H_i for a site occupation of n bosons per site. The trapping potential is a slowly varying potential, therefore the numerator varies locally following $\mu - V(r) = \mu - \frac{1}{2} m\omega^2 r^2$ [85] with μ the chemical potential at the center of the trap and ω the trap frequencies, this means that at the center of the trap there are n_{max} bosons per site. As $(\mu - V(r))/U$ decreases as we get further away from the trap center, we will be in the situation where $n_{max} - 2 < (\mu - V(r))/U < n_{max} - 1$ and there will be $n_{max} - 1$ bosons per site. And so on until the occupation per site reaches 0. Such atomic distribution is often referred to as a wedding cake distribution.

It is difficult to be quantitative on the exact distribution we expect since it depends on the exact form of the potential, and precise waist calibrations are difficult. In a crude model, we may estimate the maximum number of atoms in order to have only singly occupied sites N_{singly}^{Max}. Consider an isotropic lattice filled only with one atom per

site, and if an extra atom could be added it would be the first doubly occupied site. It costs the interaction energy U to create a doubly occupied site. Therefore we have:

$$\frac{1}{2}m\omega^2 R_1^2 = U \tag{8.13}$$

with ω the trapping frequency associated to the slowly varying potential, and R_1 the spatial extension of the isotropic gas. The maximum number of singly occupied sites can be deduced from:

$$\frac{4}{3}\pi \frac{R_1^3}{\frac{\lambda}{2}\frac{\lambda}{2}\frac{\lambda}{2\sin(\pi/8)}} = N_{singly}^{Max}. \tag{8.14}$$

We can estimate from a depth of 75 E_r and a laser waist of 50 μm, that the trapping frequency along the lattice beam is $\omega_{Lat} \sim 2\pi 200$ Hz. The mean trapping frequency of the IR is $\omega_{IR} \sim 2\pi \times 300$ Hz, thus the frequency of the total slowly varying potential is of the order:

$$\begin{aligned} \omega &= \sqrt{\omega_{IR}^2 + \omega_{Lat}^2} \\ &= 2\pi \times 360 \text{ Hz}. \end{aligned} \tag{8.15}$$

We then deduce $R_1 = 4.1$ μm, so that $N_{singly}^{Max} \sim 6000$ atoms. In the experiment (with typically 1 to 2 10^4 atoms loaded in the lattice), we do not expect to have only singly occupied sites.

This model may be extended to the case of doubly occupied sites. This time we must consider the gas to be in the situation where an extra atom would result in a triply occupied site. Let us call R_1' the radius for singly occupied sites and R_2' for doubly occupied sites. At the edge of the trap we have:

$$\begin{aligned} \frac{1}{2}m\omega^2 R_1'^2 &= 3U \\ U + \frac{1}{2}m\omega^2 R_2'^2 &= 3U. \end{aligned} \tag{8.16}$$

The maximum atom number N_{double}^{Max} for which we can have at most 2 atoms per site is:

$$N_{double}^{Max} = \frac{4}{3}\pi \frac{(R_1'^3 - R_2'^3)}{(\frac{\lambda}{2})^3 \frac{1}{\sin(\pi/8)}} + \frac{4}{3}\pi \left(\frac{R_2'}{\frac{\lambda}{2}}\right)^3 \frac{1}{\sin(\pi/8)} \times 2 \tag{8.17}$$

$$\sim 35000. \tag{8.18}$$

with $R_1' = 7.1$ μm and $R_2' = 5.8$ μm. In the experiment we therefore expect to have doubly occupied sites and singly occupied sites.

To determine the percentage of atoms occupying doubly occupied sites, we performed the following experiment: we load 10^4 atoms in the lattice in spin state $m_s = -3$

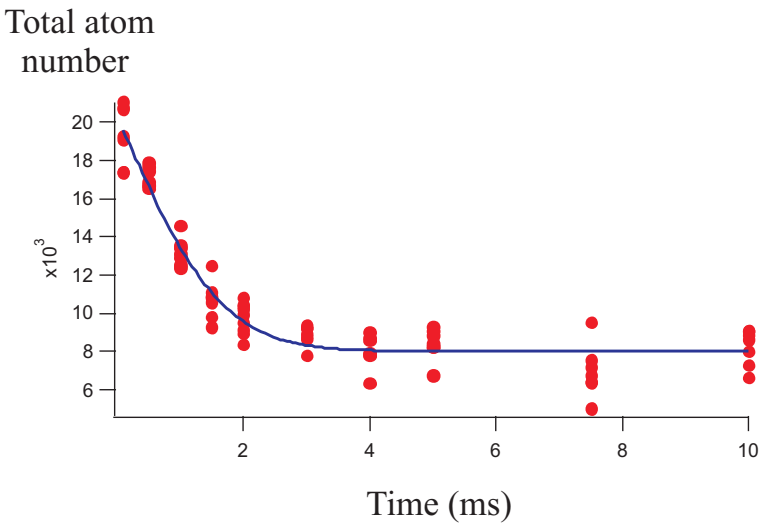

Figure 8.5: Measurement of the number of doubly occupied sites. We load atoms in the lattice in spin state $m_s = -3$. We perform an π RF pulse in order to promote atoms to $m_s = +3$. We then measure the number of atoms as a function of the time. We observe a decrease in atom number until a plateau is hit. We interpret the losses due to dipolar relaxation between atoms in the same site. We therefore estimate that 40% of the atoms occupy singly occupied sites.

deep in the Mott regime at a lattice depth of $V_0 = 3\times$ 25 E_r. We then perform a radio frequency pulse in order to transfer atoms from $m_s = -3$ to $m_s = +3$. We then image the atom number as a function of time (see Fig.8.5). We observe a decrease in atom number until a plateau is hit. We interpret the losses due to dipolar relaxation between atoms in the same site. As explained in section 6.2.3, dipolar relaxation is a local process which can only take place between atoms in the same lattice site. The kinetic energy released during the experiment is large enough that atoms are expelled from the trap. From this experiment, we conclude that about 40% of the atoms occupy singly occupied sites.

8.2.4 Lattice loading

We are interested in transferring atoms from an ODT to the fundamental band of the lattice. We will perform this transfer adiabatically. The definition of the adiabatic theorem is the following: "A physical system remains in its instantaneous eigenstate if a given perturbation is acting on it slowly enough and if there is a gap between the eigenvalue and the rest of the Hamiltonian's spectrum " [199]. Mathematically this writes:

$$\frac{dV_0}{dt} << \frac{1}{h}\Delta E^2 \tag{8.19}$$

where ΔE is the difference in energy between the eigenvalue of the system's eigenstate with the closest eigenvalue of another eigenstate, and $\frac{dV_0}{dt}$ is the perturbation variation, which in our case is the trapping potential variation. There are three relevant energy scales to keep in mind while loading a lattice which we will discuss in the following.

For a lattice experiment, we want to load atoms in the lowest band and we do not want to promote any atom in excited bands. Here the relevant energy scale is the energy difference between the fundamental and the first excited bands ΔE. When loading a BEC (whose spread in momenta $\Delta p_0 \to 0$ for large atom number) in a lattice as soon as $V_0 > 0$ we have at all times during the loading $\Delta E > 4E_r$ [196] which imposes a loading time τ verifying:

$$\begin{aligned} \tau &> \frac{h}{4 \times E_r} \\ &> 20\ \mu\text{s}. \end{aligned} \tag{8.20}$$

In practice, band excitation is not a problem in our experiment where the loading time is in the ms regime. In order to perform a band mapping experiment where Bloch states are mapped onto momentum states, we must lower the lattice slower than such a timescale [200].

When loading atoms in a lattice, we need to give atoms enough time to organize themselves following the Mott distribution. If the lattice was suddenly switched on, there would be an excess of multiply occupied sites due to the fact that atoms were not able to rearrange themselves in the trap [185, 201]. The timescale associated to this adiabacity criterion is 1/U. As one enters the Mott regime, the lattice must be "organized". In our experiment, the superfluid to Mott transition was observed at $V_0 = 15\ \text{E}_r$ [37]. To perform an adiabatic loading of the lattice we will need to verify:

$$\begin{aligned} \tau &>> 1/U \\ &>> 100\ \mu\text{s}. \end{aligned} \tag{8.21}$$

The third energy scale is associated to global oscillation of atoms in the trap. The energy scale here is the trapping frequency of the optical trap. The initial trapping frequency of the ODT ω_{trap} ranges in the 300 Hz regime. The associated timescale is:

$$\begin{aligned} \tau_{trap} &= \frac{1}{\hbar\omega_{trap}} \\ \to \tau &>> \tau_{Trap} \sim 3\ \text{ms}. \end{aligned} \tag{8.22}$$

This is the dominant timescale for our lattice loading procedure. Experimentally, we perform a linear ramp of 30 ms to load the atoms. This time is optimized by performing the shortest loading-unloading sequence allowing to recover a BEC with no discernable excitations.

8.2.5 "Delta Kick cooling"

In the experiments we discuss in the following, the typical timescale for spin dynamics is the ms. This is a small timescale compared to an adiabatic unloading of the lattice (which takes approximatively 30 ms). Therefore performing an adiabatic unloading of the lattice is not an option (despite the benefit of recovering a BEC and more dense signals).

Suddenly switching off all trapping lights at the end of the experimental sequence and let the gas expand enables a measurement of the initial momentum distribution. Indeed, if the size of the gas after TOF is much larger than the initial size of the gas, the density distribution after TOF is directly mapped to the initial momentum distribution, which is nothing else than the Fourier transform of the density distribution. When atoms are loaded in an optical lattice in the Mott regime, the wavefunction describing a particle in a lattice site is a Wannier function [110]. Deep in the Mott regime, the Wannier function is close to a gaussian (the ground statewavefunction associated to a particle in a harmonic trap is a gaussian). The Fourier transform of a gaussian is a gaussian. The width of the momentum distribution of each spin population is much larger than in the BEC case, so that we should wait longer times for spatially separating spin states. A longer TOF results in a less favorable signal to noise ratio. In practice, we can not perform such an experimental procedure since we then hardly detect any atomic signal.

To correct for this drawback, we first perform an unloading of the lattice in 100 μs. This time was chosen short enough compared to the spin dynamics timescale, but long enough to narrow the imaged momentum distribution thanks to better adiabatic following of the cloud, at least at the start of the unloading ramp. We then perform a focus of the momentum distribution along the Stern-Gerlach axis, inspired by the delta kick cooling technique [202]. This technique relies on free expansion of the gas and a subsequent application of a pulsed potential (referred to as kick) which "freezes" the momentum distribution. If the initial gas can be assumed to be a point object, and the kick can be as short and as powerful as possible, the momentum distribution can be efficiently frozen. In practice, the initial condition for expansion is far from a point object and we cannot perform a very powerful kick: we did not achieve freezing of the momentum distribution. However, we manage to significantly squeeze the momentum distribution along the Stern and Gerlach separation direction with the following sequence: after a time t_1 of free expansion we turn on the IR trap (at the same power as before the free expansion) for a time t_2 which applies a force to the atoms. Experimentally, we find $t_1 = t_2 = 0.7$ ms gives an optimal signal to noise ratio. The experimental ramp and an absorption image with such a technique is shown Fig.8.6.

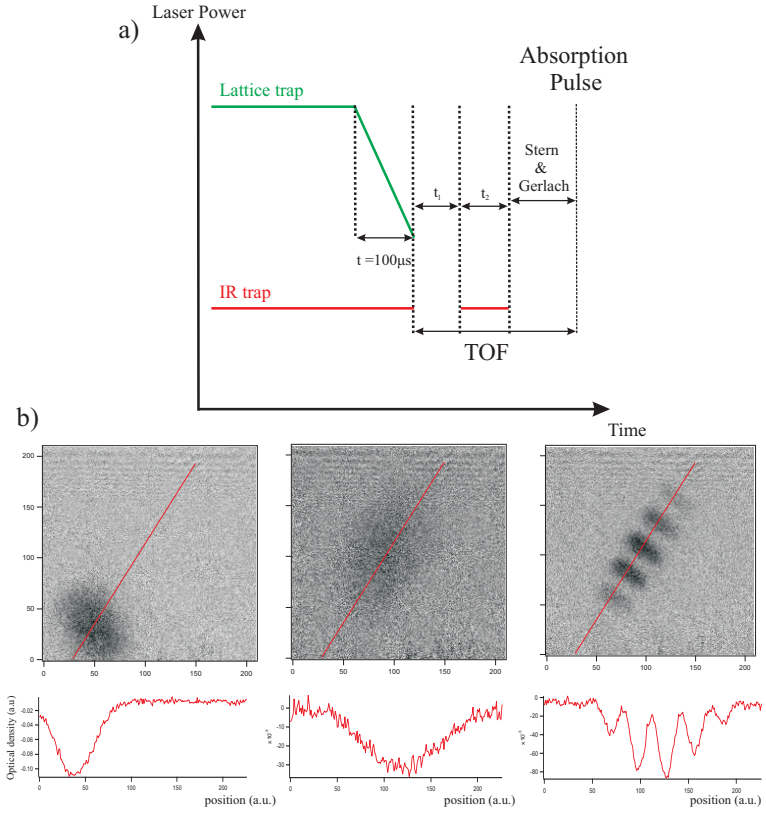

Figure 8.6: a) Experimental ramp in order to perform a delta kick cooling like absorption measurement. b) Absorption images with the corresponding integrated optical density in (a.u.) demonstrating the importance of the delta kick cooling protocol. For all images atoms were loaded in a lattice. For the first image we all atoms are in $m_s = -3$ and we did not perform the shock cooling protocol. For the second image, we performed a $\pi/2$ RF pulse (the spin distribution is given in Table8.1) but no delta kick cooling protocol. We do not resolve different spin states. On the third image we performed a $\pi/2$ RF pulse and a delta kick cooling protocol. We are able to resolve the different spin states.

8.3 Spin dynamics from m_s = -2 as a function of lattice depth

I will start by briefly presenting an experiment performed during Aurélie de Paz's thesis [37]. In this experiment, atoms were loaded in the lattice and prepared in an out of equilibrium spin state. The observed spin dynamics is interpreted as resulting from contact, dipole dipole and super-exchange interactions. The data is well accounted for by an inhomogeneous mean field theory at low lattice depth and by a beyond mean field theory at large lattice depth.

8.3.1 Experimental protocol and data

The experimental protocol is described in detail in [37]. It consists in using a tensor light shift to prepare a majority of atoms in m_s = -2. Then spin dynamics is monitored as a function of lattice depth V_0. We measure, after a variable hold time t, the spin populations by means of a Stern-Gerlach procedure. A typical evolution for V_0 =16 E_r is shown Fig.8.7. Only the m_s = -3, -2, -1 and 0 spin components are significantly populated as the system evolves, and they display a rather complex behaviour as a function of time (see Fig.8.7).

In order to simplify the discussion, we focus our attention onto the observable given by the ratio n_{-3}/n_{-2} of m_s = -3 and $m_s = -2$ populations, since they are the most populated components. Experimentally, we find two distinct regimes depending on the value of the lattice depth. We plot in Fig.8.8a the typical results corresponding to the two extreme lattice depths (25 E_r and 3 E_r), showing quite different spin dynamics. In the Mott phase at short times we observe (< 0.5 ms, see the inset) a strongly damped oscillation, and then at longer times a second oscillation. In the superfluid phase the spin dynamics is better described by an exponential. All these features are present in the data from 3 E_r to 25 E_r (see [37, 203]). Fig.8.8b shows the measured frequency associated to the observed fast (black points) and slow oscillations (red triangles).

8.3.2 Physical interpretation at low lattice depth

a) Model

At low lattice depth the gas is in the superfluid phase and we will use the Gross Pitaevskii equation. This is a mean field description of the gas where the total wavefunction can be written as the product of N independent wavefunctions with a mean field interaction. $\Psi_0(r,t)$ is the expectation value of the boson field operator $< \hat{\Psi}(r,t) >$. In the case of an internal degree of freedom such as the spin, $\Psi_0(r,t)$ is a

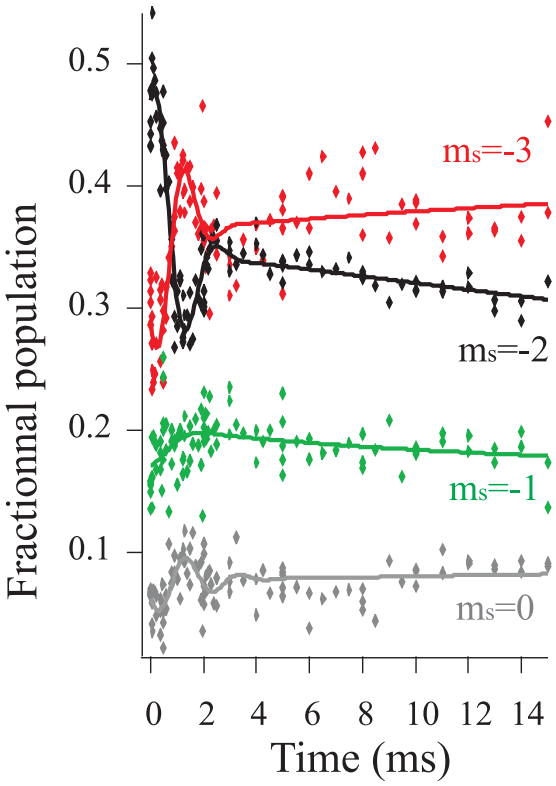

Figure 8.7: Measurement of the spin components as a function of time for $V_0 = 16E_r$. Lines are guide to the eye.

complex vector, each component associated to a spin state. For s=3 we have:

$$\Psi_0(r,t) = \begin{pmatrix} \alpha_{-3}(r,t) \\ \alpha_{-2}(r,t) \\ \alpha_{-1}(r,t) \\ \alpha_0(r,t) \\ \alpha_{+1}(r,t) \\ \alpha_{+2}(r,t) \\ \alpha_{+3}(r,t) \end{pmatrix}.$$

The exact form of the Gross-Pitaevskii equation depends on the spin of the atoms, and can be found in [155] . For a spin $f = 1$ atom it writes:

$$\begin{aligned} i\hbar\frac{\partial\alpha_m}{\partial t} &= \left[\frac{-\hbar^2\nabla^2}{2M} + U_{trap}(r) - pm + qm^2\right]\alpha_m \\ &+ c_0 n\alpha_m + c_2 \sum_{m'=-1}^{1} F.f_{m,m'}\alpha_{m'} + c_{dd} \sum_{m'=-1}^{1} b_m.f_{m,m'}\alpha_{m'} \end{aligned} \tag{8.23}$$

where c_0 and c_2 are respectively the spin independent and spin-dependent contact

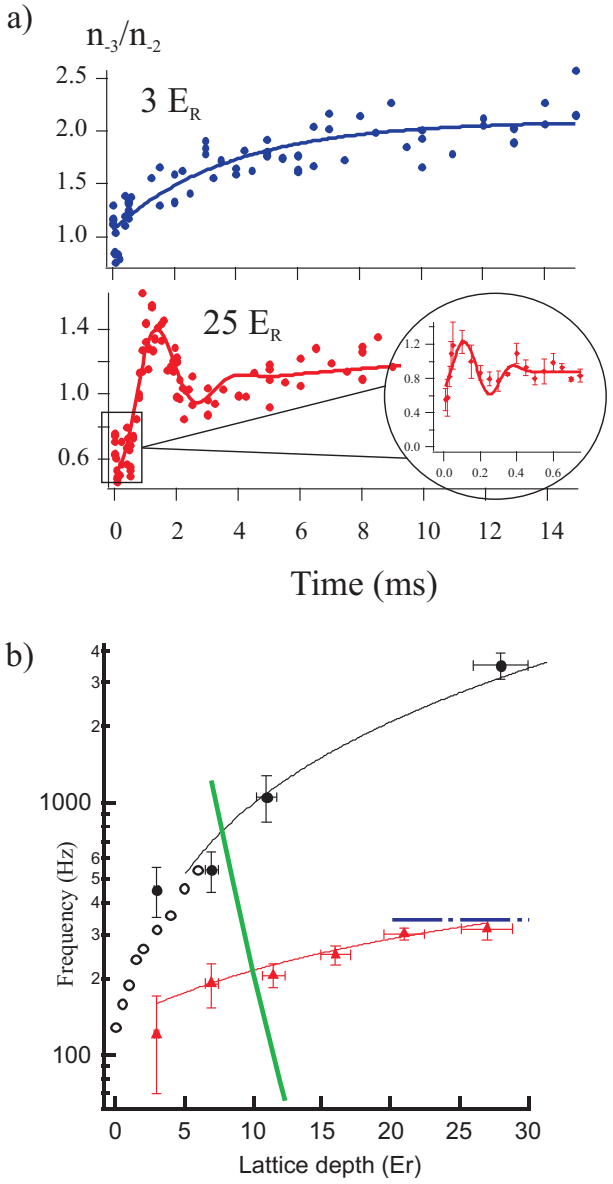

Figure 8.8: a) Time evolution of observable n_{-3}/n_{-2} for two extreme lattice depths (27 E_r and 3 E_r) corresponding respectively to the Mott regime and the superfluid regime. At large lattice depths, we observe at short times a strongly damped oscillation and then at longer times a second oscillation. For the low lattice depths the spin dynamics can be described by an exponential. Lines are guides for the eye resulting from fits. b) Frequency of fast (black points) and slow (red triangles) oscillations. The black solid line corresponds to spin-exchange frequency associated to intrasite contact interactions in doubly occupied sites, while the black open circles correspond to a numerical simulation of Gross-Pitaevskii equation. The red curve is a guide to the eye for the spin-exchange frequency associated to intersite dipolar interactions between doubly occupied sites. The blue dot-dashed line shows the prediction in the Mott regime (see text). The frequency of super-exchange process is given by the green solid line. Error bars in frequency and amplitude result from the statistical uncertainty in the fits.

interactions, dipolar interactions are described by the term proportional to c_{dd}, M is the mass, and U_{trap} is the external trapping potential. F is the spin expectation value: $F = \sum_{m,m'} \alpha^*_m f_{m,m'} \alpha_{m'}$. p accounts for the linear Zeeman effect (which can be set by the magnetic field when magnetization is free or by a Lagrange multiplier when magnetization is fixed) and q is the quadratic Zeeman effect. b is the effective dipole field defined by

$$b_\nu = \int dr' \sum_{\nu\nu'} Q_{\nu,\nu'}(r - r') F_{\nu'}(r') \tag{8.24}$$

where

$$Q_{\nu,\nu'}(r) = \frac{\delta_{\nu,\nu'} - 3 r_\nu r_{\nu'}}{r^3}. \tag{8.25}$$

As explicitly shown in eq.(8.23), the last two terms (which are interaction terms) are responsible for the coupling of different $\alpha_i(r,t)$. For example, within the Single Mode Approximation (i.e. assuming that all spin states share the same spatial dependence and only spin components vary in time), the evolution due to contact interaction for a spin 1 gas with $p = q = 0$ is (here, we only explicit spin mixing terms):

$$\begin{aligned} i\hbar\dot{\alpha}_{-1} &= c_2[(|\alpha_{-1}|^2 + |\alpha_0|^2 - |\alpha_{+1}|^2)\alpha_{-1} + \alpha_0^2 \alpha^*_{+1}] \\ i\hbar\dot{\alpha}_{0} &= c_2[(|\alpha_{-1}|^2 + |\alpha_{+1}|^2)\alpha_{0} + 2\alpha_{-1}\alpha_{+1}\alpha^*_{0}] \\ i\hbar\dot{\alpha}_{+1} &= c_2[(|\alpha_{+1}|^2 + |\alpha_0|^2 - |\alpha_{-1}|^2)\alpha_{+1} + \alpha_0^2 \alpha^*_{-1}]. \end{aligned}$$

These terms are often called spin-mixing terms, and have already been observed in experiments [112, 204].

b) Results

P.Pedri's simulation of eq.(8.23) for a spin 3, where the spatial dependence of the wavefunction was explicitly taken, show that spin dynamics is roughly twice faster when dipole-dipole interactions are not included in the simulations. This illustrates the importance of dipole dipole interactions in the dynamics in the superfluid regime, even though dipole dipole interactions are much weaker than contact interactions.

With P.Pedri, we developed a mean field model using the Single Mode Approximation. The spatial dependence was included by spatially averaging the contribution of each energy term. We find that this approximation fails to account for the dynamics. We show the results of the simulations with and without including dipole-dipole interactions Fig.8.9. Within the SMA the contribution of dipole-dipole interaction is weak: due to the anisotropy of dipole dipole interaction it almost vanishes when taking the spatial average. This is very different to the inhomogeneous simulations.

In P.Pedri's simulation, as shown by Fig.8.10, we can see that spin dynamics are inhomogeneous. This inhomogeneous mean field description reproduces well the exponential trend of the data. This agreement implies that interactions do not create quantum correlations between particles.

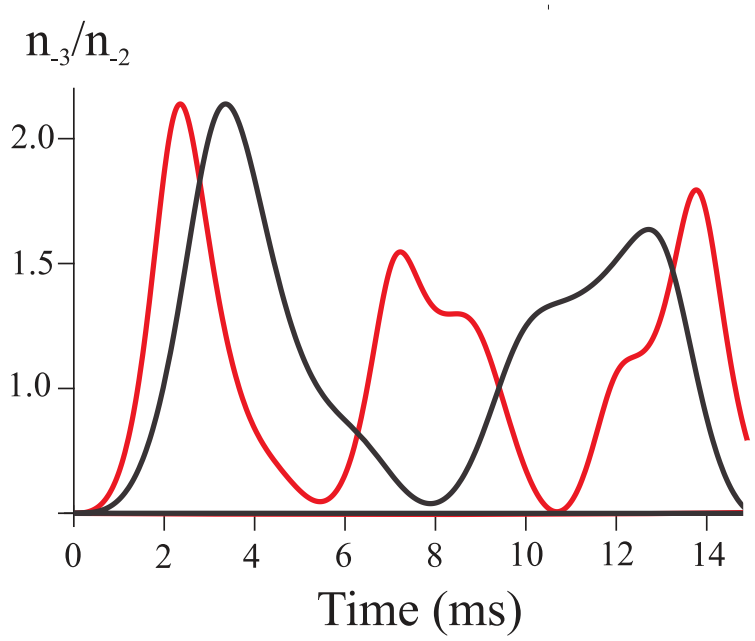

Figure 8.9: Results of numerical simulations of the Gross-Pitaevskii equation using the Single Mode Approximation with no lattice on. Evolution of n_{-3}/n_{-2} as a function of time with DDI (red) and without including DDI in the simulation (black). In these simulations, the contribution of DDI is too weak to account for the dynamics.

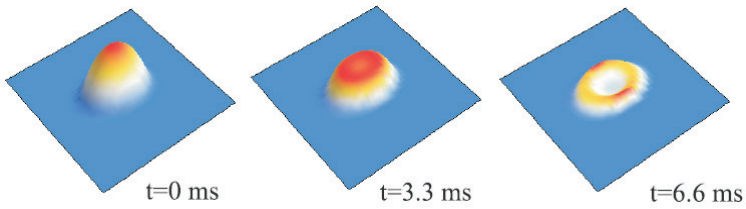

Figure 8.10: Results of numerical simulations of the Gross-Pitaevskii equation without using the Single Mode Approximation with a lattice depth of $V_0 = 7E_r$ (simulation performed by P.Pedri). The graph shows a cut of the density of the atoms in m_s = -2 state along a horizontal plane. Clearly, spin dynamics is not homogeneous.

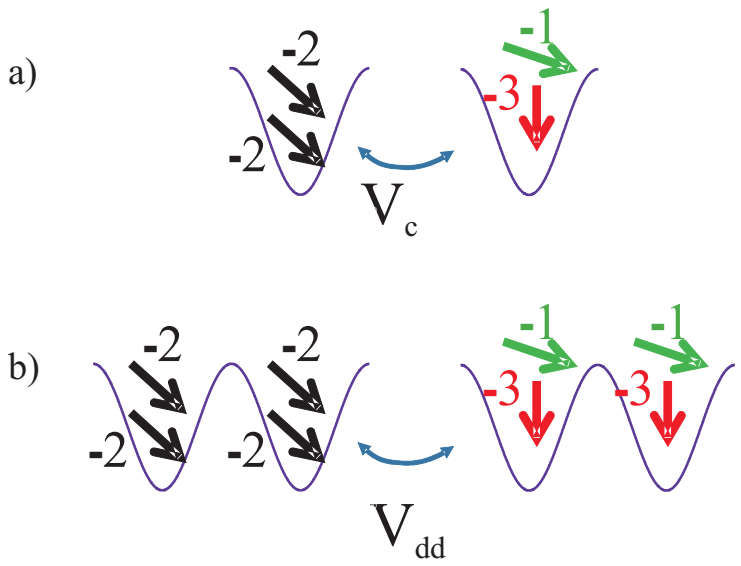

Figure 8.11: Scheme illustrating the different physical process. a) Intrasite Spin dynamics associated to contact interaction in a doubly occupied site. b) Intersite Spin dynamics associated to DDI between doubly occupied sites.

8.3.3 Physical interpretation at large lattice depth

At large lattice depths, where the strength of interactions have grown, the system is not superfluid anymore. Spin dynamics in this regime cannot be described by the Gross-Pitaevskii equation (i.e. a mean field theory) and one has to develop a theory with correlations to account for the data. We focus on the frequencies of the two oscillations observed in the Mott phase (see Fig.8.8b).

We interpret the higher frequency as a result of the intrasite spin-exchange dynamics ($|-2,-2> \rightarrow \frac{1}{\sqrt{2}}(|-3,-1> + |-1,-3>)$ arising from spin-dependent contact interactions in doubly occupied sites (see Fig.8.11a). The observed frequency of 3.6±0.4 kHz is in good agreement with the theoretical frequency $\frac{4\pi\hbar}{2\sqrt{2}m}(a_6 - a_4)n_0$ estimated at 3.1 ± 0.5 kHz (see subsection 3.2.2). Here, n_0 is the peak density in a doubly occupied lattice site and is estimated to be $n_0 \approx 6.3 \times 10^{20}$ at.m^{-3}, m the atom mass; a_6 and a_4 are the scattering lengths of the $S = 6$ and $S = 4$ molecular channels, respectively.

The lower frequency is associated to DDI between doubly occupied sites of different lattice sites. This process is described in detail in [203] and schematically represented in Fig.8.11b. The contribution of DDI to the Hamiltonian is $\hat{H}_{dip}^{eff}$ (see eq.(6.13)). We calculated the time evolution of the population N_{-2} in the state $m_s = -2$ using perturbation theory in the Heisenberg picture. The many-body Hamiltonian takes into account the interaction of one doubly occupied lattice site i with all its neighbors j by a pairwise DDI. Using a Taylor expansion, the expression of the population in $m_s =$

-2 reads:

$$N_{-2}(t) = \sum_{n=0}^{\infty} M_n t^n \tag{8.26}$$

The first non vanishing moment is M_2 and describes spin dynamics up to second order of perturbation theory. Explicitly we have [37, 203]:

$$M_2 = -\frac{1}{\hbar^2} \sum_{j \neq i} V_{dd}^{(4,4)\leftrightarrow(3,5)} (r_i - r_j)^2. \tag{8.27}$$

where $V_{dd}^{(4,4)\leftrightarrow(3,5)}(r_i - r_j)$ is the dipolar spin-exchange matrix element $< S = 6, m_S = 4; S = 6, m_S = 4|\hat{V_{dd}}|S = 6, m_S = 3; S = 6, m_S = 5 >$ between sites i and j. For two nearest neighbours we compute $V_{dd}^{(4,4)\leftrightarrow(3,5)}(\lambda/2) \approx h\times$ 100 Hz. From M_2, we can extract an estimate of the spin oscillation frequency:

$$\begin{aligned} \cos^2(\pi\nu t) &\approx 1 - M_2 t^2 \\ \rightarrow \nu &= \frac{1}{\pi}\sqrt{M_2} \\ &\approx 200 \text{ Hz}. \end{aligned} \tag{8.28}$$

The frequency extracted is about twice smaller than the observed spin oscillation frequency of about 400 Hz. This perturbative approach was applied up to fourth order to the case of an assembly of doubly occupied sites in a state $|S = 6, M_S = -4 >$. The result of this calculation increases the frequency by a factor of 2 and therefore shows good agreement with the observed frequencies obtained deep in the Mott regime.

The interpretation of eq.(8.26) and eq.(8.27) to the case of singly occupied sites is that an initial many body state $\Psi_{ini} = |-2, -2, ..., -2 >$ (where the spin state of each atom in each lattice site is explicitly written down) is coupled through dipolar interaction to the following many body state:

$$\begin{aligned} \Psi_{fin} &= \frac{1}{\sqrt{\sum_{i<j} V_{dd}^{(2,2)\leftrightarrow(3,1)}(r_i - r_j)^2}} \\ &\times \sum_{i<j} V_{dd}^{(2,2)\leftrightarrow(3,1)}(r_i - r_j)|-2, ..., -2, i: -1, -2, ..., -2, j: -3, -2, ..., -2 > \end{aligned} \tag{8.29}$$

where $|-2, ..., -2, i: -1, -2, ..., -2, j: -3, -2, ..., -2 >$ describes a state where all lattice site are in spin state $m_s = -2$ except sites i and j which are respectively in spin states $m_s = -1$ and $m_s = -3$. The rate of coupling between Ψ_{ini} and Ψ_{fin} is given by eq.(8.28). This many-body physical picture clearly indicates that the initial state is coupled to a state which shows quantum correlations.

From the good agreement in timescales between our model and the experiments we suggest that we have quantum correlations in our system.

8.3.4 Conclusion

Our study described in these paragraphs indicate that beyond mean field effects (i.e. quantum correlations) only occur in deep lattices. For weak lattices, we find that the GP equation is able to quantitatively reproduce our data. This dynamics results from a combined effect of contact and dipolar interaction, and my contribution was to show that the inhomogeneity of the gas needs to be taken into account in order to understand the interplay between local and non local forces.

It is in fact not obvious that beyond mean field effects cannot occur without a lattice (see for example [205]). Inspired by a proposal from A.M Rey, we therefore decided to modify the way we excite the spins by rotating them. Indeed, as we will now see, it is predicted that such a procedure followed by spin-spin interaction could lead to significant quantum correlations and therefore beyond mean field effects, even without a lattice.

8.4 Spin dynamics following a rotation of the spins

Following a proposal from A.M. Rey of JILA we decided to investigate spin dynamics due to dipole-dipole interactions after a rotation of all individual spins. Let us first compare the effective dipole-dipole Hamiltonian $\hat{H}_{dip}^{eff}$ to the Heisenberg Hamiltonian:

$$\begin{aligned} \hat{H}_{Hei} &= \sum_i \hat{\vec{S}}_i.\hat{\vec{S}}_{i+1} \\ &= \sum_i \hat{S}_{i,x}.\hat{S}_{i+1,x} + \hat{S}_{i,y}.\hat{S}_{i+1,y} + \hat{S}_{i,z}.\hat{S}_{i+1,z} \end{aligned} \tag{8.30}$$

The Heisenberg Hamiltonian is invariant by rotation (in literature this is called SO(3) symmetry). Therefore if an eigenstate of the Heisenberg Hamiltonian is rotated, it remains an eigenstate and no dynamics is expected. After spin rotation all the spins are pointing in the same direction ($\hat{\vec{S}}_i = \hat{\vec{S}}_{i+1} = \hat{\vec{S}}$). Since the Heisenberg Hamiltonian commutes with $\hat{\vec{S}}^2$, $< \hat{\vec{S}}^2 >$ is a conserved quantity when the evolution of a system is governed by the Heisenberg Hamiltonian.

Let us now introduce the following Hamiltonian:

$$\Delta\hat{H} = \frac{3}{2}\hat{S}_{1z}\hat{S}_{2z}. \tag{8.31}$$

We may now write the spin part of the effective dipolar Hamiltonian in the following way:

$$\begin{aligned} \hat{H}_{dip}^{eff} &= -\frac{1}{2}\hat{H}_{Hei} + \Delta\hat{H} \\ &= -\frac{1}{2}\hat{H}_{Hei} + \frac{3}{2}\hat{S}_{1z}\hat{S}_{2z}. \end{aligned} \tag{8.32}$$

$\hat{H}_{dip}^{eff}$ is invariant by rotation around z but not around another coordinate axis. Therefore if an eigenstate of $\hat{H}_{dip}^{eff}$ is rotated around an other axis than z (around x for example), we expect dynamics.

In the following I shall present experiments where we observed spin dynamics after a rotation induced by a RF pulse. Fig.8.12 is a cartoon illustrating the principle of our experiment. Moreover, $\hat{H}_{dip}^{eff}$ does not commute with $\hat{\vec{S}}^2$ (this can be seen from eq.(8.32)). $< \hat{\vec{S}}^2 >$ is therefore not a conserved quantity under the evolution of dipolar interactions.

The experiments were performed in the superfluid and in the Mott regime. In the first case, the dynamics is compared to a mean field theory. In the lattice where interactions are stronger, we expect quantum correlations to form and mean field theory to break down, so that we compare our results both with a mean field and a beyond mean field theory. More precisely, A.M. Rey predicts that for $\theta = \frac{\pi}{2}$ the dynamics should create quantum correlations and that for $\theta \sim 0$ dynamics should be accounted for by a classical mean field theory [206, 207].

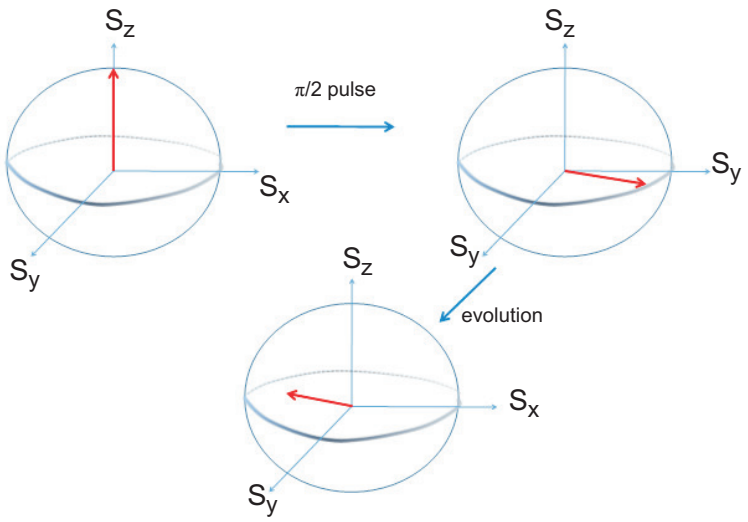

Figure 8.12: Cartoon representing a Bloch Sphere in order to describe the experiment. At the start of the experiment the collective spin of the gas is aligned with the external magnetic field. We then tilt the spin by an angle θ (in the cartoon, $\theta = \pi/2$). The spin precesses around the magnetic field and spin dynamics occur due to interactions between atoms. In particular, the total spin can be reduced in which case projection along z will lead to different output with time.

8.4.1 Initial spin state preparation

The initial out of equilibrium spin state is produced by a RF pulse. In the following I shall recall general results of a spin in a static field submitted to a RF excitation and show how it applies for spin 3 Chromium.

A spin in a RF field

Let us consider an atom of spin s in a static magnetic field $\vec{B}_0 = B_0\vec{e}_z$ of Larmor frequency ω_0. The coupling between the spin and the magnetic field is $\gamma\vec{s}.\vec{B}_0$ with γ the gyromagnetic factor. An antenna can produce an oscillatory magnetic field $\vec{B_1}(t) = \frac{2\hbar}{\gamma}\Omega_1\cos(\omega t)\vec{u}$ with $\vec{u}$ a unit vector representing the direction of the field created by the antenna. In the following, for the sake of simplicity we will consider that the field created by the antenna is along the direction $\vec{u} = \vec{e_x}$. The Hamiltonian of a spin $\hat{S}$ in such a field takes the form:

$$\begin{aligned} \hat{H} &= \gamma\hat{\vec{S}}.\vec{B}_0 + \gamma\hat{\vec{S}}.\vec{B}_1 \\ &= \gamma B_0\hat{S}_z + \gamma B_1\cos(\omega t)\hat{S}_x \end{aligned} \tag{8.33}$$

This time dependant problem is equivalent to solving an effective Hamiltonian $\hat{H}_{eff}$ in the rotating frame around $\vec{z}$ at frequency ω. In this frame, applying the rotating

wave approximation (in practice valid for $\Omega_1 << \omega$), it can be shown [184] that:

$$\hat{H}_{eff} = (\omega_0 - \omega)\hat{S}_z + \Omega_1 \hat{S}_x. \tag{8.34}$$

with $\omega_0 = \gamma B_0/\hbar$ the Larmor frequency and $\Omega_1 = \gamma B_1/\hbar$ the Rabi frequency. In the experiments performed in this chapter, we will typically have $B_0 \approx 357$ mG and a Larmor frequency of $\omega_0 \approx 1$ MHz

The evolution of the wavefunction is given by the evolution operator:

$$|\psi(t)>= e^{i\hat{H}_{eff}t/\hbar}|\psi(t=0)> . \tag{8.35}$$

The probability of finding the spin of the atom in one of the stretched states (i.e. for s=3 $|m_s = -3>_z$ or $|m_s = +3>_z$) oscillates at a period $2\pi/\Omega$ where $\Omega = \sqrt{\Omega_1^2 + \delta^2}$ with $\delta = \omega_0 - \omega$ the detuning between the Larmor frequency and RF frequency, Ω is defined as the generalized Rabi frequency.

Starting with $|\psi(t=0)> = |m_s = -3>_z$ this leads to a Rabi Oscillation at a frequency Ω. We show in Fig.8.13 the magnetization of the gas as a function of the RF pulse duration. The RF power is tuned so that the magnetization of the gas oscillates at $\Omega = 2\pi\times$ 25 kHz. Magnetization oscillates between the two extreme values -3 and +3, demonstrating a resonant RF excitation ($\delta = 0$) .

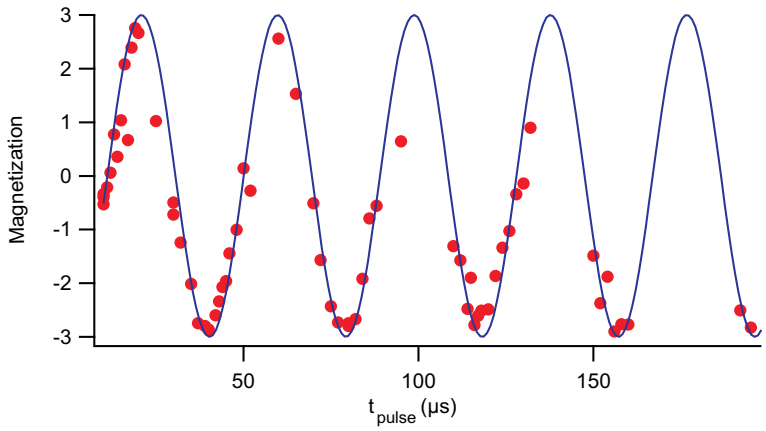

Figure 8.13: Magnetization along z of the gas as a function of the Rabi pulse for a resonant excitation (the Rabi oscillation starts at M $\approx$ 0 because the smallest pulse time here corresponds to a pulse close to $\pi/2$). Solid line is the result of a sinusoidal fit.

Table 8.1 shows the spin composition of the gas, initially polarized in m_s= -3, after different RF pulse times performed at resonance ($\delta = 0$).

D.C. magnetic field fluctuations lead to fluctuations of the Larmor frequency and therefore of δ. If the fluctuations in δ are comparable to Ω_1, from shot to shot we can have Rabi oscillations at different frequencies. This destroys the reproducibility of the RF pulse. We therefore lock the magnetic field (see [178] for magnetic field

	N_{-3}/N_{Tot}	N_{-2}/N_{Tot}	N_{-1}/N_{Tot}	N_0/N_{Tot}	N_{+1}/N_{Tot}	N_{+2}/N_{Tot}	N_{+3}/N_{Tot}
t=0	1.0	0	0	0	0	0	0
$t = t_{\pi/8}$	0.792	0.188	0.019	0.001	0	0	0
$t = t_{\pi/4}$	0.387	0.398	0.171	0.039	0.005	0	0
$t = t_{0.7\pi}$	0.148	0.332	0.312	0.156	0.044	0.007	0
$t = t_{\pi/2}$	0.016	0.094	0.234	0.313	0.234	0.094	0.016
$t = t_{\pi}$	0	0	0	0	0	0	1.0

Table 8.1: Theoretical Relative populations in different spin states depending on the duration of the RF pulse and for $\delta = 0$

stabilization). Once the magnetic field is locked, we estimate $\delta \leq 1$ kHz. With Ω_1 = 25 kHz, we produce RF pulses with Rabi frequency $\Omega = 2\pi\times$ 25 $\pm$ 0.02 kHz. However, other source of noise may contribute: noise in RF amplifier, jitter in the time sequences,... In total, we estimate experimentally the absolute calibration of the RF pulse to be in the 10 % level, but the pulse can be reproduced with accuracy at the percent level.

The frequency of the RF field must be well defined in frequency in order to perform a well calibrated RF pulse. Since the RF field is turned on for a certain window of time, there will necessarily be a frequency broadening of the RF frequency. The condition for a well defined Rabi frequency is $\omega >> \Omega_1$, then the RF field may oscillate many times before the end of the RF pulse and limits the broadening in frequency.

Imaging calibration

For the experiment performed in this section, we will compare our data with numerical simulations for each spin state. It is therefore crucial to evaluate correctly the absolute atom number in each spin state. For each data taking we attribute correcting coefficients to each spin states. These coefficients are found by performing calibrated RF pulses. With the knowledge of the total atom number and the relative populations expected for each Rabi pulse we can deduce the imaging coefficients of the different spin states. For example, with a Rabi pulse t_π we deduce the coefficient associated to $m_s = +3$, with $t_{\pi/2}$ we deduce the coefficients of $m_s = 0$, 1, and -1, $t_{\pm\pi/4}$ yields the coefficient of $m_s = \mp$ 2 (see Table 8.1). Let λ_i be the coefficient for spin state i.

Typical coefficient values are:

$$\begin{pmatrix} \lambda_{-3} = 1 \\ \lambda_{-2} = 1.1 \\ \lambda_{-1} = 1.4 \\ \lambda_{0} = 2.2 \\ \lambda_{+1} = 4.3 \\ \lambda_{+2} = 5.4 \\ \lambda_{+3} = 6 \end{pmatrix}.$$

8.4.2 Spin dynamics in the bulk

The experiment

We prepare a BEC in $m_s = -3$ and apply a magnetic field of 1 MHz along the z direction. The trap frequencies are $\nu_{x,y,z} = (166,395,235)$ Hz. The peak atomic density for $N = 10^4$ atoms is $n_0 = 1.1 \times 10^{20}$ at·m^{-3}.

We then perform a resonant RF pulse achieving rotation of individual spins with a Rabi angle ranging from $\frac{\pi}{8}$ up to $\frac{\pi}{2}$. We then let the system evolve for a time t and measure the relative populations in each spin state after a Stern and Gerlach separation.

In the following I will call z the axis corresponding to the direction of the magnetic field, that we changed between experiments.

Experimental results

In Fig.8.14 we show the total atom number N_{Tot} after a $\frac{\pi}{2}$ RF pulse as a function of time. We also show the magnetization M of the gas ($M = \sum_i \frac{iN_i}{N_{Tot}}$) for RF pulses ranging from $\frac{\pi}{8}$ to $\frac{\pi}{2}$. The total atom number decreases rapidly in time. This feature can be seen for all RF pulses. We will therefore normalize the population of each spin state by the total atom number. Magnetization remains roughly constant throughout the experiment.

In Fig.8.15 we show the evolution of the relative spin populations for different RF pulses. Each color corresponds to a different spin state. For the smallest RF tilt, barely any spin dynamics takes place (Fig.8.15a). However, when the tilt is increased (Fig.8.15b and c), we observe increasing spin dynamics.

Losses and conserved magnetization interpretation

We attribute the losses to dipolar relaxation. A pair of atoms in a spin excited states can collide through DDI and transfer their magnetic energy into kinetic energy. This process releases 1 or 2 MHz magnetic energy into kinetic energy for the pair of colliding atoms (depending on the collisional channel, see subsection 3.1.2). We estimate the depth of our optical potential to be of the order of 20 kHz which is much smaller than

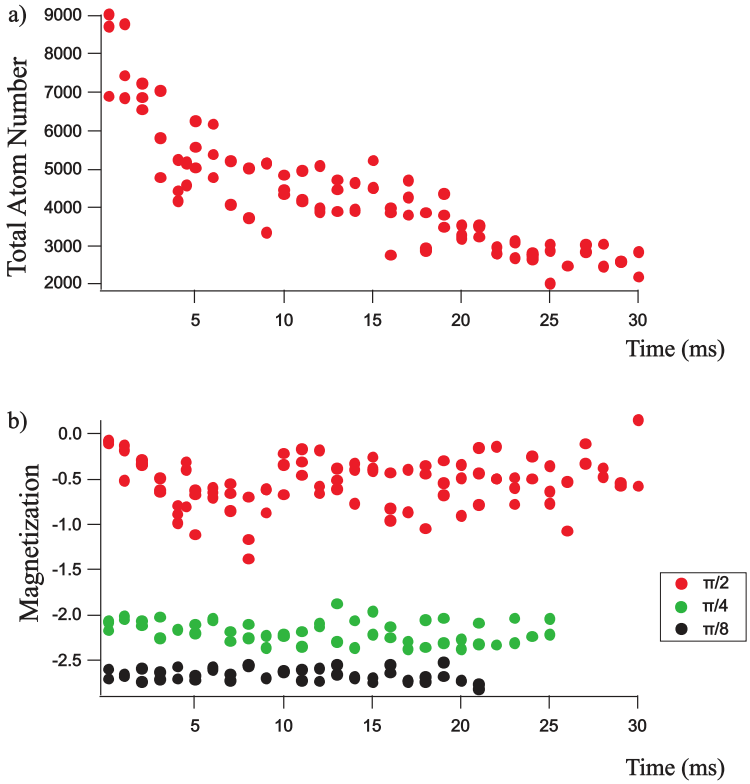

Figure 8.14: a) Total atom number for a $\frac{\pi}{2}$ pulse and b) Magnetization as a function of t for different RF pulses. We attribute the losses to dipolar relaxation collisions: the magnetic energy released during the collision is large enough that the pair of atoms escape from the trap. This argument is supported by the fact that magnetization remains roughly constant during the experiment.

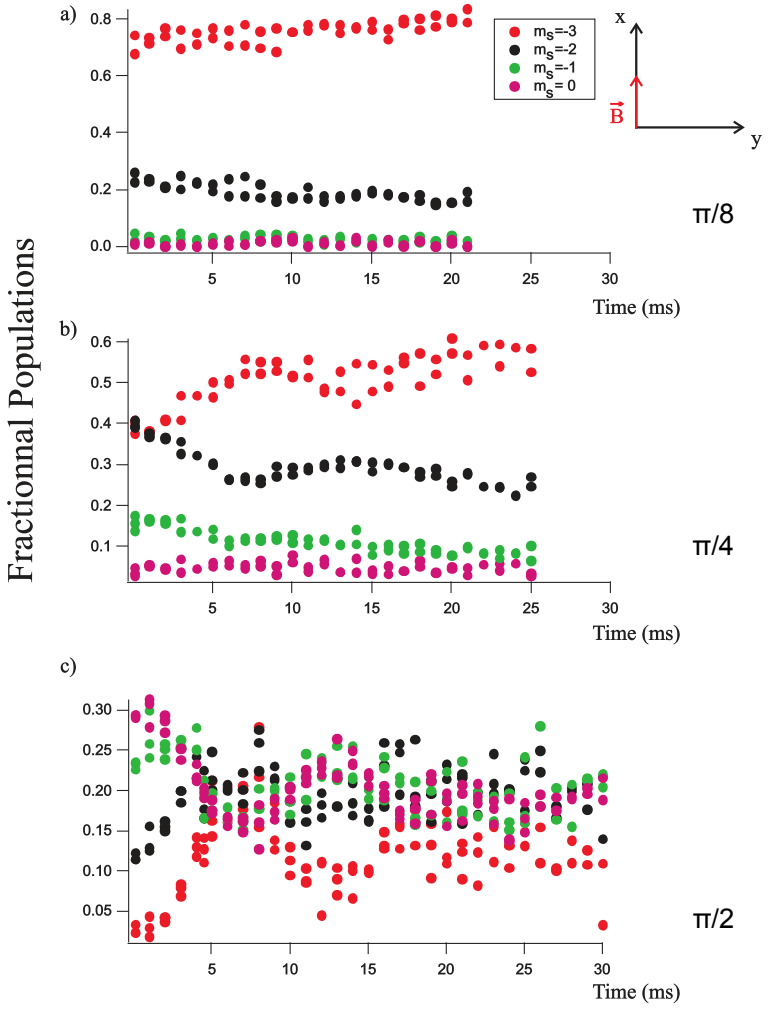

Figure 8.15: Evolution of the relative populations in each spin state as a function of time for different RF pulses: a) $\frac{\pi}{8}$ RF pulse, b) $\frac{\pi}{4}$ RF pulse, and c) $\frac{\pi}{2}$ RF pulse. Each color corresponds to a different spin state. For clarity, we only show the plots for $m_s \leq 0$. Spin dynamics is observed for the larger RF pulses.

the kinetic energy gained by a non magnetization conserving collision. Therefore atoms remaining in the trap have only experienced magnetization conserving collisions. This scenario is confirmed by the fact that magnetization is almost constant during the experiment (see Fig.8.14).

To interpret our data we therefore normalize the atom number in a spin state by the total atom number and consider only magnetization conserving terms in the Hamiltonian. The dipolar Hamiltonian then reads:

$$\hat{H}_{dip}^{eff} = \hat{S}_{1z}\hat{S}_{2z} - \frac{1}{4}(\hat{S}_{1+}\hat{S}_{2-} + \hat{S}_{1-}\hat{S}_{2+}). \tag{8.36}$$

Classical dynamics

As introduced earlier in section 6.1, N classical spins precess around the axis defined by the sum of the external magnetic field and the field created by all the dipoles. Experimentally for a trapped system, the local field seen by one atom (created by all the other dipoles) depends on space due to the spatial inhomogeneity of the atomic sample. This leads to a inhomogeneous precession. However, locally spins remain aligned. Therefore, no spin dynamics is expected and we must go beyond this classical interpretation in order to account for the dynamics.

Contact dynamics

A RF pulse tilts the spin of the gas by an angle θ around the axis defined by the RF field (which we refer to as $\vec{x}$ in the following). This results in a rotation of the initial state $|\psi_0>=|s=3,m_s=-3>_z$:

$$|\psi(t=0)> = |s=3,m_s=-3>_\theta . \tag{8.37}$$

In the molecular basis, after the RF pulse a pair of atoms are in state $|S=6,M_S=-6>_\theta$. This state is an eigenstate of the molecular potential a_6 no matter θ. Contact dynamics therefore does not trigger any extra spin dynamics after the RF pulse.

Dipolar dynamics

The case of dipolar interactions is different. $|s=3,m_s=-3;s=3,m_s=-3>_z$ is an eigenstate of $\hat{H}_{dip}^{eff}$, however $|s=3,m_s=-3;s=3,m_s=-3>_\theta$ is not. Therefore after the RF pulse atoms are coupled to each other through dipole-dipole interactions and we can therefore expect the prepared state to evolve.

More precisely, let us perform a change of basis associated to a rotation around $\vec{x}$ axis by an angle θ. The vectors of the new basis $(\vec{u}_{x'},\vec{u}_{y'},\vec{u}_{z'})$ can be expressed as a function of the old basis $(\vec{u}_x,\vec{u}_y,\vec{u}_z)$:

$$\begin{aligned}\vec{u}_x &= \vec{u}_{x'}\\ \vec{u}_y &= \cos\theta\vec{u}_{y'} - \sin\theta\vec{u}_{z'}\\ \vec{u}_z &= \sin\theta\vec{u}_{y'} + \cos\theta\vec{u}_{z'}\end{aligned} \tag{8.38}$$

We can then express the spin operators of the new basis:

$$\begin{aligned}\hat{S}_x &= \hat{S}_{x'} \\ \hat{S}_y &= \cos\theta\hat{S}_{y'} - \sin\theta\hat{S}_{z'} \\ \hat{S}_z &= \sin\theta\hat{S}_{y'} + \cos\theta\hat{S}_{z'}\end{aligned} \tag{8.39}$$

and deduce the expressions of the spin rising and lowering operators of the new basis:

$$\begin{aligned}\hat{S}_{+'} &= \hat{S}_{x'} + i\hat{S}_{y'} \\ \hat{S}_{-'} &= \hat{S}_{x'} - i\hat{S}_{y'}\end{aligned} \tag{8.40}$$

We may now express the effective dipolar Hamiltonian $\hat{H}^{eff}_{dip'}$ after a rotation θ around the $\vec{x}$ axis:

$$\begin{aligned}\hat{H}^{eff}_{dip'} &= \hat{S}_{1z'}\hat{S}_{2z'}\big[\cos^2\theta - \frac{1}{2}\sin^2\theta\big] + (\hat{S}_{1+'}\hat{S}_{2-'} + \hat{S}_{1-'}\hat{S}_{2+'})\big[\frac{1}{8} - \frac{3}{8}\cos^2\theta\big] \\ &+ \hat{S}_{1z'}(\hat{S}_{2+'} + \hat{S}_{2-'})\big[\frac{\cos\theta}{2} + \frac{1}{2}\frac{\sin\theta\cos\theta}{2}\big] \\ &+ \hat{S}_{2z'}(\hat{S}_{1+'} + \hat{S}_{1-'})\big[\frac{\cos\theta}{2} + \frac{1}{2}\frac{\sin\theta\cos\theta}{2}\big] \\ &+ \hat{S}_{1-'}\hat{S}_{2-'}\big[\frac{3}{8} - \frac{3}{8}\cos^2\theta\big] \\ &+ \hat{S}_{1+'}\hat{S}_{2+'}\big[\frac{3}{8} - \frac{3}{8}\cos^2\theta\big]\end{aligned} \tag{8.41}$$

Performing second quantization and applying a mean field approximation, we can compute the evolution of the different spin states under the influence of $\hat{H}^{eff}_{dip'}$. The evolution is given by the dipolar term of the GPE. If we focus on the evolution of spin state $|m_s = -2>_\theta$ due to collisions between $|m_s = -3>_\theta$ atoms we have:

$$i\hbar\frac{d\alpha^{(\theta)}_{-2}}{dt} \propto (\frac{3}{8} - \frac{3}{8}\cos^2\theta)\alpha^{*(\theta)}_{-2}\alpha^{(\theta)}_{-3}\alpha^{(\theta)}_{-3} + \overbrace{(\frac{3}{8}\sin 2\theta)}^{C(\theta)}\alpha^{*(\theta)}_{-3}\alpha^{(\theta)}_{-3}\alpha^{(\theta)}_{-3}. \tag{8.42}$$

No matter the angle imprinted by the RF pulse, the initial state is the stretched state $|m_s = -3>_\theta$, therefore $\alpha^{(\theta)}_{-2}(t = 0) = 0$. Only the last term in eq.(8.42) does not involve $\alpha^{(\theta)}_{-2}$ and will drive the initial dynamics by producing an initial population in $|m_s = -2>_\theta$[6] which will then allow for contributions of the other terms in eq.(8.42).

For the specific case of a $\pi/2$ RF pulse, the coefficient $C(\theta = \frac{\pi}{2})$ vanishes. No seed in $|m_s = -2>_\theta$ is produced and mean field theory predicts no dynamics. This seed could

[6] commonly called "seed"

be produced by quantum fluctuations and/or beyond mean field effects. However, the seed which could trigger dynamics for the $\pi/2$ RF pulse (Fig.8.15c) has a less appealing origin. The initial population in $|m_s = -2 >_\theta$ could be actually produced by another term in the Hamiltonian, the quadratic light shift term. In addition, the presence of a residual magnetic gradient has to be taken into account. We are currently investigating the impact of a quadratic term and magnetic field gradient on the dynamics.

After investigating a number of magnetic field directions (presumably associated to different values of the quadratic shift q) we found a direction of the magnetic field with no observed spin dynamics (see Fig.8.16). We checked that no magnetic gradient is present (by comparing the ballistic expansion of an $m_s = -3$ gas after turning off trapping potentials to the one of $m_s = +3$). The absence of any dynamics testifies that the quadratic shift is then small. Therefore, to the best of our knowledge at the time of this writing we make the following statement: when no quadratic term is present nor any magnetic gradient we find no dynamics.

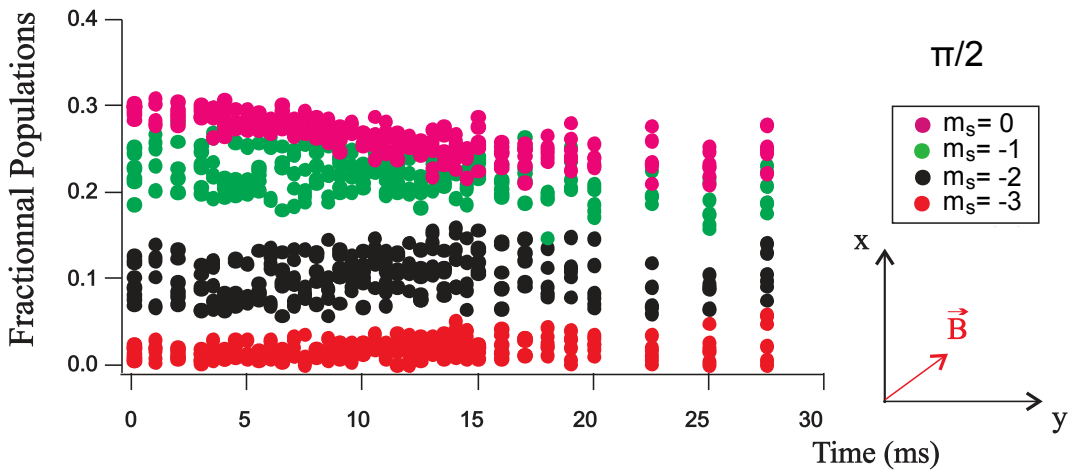

Figure 8.16: Evolution of the relative populations in each spin state as a function of time for a $\frac{\pi}{2}$ RF pulse for a different magnetic field direction than for Fig.8.15. We do not observe any magnetic gradient. The absence of any dynamics, in agreement with a mean field theory with no quadratic light shift term, indicates that q is then small.

Purely dipolar dynamics?

For the magnetic field direction where we do not observe any magnetic gradient and inferred a small value of q, we do not expect any dynamics due to contact interactions. Atoms interact through the S=6 molecular potential. And as discussed above, for the specific case of $\frac{\pi}{2}$ pulse, we do not expect any dipolar dynamics. However, for any other angle of RF pulse, we expect the initial dynamics to be exclusively due to dipole-dipole interactions.

We performed a $\frac{\pi}{4}$ pulse experiment for the magnetic field direction where the magnetic gradient is small and q is inferred to be small. The result of this experiment is shown Fig.8.17. We can see "large" spin dynamics. The full lines are mean field simulations performed by K.Kechadi and P.Pedri, which agree well with the data for short times.

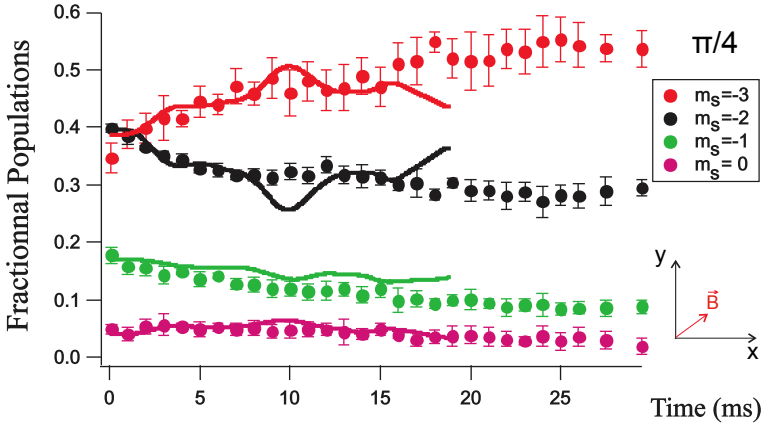

Figure 8.17: Evolution of the relative populations in each spin state as a function of time for a $\frac{\pi}{4}$ RF pulse with the magnetic field along the direction which cancelled dynamics for the $\frac{\pi}{2}$ RF pulse . The full lines are mean field simulations (performed by K. Kechadi and P. Pedri) where $q = 0$ is assumed. Simulations confirm that initial dynamics are purely dipolar.

This dynamics is in principle triggered by dipole-dipole collisions. As discussed above, simulations performed for $\frac{\pi}{4}$ pulse with $q_z = 0$ Hz and without any dipolar interactions show no dynamics. After the initial dipolar dynamics, then contact collisions may play a role. This is being investigated by Kaci Kechadi. For the moment, the general trend is well described by mean field Gross Pitaevskii equations.

In the following section we will perform similar experiments but in a strongly interacting regime by loading atoms in an optical lattice.

8.4.3 Spin dynamics in the lattice

In the previous section, we saw that no spin dynamics occurs after a RF pulse provided there are no magnetic field gradients nor quadratic light shift. In a lattice, we should have the advantage of not being sensitive to contact interactions in singly occupied sites. Also, eq.(8.42) illustrates the importance of a seed in $|m_s = -2 >_y$ (i.e. for a $\pi/2$ pulse). In the BEC case Bose stimulation helps defining a most populated mode and strengthens mean field approximations. In the lattice case, number occupation is close to 1 and Bose stimulation has a less important role, which helps quantum fluctuations drive the dynamics. We will therefore load atoms in the lattice and reproduce the same experiment. The lattice characteristics were presented in section 8.2.

The experimental protocol is the following: we prepare a BEC in $|m_s = -3 >_z$ and load atoms in an optical lattice in the Mott regime with a lattice depth of $V_0 = 25$ E_r along each axis. In this regime, our atomic distribution follows the wedding cake distribution with a core of doubly occupied site surrounded by a shell of singly occupied sites. Typically 60% of our atoms are in doubly occupied sites. We apply a magnetic field of $g_s\mu_B B/h$ =1 MHz along the z direction. We then perform a resonant RF pulse implementing spin rotations from $\frac{\pi}{8}$ up to $\frac{\pi}{2}$. We then let the system evolve for a time t, and then measure the relative populations in each spin state with a Stern-Gerlach sequence.

Results

In Fig.8.18 we show the total atom number N_{Tot} as a function of time along with the magnetization of the gas after different RF pulses. The total number of atoms decreases in time with two distinct regimes[7]. For the $\pi/2$ experiment shown here, the total atom number is strongly reduced within the first 5 ms by more than 50%. At larger times such fast losses cease, and the total atom number undergoes a much slower decrease. The magnetization of the gas is slightly lowered for increasing times. We observe that the larger the RF pulse the more magnetization decreases in time.

Fig.8.19 shows the spin dynamics resulting from this experiment for different RF pulses. For small RF pulses, we hardly observe any dynamics. As we increase the RF pulses, the trend of the evolution of population in different spin states is more and more evolution with larger amplitudes.

8.4.4 Interpretation

After the RF pulse, doubly occupied sites are in $|S = 6, m_S = -6 >_\theta$ and singly occupied sites are in $|s = 3, m_s = -3 >_\theta$.

Losses interpretation

Again, we attribute losses to dipolar relaxation collisions. The depth of the optical potential is estimated to be $V_0 = 3\times$ 25 $E_r \sim$ h $\times$ 0.975 MHz. This indicates that a pair of atoms which undergo a dipolar relaxation event will leave the trap and will result in losses as can be seen in the experiment (see Fig.8.18) as the magnetic field is $g_s\mu_B B/h = 1$ MHz (future experiments should raise the magnetic field to increase the validity of our statement). However, contrarily to the case in the bulk, the total atom number stops diminishing after approximatively 5 ms. We interpret this as the moment when the system does not contain any doubly occupied sites anymore. Despite the fact that DDI are long-range, dipolar relaxation at $g_s\mu_B B/h = 1$ MHz are short-ranged as

[7] These two regimes are observed for all RF pulses. Here, for clarity, we show only the result of the $\pi/2$ experiment.

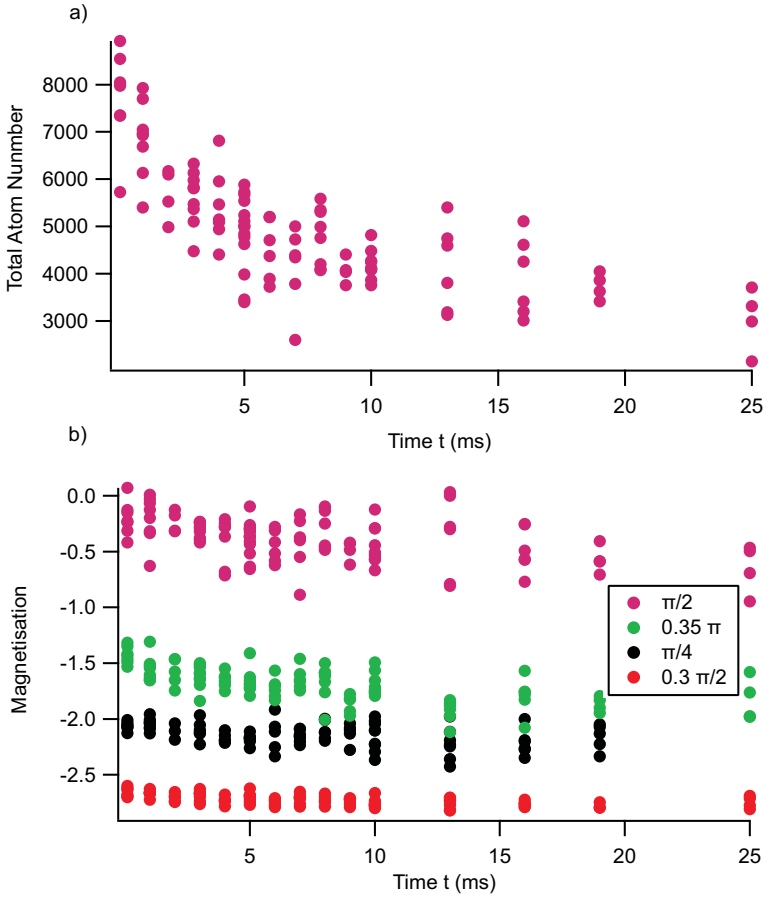

Figure 8.18: a) Total atom number for a $\frac{\pi}{2}$ pulse and b) magnetization as a function of t for different RF Pulse. We attribute the losses to dipolar relaxation collision in doubly occupied sites: the magnetic energy released during the collision is large enough that the pair of atoms escape from the trap. This argument is supported by the fact that magnetization remains constant and losses are suppressed after $t \approx 5$ ms.

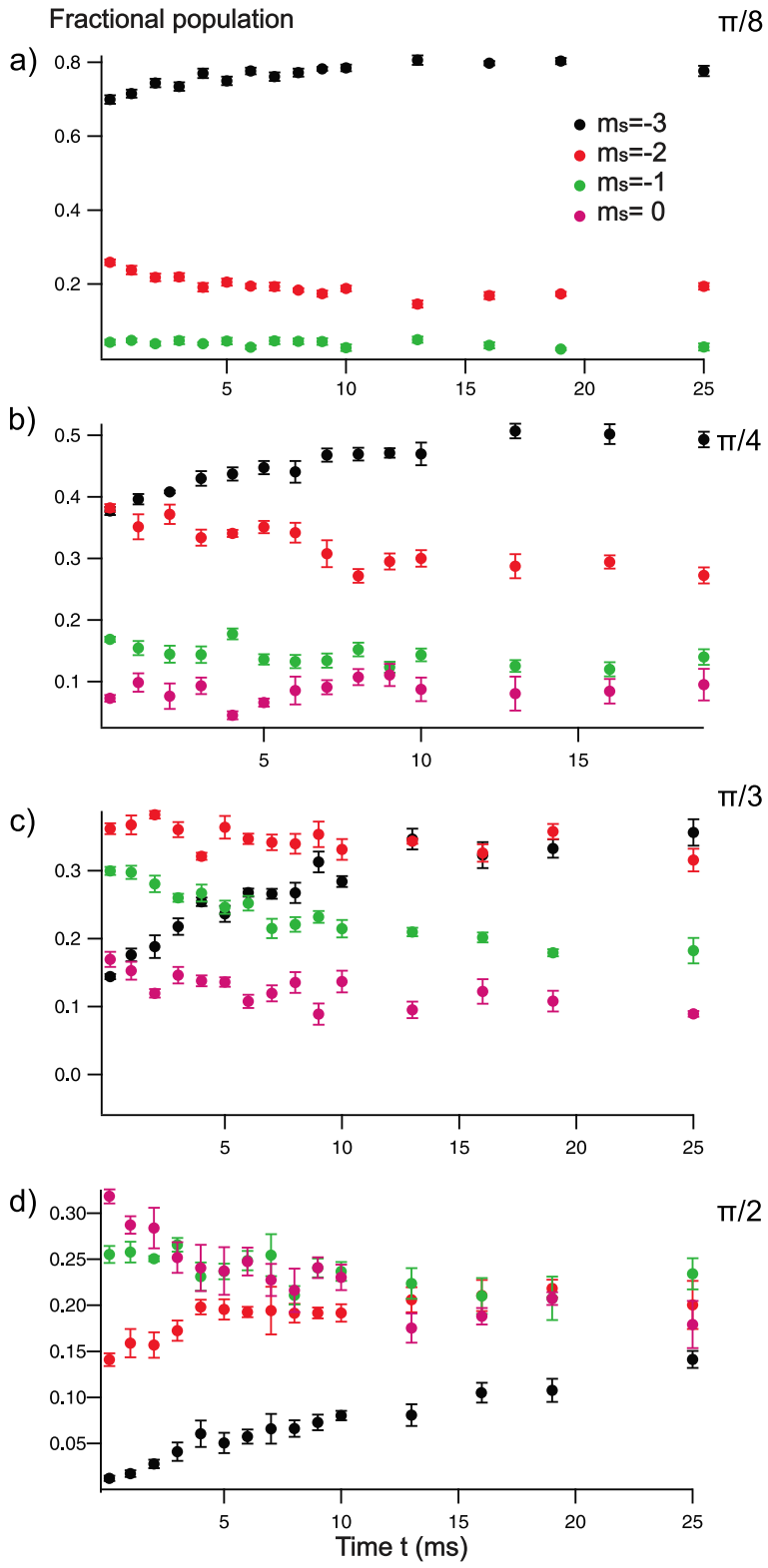

Figure 8.19: Evolution of the relative populations in each spin state as a function of time for different RF pulses and a lattice depth of $V_0 = 25\ E_r$. From top to bottom the RF pulses are a) $\pi/8$, b) $\pi/4$, c) $\pi/3$, d) $\pi/2$. For clarity, we only show the plots for $m_s \leq 0$. For each spin rotation, we observe spin dynamics.

discussed in section 6.2.3. At such magnetic fields, the typical inter-particle distance R_{RD} at which a dipolar relaxation collision occurs is $R_{RD} = 23$ nm, which is much smaller than the distance between two lattice sites. A dipolar collision event can only take place between atoms in the same lattice site. Thus only doubly occupied sites may suffer from dipolar relaxation collisions. When all the doubly occupied sites have experienced a dipolar relaxation collision, the total number of atoms ceases to decrease. Thus, there are two distinct regimes. For times shorter than 5 ms we interpret our dynamics as resulting from doubly and singly occupied sites, whereas for $t > 5$ ms dynamics results from interactions between singly occupied sites.

In our model, we will again neglect magnetization changing collisions, which is justified by the fact that magnetization is roughly constant during the experiment. Nevertheless, as the losses are spin dependent, their influence cannot be neglected in the first 5 ms. Therefore this model is well suited to account for the dynamics only after the first 5 ms.

Doubly occupied sites dynamics

The dynamics of doubly occupied sites can, *a priori*, arise both from contact and dipole-dipole interaction.

Similarly as in the bulk, contact interactions cannot trigger any spin dynamics. After the RF pulse, the doubly occupied site is in spin state $|S = 6, m_S = -6 >_\theta$ which is an eigenstate of the molecular potential a_6. However, dipole dipole interactions and the quadratic Zeeman effect will couple $|S = 6, m_S = -6 >_\theta$ to other molecular states which triggers spin exchange due to contact interactions. The dynamics due to doubly occupied sites is somehow complicated. However, as discussed above, doubly occupied sites suffer from dipolar relaxation collisions and will rapidly be lost. This simplifies the analysis of our data in the sense that when the total atom number hits the plateau ($t \geq 5$ ms), we are only left with singly occupied sitess which do not experience any spin exchange due to contact interactions. Fig.8.20 illustrates these two experimental regimes: Fig.8.20a represents the beginning of the experiment where we have a doubly occupied core surrounded by singly occupied sites; Fig.8.20b corresponds to the experiment after 5 ms where atoms in doubly occupied sites have been lost.

Singly occupied sites dynamics

Singly occupied sitess cannot interact via contact interactions. Their dynamics will result from dipole dipole interaction. DDI will drive intersite spin dynamics and may create quantum correlations through collisions. For example, we can have

$$\begin{aligned} |s = 3, m_s = 0; s = 3, m_s = 0 >_z \quad &\rightarrow \quad \frac{1}{\sqrt{2}}(|s = 3, m_s = 1; s = 3, m_s = -1 >_z \\ &+ \quad |s = 3, m_s = -1; s = 3, m_s = 1 >_z) \end{aligned} \tag{8.43}$$

collisions, which is a correlated state.

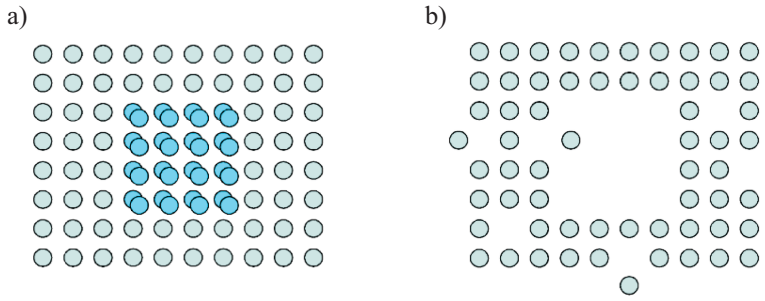

Figure 8.20: Fig.a represents the beginning of the experiment where we have a doubly occupied core surrounded by singly occupied sites; Fig.b corresponds to the experiment after 5 ms where atoms in doubly occupied sites have been lost.

Tunneling dynamics

At $V_0 = 25\ E_r$, the tunneling time is estimated to be approximatively 15 ms (eq.(8.7)). However as discussed in chapter 6, it is the super-exchange energy which sets the timescale for dynamics in the Mott regime. The super-exchange timescale exceeds one second: we may safely assume that over the experimental time there are no super-exchange events.

8.4.5 Theoretical model

The theoretical model I will briefly discuss here was developed by our collaborators A.M. Rey, J. Schachenmayer, and B. Zhu from JILA. Since dynamics induced by doubly occupied sites is complex, they focused their analysis on the dynamics produced solely by singly occupied sites (i.e. for $t > 5$ ms). They considered an initial state different than our experimental initial state, but which gives the same spin distribution as in the experiment at t = 5 ms.

They used the Truncated Wigner Approximation (TWA) in order to simulate dynamics [208]. The idea of the method is to generate an ensemble of classical fields which give the initial spin with its flucutations. For each initial configuration, the mean field dynamics is then calculated. The values obtained for spin populations result from averaging over different runs. In this approximation, all the "quantumness" lies in the initial state. There is *a priori* no justification in using this approximation. However, our collaborators checked that this model gives similar results than exact diagonalization of a plaquette of 3×2 spin 3 atoms. Moreover, the dynamics being performed by mean field equations, it is considerably less time consuming than exact diagonalization. With this method, simulations with a few 10^2 atoms can be performed ($5 \times 5 \times 5$ plaquette).

As in the bulk case, the only free parameter are the values of the quadratic light shift and magnetic gradient. In particular, they are investigating the impact of these effects on the observed dynamics. The analysis is still at an early stage. More analysis

and data taking will be necessary to discriminate whether our data agrees best with the beyond mean field TWA model or the mean field GP model.

8.4.6 Prospects

Spin dynamics accross the Mott to superfluid transition

Once q_z can be cancelled, it will be interesting to study spin dynamics triggered by a RF pulse across the Mott to superfluid transition. Similarly to what was done in section 8.3, it would then be interesting to see if we observe or not a similar mean field/ beyond mean field transition by taking data at intermediate lattice depths.

A particularly appealing configuration would be to perform a large RF pulse ($\sim \pi/2$) with the atoms loaded in an intermediate lattice depth regime. In this regime, it would be interesting to see if quantum correlations may arise due to contact, dipolar and super-exchange interactions.

It has been stressed above that for a homogeneous system classical dynamics is characterized by the fact that the total spin S is constant. A change in S may therefore characterize the departure from classical magnetism. Close to the Mott transition, changing the total S of a pair of atoms costs $\Delta = J^2/U_S - J^2/U_{S-2}$ with U_S the interaction strength for particles interacting through the molecular potential S. This process is allowed for $\Delta < V_{dd}$. One may then expect an interplay between super-exchange and dipolar interactions close to the Mott transition. It would be also very interesting to perform experiments in this regime because there are no available theoretical models.

Tuning the strength of dipolar interactions

As mentioned in subsection 3.1.2, the spatial part of the dipolar Hamiltonian is proportional to $(1 - 3\hat{z}^2)$, with $\hat{z}$ the normalized axis between the magnetic field and the dipoles. Due to the anisotropy of the lattice, the importance of the dipolar interaction could be tuned by changing the direction of the magnetic field.

Getting rid of doubly occupied sites

As mentioned above, the initial dynamics in presence of doubly occupied sites is complicated for simulations. The team is now performing an experiment with no doubly occupied sites. This is achieved by performing a π pulse once the atoms are loaded in the lattice. Then only doubly occupied sites are lost through dipolar relaxation processes. Then another RF pulse is performed to rotate the spin and observe spin dynamics due to singly occupied sites only.

8.4.7 Conclusion

Establishing quantum correlations in an atomic ensemble is not trivial. Here we measured spin dynamics in a BEC following a spin rotation. These dynamics can be accounted for by a mean field calculation. A possible interpretation is that interactions in the bulk are too weak to create any correlations and thus mean field theory prevails. We then loaded atoms in the lattice in order to selectively increase the role of dipolar interactions. We measured spin dynamics. Preliminary comparison with theory indicate that we have a (weakly) correlated system, although we are still investigating the impact of magnetic field gradients and quadratic light shits on the dynamics.

To go further in our measurements, we could measure population fluctuations in each spin state (for example $< n_{-3}^2 >$ - $< n_{-3} >^2$). Combined with measurements of spin populations in a different basis, we could perhaps violate an inequality serving as an entanglement witness. However, finding the appropriate entanglement witness for our system is not trivial and is the subject of a collaboration with P.Millman and T.Coudreau of University Paris 7.

Another possibility would be to measure the total spin of the gas. Indeed the length of the transverse spin $S_\perp$ should be reduced due to beyond mean field effects [209]:

$$S_\perp(t) \underbrace{=}_{t\to 0} S_\perp(t=0)\left(1 - t^2\Big(\underbrace{\Delta B^2}_{\text{Variance of mean field}} + \underbrace{\frac{1}{N}\sum V_{ij}^2}_{\text{Beyond mean field effects}}\Big)\right). \tag{8.44}$$

$S_\perp(t)$ could be measured by performing a $\frac{\pi}{2}$ pulse at the end of the experimental sequence, just before the imaging process and varying the phase of the two relative $\pi/2$ pulses. However this measurement needs a very good calibration of the detectivity of each spin state.

Conclusion

Let us summarize the main results of this thesis.

- Production of a ^{53}Cr Fermi sea: we optimized the loading of fermionic atoms in an Optical Dipole Trap and then performed combined evaporation with the boson. This produces a ^{53}Cr Fermi sea at $T/T_F = 0.66 \pm 0.08$ with up to 10^3 atoms. Analysis of the evaporation sequence enabled us to extract the value of the inter-isotope scattering length $a_{BF} = 80 \pm 10 a_B$.

- Study of the competition between Bose Einstein Condensate and spin dynamics: we prepared a thermal multi-spin component gas and rapidly cooled the gas across the Bose Einstein phase transition. We observe that BEC in spin excited states are difficult to produce because the increase in density due to condensation triggers fast spin exchange dynamics which deplete the condensates because not all spin states have a saturated thermal gas.

- Demonstration of a new cooling mechanism using the spin degrees of freedom to store and remove entropy from a ferromagnetic BEC. Although the temperatures obtained in our experiment are not record breaking, the reduction of entropy is significant and the gain in phase space density in principle diverges for low temperatures. We propose that this experiment could be applied to non dipolar species where extremely low entropies could be obtained. It is relatively humoristic to think that this experiment was thought for and demonstrated with Chromium, but Chromium actually seems to be one of the species where our cooling mechanism is the most limited in temperature and the hardest to perform in the laboratory.

- Preparation of atoms in a double well trap, atoms of each well prepared in opposite spin states. The experimental system can be described by two giant spins interacting via dipole-dipole interactions. We found that these giant spins behave as two classical magnets and in practice we observe no spin dynamics. We took advantage of such a spin preparation, and merged the two wells of the trap. We elaborated a model to account for the observed spin dynamics. We deduced the scattering length $a_0 = 13.5 \pm^{15}_{10} a_B$ with a_B the Bohr radius. The value of the scattering length has profound significance for the ground state properties of Chromium, which is then expected to be cyclic. It will be interesting to see if this phase at low magnetic field can be obtained.

- Spin dynamics with and without lattice due to dipole-dipole and contact interactions. The goal is to understand and try to observe how quantum correlations may appear in our system.

Let us now outline a few possibilities for future research on the experiment.

The production of a dipolar Fermi sea will provide a new tool for the team to study magnetism. Due to the relatively high temperature of the gas, bulk effects due to Fermi-Dirac statistics are out of reach. However in a lattice, the relevant energy scale is not the Fermi energy but the recoil energy. We should then be able to succesfully load atoms in the lowest energy band. Dipolar fermions in a lattice will be an exciting avenue to explore out-of-equilibrium effects associated to spin dynamics. Then, phenomena where transport and magnetism are coupled could be observed.

We performed an experiment where a thermal multi-spin component gas was rapidly cooled across the Bose Einstein Condensation phase transition in presence of interactions. We understood the physical processes at stake in order to produce a BEC in several spin states. This work could stimulate further theoretical and experimental studies concerning the condensation of atoms with a spin degree of freedom, in particular to better understand the observed magnetization fluctuations and how they may relate to symmetry breaking.

Finally, at the end of my PhD we performed out of spin equilibrium experiments in a single well trap or in a 3D optical lattice. The spin excitations is performed by rotating the spin with use of a radio frequency pulse. We present here preliminary results. We are currently investigating what are the correct theoretical approaches which match best our data. The possibility that entanglement may spread in our lattice system is exciting, and this question (along with how we could reveal entanglement) is expected to be one of the central subjects in Lucas Gabardos' thesis.

This concludes my thesis, which is just one more chapter in the Chromium story and I await the next chapter with excitement!

Annexes

CHAPTER 9

The χ^2 test

The χ^2 test gives a criterion for verifying, on probabilistic grounds, the consistency of a theoretical hypothesis with a set of experimental data. In this annexes, we present how we applied the χ^2 test to extract the experimental value of the scattering length through the S=0 molecular potential a_0

We simulate dynamics using eq.(3.49) for different values of a_0. For each value of a_0 we have a certain χ^2, which for the moment can be considered as a merit function and compares how likely the model describes the data. We consider the optimal value of a_0 as the one minimising χ^2.

In our experiment, we consider that fluctuations follow a normal distribution. Therefore, the probability that an experimentally measured value $\bar{x}_i$ of uncertainty w_i at a time t_i is at a distance $\bar{x}_i - x_i$ of the theoretical value x_i given by the model follows:

$$P(x_i) = \frac{1}{\sqrt{2\pi w_i^2}} \exp[-\frac{(\bar{x}_i - x_i)^2}{2w_i^2}]. \tag{9.1}$$

For N independent abscissa points, the combined probability is:

$$P_{Tot} = \prod_{i=1}^{N} P(x_i) \tag{9.2}$$

The model which best fits the data will be the one with the closest values of $\bar{x}_i$ and x_i, and will therefore maximize P_{Tot}. This is equivalent to minimizing:

$$\tilde{\chi}^2 = \frac{\chi^2}{N} = \frac{1}{N} \sum_{i=1}^{N} \frac{(\bar{x}_i - x_i)^2}{2w_i^2}. \tag{9.3}$$

In our analysis, $\tilde{\chi}^2$ is a function of a_0. The minimum of this function, $\tilde{\chi}^2_{min}$, corresponds to the value of a_0 for which the simulation and the experimental data are the closest, therefore the most probable value of a_0 according to our model.

Now that the optimal value of a_0 is found, we make a theoretical hypothesis that the value of a_0 which minimizes χ^2 is the "real" value of a_0 set by nature. The theoretical value of each experimental point y_i can be determined. The experimental values $\bar{y}_i$ can now be thought of as random variables distributed around y_i. As a consequence, $\tilde{\chi}^2$ is also a random variable. The probability distribution of $\tilde{\chi}^2$ is well known in statistical

theory ([210] or [211]) and it evaluates the probability of obtaining $\tilde{\chi}^2$ values larger or smaller than the value actually obtained by the experiment. It can be shown, that the $\tilde{\chi}^2$ distribution for one fitting parameter is the same distribution as that of the square of a single normal distribution. One finds that statisically a value of $\tilde{\chi}^2$ smaller than $\tilde{\chi}^2_{min}+1$ happens 68.3 percent of the time. A value of $\tilde{\chi}^2$ smaller than $\tilde{\chi}^2_{min}+4$ happens 95 percent of the time. This fixes the statistical uncertainties on a_0.

To conclude, the optimal value of a_0 will be given by $\tilde{\chi}^2(a_0)=\chi^2_{min}$, and the statistical uncertainties Δa_0 by $\tilde{\chi}^2(a_0 \pm \Delta a_0)=\tilde{\chi}^2_{min}\pm 1$ for a 68.3% confidence level.

CHAPTER 10

Spin filtering a BEC: inclusion of interactions

In the thesis, we developp a non interacting model to describe the data. The following annexes describes the model when interactions are included. Having not participated to this model, the following is extracted from the Supplementary Material associated to the Spin Filtering paper.

In the main text we have developed our theoretical treatment based on the thermodynamics of non-interacting bosons, which provides good agreement with our experimental data with ^{52}Cr. However the temperatures that we have been able to study are limited to 0.5 times the critical temperature. One might wonder whether our cooling scheme remains as efficient as predicted by our non-interacting model at extremely low temperatures.

In this Supplemental Material we use Bogoliuobov theory, and show that interactions between atoms do not deteriorate our cooling scheme, but in fact make it more efficient.

We consider a spin 1 BEC in a polar state, and calculate the reduction in entropy that can be achieved with one cooling cycle, when taking into account the interactions. We assume an homogeneous gas trapped in a volume V; while this hypothesis leads to considerable simplifications for calculations compared to the trapped gas case, it does allow an estimate of the effects of interactions at low temperatures.

10.1 Description of the calculations

As the BEC is polar, there is only Bose Einstein condensation in the absolute ground state $m_s = 0$ [155]. In the initial state, the initial temperature T_i is low enough that there is a condensed fraction. The quadratic effect q_i is large enough to ensure that there are only thermal excitations in $m_s = 0$. In the final state the quadratic effect is lowered, and q_f ensures thermal population of the excited spin states $m_s = \pm 1$. The filtering process is then performed in order to selectively get rid of atoms in $m_s = \pm 1$. We first determine the final temperature T_f, assuming energy conservation. Then the entropy per atom after spin filtering is compared to the initial entropy per atom.

10.1.1 Energies

Explicit formula for the Bogoliubov energy excitation spectra of a polar spin 1 Bose gas are given in reference [155]. An important result is that the mode corresponding to $m_s = 0$ is decoupled from the other two modes which are degenerate and correspond to quasiparticles containing $m_s = \pm 1$ excitations. Energy spectra are $E_0(k) = \sqrt{\epsilon_k(\epsilon_k + 2c_0 n)}$ and $E_{\pm 1,q}(k) = \sqrt{(\epsilon_k + q)(\epsilon_k + q + 2c_1 n)}$, with $\epsilon_k = \hbar^2 k^2/2m$, $c_0 = \frac{4\pi\hbar^2}{3m}(a_0 + 2a_2)$, $c_1 = \frac{4\pi\hbar^2}{3m}(a_2 - a_0)$, m the mass of one atom, and q the quadratic effect.

To calculate the initial and final energies, we use the Bose statistics applied to Bogoliubov excitations, in presence of a macroscopically populated Bose-Einstein condensate:

$$\frac{E_i}{V} = \int_0^\infty 4\pi k^2 \frac{E_0(k)}{e^{\beta_i E_0(k)} - 1} dk \tag{10.1}$$

$$\frac{E_f}{V} = \int_0^\infty 4\pi k^2 \left(\frac{E_0(k)}{e^{\beta_f E_0(k)} - 1} + \frac{2E_{\pm 1,q_f}(k)}{e^{\beta_f E_{\pm 1,q_f}} - 1} \right) dk \tag{10.2}$$

with $\beta_{i,f}$ equal to respectively $(k_B T_{i,f})^{-1}$. As the ground state energy does not change, T_f is given by the condition $E_i = E_f$. We numerically find T_f for given values of the initial density n_i, initial temperature T_i, and final quadratic effect q_f.

10.1.2 Number of Excitations

In order to perform number counting following spin filtering, we calculate the density of particles in $m_s = \pm 1$:

$$n_{\pm 1,f} = \int_0^\infty \frac{4\pi k^2 dk}{(2\pi)^3} \left(|v_k|^2 + \frac{|u_k|^2 + |v_k|^2}{e^{\beta_f E_{\pm 1,q}(k)} - 1} \right) \tag{10.3}$$

with u_k and v_k the Bogoliubov coefficients given in [155].

10.1.3 Entropies

Both for the initial configuration, and the final one following the filtering of spin excited atoms, there are only atoms in $m_s = 0$. Therefore in both cases the entropy comes from excitations in $m_s = 0$. The entropies per atom $s_{i,f}$ are evaluated with the formula:

$$\frac{s_{i,f}}{k_B} = \int_0^\infty \frac{4\pi k^2 dk}{(2\pi)^3 n_{i,f}} \left(\frac{x_{i,f}}{e^{x_{i,f}} - 1} - \log\left(1 - e^{-x_{i,f}}\right) \right) \tag{10.4}$$

with $x_{i,f} = \beta_{i,f} E_{0,q}(k)$, and $n_f = n_i - 2n_{\pm 1,f}$.

10.2 Results

We assume an initial density $n_i = 10^{20}$ m^{-3}. The interaction parameters are the ones of sodium, $a_2 = 52\ a_{Bohr}$ and $a_2 - a_0 = 2.5\ a_{Bohr}$ [204]. The non-interacting critical temperature $T_{ci} = \frac{2\pi\hbar^2}{mk_B}(\frac{n_i}{g_{3/2}})^{2/3}$ is equal to 1.5 μK. A temperature of 1 nK corresponds to $7 \times 10^{-4} T_{c0}$, and to $1.4 \times 10^{-2}\ n_i c_0$.

The ratio of entropies per atom $\frac{s_f}{s_i}$ is plotted in Fig.10.1 as a function of the initial temperature in unit of the critical temperature without interactions, for a value of $q_f = 0.01\ nc_0$. This value allows one to reach temperatures below 1 nK. As Bogoliubov calculations are only valid for large enough BEC fractions, we consider only low enough initial temperatures.

Fig.10.1 shows the results of our calculations taking into account interactions, and are compared to the results obtained with no interactions. For the latter, the maximal entropy reduction efficiency obtained for $q \to 0$ and $T_i \to 0$ is equal to $3^{-3/5}$. Our results show that interactions increase the efficiency for the entropy reduction after one cycle.

The limit at $q \to 0$ and $T_i \to 0$ for the interacting case, which corresponds to the best reduction in entropy, can be derived analytically:

$$\left(\frac{s_f}{s_i}\right)_{min} = \left(2\left(\frac{c_0}{c_1}\right)^{3/2} + 1\right)^{-3/4} \tag{10.5}$$

when neglecting the quantum depletion in $m_s = \pm 1$.

For Na the numerical value for this optimal ratio is very low (5.7×10^{-3}). It is due to the small difference between a_0 and a_2. Physically this much smaller limit than the non-interacting case can be interpreted easily. When $q \to 0$, both the excitation spectra of $m_s = 0$ and $m_s = \pm 1$ become phonon-like as $k \to 0$, but with very different linear slopes: they are proportional respectively to $c_0^{1/2}$ and $c_1^{1/2}$. Therefore thermal population of excitations with $m_s = \pm 1$ become much larger than those in $m_s = 0$, hence the great efficiency to spin filter $m_s = \pm 1$ atoms.

In other words, when $q \to 0$, the density of states and the number of available states at a given energy is larger in the spin excited states $m_s = \pm 1$ than in the lower energy state $m_s = 0$, in strong contrast with the non-interactive case for which the two spectra are identical. As a consequence when $q \to 0$ most of the thermal atoms leave $m_s = 0$, which leads to a very efficient reduction in entropy after spin filtering $m_s = \pm 1$ states.

There is ultimately a limit for our cooling process arising from the quantum deple-

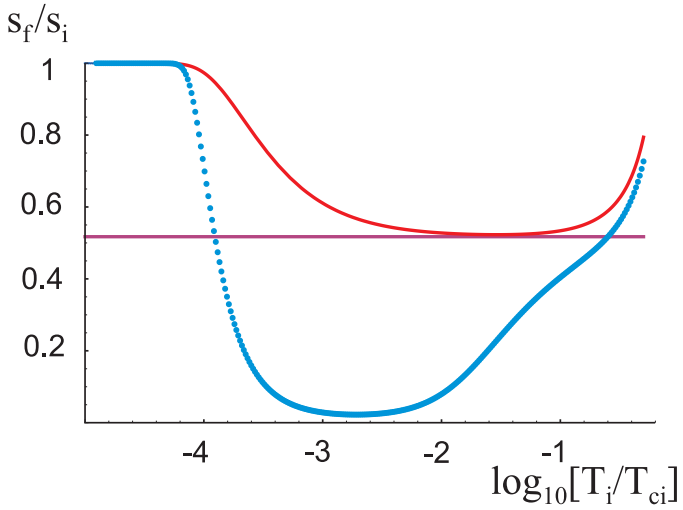

Figure 10.1: Comparison of entropy reduction efficiency in the case of Na in the homogeneous case, for a quadratic shift $q_f = 0.01$ times the initial chemical potential. Initial temperatures are in units of the non-interacting critical temperature. Without taking into account interactions (red line), the reduction is significant and approaches its limit (horizontal line, see text) over a wide range of temperatures. When taking into account the interactions (blue points), the reduction is even better, and can reach in particular very small values at very low temperatures. The entropy reduction decreases at ultra low T_i due to the final value of q_f.

tion in the modes with $m_s = \pm 1$, which has the following expression [155] for $q \to 0$:

$$n_{\pm 1,qd} = n_i \frac{8}{3\pi^{1/2}} \left(n_i \left(\frac{a_2 - a_0}{3} \right)^3 \right)^{1/2} \tag{10.6}$$

When a high level of purity of the BEC is reached, spin filtering of $m_s = \pm 1$ atoms ultimately starts to affect the ground state. The numerical value for Na is $2n_{\pm 1,qd}/n_i = 8.10^{-6}$ for $n_i = 10^{20}\mathrm{m}^{-3}$: the quantum depletion is then very small in $m_s = \pm 1$.

Other kind of limitation come into play in fact, and define practical limits. For example, when the number of particles thermally excited becomes very small, filtering becomes non relevant: at temperatures of $10^{-3}T_{c0}$, there is about one particle thermally excited for BECs with 10^6 atoms. This signals the breakdown of one approximation of our model, i.e. the thermodynamics limit. Therefore Fig.10.1 shows that the spin filtering process is efficient in the whole experimentally relevant temperature domain (i.e. when the number of thermal excitations is larger than one). For instance, starting with an initial temperature of $10^{-2}T_{c0}$, a reduction of entropy by an order of magnitude is conceivable with only one cooling cycle. Our cooling scheme thus offers perspective to reach entropies per atom well below the $10^{-3}k_B$ record value which has been demonstrated in [170].

Bibliography

[1] Bose, S. N.: *Plancks gesetz und lichtquantenhypothese*. Z. Phys., **26**, 178, (1924). V

[2] Einstein, A.: *Quantentheorie des einatomigen idealen gases*. Sitzber. Kgl. Preuss. Akad. Wiss., **1**, 3, (1925). V

[3] Phillips, William D.: *Nobel Lecture: Laser cooling and trapping of neutral atoms*. Rev. Mod. Phys., **70**, 721–741, (1998). V

[4] Cohen-Tannoudji, Claude N.: *Nobel Lecture: Manipulating atoms with photons*. Rev. Mod. Phys., **70**, 707–719, (1998). V

[5] Chu, Steven: *Nobel Lecture: The manipulation of neutral particles*. Rev. Mod. Phys., **70**, 685–706, (1998). V

[6] Anderson, M. H., Ensher, J. R., Matthews, M. R., Wieman, C. E., and Cornell, E. A.: *Observation of Bose-Einstein Condensation in a Dilute Atomic Vapor*. Science, **269**(5221), 198–201, (1995), ISSN 0036-8075. V, 75

[7] Davis, K. B., Mewes, M. O., Andrews, M. R., Druten, N. J. van, Durfee, D. S., Kurn, D. M., and Ketterle, W.: *Bose-Einstein Condensation in a Gas of Sodium Atoms*. Phys. Rev. Lett., **75**, 3969–3973, Nov 1995. V, 75

[8] Bradley, C. C., Sackett, C. A., Tollett, J. J., and Hulet, R. G.: *Evidence of Bose-Einstein Condensation in an Atomic Gas with Attractive Interactions*. Phys. Rev. Lett., **75**, 1687–1690, (1995). V

[9] Modugno, Giovanni, Ferrari, Gabriele, Roati, Giacomo, Brecha, Robert J, Simoni, A, and Inguscio, Massimo: *Bose-einstein condensation of potassium atoms by sympathetic cooling*. Science, **294**(5545), 1320–1322, (2001). V

[10] Weber, Tino, Herbig, Jens, Mark, Michael, Nägerl, Hanns Christoph, and Grimm, Rudolf: *Bose-einstein condensation of cesium*. Science, **299**(5604), 232–235, (2003). V

[11] Tiesinga, E., Verhaar, B. J., and Stoof, H. T. C.: *Threshold and resonance phenomena in ultracold ground-state collisions*. Phys. Rev. A, **47**, 4114–4122, (1993). V

[12] Vuletic, Vladan, Kerman, Andrew J., Chin, Cheng, and Chu, Steven: *Observation of Low-Field Feshbach Resonances in Collisions of Cesium Atoms*. Phys. Rev. Lett., **82**, 1406–1409, (1999). V

[13] Chin, Cheng, Grimm, Rudolf, Julienne, Paul, and Tiesinga, Eite: *Feshbach resonances in ultracold gases*. Rev. Mod. Phys., **82**, 1225–1286, (2010). V, 75

[14] Khaykovich, L, Schreck, F, Ferrari, G, Bourdel, Thomas, Cubizolles, Julien, Carr, LD, Castin, Yvan, and Salomon, Christophe: *Formation of a matter-wave bright soliton*. Science, **296**(5571), 1290–1293, (2002). V

[15] Kraemer, T, Mark, M, Waldburger, P, Danzl, JG, Chin, C, Engeser, B, Lange, AD, Pilch, K, Jaakkola, A, Nägerl, H C, *et al.*: *Evidence for efimov quantum states in an ultracold gas of caesium atoms*. Nature, **440**(7082), 315–318, (2006). V

[16] Griesmaier, Axel, Werner, Jörg, Hensler, Sven, Stuhler, Jürgen, and Pfau, Tilman: *Bose-Einstein Condensation of Chromium*. Phys. Rev. Lett., **94**, 160401, (2005). V, 10

[17] Lu, Mingwu, Burdick, Nathaniel Q., Youn, Seo Ho, and Lev, Benjamin L.: *Strongly Dipolar Bose-Einstein Condensate of Dysprosium*. Phys. Rev. Lett., **107**, 190401, Oct 2011. V, VII, 56, 133

[18] Aikawa, K., Frisch, A., Mark, M., Baier, S., Rietzler, A., Grimm, R., and Ferlaino, F.: *Bose-Einstein Condensation of Erbium*. Phys. Rev. Lett., **108**, 210401, May 2012. V, VII, 56, 133

[19] Kraft, Sebastian, Vogt, Felix, Appel, Oliver, Riehle, Fritz, and Sterr, Uwe: *Bose-Einstein Condensation of Alkaline Earth Atoms:* ^{40}Ca. Phys. Rev. Lett., **103**, 130401, Sep 2009. V

[20] Escobar, Y. N. Martinez de, Mickelson, P. G., Yan, M., DeSalvo, B. J., Nagel, S. B., and Killian, T. C.: *Bose-Einstein Condensation of* ^{84}Sr. Phys. Rev. Lett., **103**, 200402, Nov 2009. V

[21] Takasu, Yosuke, Maki, Kenichi, Komori, Kaduki, Takano, Tetsushi, Honda, Kazuhito, Kumakura, Mitsutaka, Yabuzaki, Tsutomu, and Takahashi, Yoshiro: *Spin-Singlet Bose-Einstein Condensation of Two-Electron Atoms*. Phys. Rev. Lett., **91**, 040404, Jul 2003. V

[22] DeMarco, B. and Jin, D. S.: *Onset of Fermi Degeneracy in a Trapped Atomic Gas*. Science, **285**(5434), 1703–1706, (1999). V, 48, 75

[23] Pitaevskii, L. and Stringari, S.: *Bose Einstein Condensation*. Oxford university press edition, (2003). VI, 60, 78, 101, 102, 122, 143, 165

[24] Stenger, J., Inouye, S., Stamper-Kurn, D. M., Miesner, H. J., Chikkatur, A. P., and Ketterle, W.: *Spin domains in ground-state Bose-Einstein condensates*. Nature, **396**, 345–348, (1998). VI

[25] Hall, D. S., Matthews, M. R., Ensher, J. R., Wieman, C. E., and Cornell, E. A.: *Dynamics of Component Separation in a Binary Mixture of Bose-Einstein Condensates*. Phys. Rev. Lett., **81**, 1539–1542, Aug 1998. VI

[26] Frisch, Albert, Mark, Michael, Aikawa, Kiyotaka, Ferlaino, Francesca, Bohn, John L, Makrides, Constantinos, Petrov, Alexander, and Kotochigova, Svetlana: *Quantum chaos in ultracold collisions of gas-phase erbium atoms*. Nature, **507**(7493), 475–479, (2014). VII

[27] Maier, T., Ferrier-Barbut, I., Kadau, H., Schmitt, M., Wenzel, M., Wink, C., Pfau, T., Jachymski, K., and Julienne, P. S.: *Broad universal Feshbach resonances in the chaotic spectrum of dysprosium atoms*. Phys. Rev. A, **92**, 060702, Dec 2015. VII

[28] Kadau, Holger, Schmitt, Matthias, Wenzel, Matthias, Wink, Clarissa, Maier, Thomas, Ferrier-Barbut, Igor, and Pfau, Tilman: *Observing the rosensweig instability of a quantum ferrofluid*. Nature, **530**(7589), 194–197, (2016). VII

[29] Chomaz, L, Baier, S, Petter, D, Mark, MJ, Wächtler, F, Santos, L, and Ferlaino, F: *Quantum-fluctuation-driven crossover from a dilute bose-einstein condensate to a macro-droplet in a dipolar quantum fluid*. arXiv preprint arXiv:1607.06613, (2016). VII

[30] Ferrier-Barbut, Igor, Kadau, Holger, Schmitt, Matthias, Wenzel, Matthias, and Pfau, Tilman: *Observation of Quantum Droplets in a Strongly Dipolar Bose Gas*. Phys. Rev. Lett., **116**, 215301, May 2016. VII

[31] Browaeys, Antoine, Barredo, Daniel, and Lahaye, Thierry: *Experimental investigations of dipole-dipole interactions between a few Rydberg atoms*. Journal of Physics B: Atomic, Molecular and Optical Physics, **49**(15), 152001, (2016). VII, 56

[32] Ni, K. K., Ospelkaus, S., Miranda, M. H. G. de, Pe'er, A., Neyenhuis, B., Zirbel, J. J., Kotochigova, S., Julienne, P. S., Jin, D. S., and Ye, J.: *A High Phase-Space-Density Gas of Polar Molecules*. Science, **322**(5899), 231–235, (2008), ISSN 0036-8075. VII, 27, 76

[33] Park, Jee Woo, Will, Sebastian A., and Zwierlein, Martin W.: *Ultracold Dipolar Gas of Fermionic ^{23}Na^{40}K Molecules in Their Absolute Ground State*. Phys. Rev. Lett., **114**, 205302, May 2015. VII

[34] Yan, Bo, Moses, Steven A., Gadway, Bryce, Covey, Jacob P., Hazzard, Kaden R. A., Rey, Ana Maria, Jin, Deborah S., and Ye, Jun: *Observation of dipolar spin-exchange interactions with lattice-confined polar molecules*. Nat. Phys., **501**, 521–525, (2013). VII, 56, 169

[35] Barredo, Daniel, Labuhn, Henning, Ravets, Sylvain, Lahaye, Thierry, Browaeys, Antoine, and Adams, Charles S.: *Coherent Excitation Transfer in a Spin Chain of Three Rydberg Atoms*. Phys. Rev. Lett., **114**, 113002, Mar 2015. VII

[36] Barredo, Daniel, Léséleuc, Sylvain de, Lienhard, Vincent, Lahaye, Thierry, and Browaeys, Antoine: *An atom-by-atom assembler of defect-free arbitrary two-dimensional atomic arrays*. Science, **354**(6315), 1021–1023, (2016). VII

[37] Paz, A. de: *Echange de spin et dynamique d'aimantation d'un gaz quantique dipolaire*. PhD thesis, Laboratoire de Physique des Lasers, Université Paris 13 Nord, (2015). VIII, 21, 63, 64, 66, 174, 175, 176, 180, 181, 182, 194, 195, 202, 205, 211

[38] Beaufils, Q.: *Condensation de Bose-Einstein du Chrome et étude de collisions inélastiques dues aux interactions dipolaires*. PhD thesis, Laboratoire de Physique des Lasers, Université Paris 13 Nord, (2009). 3, 8

[39] Chicireanu, R., Pouderous, A., Barbé, R., Laburthe-Tolra, B., Maréchal, E., Vernac, L., Keller, J. C., and Gorceix.: *Simultaneous magneto-optical trapping of bosonic and fermionic chromium atoms*. Phys. Rev. A, **73**, 053406, (2006). 3, 27, 28, 31, 34, 48

[40] Chicireanu, R., Beaufils, Q., Pouderous, A., Laburthe-Tolra, B., Maréchal, E., Porto, J. V., Vernac, L., Keller, J. C., and Gorceix, O.: *Accumulation and thermalization of cold atoms in a finite-depth magnetic trap*. Phys. Rev. A, **76**, 023406, (2007). 4

[41] Chicireanu, R., Beaufils, Q., Pouderous, A., Laburthe-Tolra, B., Maréchal, E., Vernac, L., Keller, J. C., and Gorceix, O.: *Accumulation of chromium metastable atoms into an optical trap*. The European Physical Journal D, **45**, 189–195, (2007). 4, 12

[42] Beaufils, Q., Chicireanu, R., Pouderous, A., Souza Melo, W. de, Laburthe-Tolra, B., Marechal, E., Vernac, L., Keller, J. C., and Gorceix, O.: *Averaging out magnetic forces with fast rf sweeps in an optical trap for metastable chromium atoms*. Phys. Rev. A, **77**, 053413, (2008). 4, 15, 36

[43] Beaufils, Q., Chicireanu, R., Zanon, T., Laburthe-Tolra, B., Maréchal, E., Vernac, L., Keller, J. C., and Gorceix, O.: *All-optical production of chromium Bose-Einstein condensates*. Phys. Rev. A, **77**, 061601, (2008). 4, 12, 28, 36, 86

[44] *Nist Atomic Spectra Database*. 4, 41

[45] Weinstein, J. D.: *Magnetic Trapping of Atomic Chromium and Molecular Calcium Monohydride*. PhD thesis, Harvard University, (2001). 4

[46] Stuhler, J.: *Kontinuierliches Laden einer Magnetfalle mit lasergekuhlten Chromatomen*. PhD thesis, Universitat Konstanz, (2001). 4

[47] Bradley, C. C., McClelland, J. J., Anderson, W. R., and Celotta, R. J.: *Magneto-optical trapping of chromium atoms*. Phys. Rev. A, **61**, 053407, (2000). 4

[48] Stuhler, J., Schmidt, P. O., Hensler, S., Werner, J., Mlynek, J., and Pfau, T.: *Continuous loading of a magnetic trap*. Phys. Rev. A, **64**, 031405, (2001). 4

[49] Hänsch, T.W. and Couillaud, B.: *Laser Frequency stabilization by polarization spectroscopy of a reflecting reference cavity*. Optics Comm., **35**, 441, (1980). 8

[50] Chicireanu, R.: *Studies of cold chromium atoms in magnetic and optical traps: steps towards Bose-Einstein Condensation*. PhD thesis, Laboratoire de Physique des Lasers, Université Paris 13 Nord, (2007). 10, 31, 32, 35

[51] Walker, Thad, Sesko, David, and Wieman, Carl: *Collective behavior of optically trapped neutral atoms*. Phys. Rev. Lett., **64**, 408–411, Jan 1990. 10

[52] Savard, T. A., O'Hara, K. M., and Thomas, J. E.: *Laser-noise-induced heating in far-off resonance optical traps*. Phys. Rev. A, **56**, R1095–R1098, (1997). 11, 14

[53] Friebel, S., D'Andrea, C., Walz, J., Weitz, M., and Hänsch, T. W.: *CO_2-laser optical lattice with cold rubidium atoms*. Phys. Rev. A, **57**, R20–R23, (1998). 12

[54] Bismut, G., Pasquiou, B., Ciampini, D., Laburthe-Tolra, B., Maréchal, E., Vernac, L., and Gorceix, O.: *Optimized loading of an optical dipole trap for the production of chromium BECs*. Applied Physics B: Lasers and Optics, **102**, 1–9, (2011). 12, 27, 28, 36, 45

[55] Ketterle, Wolfgang, Davis, Kendall B., Joffe, Michael A., Martin, Alex, and Pritchard, David E.: *High densities of cold atoms in a darkspontaneous-force optical trap*. Phys. Rev. Lett., **70**, 2253–2256, (1993). 12

[56] Lahaye, T, Menotti, C, Santos, L, Lewenstein, M, and Pfau, T: *The physics of dipolar bosonic quantum gases*. Reports on Progress in Physics, **72**, 126401, (2009). 15, 45

[57] W. Ketterle, D.S. Durfee, D.M. Stamper Kurn: *Making, Probing, Understanding Bose Einstein Condensates*. Contribution to the proceedings of the 1998 Enrico Fermi summer school on Bose-Einstein condensation in Varenna, Italy. 15

[58] Ketterle, Wolfgang and Druten, N.J. Van: *Evaporative Cooling of Trapped Atoms*. Volume **37** of *Advances In Atomic, Molecular, and Optical Physics*, pages 181 – 236. Academic Press, (1996). 16, 87

[59] Luiten, O. J., Reynolds, M. W., and Walraven, J. T. M.: *Kinetic theory of the evaporative cooling of a trapped gas*. Phys. Rev. A, **53**, 381–389, (1996). 16, 87

[60] Pouderous, A.: *Refroidissement et piégeage d'atomes de chrome*. PhD thesis, Laboratoire de Physique des Lasers, Université Paris 13 Nord, (2007). 17

[61] Dalfovo, Franco, Giorgini, Stefano, Pitaevskii, Lev P., and Stringari, Sandro: *Theory of Bose-Einstein condensation in trapped gases*. Rev. Mod. Phys., **71**, 463–512, (1999). 19

[62] Castin, Y. and Dum, R.: *Bose-Einstein Condensates in Time Dependent Traps*. Phys. Rev. Lett., **77**, 5315–5319, Dec 1996. http://link.aps.org/doi/10.1103/PhysRevLett.77.5315. 19

[63] Sadler, L. E., Higbie, J. M., Leslie, S. R., Vengalattore, M., and Stamper-Kurn, D. M.: *Spontaneous symmetry breaking in a quenched ferromagnetic spinor Bose-Einstein condensate* . Nature, **443**, 312–315, (2006). 19

[64] *Andor Specification sheet*. 20

[65] Ockeloen, C.F.: *Probing fluctuations in a lattice of mesoscopic atomic ensembles*. Master's thesis, van der Waals-Zeeman Institute, University of Amsterdam, 2010. 24

[66] Lu, Mingwu, Burdick, Nathaniel Q., and Lev, Benjamin L.: *Quantum Degenerate Dipolar Fermi Gas*. Phys. Rev. Lett., **108**, 215301, (2012). 27, 48, 56, 76

[67] Aikawa, K., Frisch, A., Mark, M., Baier, S., Grimm, R., and Ferlaino, F.: *Reaching Fermi Degeneracy via Universal Dipolar Scattering*. Phys. Rev. Lett., **112**, 010404, (2014). 27, 48, 56, 76

[68] Bismut, G.: *Excitations d'un Condensat de Bose Einstein dipolaire*. PhD thesis, Laboratoire de Physique des Lasers, Université Paris 13 Nord, (2012). 28

[69] Drever, R. W. P., Hall, J. L., Kowalski, F. V., Hough, J., Ford, G. M., Munley, A. J., and Ward, H.: *Laser phase and frequency stabilization using an optical resonator*. Applied Physics B, **31**(2), 97–105, (1983), ISSN 1432-0649. 28

[70] Stam, K. M. R. van der, Ooijen, E. D. van, Meppelink, R., Vogels, J. M., and Straten, P. van der: *Large atom number Bose-Einstein condensate of sodium*. Review of Scientific Instruments, **78**(1), (2007). 35

[71] Ertmer, W., Johann, U., and Mosmann, R.: *Measurement of the Nuclear Quadrupole Moment of ^{53}Cr by Laser-RF Double Resonance*. Z. Phys. A, Atoms and Nuclei, **309**, (1982). 39, 40

[72] Becker, U, Teppner, U, and Wusthof, U: *Hyperfine structure of the ^{7}P states in the configurations $3d^5 4p$ and $3d^4 4s4p$ of ^{53}Cr*. J. Phys. B: Atomic and Molecular Physics, **11**(14), 2435, (1978). 39, 42, 44

[73] Jarosz, A, Stefanska, D, Elantkowska, M, Ruczkowski, J, Buczek, A, Furmann, B, Glowacki, P, Krzykowski, A, Piatkowski, L, Stachowska, E, and Dembczynski, J: *High precision investigations of the hyperfine structure of metastable levels in a chromium atom*. Journal of Physics B: Atomic, Molecular and Optical Physics, **40**(13), 2785, (2007). 40, 44

[74] Metcalf, H.J. and Straten, P. van der: *Laser Cooling and Trapping*. Springer edition, (1999). 39, 46, 187

[75] W. J. Childs, L. S. Goodman, D. von Ehrenstein: *Magnetic hyperfine interaction of 53cr*. Physical Review, **132**, 2128–2135, (1963). 42

[76] Furmann, B., Jarosz, A., Stefanska, D., Dembczynski, J., and Stachowska, E.: *Isotope shift in chromium*. Spectrochimica Acta Part B: Atomic Spectroscopy, **60**(1), 33 – 40, (2005). 42

[77] Truscott, Andrew G., Strecker, Kevin E., McAlexander, William I., Partridge, Guthrie B., and Hulet, Randall G.: *Observation of Fermi Pressure in a Gas of Trapped Atoms* . Science, **291**(5513), 2570–2572, (2001), ISSN 0036-8075. 48, 75

[78] Schreck, F., Khaykovich, L., Corwin, K. L., Ferrari, G., Bourdel, T., Cubizolles, J., and Salomon, C.: *Quasipure Bose-Einstein Condensate Immersed in a Fermi Sea* . Phys. Rev. Lett., **87**, 080403, Aug 2001. 48, 75

[79] Tolra, B. Laburthe, O'Hara, K. M., Huckans, J. H., Phillips, W. D., Rolston, S. L., and Porto, J. V.: *Observation of Reduced Three-Body Recombination in a Correlated 1D Degenerate Bose Gas*. Phys. Rev. Lett., **92**, 190401, May 2004. 51

[80] Rauer, B., Grisins, P., Mazets, I. E., Schweigler, T., Rohringer, W., Geiger, R., Langen, T., and Schmiedmayer, J.: *Cooling of a One-Dimensional Bose Gas*. Phys. Rev. Lett., **116**, 030402, Jan 2016. 51

[81] Gring, M., Kuhnert, M., Langen, T., Kitagawa, T., Rauer, B., Schreitl, M., Mazets, I., Smith, D. Adu, Demler, E., and Schmiedmayer, J.: *Relaxation and Prethermalization in an Isolated Quantum System*. Science, **337**(6100), 1318–1322, (2012), ISSN 0036-8075. 51

[82] Billy, Juliette, Josse, Vincent, Zuo, Zhanchun, Bernard, Alain, Hambrecht, Ben, Lugan, Pierre, Clément, David, Sanchez-Palencia, Laurent, Bouyer, Philippe, and Aspect, Alain: *Direct observation of anderson localization of matter waves in a controlled disorder*. Nature, **453**(7197), 891–894, (2008). 51

[83] Werner, J., Griesmaier, A., Hensler, S., Stuhler, J., Pfau, T., Simoni, A., and Tiesinga, E.: *Observation of Feshbach Resonances in an Ultracold Gas of* ^{52}Cr. Phys. Rev. Lett., **94**, 183201, May 2005. 51, 55, 71, 93

[84] Gribakin, G. F. and Flambaum, V. V.: *Calculation of the scattering length in atomic collisions using the semiclassical approximation*. Phys. Rev. A, **48**, 546–553, Jul 1993. 51, 92, 93, 94

[85] Pethick, C.J. and Smith, H.: *Bose Einstein Condensation in Dilute Gases*. Cambridge university press edition, (2008). 52, 53, 62, 199

[86] Cohen-Tannoudji, C.: *Leçons du Collège de France. Condensation de Bose-Einstein des gaz atomiques ultra froids : effets des interactions*. (1998-1999). 53

[87] Pasquiou, B., Bismut, G., Beaufils, Q., Crubellier, A., Maréchal, E., Pedri, P., Vernac, L., Gorceix, O., and Laburthe-Tolra, B.: *Control of dipolar relaxation in external fields*. Phys. Rev. A, **81**, 042716, (2010). 55, 57, 58, 69, 71, 92, 93, 94, 99, 136, 170

[88] Lahaye, T., Koch, T., Frohlich, B., Fattori, M., Metz, J., Griesmaier, A., Giovanazzi, S., and Pfau, T.: *Strong dipolar effects in a quantum ferrofluid*. Nature, **448**, 672–675, (2007). 55

[89] Bismut, G., Pasquiou, B., Maréchal, E., Pedri, P., Vernac, L., Gorceix, O., and Laburthe-Tolra, B.: *Collective Excitations of a Dipolar Bose-Einstein Condensate*. Phys. Rev. Lett., **105**, 040404, (2010). 55

[90] Bismut, G., Laburthe-Tolra, B., Maréchal, E., Pedri, P., Gorceix, O., and Vernac, L.: *Anisotropic Excitation Spectrum of a Dipolar Quantum Bose Gas*. Phys. Rev. Lett., **109**, 155302, Oct 2012. 55

[91] Paz, A. de, Sharma, A., Chotia, A., Maréchal, E., Huckans, J. H., Pedri, P., Santos, L., Gorceix, O., Vernac, L., and Laburthe-Tolra, B.: *Nonequilibrium Quantum Magnetism in a Dipolar Lattice Gas*. Phys. Rev. Lett., **111**, 185305, Oct 2013. 56, 57, 64, 65, 66, 181

[92] S Donley, Elizabeth A., Claussen, Neil R., Cornish, Simon L., Roberts, Jacob L., Cornell, Eric A., and Wieman, Carl E.: *Dynamics of collapsing and exploding bose-einstein condensates*. Nature, **412**, 295–299, (2001). 56

[93] Lahaye, T., Metz, J., Fröhlich, B., Koch, T., Meister, M., Griesmaier, A., Pfau, T., Saito, H., Kawaguchi, Y., and Ueda, M.: *d-Wave Collapse and Explosion of a Dipolar Bose-Einstein Condensate*. Phys. Rev. Lett., **101**, 080401, (2008). 56

[94] Metz, J, Lahaye, T, Fröhlich, B, Griesmaier, A, Pfau, T, Saito, H, Kawaguchi, Y, and Ueda, M: *Coherent collapses of dipolar Bose-Einstein condensates for different trap geometries*. New Journal of Physics, **11**, 055032, (2009). 56

[95] Stuhler, J., Griesmaier, A., Koch, T., Fattori, M., Pfau, T., Giovanazzi, S., Pedri, P., and Santos, L.: *Observation of Dipole-Dipole Interaction in a Degenerate Quantum Gas*. Phys. Rev. Lett., **95**, 150406, (2005). 57

[96] Tang, Y., Sykes, A. G., Burdick, N. Q., DiSciacca, J. M., Petrov, D. S., and Lev, B. L.: *Anisotropic Expansion of a Thermal Dipolar Bose Gas*. Phys. Rev. Lett., **117**, 155301, Oct 2016. 57

[97] Pasquiou, B., Maréchal, E., Vernac, L., Gorceix, O., and Laburthe-Tolra, B.: *Thermodynamics of a Bose-Einstein Condensate with Free Magnetization*. Phys. Rev. Lett., **108**, 045307, Jan 2012. 57, 95, 112, 113, 114, 115, 118, 158

[98] Pasquiou, B., Bismut, G., Maréchal, E., Pedri, P., Vernac, L., Gorceix, O., and Laburthe-Tolra, B.: *Spin Relaxation and Band Excitation of a Dipolar Bose-Einstein Condensate in 2D Optical Lattices*. Phys. Rev. Lett., **106**, 015301, (2011). 57

[99] Pasquiou, B., Maréchal, E., Bismut, G., Pedri, P., Vernac, L., Gorceix, O., and Laburthe-Tolra, B.: *Spontaneous Demagnetization of a Dipolar Spinor Bose Gas in an Ultralow Magnetic Field*. Phys. Rev. Lett., **106**, 255303, (2011). 57, 112

[100] Santos, L. and Pfau, T.: *Spin-3 Chromium Bose-Einstein Condensates*. Phys. Rev. Lett., **96**, 190404, (2006). 57, 73, 110, 111

[101] Kawaguchi, Yuki, Saito, Hiroki, and Ueda, Masahito: *Einstein-de Haas Effect in Dipolar Bose-Einstein Condensates*. Phys. Rev. Lett., **96**, 080405, (2006). 57

[102] Gawryluk, Krzysztof, Brewczyk, Mirosław, Bongs, Kai, and Gajda, Mariusz: *Resonant Einstein˘de Haas Effect in a Rubidium Condensate*. Phys. Rev. Lett., **99**, 130401, Sep 2007. 57

[103] Hensler, S., Werner, J., Griesmaier, A., Schmidt, P.O., Görlitz, A., Pfau, T., Giovanazzi, S., and Rzazewski, K.: *Dipolar relaxation in an ultra-cold gas of magnetically trapped chromium atoms*. Applied Physics B: Lasers and Optics, **77**, 765–772, (2002). 57

[104] Monroe, C. R., Cornell, E. A., Sackett, C. A., Myatt, C. J., and Wieman, C. E.: *Measurement of Cs-Cs elastic scattering at T =30 μK*. Phys. Rev. Lett., **70**, 414–417, Jan 1993. 60

[105] Hart, Russell A., Xu, Xinye, Legere, Ronald, and Gibble, Kurt: *A quantum scattering interferometer*. Nature, **446**, 892–895, (2007). 60

[106] Davis, Kendall B., Mewes, Marc Oliver, Joffe, Michael A., Andrews, Michael R., and Ketterle, Wolfgang: *Evaporative Cooling of Sodium Atoms*. Phys. Rev. Lett., **75**, 2909–2909, Oct 1995. 60

[107] Pechkis, H. K., Wrubel, J. P., Schwettmann, A., Griffin, P. F., Barnett, R., Tiesinga, E., and Lett, P. D.: *Spinor Dynamics in an Antiferromagnetic Spin-1 Thermal Bose Gas*. Phys. Rev. Lett., **111**, 025301, Jul 2013. 61

[108] Ebling, Ulrich, Krauser, Jasper Simon, Fläschner, Nick, Sengstock, Klaus, Becker, Christoph, Lewenstein, Maciej, and Eckardt, André: *Relaxation Dynamics of an Isolated Large-Spin Fermi Gas Far from Equilibrium*. Phys. Rev. X, **4**, 021011, Apr 2014. 61, 63

[109] He, Xiaodong, Zhu, Bing, Li, Xiaoke, Wang, Fudong, Xu, Zhi Fang, and Wang, Dajun: *Coherent spin-mixing dynamics in thermal* ^{87}Rb *spin-1 and spin-2 gases*. Phys. Rev. A, **91**, 033635, Mar 2015. 61

[110] Bloch, Immanuel, Dalibard, Jean, and Zwerger, Wilhelm: *Many-body physics with ultracold gases*. Rev. Mod. Phys., **80**, 885–964, Jul 2008. 64, 165, 166, 198, 203

[111] Paz, A. de, Naylor, B., Huckans, J., Carrance, A., Gorceix, O., Maréchal, E., Pedri, P., Laburthe-Tolra, B., and Vernac, L.: *Dipolar atomic spin ensembles in a double-well potential*. Phys. Rev. A, **90**, 043607, Oct 2014. 66

[112] Chang, Ming Shien, Qin, Qishu, Zhang, Wenxian, You, Li, and Chapman, Michael S.: *Coherent spinor dynamics in a spin-1 Bose condensate*. Nature Physics, **1**, 111–116, (2005). 69, 132, 208

[113] Fattori, M., Koch, T., Goetz, S., Griesmaier, A., Hensler, S., Stuhler, J., and Pfau, T.: *Demagnetization cooling of a gas*. Nat. Phys., **2**, 765–768, (2006). 69, 115, 153

[114] O'Hara, K. M., Granade, S. R., Gehm, M. E., Savard, T. A., Bali, S., Freed, C., and Thomas, J. E.: *Ultrastable* CO_2 *Laser Trapping of Lithium Fermions*. Phys. Rev. Lett., **82**, 4204–4207, May 1999. 75

[115] Roati, G., Riboli, F., Modugno, G., and Inguscio, M.: *Fermi-Bose Quantum Degenerate* ^{40}K-^{87}Rb *Mixture with Attractive Interaction*. Phys. Rev. Lett., **89**, 150403, Sep 2002. 75

[116] O'Hara, K. M., Hemmer, S. L., Gehm, M. E., Granade, S. R., and Thomas, J. E.: *Observation of a Strongly Interacting Degenerate Fermi Gas of Atoms*. Science, **298**(5601), 2179–2182, (2002), ISSN 0036-8075. 75

[117] Gehm, M. E., Hemmer, S. L., Granade, S. R., O'Hara, K. M., and Thomas, J. E.: *Mechanical stability of a strongly interacting Fermi gas of atoms*. Phys. Rev. A, **68**, 011401, Jul 2003. 75

[118] Bourdel, T., Cubizolles, J., Khaykovich, L., Magalhães, K. M. F., Kokkelmans, S. J. J. M. F., Shlyapnikov, G. V., and Salomon, C.: *Measurement of the Interaction Energy near a Feshbach Resonance in a* ^{6}Li *Fermi Gas*. Phys. Rev. Lett., **91**, 020402, Jul 2003. 75

[119] Dieckmann, K., Stan, C. A., Gupta, S., Hadzibabic, Z., Schunck, C. H., and Ketterle, W.: *Decay of an Ultracold Fermionic Lithium Gas near a Feshbach Resonance*. Phys. Rev. Lett., **89**, 203201, Oct 2002. 75

[120] Cubizolles, J., Bourdel, T., Kokkelmans, S. J. J. M. F., Shlyapnikov, G. V., and Salomon, C.: *Production of Long-Lived Ultracold* Li_2 *Molecules from a Fermi Gas*. Phys. Rev. Lett., **91**, 240401, Dec 2003. 75

[121] Cindy A. Regal, Christopher Ticknor1, John L. Bohn and Jin, Deborah S.: *Creation of ultracold molecules from a Fermi gas of atoms*. Nature, **424**, 47–50, (2003). 75

[122] Jochim, S., Bartenstein, M., Altmeyer, A., Hendl, G., Chin, C., Denschlag, J. Hecker, and Grimm, R.: *Pure Gas of Optically Trapped Molecules Created from Fermionic Atoms*. Phys. Rev. Lett., **91**, 240402, Dec 2003. 75

[123] Strecker, Kevin E., Partridge, Guthrie B., and Hulet, Randall G.: *Conversion of an Atomic Fermi Gas to a Long-Lived Molecular Bose Gas*. Phys. Rev. Lett., **91**, 080406, Aug 2003. 75

[124] Markus Greiner, Cindy A. Regal and Jin, Deborah S.: *Emergence of a molecular Bose-Einstein condensate from a Fermi gas*. Nature, **426**, 537–540, (2003). 75

[125] Jochim, S., Bartenstein, M., Altmeyer, A., Hendl, G., Riedl, S., Chin, C., Hecker Denschlag, J., and Grimm, R.: *Bose-Einstein Condensation of Molecules*. Science, **302**(5653), 2101–2103, (2003), ISSN 0036-8075. 75

[126] Zwierlein, M. W., Stan, C. A., Schunck, C. H., Raupach, S. M. F., Kerman, A. J., and Ketterle, W.: *Condensation of Pairs of Fermionic Atoms near a Feshbach Resonance*. Phys. Rev. Lett., **92**, 120403, Mar 2004. 75

[127] Bourdel, T., Khaykovich, L., Cubizolles, J., Zhang, J., Chevy, F., Teichmann, M., Tarruell, L., Kokkelmans, S. J. J. M. F., and Salomon, C.: *Experimental Study of the BEC-BCS Crossover Region in Lithium 6*. Phys. Rev. Lett., **93**, 050401, Jul 2004. 76

[128] Bartenstein, M., Altmeyer, A., Riedl, S., Jochim, S., Chin, C., Denschlag, J. Hecker, and Grimm, R.: *Crossover from a Molecular Bose-Einstein Condensate to a Degenerate Fermi Gas*. Phys. Rev. Lett., **92**, 120401, Mar 2004. 76

[129] Zwierlein, M. W., Abo-Shaeer, J. R., Schirotzek, A., Schunck, C. H., and Ketterle, W.: *Vortices and superfluidity in a strongly interacting Fermi gas*. Nature, **435**, 1047–1051, (2005). 76

[130] Jördens, Robert, Strohmaier, Niels, Günter, Kenneth, Moritz, Henning, and Esslinger, Tilman: *A Mott insulator of fermionic atoms in an optical lattice*. Nature, **455**, 204–207, (2008). 76

[131] Greif, Daniel, Parsons, Maxwell F., Mazurenko, Anton, Chiu, Christie S., Blatt, Sebastian, Huber, Florian, Ji, Geoffrey, and Greiner, Markus: *Site-resolved imaging of a fermionic Mott insulator*. Science, **351**(6276), 953–957, (2016), ISSN 0036-8075. 76

[132] Fukuhara, Takeshi, Takasu, Yosuke, Kumakura, Mitsutaka, and Takahashi, Yoshiro: *Degenerate Fermi Gases of Ytterbium*. Phys. Rev. Lett., **98**, 030401, Jan 2007. 76

[133] Stellmer, Simon, Grimm, Rudolf, and Schreck, Florian: *Production of quantum-degenerate strontium gases*. Phys. Rev. A, **87**, 013611, Jan 2013. 76

[134] Hofrichter, Christian, Riegger, Luis, Scazza, Francesco, Höfer, Moritz, Fernandes, Diogo Rio, Bloch, Immanuel, and Fölling, Simon: *Direct Probing of the Mott Crossover in the SU(N) Fermi-Hubbard Model*. Phys. Rev. X, **6**, 021030, Jun 2016. 76

[135] Gorshkov, AV, Hermele, M, Gurarie, V, Xu, C, Julienne, PS, Ye, J, Zoller, P, Demler, E, Lukin, MD, and Rey, AM: *Two-orbital su (n) magnetism with ultracold alkaline-earth atoms*. Nature Physics, **6**(4), 289–295, (2010). 76

[136] Park, Jee Woo, Will, Sebastian A., and Zwierlein, Martin W.: *Ultracold Dipolar Gas of Fermionic ^{23}Na^{40}K Molecules in Their Absolute Ground State*. Phys. Rev. Lett., **114**, 205302, May 2015. 76

[137] Huang, Kerson: *Statistical Mechanics*. John wiley and sons edition, (2000). 76, 95, 100, 102

[138] DeMarco, Brian: *Quantum behavior of an atomic Fermi gas*. PhD thesis, University of Colorado, (2001). 78

[139] O'Hara, K. M., Gehm, M. E., Granade, S. R., and Thomas, J. E.: *Scaling laws for evaporative cooling in time-dependent optical traps*. Phys. Rev. A, **64**, 051403, Oct 2001. 87

[140] Bourgain, R., Pellegrino, J., Fuhrmanek, A., Sortais, Y. R. P., and Browaeys, A.: *Evaporative cooling of a small number of atoms in a single-beam microscopic dipole trap*. Phys. Rev. A, **88**, 023428, Aug 2013. 87

[141] deCarvalho, Robert and Doyle, John: *Evaporative cooling at low trap depth*. Phys. Rev. A, **70**, 053409, Nov 2004. 88

[142] deCarvalho, R.: *Inelastic Scattering of Magnetically Trapped Atomic Chromium*. PhD thesis, Harvard University, (2003). 90

[143] Simoni, A. private communication. 92, 95

[144] Flambaum, V. V., Gribakin, G. F., and Harabati, C.: *Analytical calculation of cold-atom scattering*. Phys. Rev. A, **59**, 1998–2005, Mar 1999. 92, 93, 94

[145] ć, Zoran Pavlovi, Roos, Björn O., Côté, Robin, and Sadeghpour, H. R.: *Collisional properties of trapped cold chromium atoms*. Phys. Rev. A, **69**, 030701, Mar 2004. 93

[146] Ferrier-Barbut, I., Delehaye, M., Laurent, S., Grier, A. T., Pierce, M., Rem, B. S., Chevy, F., and Salomon, C.: *A mixture of Bose and Fermi superfluids*. Science, **345**(6200), 1035–1038, (2014), ISSN 0036-8075. 94

[147] Mølmer, Klaus: *Bose Condensates and Fermi Gases at Zero Temperature*. Phys. Rev. Lett., **80**, 1804–1807, Mar 1998. 95

[148] Colzi, Giacomo, Durastante, Gianmaria, Fava, Eleonora, Serafini, Simone, Lamporesi, Giacomo, and Ferrari, Gabriele: *Sub-Doppler cooling of sodium atoms in gray molasses*. Phys. Rev. A, **93**, 023421, Feb 2016. 95

[149] Wall, M L, Maeda, K, and Carr, Lincoln D: *Realizing unconventional quantum magnetism with symmetric top molecules*. New Journal of Physics, **17**(2), 025001, (2015). 96

[150] L., Gabardos: *Transitions radiofréquences entre états hyperfins du Chrome 53: Vers son imagerie résolue en spin*. Master's thesis, Laboratoire de Physique des Lasers, Université Paris 13 Nord, 2016. 97

[151] Santos, L., Fattori, M., Stuhler, J., and Pfau, T.: *Spinor condensates with a laser-induced quadratic Zeeman effect*. Phys. Rev. A, **75**, 053606, (2007). 103

[152] Grimm, Rudolf, Weidemüller, Matthias, and Ovchinnikov, Yurii B.: *Optical Dipole Traps for Neutral Atoms*. Volume **42** of *Advances In Atomic, Molecular, and Optical Physics*, pages 95 – 170. Academic Press, (2000). 103, 192

[153] Isoshima, Tomoya, Ohmi, Tetsuo, and Machida, Kazushige: *Double Phase Transitions in Magnetized Spinor Bose-Einstein Condensation*. Journal of the Physical Society of Japan, **69**, 3864–3869, (2000). 104, 105, 110, 127

[154] Ho, Tin Lun: *Spinor Bose Condensates in Optical Traps*. Phys. Rev. Lett., **81**, 742–745, (1998). 109, 110

[155] Kawaguchi, Yuki and Ueda, Masahito: *Spinor Bose-Einstein condensates*. Physics Reports, **520**(5), 253 – 381, (2012), ISSN 0370-1573. Spinor Bose-Einstein condensates. 110, 111, 206, 237, 238, 240

[156] Jacob, David, Shao, Lingxuan, Corre, Vincent, Zibold, Tilman, De Sarlo, Luigi, Mimoun, Emmanuel, Dalibard, Jean, and Gerbier, Fabrice: *Phase diagram of spin-1 antiferromagnetic Bose-Einstein condensates*. Phys. Rev. A, **86**, 061601, Dec 2012. 110

[157] Liu, Y., Jung, S., Maxwell, S. E., Turner, L. D., Tiesinga, E., and Lett, P. D.: *Quantum Phase Transitions and Continuous Observation of Spinor Dynamics in an Antiferromagnetic Condensate*. Phys. Rev. Lett., **102**, 125301, Mar 2009. 110

[158] Zhang, Wenxian, Yi, Su, and You, L.: *Bose-Einstein condensation of trapped interacting spin-1 atoms*. Phys. Rev. A, **70**, 043611, Oct 2004. 110

[159] Diener, Roberto B. and Ho, Tin Lun: *^{52}Cr Spinor Condensate: A Biaxial or Uniaxial Spin Nematic*. Phys. Rev. Lett., **96**, 190405, (2006). 111

[160] Kechadi, K.: *To appear in (2018)*. PhD thesis, Laboratoire de Physique des Lasers, Université Paris 13 Nord. 111

[161] Miesner, H. J., Stamper-Kurn, D. M., Andrews, M. R., Durfee, D. S., Inouye, S., and Ketterle, W.: *Bosonic Stimulation in the Formation of a Bose-Einstein Condensate*. Science, **279**(5353), 1005–1007, (1998), ISSN 0036-8075. 114

[162] Navon, Nir, Gaunt, Alexander L., Smith, Robert P., and Hadzibabic, Zoran: *Critical dynamics of spontaneous symmetry breaking in a homogeneous Bose gas*. Science, **347**(6218), 167–170, (2015), ISSN 0036-8075. 114

[163] Chomaz, Lauriane, Corman, Laura, Bienaimé, Tom, Desbuquois, Rémi, Weitenberg, Christof, Nascimbène, Sylvain, Beugnon, JérÃ´me, and Dalibard, Jean: *Emergence of coherence via transverse condensation in a uniform quasi-two-dimensional Bose gas*. Nat Commun, **6**, 892–895, (2007). 114

[164] Tammuz, Naaman, Smith, Robert P., Campbell, Robert L. D., Beattie, Scott, Moulder, Stuart, Dalibard, Jean, and Hadzibabic, Zoran: *Can a Bose Gas Be Saturated?* Phys. Rev. Lett., **106**, 230401, Jun 2011. 119

[165] Jackson, B. and Zaremba, E.: *Quadrupole Collective Modes in Trapped Finite-Temperature Bose-Einstein Condensates*. Phys. Rev. Lett., **88**, 180402, Apr 2002. 124

[166] Góral, Krzysztof, Gajda, Mariusz, and Rzażewski, Kazimierz: *Multi-mode description of an interacting Bose-Einstein condensate*. Opt. Express, **8**(2), 92–98, Jan 2001. 124

[167] Brewczyk, M., Gajda, M., and Rzażewski, K.: *Classical fields approximation for bosons at nonzero temperatures*. Journal of Physics B: Atomic, Molecular and Optical Physics, **40**(2), R1, (2007). 124

[168] Karpiuk, Tomasz, Brewczyk, Mirosław, Gajda, Mariusz, and Rzażewski, Kazimierz: *Constructing a classical field for a Bose-Einstein condensate in an arbitrary trapping potential: Quadrupole oscillations at nonzero temperatures*. Phys. Rev. A, **81**, 013629, Jan 2010. 124, 125

[169] Law, C. K., Pu, H., and Bigelow, N. P.: *Quantum Spins Mixing in Spinor Bose-Einstein Condensates*. Phys. Rev. Lett., **81**, 5257–5261, (1998). 133

[170] Olf, Ryan, Fang, Fang, Marti, G Edward, MacRae, Andrew, and Stamper-Kurn, Dan M: *Thermometry and cooling of a bose gas to 0.02 times the condensation temperature*. Nature Physics, **11**(9), 720–723, (2015). 134, 135, 157, 158, 240

[171] Leanhardt, AE, Pasquini, TA, Saba, M, Schirotzek, A, Shin, Y, Kielpinski, David, Pritchard, DE, and Ketterle, W: *Cooling bose-einstein condensates below 500 picokelvin*. Science, **301**(5639), 1513–1515, (2003). 134

[172] Greif, D., Uehlinger, T., Jotzu, G., Tarruell, L., and Esslinger, T.: *Short-range quantum magnetism of ultracold fermions in an optical lattice*. Science, **340**, 1307–1310, (2013). 134, 168

[173] Hart, Russell A, Duarte, Pedro M, Yang, Tsung Lin, Liu, Xinxing, Paiva, Thereza, Khatami, Ehsan, Scalettar, Richard T, Trivedi, Nandini, Huse, David A, and Hulet, Randall G: *Observation of antiferromagnetic correlations in the hubbard model with ultracold atoms*. Nature, **519**(7542), 211–214, (2015). 134, 168

[174] Boll, Martin, Hilker, Timon A, Salomon, Guillaume, Omran, Ahmed, Nespolo, Jacopo, Pollet, Lode, Bloch, Immanuel, and Gross, Christian: *Spin-and density-resolved microscopy of antiferromagnetic correlations in fermi-hubbard chains*. Science, **353**(6305), 1257–1260, (2016). 134

[175] C. Salomon, G. Shlyapnikov and Cugliandolo, L. F. (editors): *Many-Body Physics with ultracold gases, Proceedings of the Les Houches Summer School, Session XCIV*. Oxford university press edition, (2010). 134

[176] Bernier, Jean Sébastien, Kollath, Corinna, Georges, Antoine, De Leo, Lorenzo, Gerbier, Fabrice, Salomon, Christophe, and Köhl, Michael: *Cooling fermionic atoms in optical lattices by shaping the confinement*. Phys. Rev. A, **79**, 061601, Jun 2009. 135

[177] Medley, Patrick, Weld, David M., Miyake, Hirokazu, Pritchard, David E., and Ketterle, Wolfgang: *Spin Gradient Demagnetization Cooling of Ultracold Atoms*. Phys. Rev. Lett., **106**, 195301, May 2011. 135

[178] Pasquiou, B.: *Effects of dipole-dipole interaction on magnetic properties of a chromium condensate* . PhD thesis, Laboratoire de Physique des Lasers, Université Paris 13 Nord, (2011). 136, 215

[179] Lewandowski, H. J., McGuirk, J. M., Harber, D. M., and Cornell, E. A.: *Decoherence-Driven Cooling of a Degenerate Spinor Bose Gas*. Phys. Rev. Lett., **91**, 240404, Dec 2003. 143

[180] Schmidutz, Tobias F., Gotlibovych, Igor, Gaunt, Alexander L., Smith, Robert P., Navon, Nir, and Hadzibabic, Zoran: *Quantum Joule-Thomson Effect in a Saturated Homogeneous Bose Gas*. Phys. Rev. Lett., **112**, 040403, Jan 2014. 143

[181] Sarlo, Luigi De, Shao, Lingxuan, Corre, Vincent, Zibold, Tilman, Jacob, David, Dalibard, Jean, and Gerbier, Fabrice: *Spin fragmentation of Bose-Einstein condensates with antiferromagnetic interactions*. New Journal of Physics, **15**(11), 113039, (2013). 157

[182] Corre, V., Zibold, T., Frapolli, C., Shao, L., Dalibard, J., and Gerbier, F.: *Spin-1 condensates at thermal equilibrium: A SU(3) coherent state approach*. EPL (Europhysics Letters), **110**(2), 26001, (2015). 157

[183] Kashurnikov, V. A., Prokof'ev, N. V., and Svistunov, B. V.: *Revealing the superfluidˇMott-insulator transition in an optical lattice*. Phys. Rev. A, **66**, 031601, Sep 2002. 159

[184] Cohen-Tannoudji, C., Diu, B., and Laloë, F.: *Quantum Mechanics Vol I and II*. Hermann, editeur des sciences et des arts edition, (1998). 163, 215

[185] Greiner, Markus, Mandel, Olaf, Esslinger, Tilman, Hänsch, Theodor W, and Bloch, Immanuel: *Quantum phase transition from a superfluid to a mott insulator in a gas of ultracold atoms*. nature, **415**(6867), 39–44, (2002). 165, 202

[186] Giamarchi, T., Lucci, A., and Berthod, C.: *Lecture notes:Many Body physics*. University of Geneva, (2008-2013). 167

[187] Anderson, PW: *Present status of the theory of the high-tc cuprates*. Low Temperature Physics, **32**(4), 282–289, (2006). 167

[188] Auerbach, Assa: *Interacting electrons and quantum magnetism*. Springer Science & Business Media, (2012). 167

[189] *List of fermi temperautre for different solids*. http://hyperphysics.phy-astr.gsu.edu/HBase/tables/fermi.html. Accessed: 2016-10-15. 168

[190] *Phase diagram of a high tc superconductor*. http://atomcool.rice.edu/research/3d-lattice/. Accessed: 2016-10-10. 168

[191] Abragam, Anatole: *The principles of nuclear magnetism*. Number 32. Oxford university press, (1961). 169

[192] Paz, A. de, Chotia, A., Maréchal, E., Pedri, P., Vernac, L., Gorceix, O., and Laburthe-Tolra, B.: *Resonant demagnetization of a dipolar Bose-Einstein condensate in a three-dimensional optical lattice*. Phys. Rev. A, **87**, 051609, May 2013. 170

[193] Stamper-Kurn, Dan M. and Ueda, Masahito: *Spinor Bose gases: Symmetries, magnetism, and quantum dynamics*. Rev. Mod. Phys., **85**, 1191–1244, Jul 2013. 173

[194] Carrance, A.: *Pieges optiques pour des condensats de chrome*. Master's thesis, Laboratoire de Physique des Lasers, Université Paris 13 Nord, 2013. 174

[195] Kasevich, Mark and Chu, Steven: *Atomic interferometry using stimulated Raman transitions*. Phys. Rev. Lett., **67**, 181–184, Jul 1991. 180

[196] Denschlag, J Hecker, Simsarian, J E, Häffner, H, McKenzie, C, Browaeys, A, Cho, D, Helmerson, K, Rolston, S L, and Phillips, W D: *A Bose-Einstein condensate in an optical lattice*. Journal of Physics B: Atomic, Molecular and Optical Physics, **35**(14), 3095, (2002). 196, 202

[197] Ovchinnikov, Yu. B., Müller, J. H., Doery, M. R., Vredenbregt, E. J. D., Helmerson, K., Rolston, S. L., and Phillips, W. D.: *Diffraction of a Released Bose-Einstein Condensate by a Pulsed Standing Light Wave*. Phys. Rev. Lett., **83**, 284–287, Jul 1999. 196

[198] Fisher, Matthew P. A., Weichman, Peter B., Grinstein, G., and Fisher, Daniel S.: *Boson localization and the superfluid-insulator transition*. Phys. Rev. B, **40**, 546–570, Jul 1989. 199

[199] Born, M. and Fock, V.: *Beweis des adiabatensatzes*. Zeitschrift fur Physik, **51**, 165–180, March 1928. 201

[200] Bloch, Immanuel: *Ultracold quantum gases in optical lattices*. Nature Physics, **1**(1), 23–30, (2005). 202

[201] Orzel, Chad, Tuchman, AK, Fenselau, ML, Yasuda, M, and Kasevich, MA: *Squeezed states in a bose-einstein condensate*. Science, **291**(5512), 2386–2389, (2001). 202

[202] Ammann, Hubert and Christensen, Nelson: *Delta Kick Cooling: A New Method for Cooling Atoms*. Phys. Rev. Lett., **78**, 2088–2091, Mar 1997. 203

[203] Paz, A. de, Pedri, P., Sharma, A., Efremov, M., Naylor, B., Gorceix, O., Maréchal, E., Vernac, L., and Laburthe-Tolra, B.: *Probing spin dynamics from the Mott insulating to the superfluid regime in a dipolar lattice gas*. Phys. Rev. A, **93**, 021603, Feb 2016. 205, 210, 211

[204] Black, A. T., Gomez, E., Turner, L. D., Jung, S., and Lett, P. D.: *Spinor Dynamics in an Antiferromagnetic Spin-1 Condensate*. Phys. Rev. Lett., **99**, 070403, Aug 2007. 208, 239

[205] Lücke, Bernd, Peise, Jan, Vitagliano, Giuseppe, Arlt, Jan, Santos, Luis, Tóth, Géza, and Klempt, Carsten: *Detecting Multiparticle Entanglement of Dicke States*. Phys. Rev. Lett., **112**, 155304, Apr 2014. 212

[206] Kitagawa, Masahiro and Ueda, Masahito: *Squeezed spin states*. Phys. Rev. A, **47**, 5138–5143, Jun 1993. 213

[207] Kajtoch, Dariusz and Witkowska, Emilia: *Spin squeezing in dipolar spinor condensates*. Phys. Rev. A, **93**, 023627, Feb 2016. 213

[208] Polkovnikov, Anatoli: *Phase space representation of quantum dynamics*. Annals of Physics, **325**(8), 1790–1852, (2010). 228

[209] Hazzard, Kaden R. A., Manmana, Salvatore R., Foss-Feig, Michael, and Rey, Ana Maria: *Far-from-Equilibrium Quantum Magnetism with Ultracold Polar Molecules*. Phys. Rev. Lett., **110**, 075301, Feb 2013. 230

[210] Taylor, John R.: *An introduction to error analysis: The study of uncertainties in physical measurement*. Second edition, university science books edition, (1997). 236

[211] Fornasini, Paolo: *The Uncertainty in Physical Measurements: An introduction to Data Analysis in the physics Laboratory*. Springer edition, (2008). 236

Quantum gases of Chromium: thermodynamics and magnetic properties of a Bose-Einstein condensate and production of a Fermi sea

Abstract

This thesis presents experimental results performed with Quantum gases of Chromium atoms. The specificity of Chromium resides in its large electronic spin s=3 and non negligible dipole-dipole interaction between atoms.

We produced a new quantum gas, a Fermi sea of the ^{53}Cr isotope. Optimization of the co-evaporation with the ^{52}Cr bosonic isotope leads to 10^3 atoms at $T/T_F = 0.66 \pm 0.08$.

We obtained new results on thermodynamics of a spinor Bose gas. By "shock cooling" a thermal multi-spin component gas, we find that the condensation dynamics is affected by spin changing collisions. We also demonstrate a new cooling mechanism based on the spin degrees of freedom when the Bose Einstein condensate (BEC) is in the lowest energy spin state. Dipolar interactions thermally populate spin excited states at low magnetic field. Purification of the BEC is obtained by selectively removing these thermal atoms.

Finally, we present spin dynamics experiments. In a first experiment, spin dynamics following preparation of atoms in a double well trap in opposite stretch spin states allow to measure the last unknown scattering length of ^{52}Cr: $a_0 = 13.5\pm^{15}_{10}\ a_B$ (with a_B the Bohr radius). We then present preliminary results performed in a 3D lattice and in the bulk, where spin excitation is performed by a spin rotation. We investigate for different experimental configurations which of a theory with or without quantum correlations fits best our data.

Keywords: Bose-Einstein condensate, Fermi sea, dipolar interactions, thermodynamics for magnetism, cooling, optical lattices.

Gaz quantiques de Chrome: propriétés thermodynamiques et magnétiques d'un condensat de Bose-Einstein et production d'une mer de Fermi

Résumé

Le manuscrit présente des expériences réalisées avec des gaz quantiques de Chrome, un élément présentant un large spin électronique s=3 et des interactions dipolaires non négligeables.

Nous avons produit un nouveau gaz quantique, une mer de Fermi avec l'isotope ^{53}Cr contenant jusqu'à 1000 atomes à $T/T_F = 0.66 \pm 0.08$, en optimisant la co-évaporation avec l'isotope bosonique.

Nous avons obtenu de nouveaux résultats sur la thermodynamique d'un condensat de Bose Einstein (CBE) avec degré de liberté de spin. En refroidissant rapidement un gaz thermique multi-composante, nous observons que la dynamique de condensation est affectée par les collisions d'échange de spin. Nous démontrons aussi un nouveau mécanisme de refroidissement, utilisant le degré de liberté de spin, lorsque le CBE est produit dans le niveau de spin de plus basse énergie. Les interactions dipolaires peuplent thermiquement les états de spin excités à bas champ magnétique, et une purification du CBE est obtenue en retirant sélectivement ces atomes.

Enfin nous présentons des expériences de dynamique de spin. Dans une première expérience, cette dynamique est obtenue en utilisant un double puits avec des états de spin opposés. Ceci a permis une première mesure d'une des longueurs de diffusion du ^{52}Cr: $a_0 = 13.5\pm^{15}_{10}\ a_B$. Nous présentons également des résultats préliminaires dans un piège harmonique et dans un réseau 3D. La dynamique de spin est produite par rotation du spin des atomes. La comparaison avec la théorie nous permet de mettre en évidences l'apparition de corrélations quantiques.

Mot clés: Condensation de Bose Einstein, mer de Fermi, interactions dipolaires, thermodynamique du magnétisme, refroidissement, réseaux optiques, échange de spin.